Transport Phenomena on the Channel-Rib Scale of Polymer Electrolyte Fuel Cells

A dissertation submitted to

ETH ZURICH

for the degree of

Doctor of Sciences

presented by

RETO FLÜCKIGER

Dipl. Masch. Ing. ETH Zurich

born 26.05.1978

citizen of Switzerland

accepted on the recommendation of

Prof. Dr. Alexander Wokaun, examiner

Prof. Dr. Dimos Poulikakos, co-examiner

Dr. Günther G. Scherer, co-examiner

Dr. Felix N. Büchi, co-examiner

2009

"Computers are useless. They can only give you answers."
Pablo Picasso, Spanish cubist painter, (1881 - 1973)

Abstract

The channel-rib scale in PEFC is typically a few millimeters large and composed of a gas distributing channel, a current collecting rib and a membrane electrode assembly (MEA) between the anode and cathode side of the cell. The motivation for a thorough investigation of the channel-rib scale is given by the close coupling of losses to the next higher cell and next lower catalyst scale. Experimental channel-rib current density distributions showed significant differences between channel and rib behavior. This was mainly attributed to mass and charge transport effects. Due to the complexity of the system, a full understanding and quantification of losses was not possible with experiments only. Although numerical models of the channel-rib scale are widespread they have limited predictive capabilities due to an insufficient parameterization or a lack of experimental validation.

In this dissertation a sound material characterization of porous components built the foundation for a multiphysics finite element model in COMSOL (cf. Chap. 7). Experimental details are described in Chap. 4 and the corresponding results are discussed in Chap. 5. The diffusivity of the gas diffusion layer (GDL) was considered as one of the main properties determining the maximum power density of PEFC. Due to the deficiency of conventional diffusimetry methods a novel measurement technique was developed and applied. The electrochemical diffusimetry uses Electrochemical Impedance Spectroscopy (EIS) to measure the effective ionic conductivity of the porous network, which was filled previously with electrolyte. Thereby it is assumed that the tortuosity of the porous network is the same for ion migration and gas diffusion. The electrochemical diffusimetry method provided a fast and accurate tool for an in-depth parameter study. The diffusivity of different gas diffusion layer materials was measured for the first time as a function of direction and mechanical compression. The results revealed a strong anisotropy and disproved the morphology models applied so far for the effective diffusivity of gas diffusion layers.

Besides the mass transport limitations induced by the porous structures itself, condensation of product water within the supply network can additionally reduce the power density. This phenomena is know as flooding and generally studied by neutron imaging. Another complementary visualization method for liquid water has been developed in the context of this thesis. With the TOMCAT beamline at the Swiss Light Source (SLS), X-ray tomographic microscopy with a pixel resolution below one mi-

crometer is possible. The strength of X-ray tomographic microscopy is a high spatial and temporal resolution with simultaneous contrast for water and carbon. The applicability to dry gas diffusion layers was demonstrated first by studying structural changes under mechanical compression. In the next step the water intrusion into the porous network for different capillary pressures was studied. The experiment visualized for the first time the inhomogeneous filling behavior of gas diffusion layers with a sufficient resolution. Owing to these results a liquid water retention effect at the first dense layer was revealed. None of the tested capillary pressure functions was able to reproduce this two-step filling behavior. The high potential of the method to become a standard tool for liquid water studies in PEFC was confirmed with first *in-situ* active cell experiments.

The characterization work also included a second central component of the channel-rib scale: the catalyst layer (CL). Chap. 6 describes the Fortran implementation and results of the catalyst pore scale model (CPSM). In order for the catalyst layer to promote the electrochemical reaction, it has to transport electrons, protons, gases and liquid water at the same time. The effective transport parameters of the various species are difficult to measure on the complex porous structure. With the CPSM they could be made accessible and the large range of literature values could be confined. In the first part of the model the structure is generated by a random distribution of sphere centers on a 3D grid. The subsequent labeling routine marks the gaseous, ionic and electric phases depending on the carbon particle radius and ionomer layer thickness. The solution algorithm solves the uncoupled potential equation for all three phases and directions on the generated structure sequentially. The results were carefully verified in terms of input parameters, representative element volume (REV), randomness and grid independency. The variation of input parameters showed a significant percolation effect for diffusion and conduction. Finally a best fit for the catalyst layer used in the channel-rib model and an optimized catalyst layer structure were proposed.

Based on the thorough material characterization a mechanistic model of the channel-rib scale was implemented (cf. Chap. 7). The model accounts for Stefan Maxwell multicomponent diffusion, liquid water transport and electric charge transport in the gas diffusion and catalyst layers. Ionic charge and membrane water transport are considered in the catalyst layers and the membrane. Furthermore momentum transport in the gas diffusion layers has been included to study the effect of rib compression. The coupling of the physics is done via electrochemical reaction, condensation-evaporation and absorption-desorption rates. The model physics required 23 relevant material parameters of which 14 were measured, 6 were taken from literature and only 3 were fitted. The physics were then transfered step by step from a 1D

test model into the 2D channel-rib model. This allowed to follow the approach of experimental and numerical channel-rib current densities. The final agreement was good for fully humidified oxygen operation. The validation of this operating point provided a discrimination and quantification of channel-rib losses, which were not accessible by experiments before. However, the model failed by changing the operating parameters towards low humidity and low oxygen partial pressures while keeping the material parameters constant. Several weak points of the existing model were identified and presented for future improvements.

The output of this thesis can be sharpened to three general conclusion. 1) Transport properties of the PEFC components have to be know exactly as a function of mechanical compression and direction in order to reproduce experimental results of the channel-rib scale with a numerical model. 2) A validated channel-rib model provides quantitative field distributions and improves the understanding of the involved losses. 3) X-ray tomographic microscopy is a complementary method to neutron imaging for the quantification of porous components in PEFC and the transport of liquid water therein.

Zusammenfassung

Die Kanal-Steg Skala in Polymer Elektrolyt Brennstoffzellen (PEFC) ist typischerweise einige Millimeter gross und besteht aus einem Gasverteiler Kanal, einem Stromsammler Steg und einer Membran-Elektroden Einheit (MEA) zwischen der Anoden- und Kathodenseite der Zelle. Die Motivation für eine genaue Untersuchung der Kanal-Steg Skala ist gegeben durch die enge Kopplung von Verlusten mit der nächst höheren Zellenskala und der nächst tieferen Katalysatorskala. Experimentelle Kanal-Steg Stromdichteverteilungen haben einen signifikanten Unterschied zwischen Kanal und Steg Verhalten gezeigt. Die Unterschiede wurden hauptsächlich Massentransport und Ladungstransport Effekten zugeordnet. Wegen der Komplexität des Systems konnte bisher mit Experimenten noch kein umfangreiches Verständnis und keine vollständige Quantifizierung der Verluste erreicht werden. Obwohl numerische Modelle der Kanal-Steg Skala schon weitverbreitet sind ist ihre Aussagekraft wegen ungenügender Parametrisierung und Validierung limitiert.

In dieser Dissertation bildete eine gründliche Material Charakterisierung der porösen PEFC Komponenten die Basis für ein multiphysikalisches Finite Elemente Modell in COMSOL (vgl. Kap. 7). Experimentelle Details zur Charakterisierung werden in Kap. 4 beschrieben und die entsprechenden Resultate sind in Kap. 5 diskutiert. Die Diffusivität der Gasdiffusionsschicht (GDL) wird als eine der Haupteigenschaften betrachtet welche die maximale Leistungsdichte von PEFC's bestimmen. Wegen der Nachteile von konventionellen Diffusimetrie Methoden wurde eine neuartige Technik entwickelt und angewandt. Die elektrochemische Diffusimetrie Methode benutzt die Elektrochemische Impedanz Spektroskopie (EIS) zur Messung der effektiven ionischen Leitfähigkeit des porösen Netzwerks welches zuvor mit Elektrolyt gefüllt wurde. Dabei wird angenommen, dass die Tortuosität des Netzwerks dieselbe ist für Ionenmigration und Gasdiffusion. Die Elektrochemische Diffusimetrie Methode lieferte ein schnelles und präzises Werkzeug für eine vertiefte Parameterstudie. Die Diffusivität von verschiedenen GDL Materialien wurde zum ersten Mal als Funktion der räumlichen Ausrichtung und mechanischen Kompression gemessen. Die Resultate zeigten eine starke Anisotropie und widerlegten die bisher benutzten, morphologischen Modelle zur Diffusivitätsbestimmung von GDL's.

Neben Massentransport Limitierungen durch die porösen Strukturen selbst kann auch Kondensation von Produktwasser in den Poren die Reaktionsmittelzufuhr und

damit die Leistungsdichte zusätzlich reduzieren. Dieses Phänomen is bekannt als Flutung und wird normalerweise mit Hilfe von Neutronen Radiographie untersucht. Eine ergänzende Visualisierungsmethode für flüssiges Wasser wurde im Rahmen dieser Arbeit entwickelt. Mit der TOMCAT Strahllinie der Swiss Light Source (SLS) ist es möglich Röntgentomographie mit einer Pixel Auflösung unter einem Mikrometer durchzuführen. Die Stärke der Synchrotron Röntgentomographie ist eine hohe räumliche und zeitliche Auflösung mit gleichzeitigem Kontrast für Wasser und Kohlenstoff. Die Anwendbarkeit für trockene GDL's konte mit der Visualisierung von Strukturveränderungen unter mechanischer Belastung gezeigt werden. Im nächsten Schritt wurde das Eindringen von Wasser in das poröse Netzwerk bei verschiedenen Kapillardrücken studiert. Das Experiment visualisierte zum ersten Mal mit einer genügenden Auflösung das inhomogene Benetzungsverhalten von Gasdiffusionsschichten. Mit diesen Resultaten konte ein Staueffekt an der ersten dichten Schicht deutlich gemacht werden. Keine der getesteten, theoretischen Kapillardruck-Sättigungskurven war in der Lage diese zweistufige Benetzung zu reproduzieren. Das Potential der Synchrotron Röntgentomographie zu einer Standard Methode der Wasservisualisierung in PEFC zu werden, konte mit ersten Messungen an aktiven Zellen demonstriert werden.

Die Charakterisierung beinhaltete neben der Gasdiffusionsschicht auch eine weitere, zentrale Komponente der Kanal-Steg Skala: die Katalysatorschicht. Kap. 6 beschreibt die Fortran Implementierung und die Resultate des Katalysator Porenskalen Modells (CPSM). Damit die Katalysatorschicht die elektrochemische Reaktion antreiben kann muss sie gleichzeitig den Transport von Elektronen, Protonen, Gasen und flüssigem Wasser sicherstellen. Die effektiven Transport Parameter der verschiedenen Spezies sind an der komplexen porösen Struktur nur schwierig zu messen. Mit dem CPSM konnten diese zugänglich gemacht und damit die grosse Bandbreite von Literaturwerten eingeschränkt werden. Im ersten Teil des Modells wird die Struktur durch eine zufällige Verteilung von Kugelzentren auf einem 3D Gitter generiert. Die nachfolgende Markierungsfunktion unterscheidet Gas-, Ionomer- und Festphasen abhängig vom Kohlenstoffpartikel Radius und der Ionomer-Schichtdicke. Der Lösungsalgorithmus berechnet die ungekoppelten Potentialgleichungen für alle drei Phasen und räumlichen Ausrichtungen auf der vorgängig erstellten 3D Struktur. Die Resultate wurde sorgfältig überprüft im Hinblick auf Eingangsparameter, kleinste Wiederholungseinheit und Gitterunabhängigkeit. Die Variation der Eingangsparameter zeigte eine signifikante Perkolation der Diffusivität und elektrischen Leitfähigkeit. Schlussendlich wurde eine passende Struktur für das Kanal-Steg Modell und eine optimierte Katalysatorzusammensetzung vorgeschlagen.

Basierend auf der detaillierten Material Charakterisierung wurde ein mechanistisch-

es Modell der Kanal-Steg Skala implementiert (vgl. Kap. 7). Das Modell berücksichtigt Stefan Maxwell Multikomponenten Diffusion, Flüssigwasser Transport und Elektronen Transport in der Gasdiffusionsschicht und Katalysatorschicht. Ionen Transport und Membran Wasser Transport sind in der Katalysatorschicht und der Membran enthalten. Des Weiteren wurde der Impulstransport in der Gasdiffusionsschicht miteinbezogen zur Untersuchung von Steg Kompressionseffekten. Die Kopplung der Physik wurde über elektrochemische Reaktions-, Kondensations-/ Verdampfungs- und Absorptions-/ Desorptionsraten realisiert. Die Modell Physik benötigte 23 relevante Materialparameter von denen 14 gemessen wurden, 6 aus der Literatur stammen und nur 3 gefittet werden mussten. Die unterschiedliche Physik wurde Schritt für Schritt von einem 1D Testmodel in ein 2D Kanal-Steg Modell transferiert. Das erlaubte die Rückverfolgung der Anäherung von experimenteller und numerischer Kanal-Steg Stromdichteverteilung. Die schlussendliche Übereinstimmung war gut für vollbefeuchteten Sauerstoffbetrieb. Die Validierung dieses Betriebspunkts lieferte eine genaue Unterscheidung und Quantifizierung von Kanal-Steg Verlusten welche experimentell nicht zugänglich waren. Dennoch versagte das Modell bei einer Änderung der Betriebsparameter zu tieferen relativen Feuchtigkeiten und Sauerstoff Partialdrücken bei gleichbleibenden Materialparametern. Verschiedene Schwachpunkte und entsprechende Verbesserungsvorschläge der aktuellen Modellimplementierung konnten identifiziert werden.

Das Ergebnis dieser Arbeit kann in drei generellen Schlussfolgerungen zusammengefasst werden. 1) Für die Validierung von experimentellen Kanal-Steg Resultaten müssen die Transport Eigenschaften der PEFC Komponenten als Funktion der mechanischen Kompression und räumlichen Ausrichtung bekannt sein. 2) Ein validiertes Kanal-Steg Modell liefert quantitative Verteilungen physikalischer Grössen und verbessert das Verständnis der involvierten Verluste. 3) Synchrotron Röntgentomographie ist eine komplementäre Methode zur Neutronen Radiographie für die Quantifizierung von porösen Komponenten in PEFC und den darin stattfindenden Wasser Transport.

Acknowledgements

The seeds for this work were planted by a number of people. I am foremost grateful to Prof. A. Wokaun for giving me the unique opportunity to work towards my Ph.D. in the general energy department at PSI. I am also indebted to Günther Scherer for the possibility to profit from the broad expertise of the electrochemistry laboratory at PSI. My biggest appreciation belongs to Felix Büchi, head of the fuel cell system group. I was not only able to benefit from his scientific but also from his personal support. Prof. D. Poulikakos from the institute of energy technology at ETH deserves a special thank for his willingness to review my thesis as a co-examiner.

I had the privilege to accomplish a part of this thesis in the group of Prof. N. Djilali at the University of Victoria, Canada. The fruitful exchange was only possible thanks to the openness of Prof. N. Djilali and Prof. A. Wokaun. I owe the scientific and personal gain of this stay to Peng-Chei (Jay) Sui, who introduced me to the art of catalyst layer modeling and the Canadian way of life.

An important seed for this work was planted by Denis Kramer and Stefan Freunberger. They had the ingenious idea for the electrochemical diffusimetry method that I finally realized and applied in this thesis. I acknowledge their input and support. Another crucial seed was set by Mathias Reum with his sophisticated micro-cell setup, which delivered a valuable experimental database for my model validation. I appreciate his effort, our scientific and philosophic channel-rib discussions and the lively office environment.

During my thesis I was able to profit from another privilege: measuring at the TOMCAT beamline of the Swiss Light Source (SLS). Thanks to the unique properties of the beamline and the outstanding support of the crew, the method produced unrivaled results. Therefore I am deeply grateful to Prof. M. Stampanoni for the interdisciplinary collaboration and hope the success story continuous with my successor Jens Eller.

I was not only able to profit from wise planters but also from capable harvesters. I would like to mention and acknowledge first the extraordinary support of the fuel cell system group members during the TOMCAT measurement campaigns. Without their sleepless nights the results would not have been a quarter as good. The master student Denis Tehlar was a lucky strike. It was joy to work and discuss with him modeling and experimental issues. I thank him for his autonomy and for releasing

List of Symbols

symbol	unit	description
A	$m^2\,m^{-3}$	volume specific surface
A	m^2	cross section area
a	—	activity
b	—	Brooks-Corey fitting coefficient
C	$F\,m^{-3}$	double layer capacitance per unit volume
c	$mol\,m^{-3}$	concentration
cct	—	cathode charge transfer
act	—	anode charge transfer
CL	—	catalyst layer
CH	—	channel
D	$m^2\,s^{-1}$	diffusivity
D	m	diameter
$\underline{D}$	—	elasticity matrix
d	m	thickness
E	Pa	Young's modulus
E	V	equilibrium cell voltage
EW	$kg\,mol^{-1}$	equivalent weight
F	$C\,mol^{-1}$	Faraday constant
f	—	oxygen fraction
GDL	—	gas diffusion layer
h	—	rate constant
$\mathbf{i}$	—	imaginary number $\sqrt{-1}$
IEC	$mol\,kg^{-1}$	ion exchange capacity
I	A	integral electric current
J	$A\,m^{-3}$	volumetric current density
j	$A\,m^{-2}$	geometric current density
$\tilde{j}$	$A\,m^{-2}$	microscopic current density
k	—	relative permeability
K	m^2	absolute permeability
Kn	—	Knudsen number
$\mathbf{M}$	$kg\,m^{-2}\,s^{-1}$	mass flux vector
M	$kg\,mol^{-1}$	molar mass
MEM	—	membrane

m	–	saturation exponent for diffusivity
N	–	number of grid points
$\mathbf{N}$	$kg\,m^{-2}\,s^{-1}$	molar flux vector
n	–	electroosmotic drag coefficent
Pe	–	Peclet number
$PFSA$	–	perfluorated sulfonic acid
RH	–	relative humidity
R	$mol\,m^{-3}\,s^{-1}$	molar reaction rate
Re	–	Reynolds number
R	$J\,mol^{-1}\,K^{-1}$	ideal gas constant
R	m	radius
r	m	radius
s	m	liquid water saturation
S	$kg\,m^{-3}\,s^{-1}$	species mass source
Sc	–	Schmidt number
T	$^{\circ}K$	temperature
U	V	non-equilibrium cell voltage
u	m	x-displacement
v	m	y-displacement
$\mathbf{v}$	$m\,s^{-1}$	velocity vector
V	m^3	volume
w	–	weight fraction
x	–	molar fraction
Z	Ω	impedance

greek

α	–	charge transfer coefficient
β	–	imaginary part of index of refraction
β	$N\,m^{-1}$	Tomadakis fitting coefficient
δ	m	thickness
δ	–	real part of index of refraction
ε	–	porosity
ζ	Pa	normal stress
η	V	overpotential
θ	deg	contact angle
ι	$S\,m^{-1}$	ionic conductivity
λ	$"H_2O \text{ per } SO_3^-"$	membrane water per sulfonate group
λ	–	gas stoichiometry
λ	m	mean free path
μ	$kg\,m^{-1}\,s^{-1}$	dynamic viscosity

μ	cm^{-1}		linear absorption coefficient
ν	$-$		strain
ζ	$N\,m^{-1}$		surface tension
ρ	$kg\,m^{-3}$		density
σ	$S\,m^{-1}$		electric conductivity
σ	m		molecule diameter
τ	$-$		tortuosity
υ	$-$		Poisson's ratio
Φ	rad		phase shift angle
ϕ	V		electric potential
φ	deg		surface orientation angle
χ	V		ionic potential
ψ	Pa		shear stress
ω	$rad\,s^{-1}$		radial frequency
∇	$-$		nabla operator $(\partial/\partial x, \partial/\partial y, \partial/\partial z)$

subscript

a	anode
a	water absorption
ad	water absorption - desorption
bt	break-through
c	cathode
c	water condensation
c	capillary
C	carbon
cct	cathode charge transfer
act	anode charge transfer
ce	water condensation - evaporation
cr	critical
d	water desorption
e	water evaporation
e	electronic
eff	effective
g	gas
hor	hydrogen oxydation reaction
H_2	hydrogen
H_2O	water
i	ionic
ip	in-plane direction
kl	binary gas mixture

l	liquid
m	membrane
N_2	nitrogen
nwt	non-wetting
o	orthotropic
ohm	ohmic
orr	oxygen reduction reaction
O_2	oxygen
ref	reference conditions
SO_3^{-1}	sulfonate group
tr	threshold
tp	through-plane direction
wt	wetting
x	x-coordinate (ip direction)
y	y-coordinate (tp direction)
0	equilibrium
0	uncompressed conditions

superscript

a	anode
c	cathode
CL	catalyst layer
FF	flowfield
GDL	gas diffusion layer
i	domain
l	liquid
m	ionomer
MEM	membrane
s	solid
v	void

Contents

1 Motivation & Background

The total distance traveled by the world citizens today is around 23 billion kilometers. This figure is estimated to rise up to 105 billion kilometers by 2050 [1] due to an increasing demand in the newly industrializing countries. The car density in these countries is below 150 cars per 1000 inhabitants at the moment. With increasing wealth the density may rise up to around 600 cars per 1000 inhabitants. The growth of population in the emerging countries is additionally responsible for the quadruplication of the world mobility by 2050.

About one third of the world primary energy consumption is related to oil of which about 60% goes into the transportation sector [2]. Consequently the problems related to oil are directly linked to the individual mobility. First of all the oil reserves are finite and the production is expected to peak in the next years. Closely connected to the scarcity of energy sources for transportation are the price fluctuations and speculations. Last but not least burning fossil fuels results in local and global emissions of nitrogen oxides, sulfur dioxide and carbon dioxide.

A possible trend of future vehicle propulsion systems goes towards electrification as shown by numerous hybrid-electric vehicles emerging in the market today. Whether electric vehicles will prevail in the future is still debated [3–5]. However, if such vehicles prevail there are two promising options to provide the necessary on-board electricity: Fuel cells and batteries.

For small automotive applications the power train has to deliver an average power of around 20 kW with peaks up to 80 kW. Consequently the system has to be efficient over a wide range of operating points. Another crucial point is the power and energy per mass. Batteries have made a tremendous progress in terms of power density in the last years. However, battery electric vehicles still have a small driving range and a long recharging time limiting its use to urban areas. Another barrier for a large scale introduction of battery electric vehicles is todays grid infrastructure. If 60% of the oil primary energy has to be replaced by a renewable source and transformed to electricity to recharge the vehicles, todays grid infrastructure has to be renewed completely.

Polymer electrolyte fuel cells (PEFC) on the other hand have the advantage of superior energy densities resulting in extended driving ranges compared to batteries. The refueling with hydrogen is fast and requires no adaption of the electric grid in-

frastructure. The low operating temperature allows fast start-ups and the solid state electrolyte is especially suited for mobile applications. Hydrogen as a future carrier of renewable energy for transportation has several advantages. It can be produced from a multitude of sources such as electrolysis of water with electricity, thermo-chemical water splitting or steam reforming of natural gas. Hydrogen can be stored relatively easy compared to electricity. At the point of use, hydrogen does not emit any pollutants and if converted in a fuel cell, average tank-to-wheel efficiencies of 45% are possible. In comparison, internal combustion engines (ICE) have average tank-to-wheel efficiencies of 20% wasting twice as much fuel. Furthermore the internal combustion engine has its highest efficiency at maximum load whereas a fuel cell system can be operated efficiently at part load.

Beside the premise of a hydrogen economy and distribution infrastructure the fuel cell electric vehicle has to overcome several other barriers. First of all the cost of the power-train has to be competitive with internal combustion engines (25-35 $/kW). The US department of energy defined a goal of 30 $/kW by 2015 [6] excluding the hydrogen storage and electric drive. Today the cost for prototype fuel cell systems are around 1000 $/kW with the catalyst layer, membrane and bipolar plate having the biggest share [7]. Another issue is the durability of the membrane and catalyst layer. 5000 hours of operation with cycling is required by 2015 in order to be competitive with ICE [6]. Some systems have demonstrated steady state lifetimes up to 20000 hours but under the dynamic load changes of an urban driving cycle, acceptable degradation has not been achieved over 2000 hours. Finally the power density of the fuel cell system excluding hydrogen storage and electric drive has to increase from around 300 to 650 W/kg by 2015 [6].

The high power density in a polymer electrolyte fuel cell is mainly limited by the supply of oxygen to the reaction site. This supply is driven by convective transport from the compressor to the stack and to the single cell. In the single cell the transport on the last few millimeters is dominated by diffusion through porous media. Water produced by the electrochemical reaction tends to accumulate in these pores and additionally impedes the oxygen transport. Therefore it is of prime importance to understand gas diffusion and liquid water transport effects on the scale of a few millimeters around the reaction area. This area is the so called channel-rib scale.

In this thesis a computational model of the channel-rib scale is developed. Due to limited accessibility, *in-situ* experiments on this scale are difficult. Some values of interest are even impossible to measure and solely rely on model predictions. However, the quality of the model is only as good as the transport parameters that are employed. Most of the models so far are based on inaccurate parameterizations. Especially the diffusion properties of the porous structures and its dependencies are

poorly understood. Therefore a new *ex-situ* measurement method to study diffusion effects in porous materials is developed.

The water transport and the resulting distribution in the porous media is imaged using X-ray tomography with an unrivaled resolution. This high resolution allows for more fundamental insights into the liquid-solid interactions and provides a solid foundation for the development of appropriate water transport models. Finally the results of these *ex-situ* characterizations are used to improve the model predictions of a channel-rib model and to understand the complex coupling of the different physics. A fully validated channel-rib model will allow design and material optimization studies to improve the reactant supply and consequently the power densities of future PEFC systems.

2 Introduction

In 1839, the Swiss chemist Christian Friedrich Schönbein and the British lawyer and physicist William Grove first published the principle of a fuel cell [8]. However, due to the invention of the electric generator around 1831, the development of the internal combustion engine and the discovery of cheap and abundant oil around 1860, it took more than a century until the fuel cell principle was first used in a real application. NASA successfully used and still uses alkaline fuel cells during space flights. Since then industry began to recognize the commercial potential of fuel cells. With the energy crisis 1973 and increased environmental concerns fuel cell research and development gained significant financial support. As a consequence hundreds of companies and research institutes are working towards commercialization of fuel cells while dealing with performance, durability and cost issues.

A fuel cell is an electrochemical reactor that takes a fuel and an oxidant (oxygen) as input and produces electricity and heat as output. The chemical energy of the fuel is directly converted into electric energy. In contrast to a battery a fuel cell is continuously supplied with fuel and can therefore not be depleted. The fuel is stored in an external tank. A fuel cell is therefore comparable to a combustion engine, which is a thermal reactor, in terms of continuous fuel supply. The reversible efficiency of the conversion from chemical energy to mechanical energy in combustion engines is limited by the Carnot efficiency [9] while the reversible efficiency of a fuel cell is given by the ratio of Gibbs free energy and enthalpy. The fuel cell reversible efficiency is thus significantly higher at lower temperatures due to the lower entropy production.

Besides the high efficiency, fuel cells produce no NO_x or particulate matter at the point of conversion. If the fuel is produced from renewable sources (e.g. biomass) even the CO_2 cycle is closed. Another advantage of fuel cells compared to combustion engines is the absence of moving parts which make them potentially long-lasting and allow silent operation. Unlike batteries, fuel cells can scale the available power (size of the cell) and energy (size of the fuel tank) independently. The external fuel storage allows continuous operation or fast refueling and a high overall energy density. The energy and power densities of different conversion/storage devices are compared in Table 2.1. Compared to the benchmark of internal combustion engines, todays lithium ion batteries are inferior in terms of energy density while todays polymer electrolyte fuel cells are inferior in terms of power density.

conversion/storage technology	energy density / $Wh\,kg^{-1}$	power density / $W\,kg^{-1}$
internal combustion engine*	700-1500	100-1000
lithium ion battery [10]	110-160	100-1000
supercapacitor [11]	0.05-10	$10\text{-}10^5$
polymer electrolyte fuel cell* [6]	200-1000	10-420

Table 2.1: Comparison of energy and power densities of different energy conversion/storage devices (status 2005).* the weight of the tank is not considered.

This thesis focuses on the H_2/O_2 polymer electrolyte fuel cell (PEFC), which is named after the polymer membrane used as the electrolyte. The PEFC is especially suited for the fuel cell electric vehicle (FCEV) application due to the solid polymer and the low operating temperature. The main barriers for successful FCEV's are high cost of catalyst and membrane [7], low power density, lifetime under dynamic conditions and hydrogen on-board storage issues.

2.1 PEFC Working Principle

Fig. 2.1 shows the components and schematic assembly of a polymer electrolyte fuel cell. The steps required to produce electricity in a PEFC are described in the following.

Transport of Reactants

Hydrogen and oxygen have to be feed continuously from the tank and/or ambient air to the active area of the cell. The convective transport on system level is accomplished by overpressure or a compressor and has to be controlled carefully depending on the current density and stoichiometry of the cell. On cell level the reactants are distributed over the entire cell area by convection in a channel structure, the so called flowfield. The flowfield is machined into the bipolar plate (BIP) which electrically connects anode and cathode of two adjacent cells in a stack (serial connection). After distribution over the cell area the gases reach the active sites in the catalyst layers (CL_a, CL_c) mainly by diffusion through the porous gas diffusion layers (GDL_a, GDL_c).

Electrochemical Reactions

The porous catalyst layers coated on both sides of the membrane (MEM) are typically made of catalyst nanoparticles supported on carbon and bonded by a polymer electrolyte matrix. This ensures a high surface area and close contact of electric, ionic and
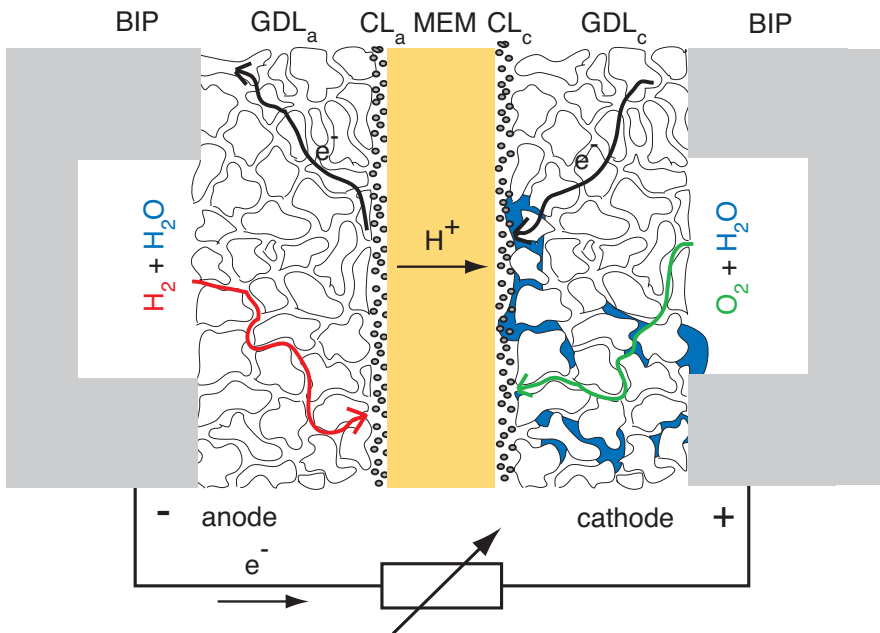
Figure 2.1: Schematic of the working principle of a PEFC. Humidified reactant gases are feed through the channels of the bipolar plates (BIP) and diffuse through the gas diffusion layers to the reaction sites in the catalyst layers. Electrons freed in the CL_a pass over the external circuit and load to the cathode side where they recombine with protons that moved through the electrolyte and with oxygen to water. Product water has to pass mainly the GDL_c in liquid or gaseous form.

gaseous phases required for the electrochemical half cell reactions. The oxidation of H_2 takes place in the anode CL and the reduction of O_2 in the cathode CL. Without catalyst the reaction rates at $70\,°C$ operating temperature would be much too slow. Typically platinum is used as catalyst due to the optimal absorption-desorption ability for H and O intermediates. A possible reaction pathway for the hydrogen oxidation reaction (HOR) is the adsorption of an hydrogen molecule on two adjacent active Pt sites

$$H_2 + 2Pt \rightleftharpoons 2Pt\text{-}H \tag{2.1}$$

with the subsequent desorption of two protons and the release of two electrons

$$2Pt\text{-}H \rightleftharpoons 2Pt + 2H^+ + 2e^- \tag{2.2}$$

The overall HOR half cell reaction reads

$$H_2 \rightleftharpoons 2H^+ + 2e^- \tag{2.3}$$

The oxygen reduction reaction (ORR) in the cathode CL is one of the rate limiting steps in PEFC and has therefore been studied extensively. A possible reaction mechanism taken from Hamann and Vielstich [12] is presented below. Molecular oxygen adsorbs on an active Pt site

$$O_2 + Pt \rightleftharpoons Pt\text{-}O_2 \tag{2.4}$$

Together with an electron and proton from the HOR an adsorbed HO_2 intermediate is formed:

$$Pt\text{-}O_2 + H^+ + e^- \rightleftharpoons Pt\text{-}HO_2 \tag{2.5}$$
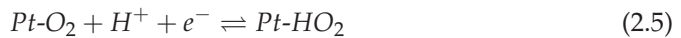
Using an additional adjacent active site the intermediate is split into an adsorbed hydroxyl and adsorbed oxygen atom

$$Pt\text{-}HO_2 + Pt \rightleftharpoons Pt\text{-}OH + Pt\text{-}O \tag{2.6}$$
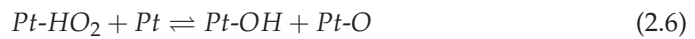
This step is rate limiting for this reaction pathway. Finally with three additional protons and electrons from the HOR, two water molecules are desorbed

$$Pt\text{-}OH + Pt\text{-}O + 3H^+ + 3e^- \rightleftharpoons 2Pt + 2H_2O \tag{2.7}$$
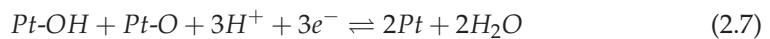
The overall ORR half cell reaction reads

$$O_2 + 4H^+ + 4e^- \rightleftharpoons 2H_2O \tag{2.8}$$

In the overall PEFC reaction equation charge balance is maintained and for every electron produced in the anode CL a proton must migrate through the electrolyte to the cathode CL.

$$H_2 + \frac{1}{2}O_2 \rightleftharpoons H_2O \tag{2.9}$$

Transport of Charge

The polymer electrolyte membrane (MEM) spatially separates the fuel H_2 and oxidant O_2. It ensures that the two half cell reactions take place separately. However, gas cross over can take place resulting in a reduced cell voltage. The ionic conductivity of the polymer membrane is strongly dependent on the water uptake of the polymer matrix. The electrons produced in the catalyst layer on the anode side can not pass the polymer membrane due to its low electric conductivity. They are collected by the gas diffusion layer, which ensures electric contact also of catalyst layer areas under flowfield channels. In the schematic of Fig. 2.1 electron transport from anode to cathode is realized by an external connection and load. In a stack electrons pass directly through the bipolar plate (BIP) reducing the ohmic resistance and complexity of the system.

Product Removal

The electric power in the external circuit is the desired product of the fuel cell. Besides electric current, water and heat are generated in the PEFC and without their removal a continuous operation would be impossible. In a stack the surface to volume ratio is insufficient for passive heat removal [13]. Therefore the BIP is normally equipped with additional channels for coolant supply. The gaseous product water produced at the cathode CL has to cross the GDL towards the flowfield channel. Thereby the water vapor pressure is likely to exceed the saturation pressure. As a consequence condensation takes place within the pores of the GDL resulting in the so called flooding, a major issue of low temperature PEFC.

2.2 PEFC Thermodynamics

2.2.1 Thermodynamic Potentials

The conversion of chemical energy into electric energy is described by thermodynamics. The first law of thermodynamics states that the change of internal energy ΔU of a system is equal to the heat supplied to the system ΔQ minus the work done by the system ΔW.

	ΔH_0 / kJ mol^{-1}	S_0 / J mol^{-1} K^{-1}	ΔG_0 / kJ mol^{-1}	E_0 / V
H_2	0	130.68	0	
O_2	0	205.14	0	
H_2O liquid	-285.83	69.91	-237.16	1.229
H_2O gaseous	-241.82	188.83	-228.61	1.185

Table 2.2: Thermodynamic data for reaction in Eq. (2.9) taken from O'Hayre [14] at standard state conditions: 1 bar, 25 °C.

$$\Delta U = \Delta Q - \Delta W = T\Delta S - \Delta W \tag{2.10}$$

Hence energy can not be generated or destroyed. The heat added to the system is proportional to the entropy change ΔS and the temperature of the system.

The enthalpy change ΔH describes the change of internal energy plus work done by the system. ΔH of the reaction in Eq. (2.9) is therefore a measure for the maximum heat of reaction. The electric work potential of a PEFC is described by the Gibbs free energy change ΔG of the reaction in Eq. (2.9), which is the difference of the enthalpy change ΔH and the entropy change ΔS.

$$\Delta G = \Delta H - T\Delta S \tag{2.11}$$

2.2.2 Standard Equilibrium Voltage

If it is assumed that the system provides only electric work, the negative of the Gibbs free energy change is equal to the electric work ΔW_e for an isothermal and isobaric reaction

$$\Delta W_e = -\Delta G_0 = -q\ E_0 = -n\ F\ E_0 \tag{2.12}$$

where q is the charge carried by n electrons, F Faraday's constant and E_0 the equilibrium voltage at standard conditions. Table 2.2 lists standard state thermodynamic data and corresponding equilibrium voltages for the reaction in Eq. (2.9).

2.2.3 Non-Standard Equilibrium Voltage

In reality a PEFC is operated under non-standard conditions such as elevated temperatures ($\sim$70 °C) and absolute pressures ($\sim$1.5 bar) and reduced reactant concentrations. The change in equilibrium voltage by a change in temperature can be determined by solving Eq. (2.12) for E_0 and differentiation for temperature. According

to O'Hayre [14] the equilibrium voltage only drops by 23 mV with an increase of 100 °C.

The effect of elevated pressures can be determined in a similar way. As the volume in Eq. (2.9) decreases, i.e. less mol are generated than consumed, the equilibrium voltage will increase. However the increase is minimal. Operation at 3 bar instead of 1 bar only increases the equilibrium voltage by 15 mV according to O'Hayre [14].

In order to study the effect of reactant and product concentration the concept of chemical potential has to be introduced. It is the change in Gibbs free energy ∂G of a system with an infinitesimal increase of a certain species by ∂n moles. The chemical potential μ_k of species k is linked to its concentration

$$\mu_k = \left(\frac{\partial G}{\partial n}\right) = \mu_{k,0} + RT \ln a_k \tag{2.13}$$

where a_k is the activity and $\mu_{k,0}$ the reference chemical potential of species k. Summing up the contribution of all species in Eq. (2.9), the Gibbs free energy change can be calculated. With the use of Eq. (2.12) the Nernst equation can be derived, which specifies the equilibrium voltage E at non-standard concentrations

$$E = E_0 - \frac{RT}{2F} \frac{a_{H_2O}}{a_{H_2} \, a_{O_2}^{0.5}} = E_0 - \frac{RT}{2F} \frac{1}{p_{H_2} \, p_{O_2}^{0.5}} \tag{2.14}$$

with R the ideal gas constant. Note that the activities of ideal gases are equal to their partial pressures. The activity of liquid water is 1 as it is a pure component. As an example the theoretical equilibrium voltage of a PEFC operated with ambient air instead of pure oxygen only drops by about 10 mV. This is negligible compared to the loss of kinetic activity by the reduction of reactant partial pressure under air operation. The equilibrium voltage in a real PEFC, also called the open circuit voltage (OCV), is only around 1 V due to hydrogen cross over and peroxide formation, which results in a mixed electrode potential at the cathode.

2.3 PEFC Overpotentials

The equilibrium cell voltages discussed so far are only valid for open circuit conditions, i.e. no electric current is drawn by the external circuit. The voltage output of a fuel cell under operation is less than thermodynamically predicted due to irreversible losses. With increasing electric current the cell voltage drops, which results in the typical current-voltage characteristic shown in Fig. 2.2. According to Faraday's law the electric current density j is proportional to the amount of fuel consumed

$$j = n \, F \, N_{H_2} \tag{2.15}$$
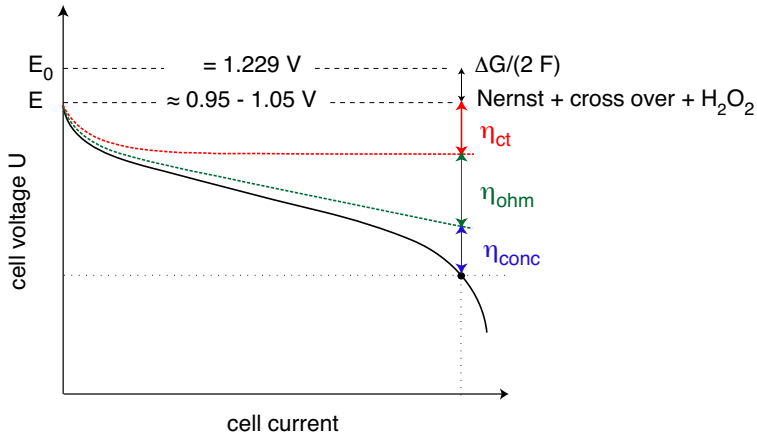
Figure 2.2: Current voltage characteristic of a PEFC showing the contribution of charge transfer overpotential η_{ct} (sum of anode and cathode contributions), ohmic overpotential η_{ohm} and concentration overpotential η_{conc} to the deviation from the thermodynamic open circuit voltage E. The figure was adapted from [15].

where N_{H_2} is the molar flux of H$_2$ [mol m^{-2} s^{-1}] and n the number of transfered electrons in the reaction. Therefore the voltage axis in Fig. 2.2 can be regarded as a measure for the efficiency of the fuel cell. The difference between operating cell voltage U and equilibrium voltage E is the overpotential, which is generally negative (Eq. (2.16)). It can be regarded as the required driving force to draw current from the system. The total overpotential is composed of three major contributions: the charge transfer overpotential at the anode η_{act} and at the cathode η_{cct}, the ohmic overpotential η_{ohm} and the concentration overpotential η_{conc}:

$$U = E - \eta_{act} + \eta_{cct} + \eta_{ohm} + \eta_{conc} \qquad (2.16)$$

2.3.1 Charge Transfer Overpotential

The charge transfer overpotential is the dominating loss in PEFC at low current densities (< 0.1 Acm^{-2}) as depicted in Fig. 2.2. It is composed of a small anodic η_{act} and a prevailing cathodic η_{cct} contribution. The charge transfer overpotential at the anode is required to overcome the activation energy involved in the charge transfer from the adsorbed H to the electrode in the HOR (Eq. (2.3)). The charge transfer overpotential at the cathode is driving the charge transfer from the electrode to the adsorbed O intermediates in the ORR (Eq. (2.8)).

By convention the interfacial potential difference (Galvani potential) is the electrode potential ϕ minus the electrolyte potential χ. The equilibrium cell voltage E is

the sum of anode and cathode Galvani potentials. However, the single Galvani potentials are not measurable. Therefore the total equilibrium cell voltage E is usually attributed to the cathode side, which results in the following definition for the single charge transfer overpotentials:

$$\eta_{cct} = \phi - \chi - E \tag{2.17}$$

$$\eta_{act} = \phi - \chi \tag{2.18}$$

The charge transfer overpotentials are a function of current and can be described by the Butler Volmer model. The current produced by an electrochemical reaction is finite and directly linked to the reaction rate. The reaction rate is the product of the rate constant k and reactant surface concentration c. Consider the following general electrochemical reaction between the oxidizing (Ox) and reducing (Re) species

$$Ox + n\,e^- \overset{k_f}{\underset{k_b}{\rightleftharpoons}} Re \tag{2.19}$$

where the reduction reaction is the forward direction. The reaction rate constants for forward k_f and backward k_b directions are exponentially dependent on the activation energies ΔG^a (Arrhenius equation)

$$k_f = k_0 \exp\left(\frac{-\Delta G^a_f}{RT}\right) \tag{2.20}$$

$$k_b = k_0 \exp\left(\frac{-\Delta G^a_b}{RT}\right) \tag{2.21}$$

where k_0 is the rate constant at equilibrium, R the ideal gas constant and T the temperature. The forward and backward activation energies are related by the charge transfer coefficient α. If the two activation energies are the same: $\alpha = 0.5$. Using Faraday's law in Eq. (2.15) together with the rate expressions in Eq. (2.20) and subtracting forward j_f and backward j_b current densities the Butler Volmer equation for single step electrochemical reactions can be derived:

$$j = j_f - j_b = j_0 \left(\frac{c_{Ox}}{c_{Ox,ref}} \exp\left(\frac{-\alpha n F \eta_{ct}}{RT}\right) - \frac{c_{Re}}{c_{Re,ref}} \exp\left(\frac{(1-\alpha)n F \eta_{ct}}{RT}\right)\right) \tag{2.22}$$

Therein the activation energies have been replaced with expressions depending on the charge transfer overpotential η_{ct} and charge transfer coefficient α. Using the convention in Eq. (2.17) the charge transfer overpotential at the cathode η_{cct} is negative

and consequently the first exponential term in Eq. (2.22) (forward direction) is dominating. The charge transfer overpotential at the anode η_{act} is positive by convention and therefore the second exponential term in Eq. (2.22) (backward direction) is dominating. At equilibrium, i.e. $j = 0$, the forward and backward current densities are the same and given by the exchange current density j_0 at standard conditions. The surface concentration of the oxidizing species c_{Ox} (i.e. O_2) is affecting the forward reaction while the surface concentration of the reducing species c_{Re} (i.e. H_2) is affecting the backward reaction. The concentrations are normalized with reference concentrations at standard conditions.

For small absolute values of η_{ct} (< 15 mV) and assuming no change in surface concentrations the Butler Volmer equation Eq. (2.22) can be linearized using Taylor series:

$$j = j_0 \, \frac{nF\eta_{\text{ct}}}{RT} \tag{2.23}$$

This linear approximation is applicable to the small anode charge transfer overpotential of the HOR reaction in PEFC. On the other hand for large negative values of η_{ct} (< -50 mV), as for the ORR in PEFC, the backward reaction term in the Butler Volmer equation (second term) becomes negligible and the Tafel approximation can be deduced

$$\eta_{\text{ct}} = \frac{RT}{\alpha nF} \, \ln j_0 - \frac{RT}{\alpha nF} \, \ln(j) \tag{2.24}$$

$$\eta_{\text{ct}} = a + b \, \ln j \tag{2.25}$$

where b is the Tafel slope. Exchange current density j_0 and charge transfer coefficient α can be determined by fitting a straight line through a semi-logarithmic plot of η_{ct} against $ln(j)$. Intrinsic values of exchange current per active catalyst area for HOR are 1×10^{-3} Acm^{-2} and for ORR 1×10^{-9} Acm^{-2} [12]. A review of different ORR catalysts including exchange current densities is given by Gasteiger et al. [16]. Knowing the constants j_0 and α the charge transfer overpotential is only a function of current density with a logarithmic increase. Therefore η_{ct} increases quickly at small current densities and slowly at high current densities.

2.3.2 Ohmic Overpotential

The ohmic overpotential becomes significant at average current densities (> 0.1 Acm^{-2}) as shown in Fig. 2.2. It is composed of an electric and ionic contribution

$$\eta_{\text{ohm}} = j \, (ASR_e + ASR_i) \tag{2.26}$$

where ASR is the area specific resistance [Ωcm^2]. The electric resistances ASR$_e$ of catalyst layer (CL), gas diffusion layer (GDL), bipolar plate (BIP) and component interfaces are about an order of magnitude lower compared to the ionic resistance ASR$_i$ of the membrane. Therefore membranes are produced as thin as possible to reduce the dominating ionic resistance. While the electric contribution to η_{ohm} can be assumed constant the ionic membrane resistance is a strong function of membrane water content. Therefore η_{ohm} only increases linearly with current at constant membrane water contents.

The best polymer electrolyte membranes employed today have a conductivity of about 10 Sm^{-1} under fully humidified conditions. This corresponds to an ohmic overpotential of 50 mV at a current density of 1 Acm^{-2} assuming a thickness of 50 μm. The ohmic resistance of a PEFC is typically measured by the high frequency response (> 10 kHz) of Electrochemical Impedance Spectroscopy (EIS) or by the immediate response of current interrupt measurements.

2.3.3 Concentration Overpotential

The concentration overpotential is relevant for high current densities (> 1 Acm^{-2}) where the reactant transport to the active sites becomes limiting. This transport bottleneck results in a depleted reactant concentration at the catalyst surface. According to Eq. (2.22) a reduced surface concentration due to reactant undersupply results in an increased charge transfer overpotential. Therefore the concentration overpotential can be seen as a charge transfer overpotential produced by reactant transport limitations.

The reactant undersupply can have different reasons. First of all low stoichiometry can cause low reactant concentration in the flowfield channel. Next the diffusive transport through the GDL or CL can be limiting especially in the presence of liquid water. Finally the solubility of reactant gases and subsequent diffusion through the polymer film in the CL may reduce the concentration on the catalyst surface. Assuming only gas diffusion bottlenecks in the GDL, the current density can be calculated as a function of catalyst surface concentration c by combination of Faraday's (Eq. (2.15)) and Fick's law (Eq. (3.14))

$$j = -n\,F\,D_{\text{kl,eff}}\,\frac{c - c_0}{\delta} \tag{2.27}$$

where c_0 is the concentration in the flowfield channel and δ the diffusion length through the GDL. By setting the surface concentration c to zero, the limiting current density can be determined. It is the maximum possible current density and can be observed in Fig. 2.2 by a vertical drop of cell voltage. Note that a cell voltage of zero is not necessarily at the limiting current density as other overpotentials can reduce the

cell voltage to zero before the transport limitation is reached. Typical limiting current densities can range from 1 to 10 Acm^{-2}. A measure for the concentration overpotential can be obtained by the low-frequency (< 1 Hz) response of EIS and fitting to a finite Warburg impedance.

2.4 PEFC Components

In the following section the main components used in a single cell are briefly described in terms of functionality, structure and manufacturing process. The membrane, catalyst layer and gas diffusion layer are often merged to the term MEA (membrane electrode assembly).

2.4.1 Polymer Electrolyte Membrane (MEM)

In PEFC a polymer electrolyte is used as the ion conductor. It separates the reactant gases, closes the charge circuit by conducting protons and avoids electric shortcut. For a polymer to be conductive for protons, fixed charge sites, free volume (porosity) and liquid water are required. The free volume is given by the polymer matrix while the fixed charge sites generally have to be added. The water can originate from the electrochemical reaction at the cathode or the external humidification of reactant gases.

Perfluorated sulfonic acid (PFSA) membranes (e.g. Nafion® from DuPont) are commonly used polymer electrolytes. The fixed charge sites are sulfonic acid ($SO_3^-H^+$) functional groups. The equivalent weight EW of a PFSA membrane is defined as the weight of the polymer per sulfonic acid group. For example Nafion® 112 has an EW of 1100 g mol^{-1} with a thickness of 0.002 inches (1 inch = 25.4 mm). The ion exchange capacity (IEC) is the reciprocal of the EW. The fixed charge site concentration is given by

$$c_{SO_3^-} = \frac{\rho}{EW} \qquad (2.28)$$

where ρ is the dry density of Nafion®. The state of understanding of the properties of Nafion® has been reviewed recently by Mauritz and Moore [17].

The common picture of proton transport through a PFSA membrane is that of a porous network of free volume walled by sulfonic acid groups. In the presence of sufficient liquid water, the protons dissociate from the sulfonic acid groups and form hydronium complexes (H_3O^+) which are mobile as in aqueous electrolytes. Therefore the ionic conductivity of PFSA membranes can be almost as high as for aqueous electrolytes but is strongly dependent on the membrane water content. The higher
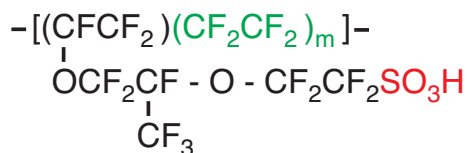
$$-[(\underset{|}{C}FCF_2)(CF_2CF_2)_m]-$$
$$OCF_2\underset{|}{C}F - O - CF_2CF_2SO_3H$$
$$CF_3$$

Figure 2.3: Chemical structure of Nafion®. The combination of the stable hydrophobic PTFE backbone (green) with the hydrophilic sulfonic acid groups (red) gives Nafion® its characteristics.

the water content the better the conductivity. Therefore the water uptake, transport and resulting distribution within the membrane is important to determine the local ionic conductivity. PFSA membranes are characterized in terms of water uptake isotherms, which specify the amount of water per sulfonic acid group λ (membrane water content) as a function of water activity.

2.4.2 Catalyst Layer (CL)

The catalyst layers on the anode and cathode side of the membrane are promoting the electrochemical reactions as described in Sec. 2.1. The charge transfers in the ORR and HOR are driven by the charge transfer overpotentials η_{ct} as discussed in Sec. 2.3.1. In order to reduce η_{ct} catalysts with high exchange current densities j_0 and catalyst layer structures with high active surface areas are used. High active surface areas of 100-300 m^2 per m^2 geometric area are obtained with highly dispersed catalyst particles (3-10 nm diameter). However, the catalyst surface area can only be considered active if the catalyst particles are electrically and ionically connected and diffusion pathways for reactant gases are not too stringent.

To ensure close contact of the three phases (electric, ionic, gas) catalyst particles are deposited from a solution of the corresponding metal salt onto carbon particles (30-50 nm diameter) as shown in the transmission electron microscopy image in Fig. 2.4. These carbon supported catalysts are then mixed with solubilized ionomer (e.g. Nafion®) to an ink which is applied on the membrane or GDL. After evaporation of the solvent a microporous structure remains with agglomerated carbon particles (0.1-1 μm diameter) which are bonded by an ionomer matrix. Coated catalyst layers are typically 10-50 μm thick with catalyst loadings of 0.1-1 mg cm^{-2}. Different catalyst layer manufacturing processes are reviewed by Litster and McLean [18]. Catalyst layer parameters available for optimization are the catalyst loading, the catalyst layer thickness, the carbon to ionomer ratio, the carbon particle size and the overall porosity. To better understand the interplay of these parameters a catalyst pore scale model was built within this thesis (cf. Chap. 6).
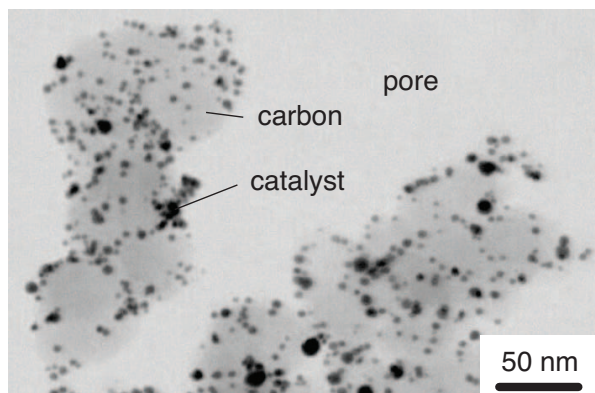
Figure 2.4: TEM image of agglomerated and catalyst-coated carbon particles [15].

2.4.3 Gas Diffusion Layer (GDL)

The characterization of different GDL's was one of the main focuses in this thesis. Despite its simplicity their properties were poorly understood. A thorough review on the characteristics of GDL's has been given recently by Cindrella et al. [19].

A GDL is structured to fulfill a multitude of requirements. It has to allow access of reactant gases to and removal of gaseous and liquid product water from the catalyst layer. Therefore it is tailored highly porous and is treated with hydrophobic polytetrafluorethylene (PTFE). Furthermore the GDL has to collect electrons from the anode CL and distribute electrons to the cathode CL. It needs to be based on a conducting substrate which is chemically inert. Therefore carbon fibers rather than metals are used. An additional hydrophobic microporous layer (MPL) between CL and GDL improves the electric contact to the CL and forces liquid water away from the GDL. Additionally the structure of the GDL has to mechanically withstand the clamping pressure of the stack which is necessary to reduce contact resistances and avoid leakages. Hence the change of properties as a function of compression is relevant. The interplay of these functions results in a high potential for optimization which is reflected in the number of recent publications about GDL's [20–35]. Structural investigations of different GDL's are presented in Sec. 5.1.

There are different manufacturers producing GDL's with slightly different processes. A good overview on the various processing routes is given in [36]. Carbon papers are normally produced in a two step carbonization process. Polymer fibers (polyacrylonitrile) of about 10 mm length and 8 µm diameter are carbonized first. In the next step they are homogeneously mixed and bonded with a binder to 150-300 µm thin layers. Locally the thickness can change by 10%. The types and amount of binder
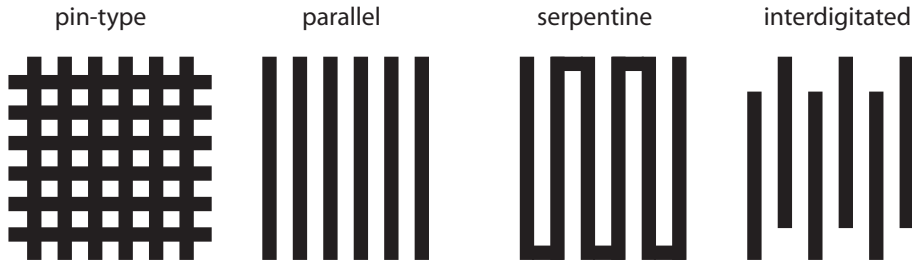
Figure 2.5: Schematics of different flowfield layouts of the bipolar plate. Black are the channels for convective reactant distribution and white the ribs for electron collection.

vary resulting in significant differences in gas transport and mechanical properties. These layers are again carbonized to make the binder solid and electrically conductive. The plain GDL's are further treated by the manufacturers with PTFE to make them hydrophobic and therewith improve the water management [20, 35, 37]. The PTFE is applied as small particles in a slurry. After evaporation of the solvent and another thermal process step, a thin layer remains on parts of the internal surface. The resulting PTFE layer is not homogeneously distributed and gradients of hydrophobicity are expected. PTFE is likely to accumulate in small pores or to form skins in the corners of fiber joints. Lim et al. [38] reported a negative effect on cell performance of an excessive hydrophobic treatment.

2.4.4 Bipolar Plate (BIP)

The bipolar plates connect the single membrane electrode assemblies (MEA) to a stack. They are connected on one side to an anode and on the other to a cathode of two cells (bipolar). Their main task is the convective distribution and removal of reactants and products and the electric connection of the MEA. They have to be impermeable and provide sufficient mechanical stability to the cell. In order to ensure heat removal, the bipolar plates are generally equipped with cooling channels. Furthermore the material needs to be chemically stable, have a low weight, low cost and good manufacturability. The arrangement and geometry of channels and current collecting ribs is called flowfield and is the main optimization parameter of the BIP. Four different flowfield layouts are shown in Fig. 2.5.

The flow in the pin-type layout is relatively unconstrained. The main disadvantage is the undersupply of corners with the largest distance from the inlet and outlet. The flow generally has a low speed and therefore a low water removal ability.

The parallel-type flowfield is relatively simple to manufacture. The short channel length reduces the pressure drop from inlet to outlet. The main disadvantage is the

low water removal ability. Due to the parallel arrangement the total mass flux is shared resulting in low channel velocities. Furthermore two parallel channels have the same pressure profile which inhibits cross convection under the ribs [39]. Once a channel is flooded with liquid water the gases simply pass through neighboring channels.

The serpentine-type flowfield is more difficult to manufacture and imposes a higher pressure drop due to the length of the channel and the high mass flux. Due to the high channel velocity liquid water is removed more easily. Furthermore the pressure gradient between two neighboring channels can result in significant cross convection with increased reactant supply and water removal under the ribs [39]. However, the bends of the serpentine are prone to water flooding as the effect of channel-channel cross convection is minimal.

In the interdigitated-type flowfield the channels are completely interrupted and the gases have to pass through the GDL from one channel to the other. The pressure drop is the highest of all flowfield types and can cause a significant parasitic load. Forcing the gases under the flowfield ribs has the advantage of superior reactant supply and water removal. However, the velocity in the channel is getting very small towards the end of the inlet channels and at the beginning of the outlet channels. As a consequence this region is prone to reactant starvation and liquid water flooding.

2.5 Channel Rib Scale

The focus of this thesis was the channel-rib scale and the transport therein. The motivation for an in-depth study and the state of knowledge of channel-rib effects is outlined in the following section.

2.5.1 Scale Coupling

There are various relevant scales in PEFC with strong bilateral couplings. The relation of stack, cell and channel-rib scale is depicted in Fig. 2.6. The stack scale includes the serial connection of single cells and endplates, which determine the boundaries for the cell scale. The stack manifolds are responsible for the parallel reactant (O_2, H_2) distribution to the single cells. The mechanical clamping pressure applied by the endplates and the tie rods defines the compression and therewith the transport properties of the gas diffusion layers (GDL). Furthermore the geometry of the stack and endplates affect the temperature of the single cells. In the other direction the single cells govern the stack voltage and flow of electric current through it. The repetitive unit of the cell scale is composed of two halves of a bipolar plate (BIP), which comprises the flowfield structure and the membrane electrode assembly (MEA). The
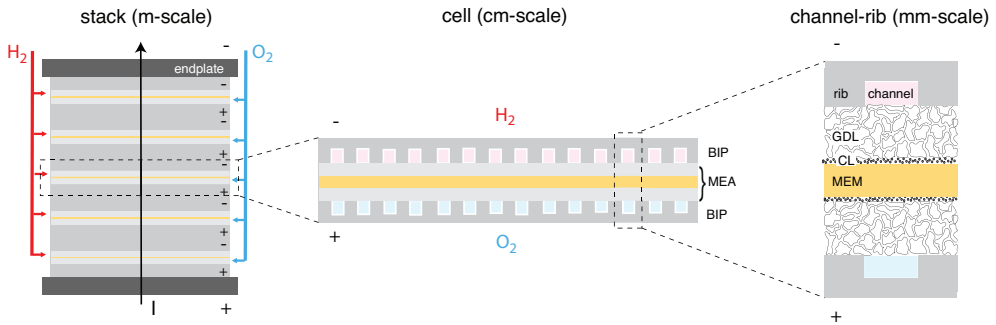
Figure 2.6: Schematics of through-plane cuts of stack, cell and channel-rib scales. The stack is feed in parallel with the reactants while the current flows in series from endplate to endplate. The single cells are connected over the bipolar plates comprising the flowfield structure. The channel-rib scale contains the smallest repeat unit of a parallel flowfield with half of a flowfield channel and rib. The schematic shows twice the smallest repeat unit for a better understanding.

flowfield structure of the BIP (cf. Sec.2.4.4) governs the reactant, product and temperature boundary conditions to the next lower channel-rib scale. It includes the MEA and half of a gas channel and current collecting rib. For a better understanding the smallest repeat unit is shown twice in Fig. 2.6 mirrored at the symmetry axis. The design of the channel-rib scale defines the accessibility of the reaction sites in the catalyst layer (CL), the membrane resistance and therewith the local current of the cell and eventually the total current of the stack. The smallest relevant scale is the catalyst layer where the actual conversion of chemical to electric energy takes place. The catalyst layer scale is characterized in detail in Chap. 6.

2.5.2 Inhomogeneities

Inhomogeneities exist on every scale and are strongly dependent on operating conditions. They cause additional losses, inefficient material and catalyst utilization and in the long run promote degradation. On the stack scale the parallel distribution of reactants can be unequal due to pressure variations in the manifolds or flooding of flowfield channels [40–42]. Furthermore the temperature of cells close to the endplates are generally lower amplifying the issue of flooding. On the cell scale the depletion of reactants along the flowfield channel can cause high current production at the inlet and low current production at the outlet [43]. However, depending on the humidity of the inlet gases and the efficiency of product water removal, the current production at the inlet can be significantly reduced. So far often neglected inhomogeneities also exist on the channel-rib scale. Due to the unavailable electric connection of the channel-GDL interface and the unavailable gas supply of the rib-GDL inter-

face, concentration, potential and temperature gradients exist perpendicular to the flowfield channels. The rib compression superimposes an additional inhomogeneity on the channel-rib scale. Finally gradients within the catalyst layer may deactivate considerable amounts of precious catalyst material.

Various experimental and computational tools exist to study inhomogeneities from the stack scale down to the catalyst scale. The following list is by no means exhaustive. Current voltage characteristics of single cells in a stack reveal inhomogeneities in reactant and temperature distribution along the stack axis. Local currents along the flowfield channels of single cells can be measured using segmented cells [43]. Combined with impedance spectroscopy, segmented cells can disclose the distribution of different losses on the area of single cells [44]. The condensation of product water along the flowfield channels can be visualized using through-plane neutron radiography [45]. Therewith catalyst layer undersupply due to flooding can be localized within the cell area. Another powerful tool to study inhomogeneities on the cell level is by local gas analysis along the flowfield channel by mass spectrometry [46]. Inhomogeneities on the channel-rib scale have been mainly studied by simulation so far [47–51]. Unfortunately missing validation experiments limit the significance of the model results. Due to the small size and restricted accessibility, *in-situ* experiments of the channel-rib scale are difficult. Recently, in-plane neutron radiography results have been published [52] showing the liquid water distribution across the channel-rib and MEA. The method and results of channel-rib current density measurements are briefly summarized in the next section as they build one of the foundations of this thesis.

2.5.3 Current Density Measurements

The inhomogeneous current production of channel and rib areas has been experimentally studied for the first time by Stefan Freunberger [53] and Mathias Reum [15, 54]. The principle is to use the bipolar plate and the gas diffusion layer as 2D shunt resistors. Thereby 30 gilded tungsten wires with a pitch of 200 μm are inserted between the catalyst layer and gas diffusion layer as shown in Fig. 2.7. By measuring the potential difference between the wires and the back of the bipolar plate and knowing the exact resistance of the components in between, the current distribution can be calculated using Laplace equation (Eq. (3.28)). The measurement principle was applied to a small differential cell with an active area of about 1.3 cm^2. To avoid reactant depletion effects and a mixing of potentials along the wires the stoichiometry of the cell was around 30. The micro cell was designed for variation of reactant compositions and humidities, temperature, GDL compression and channel-rib geometries.

A selection of quantitative results are discussed and compared with model predic-
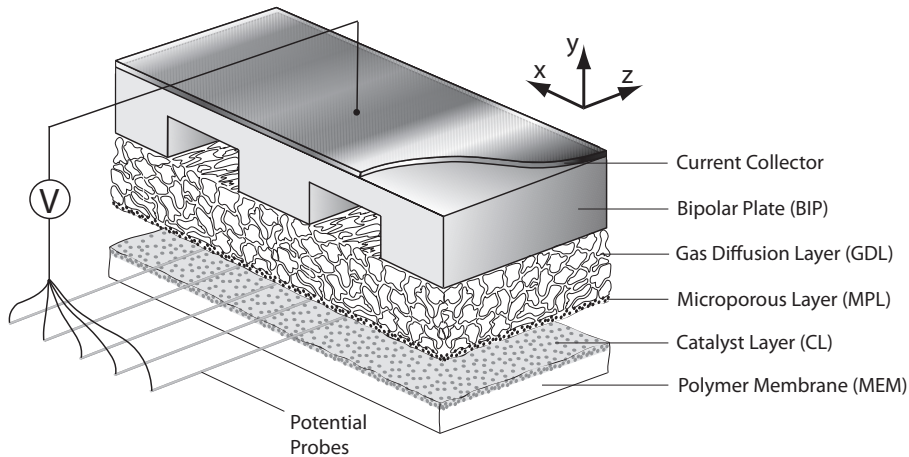
Figure 2.7: Schematic drawing of the micro cell setup for channel-rib current density distribution measurements. The local potential difference is probed between thin wires at the CL-GDL interface and the back of the BIP. In a subsequent step the local current is calculated using Laplace equation Eq. (3.28). Figure has been taken from [15].

tions in Chap. 7. At this point only the general qualitative behavior of the experimental current density profiles are explained. For a given set of above mentioned parameters the pattern of the channel-rib current density profile is only load dependent. The profile at the CL changes from a slight maximum under the rib at low load to a peak under the channel at high load. The rib-peak at low load is controlled by the low ohmic resistance of GDL and membrane under the rib. With increasing load both rib and channel currents increase until the rib reactant supply becomes insufficient. The channel current density increases further to a multiple of the average current density due to superior supply of the channel catalyst layer. Generally it was concluded that ohmic overpotentials mainly stem from the channel area while concentration overpotentials are produced under the rib area.

The variation of humidity revealed a strong sensitivity of ohmic overpotential of the channel areas while the rib overpotential was almost unaffected. This was attributed to enhanced membrane water absorption and desorption under the channels. The variation of channel-rib geometries showed that small channels and wide ribs are favorable for the water management of the cell down to oxygen molar fractions of 5%. Only below 5% oxygen molar fraction the diffusion pathways under the ribs become critical with narrow channels.

In order to fully understand the channel-rib current density measurements a computational model was required (cf. Chap. 7). The experimental data of the micro-cell served as a valuable input for the model validation. To work towards a fully valid-

ated channel-rib model exact material properties needed to be measured (cf. Chap. 5) applying established and novel methods (cf. Chap. 4).

3 Basics of Transport in PEFC

Transport of mass, charge and heat are essential for PEFC to operate. Transport limitations, in particular in the void phases, are responsible for significant losses (cf. Sec. 2.3). The basics of the transport processes taking place in PEFC are summarized in this chapter. It is kept short and does not claim completeness but should introduce important concepts. Extended equations and their parameterizations are discussed later in the channel-rib model chapter (Chap. 7). Basic properties of porous media are defined followed by a short introduction to mass and charge transport. The three main driving forces for transport in PEFC are introduced: concentration gradient, pressure gradient and potential gradient. For thorough definitions and derivations of equations appropriate references are given.

3.1 Porous Media Properties

Gas diffusion layer (GDL), microporous layer (MPL) and catalyst layer (CL) are porous components in PEFC. The macroscopic properties of these components are determined by the material composition and the microscopic pore structure. The important macroscopic properties (i.e. porosity, tortuosity, pore size distribution and permeability) are discussed in the subsequent sections. Macroscopic properties can only be applied if the sample is large enough to contain a representative unit of the microstructure. In order to derive continuum equations that are valid everywhere, the method of volume averaging has to be applied [55]. The structural information is cast into macroscopic, effective material parameters by the effective medium theory [56]. Generally the pore and solid geometries are asymmetric resulting in different macroscopic parameters for different directions (anisotropy). Furthermore the behavior of the material changes when it is subjected to mechanical stress as pores and solids are deformed. Detailed treatment of the theory of porous media and transport therein can be found in [57–62].

3.1.1 Porosity

Porous materials are multiphase system. To determine structural parameters void and solid phase are distinguished as visible in the left sketch of Fig. 3.1. Dry pore

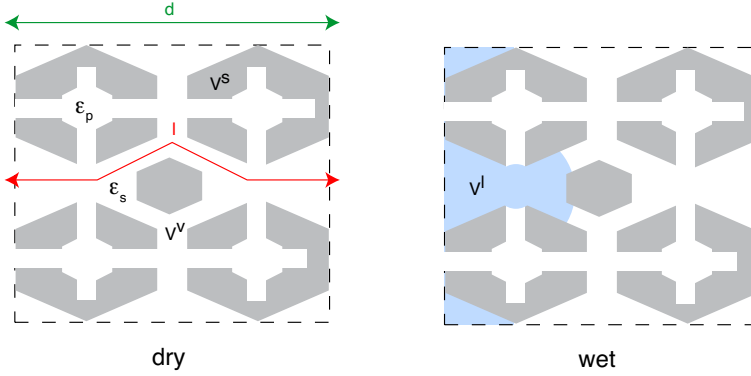**Figure 3.1:** Schematic of a dry (**left**) and wetted (**right**) porous media with a dual porosity (ε_p, ε_s), dead-ended pores and a distinct anisotropy. V^v indicates the void (white), V^l the liquid volume (blue) and V^s the solid volume (gray). d is the macroscopic and l the effective transport pathway in the void.

structure parameters solely depend on the geometry and size of the pores. The porosity ε is defined as the fraction of the total volume occupied by the pores

$$\varepsilon = \frac{V^v}{V^v + V^s} \tag{3.1}$$

where V^v is the pore or void volume and V^s the solid volume. There are three kind of pores: closed pores that are not accessible, blind or dead-ended pores that terminate within the material and through pores relevant for mass transport. The total porosity is composed of pores with different sizes. The distribution of pore volume over pore sizes is characterized by the pore size distribution. The porous materials in PEFC often have a dual porosity. They are composed of a microporous domain with a primary porosity ε_p and a macroporous domain with a secondary porosity ε_s. To understand the concept of pore size distribution the definition of a pore has to be reviewed. Dullien [57] describes a pore as follows:

"A pore is defined as a portion of pore space bounded by solid surfaces and by planes erected where the hydraulic diameter of the pore space exhibits minima, analogously as a room is defined by its walls and the doors opening to it".

Similar to the definition of a pore the definition of the pore size is not straight forward. For a real material the only direct method would be the optical investigation of a micrograph or tomography image. All other methods depend on *a priori* assumptions of the pore structure. Porosity and pore size distributions have been measured by the indirect method of mercury intrusion porosimetry (MIP) in Sec. 4.1.
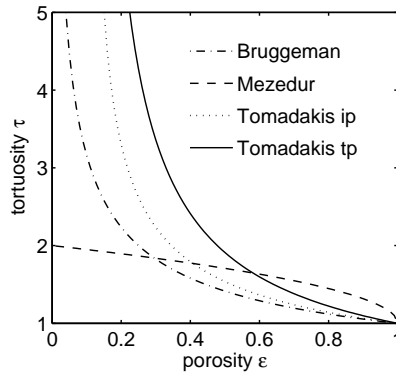
Figure 3.2: Tortuosity of different pore morphology models (Bruggeman [63], Tomadakis and Sotirchos [64], Mezedur and Kaviany [65]) as a function of porosity and in-plane (ip) / through-plane (tp) direction.

3.1.2 Tortuosity

Not all the void volume can contribute to mass transport. There may be dead-ended pores that are not interconnected with the open space as shown in Fig. 3.1. A measure for the interconnectivity of the porous network is the tortuosity τ. It is defined as the ratio of the length of a curve l to the distance of its endpoints d. In other words the tortuosity defines the deviation of the real, effective pathway from the macroscopic pathway. Note that in anisotropic materials the tortuosity has different values for different directions, is a strong function of mechanical deformation and can never be smaller than one.

Only little work has been done so far for investigating the tortuosity of porous components for PEFC. Most of the studies are based on idealized morphology models. They are compared in Fig. 3.2. The figure shows the tortuosity calculated by different morphology models as a function of porosity, a measure for the mechanical deformation. Tortuosity of GDL and CL were measured or modeled in this work and results are presented in Sec. 5.4 and Chap. 6.

The early work of Bruggeman [63] for dielectric constants with spherical inclusions is widely used to estimate the tortuosity of GDL's due to its simplicity.

$$\tau = \frac{1}{\sqrt{\varepsilon}} \tag{3.2}$$

However, its application to fibrous GDL's is doubtable. Tomadakis and Sotirchos [64] developed a random fiber model and used Monte Carlo simulations to compute anisotropic tortuosities. Their model is able to predict a percolation threshold at low porosities where τ becomes infinite as shown in Fig. 3.2. They fitted the following

equation to their simulation results:

$$\tau = \frac{1 - \varepsilon_{tr}}{\varepsilon - \varepsilon_{tr}}^{\beta} \tag{3.3}$$

In in-plane and through-plane direction they use a threshold porosity ε_{tr} of 0.11. For the other fitting parameter β they used 0.521 for in-plane and 0.785 for through-plane direction.

Other popular morphology models used for porous components in PEFC are the following: Mezedur and Kaviany [65] used 2D, ordered and random lattice-network models to predict the tortuosity of spherical catalysts over several pore length scales. They accounted for pore size distribution, coordination number (tetragonal, hexagonal) and pore blockage effects (poisoning). Nam and Kaviany [66] developed a network model for GDL's composed of stacked and randomly shifted fiber screens. They produced regular square pore spaces with a coordination number of 8. Gostick et al. [34] adapted the stochastic cubic lattice model of Ioannidis et al. [67, 68] to the fibrous structure of different GDL's. Pores were idealized as cubic bodies and the throats were ducts of square cross sections.

3.1.3 Permeability

Another macroscopic property of porous media that only depends on the porous structure is the absolute permeability K. It describes the pressure driven resistance of a slow steady newtonian fluid in a porous structure and is used by Darcy's law in Eq. (3.23). There are different models for analytical expressions of permeability. The most popular is the phenomenological Carman-Kozeny theory [57, 69, 70]:

$$K = \frac{\varepsilon \, D_h^2}{16 \, k_0 \, \tau^2} \tag{3.4}$$

$$D_h = \frac{4 \text{ x void volume}}{\text{surface area}} = \frac{4 \, \varepsilon}{A \, (1 - \varepsilon)} \tag{3.5}$$

Intuitively the permeability is proportional to the porosity ε and inversely proportional to the tortuosity τ. k_0 is a tabulated shape factor. Furthermore the permeability scales with the square of the hydraulic pore diameter D_h which results in the unit [m^2]. The hydraulic diameter D_h is used to describe the flow in non-circular cross-sections. A is the volume specific pore surface [m^{2}m^{-3}]. It is a measure for the adsorption capability of a porous material and can be obtained e.g. by BET N$_2$ physisorption or MIP. The term $k_0\tau^2$ is the so called Kozeny constant and approximately 6 for fibrous beds [71]. Measurements of GDL permeability (permeametry) as a function of compression and direction are presented in Sec. 4.2 and compared to the Carman-Kozeny theory.

3.1.4 Saturation

Condensation of product water in the porous components of PEFC is a major concern. To specify wet structure parameters an additional liquid phase has to be considered as shown in the right sketch of Fig. 3.1. Wet pore structure parameters not only depend on the geometry and size of the pores but also on the type of fluid and the properties of the pore wall material. Consequently tortuosity and permeability are changed depending on the saturation. The saturation of a wetted porous media is defined as the fraction of the total pore volume V^v occupied by the fluid V^l. Saturation is not a direct structural parameter but a state variable of the porous media.

$$s = \frac{V^l}{V^v} \tag{3.6}$$

The distribution of liquid water within a GDL has been visualized and quantified by synchrotron X-ray tomographic microscopy and is presented in Sec. 5.6.

3.1.5 Surface Tension & Contact Angle

To understand the saturation distribution within the porous media the concept of surface tension and contact angle has to be introduced. The interface of two fluids (e.g. water and air) in mechanical equilibrium is curved due to the existence of a surface tension. The surface tension ξ acts tangential to the interface changing the curvature until the pressure difference between the two fluids is counterbalanced. This equilibrium is visualized on the left of Fig. 3.3 and expressed by

$$p_l - p_g = \frac{2\,\xi}{r} \tag{3.7}$$

where p_l is the liquid water pressure, p_g the gas pressure and r the mean radius of surface curvature. The pressure on the concave side (bubble or droplet) is always greater than the pressure on the convex side.

In a three phase system fluid-fluid-solid the interfaces meet at a line of contact where the forces exerted by the surface tensions are in equilibrium. The contact angle θ is defined as the angle between the solid surface and the tangent to the fluid-fluid interface. Assuming a single circular pore with a tapered cross section (Fig. 3.3 right) is filled with a wetting fluid at a pressure p_g, the pressure of the non-wetting fluid p_l to penetrate the pore up to a radius R follows from the Young-Laplace equation:

$$p_c = p_g - p_l = \frac{2\,\xi}{R}\cos(\theta + \varphi) \tag{3.8}$$

The capillary pressure p_c is the pressure difference between the non-wetting p_l and the wetting fluid p_g. The mean radius of curvature is $R/\cos(\theta + \varphi)$ wherein φ is the
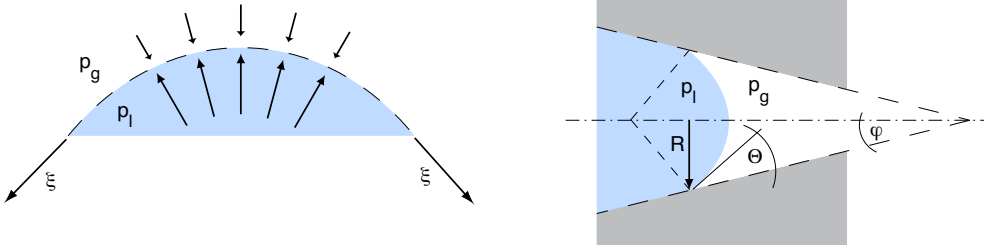
Figure 3.3: Left: interface of two fluids in mechanical equilibrium. The pressure difference $p_l - p_g$ is counterbalanced by the surface tension ξ. **Right:** Schematic of a tapered pore filled with liquid water. The wettability is determined by the contact angle θ and the orientation of the pore walls φ

surface orientation angle of the pore walls and R the local pore radius. The capillary pressure as defined by Eq. (3.8) is positive if $\theta + \varphi < 90°$ (hydrophilic) and negative if $\theta + \varphi > 90°$ (hydrophobic). Hence the wettability of a porous three phase system depends not only on the intrinsic contact angle but also on the orientation of the pore walls.

3.1.6 Capillary Pressure Function

It is apparent from Fig. 3.3 right that with increasing capillary pressure the liquid saturation s increases as the meniscus moves towards smaller pore radii. This relationship is called capillary pressure function $p_c(s)$. It has been measured for GDL's by successive states of hydrostatic equilibrium [28–31,72,73]. The typical S-shape of the capillary pressure function is due to the breakthrough pressure which is equal to the capillary pressure at the pore throat with the most constricted pore diameter. Typically the liquid saturation can not be increased up to 1 or reduced down to zero due to trapped air or liquid. Fairweather et al. [31,72] developed a microfluidic device that is able to control the saturation and measure the capillary pressure in a GDL sample (gas displacement porosimetry). Sole and Ellis [73] used a similar setup and presented capillary pressure functions with two pressure plateau.

Different models are available to correlate capillary pressure functions to measurements. They mainly evolved from geology or petrology and are compared in Fig. 3.4. Leverett [74] defined a capillary pressure function for water imbibition into clean, unconsolidated sands as a function of porosity ε and permeability K:

$$p_c(s) = \xi \, \cos \theta \, \left(\frac{K}{\varepsilon}\right)^{-\frac{1}{2}} J(s) \tag{3.9}$$

Therein ξ is the surface tension and θ the contact angle of the fluid. The Leverett J-functions $J(s)$ for hydrophobic and hydrophilic porous media are:

$$J(s) = \begin{cases} 1.417\,s - 2.12\,s^2 + 1.262\,s^3 & \text{hydrophobic} \\ 1.417\,(1-s) - 2.12\,(1-s)^2 + 1.262\,(1-s)^3 & \text{hydrophilic} \end{cases} \tag{3.10}$$

The limitation of this approach is the fact that porosity and permeability of different porous media are inadequate scaling factors for the different capillary pressure functions. The parameterization of the capillary pressure function by Leverett shown in Fig. 3.4 has been adapted to a typical hydrophobic GDL using a permeability of 2×10^{-12} m^2, a porosity of 0.7 and a contact angle of $110°$. The applicability of the Leverett approach to thin film GDL's is limited and discussed by E.C. Kumbur et al. [75].

Brooks and Corey [76] concluded from a large number of experimental soil-water capillary pressure functions that the following equation correlates reasonably well

$$p_c(s) = -p_{bt}\,(1-s)^{-1/b} \tag{3.11}$$

where p_{bt} is the break-through pressure and b a soil specific parameter. The curve shown in Fig. 3.4 is fitted to experimental data by Gostick [30]. Later Van Genuchten [77] derived a more general equation with better correlations for low liquid water saturations

$$s(p_c) = \left(1 + \left(\frac{p_c}{p_{bt}}\right)^n\right)^{-m} \tag{3.12}$$

where m and n are fitting parameters. Note that for $p_c \gg p_{bt}$ the model by Van Genuchten approaches the model by Brooks and Corey.

3.1.7 Relative Permeability

In a three-phase system of fluid-fluid-solid an additional parameter is used to describe the flow of two immiscible fluids through the porous structure. The so called relative permeability k is defined as the fraction of the absolute permeability available for convective transport of a specific fluid. Intuitively the relative permeability of a fluid scales with its saturation (Eq. (7.24)). Direct measurements for GDL's are rare [28,29] and therefore mathematical approximations are generally applied. Estimation of relative permeability as a function of saturation is possible based on capillary pressure models [76,77]. A thorough comparison of different relative permeability expressions is given by Kumbur et al. [75].
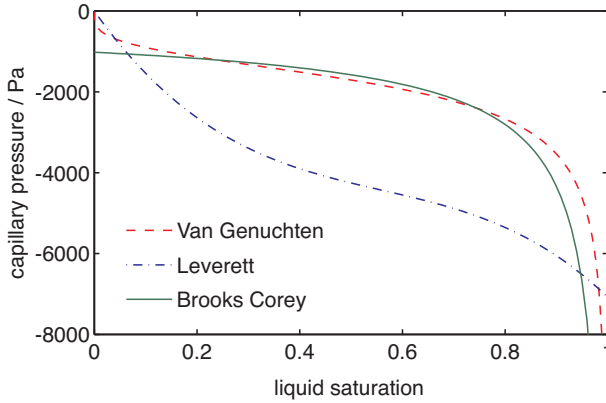
Figure 3.4: Capillary pressure function models. Van Genuchten: p_{bt} = 1000 Pa, m = 0.7262, n = 3.652 [30,77]; Leverett: K = 2 x 10^{-12} m^2, ε = 0.7, θ = 110° [74]; Brooks Corey: p_{bt} = 1020 Pa, b = 1.59 [30,76]

3.2 Mass Transport

The electrochemical reactions result in depletion of reactants and accumulation of products which have to be transported to and away from the reaction sites. The two gas transport processes that are significant in PEFC are diffusion within a concentration gradient and convection within a pressure gradient. The Peclet number Pe_{kl} for the gases k and l describes the ratio between convection and diffusion

$$Pe_{kl} = Re \cdot Sc_{kl} = \frac{l_0 \, v_0}{D_{kl}} \tag{3.13}$$

where Re is the Reynolds number, Sc the Schmidt number, D_{kl} the binary diffusivity, l_0 a characteristic length and v_0 a characteristic velocity. If $Pe_{kl} >> 1$ diffusion is negligible. In the flowfield channels convection dominates with $Pe_{kl} \sim 400$. In the GDL of a parallel flowfield $Pe_{kl} << 1$ applies and diffusion is the dominating process. However, in a serpentine flowfield in the GDL under the flowfield ribs $Pe_{kl} \sim 4$ is possible and convection has to be considered [39].

3.2.1 Diffusive Transport

As mentioned above the diffusive gas transport in PEFC is only dominant in porous domains. Diffusion in porous media includes ordinary diffusion and Knudsen diffusion. Ordinary continuum diffusion describes the relative motion of different gases while the Knudsen diffusion refers to a single gas when the pore diameter is smaller than the mean free path.

Fick's first law in Eq. (3.14) for ordinary diffusion was derived for free fluids (no porous media) and is valid with respect to the motion of the center of mass. The mass flux vector $\mathbf{N}_k$ of species k in species l is proportional to the binary diffusion coefficient D_{kl} and the density ρ or concentration c of the mixture. The driving force is the negative gradient of the weight fraction w_k, molar fraction x_k or partial pressure p_k respectively:

$$\mathbf{N}_k = -\rho \, D_{kl} \, \nabla w_k = -c \, D_{kl} \, \nabla x_k = -\frac{1}{RT} \, D_{kl} \, \nabla p_k \qquad (3.14)$$

For ordinary diffusion in a porous media a volume-averaged, effective diffusion coefficient $D_{kl,\text{eff}}$ according to the effective media theory is employed

$$D_{kl,\text{eff}} = \frac{\varepsilon}{\tau} \, D_{kl} \qquad (3.15)$$

Intuitively the diffusive flux scales with porosity ε and the inverse of tortuosity τ. The binary diffusion coefficient is inversely proportional to the absolute pressure p and molar masses M and directly proportional to the temperature T as described by the Slattery-Bird equation [78] for low pressures:

$$D_{kl} = \frac{1}{p} \, a \left(\frac{T}{\sqrt{T_{\text{cr},k} \, T_{\text{cr},l}}} \right)^b (p_{\text{cr},k} \, p_{\text{cr},l})^{\frac{1}{3}} \, (T_{\text{cr},k} \, T_{\text{cr},l})^{\frac{5}{12}} \sqrt{\left(\frac{1}{M_k} + \frac{1}{M_l} \right)} . \qquad (3.16)$$

Therein T_{cr} and p_{cr} are the critical temperature and pressure of the gases and a and b are empirical coefficients tabulated in [59]. By plugging Eq. (3.14) into the mass conservation equation and neglecting mass sources (div c = 0) the Laplace equation for potential fields is obtained

$$\nabla^2 c = 0 \qquad (3.17)$$

In gas mixtures with more than two species, the diffusive mass fluxes are interrelated and the Mawell-Stefan Eq. (3.18) for multicomponent diffusion applies

$$\mathbf{N}_k = -\rho w_k \sum_{l \neq k} D_{kl,\text{eff}} \frac{M}{M_l} \left(\nabla w_l + w_l \frac{\nabla M}{M} \right) \qquad (3.18)$$

where ρ and M are the density and molar mass of the mixture, M_l is the molar mass of species l and w is the weight fraction. In Eq. (3.18) temperature and pressure diffusion terms are neglected.

Knudsen diffusion is dominating in pores with diameters D smaller than the mean free path λ. It can be neglected if the Knudsen number is $Kn \ll 1$:

$$Kn = \frac{\lambda}{D} = \frac{k_b \, T}{\sqrt{2} \, \sigma^2 \, p} \frac{1}{D} \tag{3.19}$$

Therein k_b is the Boltzmann constant and σ the molecule diameter. If $Kn \geq 1$ the Knudsen diffusion coefficient D_{Kn} has to be used instead of D_{kl} [79]. Eq. (3.20) requires a well defined pore geometry.

$$D_{Kn} = \frac{2}{3} \left(\frac{8RT}{\pi M} \right)^{1/2} \frac{D}{2} \tag{3.20}$$

3.2.2 Convective Transport

Convective transport of gas and liquid water is dominant in the channels of a flow-field and may be significant in the porous GDL depending on the flowfield geometry. Based on Newton's second law the formulation of momentum conservation for a free moving fluid results in the famous Navier-Stokes equation. For an incompressible, Newtonian fluid (linear stress-strain curve) the Navier-Stokes equation can be simplified to

$$\rho \left(\frac{\partial \mathbf{v}}{\partial t} + \mathbf{v} \nabla \mathbf{v} \right) = -\nabla p + \mu \nabla^2 \mathbf{v} \tag{3.21}$$

where $\mathbf{v}$ is the velocity vector, p the fluid pressure and μ the dynamic viscosity [kgm^{-1}s^{-1}]. The density ρ times the acceleration terms on the left hand specifies the inertia of the fluid. The second acceleration term on the left hand side describes the convective acceleration due to a geometry change. The terms on the right hand side describe the body forces in [Nm^{-3}] induced by pressure differences and the shear stresses $\mu \nabla \mathbf{v}$ in the fluid. Assuming a stationary creeping flow with low velocities or high viscosities (Re $<< 1$) the acceleration terms can be neglected and Stokes equation follows

$$0 = -\nabla p + \mu \nabla^2 \mathbf{v} \tag{3.22}$$

The porous-media analog of the Navier-Stokes equation is Darcy's law. It states that the fluid velocity is linear to the negative of the fluid pressure gradient and the fluid permeability in the porous media

$$\mathbf{v} = -\frac{k \, K}{\mu} \nabla p \tag{3.23}$$

where k is the relative permeability and K the absolute permeability of the porous media. Note that the superficial velocity used in Darcy's law is not the pore velocity but calculated for the entire flow cross section. Eq. (3.23) is valid for low velocities

assuming incompressibility and no wall shear. For turbulent flow in porous media the Forchheimer extension with a non-linear flow resistance term has to be applied [61]. To account for wall shear at the boundaries of the porous media the Brinkmann extension to Darcy's law has to be used. To account for the compressibility of the gases, the pressure corrected Darcy's law has to be applied [57]:

$$\mathbf{v_2} = -\frac{k\,K}{\mu}\,\frac{p_2^2 - p_1^2}{2p_2 L} \tag{3.24}$$

It is derived by integration of the differential form in Eq. (3.23) from inlet (subscript 1) to outlet (subscript 2) and by ensuring mass conservation ($v_1 p_1 = v_2 p_2$) over the thickness L.

3.2.3 Membrane Water Transport

The membranes used in PEFC take up significant amount of water. On the one hand the membrane requires water to be ionically conductive. On the other hand the volume increase due to swelling, which is around 20% depending on membrane type, is considered responsible for mechanical degradation of the membrane structure. Many experimental studies exist which relate the humidity conditions in the cell to the membrane water content by water uptake isotherms (Eq. (7.27)). During operation asymmetric humidity conditions exists resulting in membrane water content concentration gradients. The diffusive transport due to this gradient is described by the membrane water diffusivity (Eq. (7.28)), which is itself a function of membrane water content. Another transport mechanism of water in the membrane is the electroosmotic drag caused by the protons moving from the anode to the cathode. Due to the dependency on current density it can dominate the diffusive transport under certain conditions.

3.3 Charge Transport

The electrochemical reactions convert gases into charged species which have to be transported to and away from the active layers. Transport of ions (protons) in PEFC is far more stringent compared to transport of electrons. Although the two processes are fundamentally different the driving force is a potential difference in both cases.

3.3.1 Electric Charge Transport

An electric conductor contains mobile valence electrons. When an electric potential difference ϕ is applied the electrons move producing an electric current density j.

According to Ohm's law the current I per cross section area A is proportional to the electric conductivity σ

$$\mathbf{j} = \frac{\mathbf{I}}{A} = -\sigma \, \nabla \phi \tag{3.25}$$

In a composite or porous material the electric conductivity is a function of space x. Charge conservation without sources (div j = 0) results in the following differential equation

$$\nabla (\sigma(x) \nabla \phi) = 0 \tag{3.26}$$

If volume averaging is applied, the effective conductivity σ_{eff} is independent of space coordinate x. Similar to the effective diffusivity in Eq. (3.15) the effective electric conductivity scales with the volume fraction ε and the reciprocal of the tortuosity τ of the conducting phase

$$\sigma_{\text{eff}} = \frac{\varepsilon}{\tau} \, \sigma \tag{3.27}$$

By using the volume averaged effective conductivity the charge conservation (div j = 0) simplifies to Laplace's equation for potential fields

$$\nabla^2 \phi = 0 \tag{3.28}$$

The resistance R of a porous, ohmic conductor (independent of voltage, current and temperature) is a function of effective conductivity and geometry

$$R = \frac{l}{\sigma_{\text{eff}} \, A} \tag{3.29}$$

where l is the length of the conductor. The effect of increasing electric resistance at high temperature and current can be ignored for PEFC and therefore the electrical conductive components in PEFC (GDL, CL, BIP) are considered as ohmic resistors.

3.3.2 Ionic Charge Transport

The ionic charge transport mechanism and the ionic conductivity strongly depend on the employed electrolyte class. However, the macroscopic transport of ions in terms of ionic current density can also be described by Ohm's law

$$\mathbf{j} = -\iota \, \nabla \chi \tag{3.30}$$

wherein the ionic potential is expressed as χ while the ionic conductivity is reflected as ι.

4 Characterization Methods

Characterization methods for porous media can be categorized into microscopic and macroscopic experimental techniques [80]. The microscopic techniques such as X-ray tomographic microscopy and high-resolution light and electron microscopy examine small areas of the sample and reveal structural detail. These microscopic methods help understanding the macroscopic properties. Based on microscopic data macroscopic properties such as porosity, tortuosity, permeability and capillary pressure function (cf. Sec. 3.1) are not determinable. An exception is the computational determination of properties of 3D structures obtained by X-ray tomographic microscopy [81]. On the other hand the macroscopic techniques such as mercury intrusion porosimetry, gas adsorption porosimetry, electrochemical diffusimetry and permeametry investigate large sample volumes. They directly measure volume averaged structure and flow properties and generally rely on geometric models with constricted validity.

This chapter describes newly developed and applied experimental and computational characterization techniques. After a short review of porosimetry and permeametry methods an in-depth description of the electrochemical diffusimetry and X-ray tomographic microscopy methods follow. The electrochemical diffusimetry method was developed, validated and applied in the context of this thesis. Synchrotron-based X-ray tomographic microscopy was adapted and applied to gas diffusion layers. At the end of this chapter the computational characterization method of realistic GDL structures based on X-ray tomographic microscopy is introduced in order to bridge the gap between experimental and computational techniques. The results of the discussed methods are presented in Chap. 5.

4.1 Porosimetry

Porosimetry determines the total pore volume, the pore size distribution and the most constricted and average pore diameter. A comprehensive comparison of different porosimetry methods is given by Aksayha et al. [80]. As discussed in Sec. 3.1.1 pores in irregular structures, such as gas diffusion layers, have many diameters. Depending on the applied porosimetry technique different pore diameters can result from the measurement.

4.1.1 Extrusion Flow Porosimetry

In extrusion flow porosimetry (also called capillary flow porosimetry) a wetting liquid is used to fill the pores. The pressure of the non-wetting gas is increased to remove the wetting liquid and permit gas flow. Gas only flows if the break-through pressure p_{bt} is exceeded (cf. Sec. 3.1.6). A flow meter detects the presence of pores by measuring the increase in flow rate as a function of differential pressure. The relative permeability as a function of saturation (cf. Sec. 3.1.7) can be calculated by an additional gravimetric or volumetric measurement of the residual liquid volume in the sample. Extrusion flow porosimetry only measures the most constricted pore diameters of through pores at the pore throats. With gas adsorption porosimetry and mercury intrusion porosimetry all diameters of through and blind pores are measurable. A setup similar to extrusion flow porosimeter has been built for the water intrusion experiment in Sec. 4.4.4.

4.1.2 Gas Adsorption Porosimetry

A gas exposed to a clean surface forms an adsorbate layer. The properties of this adsorbate depends on pressure, temperature and nature of the gas. In gas adsorption porosimetry the amount of gas adsorbed is measured as a function of gas pressure below its saturation pressure. At low relative pressures a monolayer is formed and the amount of adsorbed gas is proportional to the pore surface area according to the BET theory [82]. At high relative pressures condensation starts in the most narrow sections of the pores and continues with increasing gas pressure towards wider parts. The total pore volume can be calculated from the volume of condensed gas for pore diameters smaller than 2 μm [80]. This makes gas adsorption porosimetry usable to investigate the catalyst layer of PEFC (cf. Chap. 6).

4.1.3 Mercury Intrusion Porosimetry

Mercury intrusion porosimetry (MIP) can be used for measuring the pore volume and pore size distribution over the range of 200 μm to 30 nm [80]. Mercury is a non-wetting liquid and has a contact angle larger than 90° with most solid-air combinations. Initially the GDL sample is surrounded by the non-wetting mercury and pores are not filled spontaneously. With increasing mercury pressure successively smaller pores are filled. Thereby mercury enters the GDL from all sides and the diameters of through pores can be correctly measured. The relationship between the mercury pressure p_{Hg} and the pore diameter D can be described by the Young Laplace equation (Eq. (3.8)) which is also known as Washburn's equation [83]

$$p_{\text{Hg}} = -\frac{4}{D}\, \zeta_{\text{Hg}} \cos\theta \tag{4.1}$$

where ζ_{Hg} is the surface tension of Hg ($0.48\ \text{Nm}^{-1}$) and θ the average contact angle of Hg on a PTFE-carbon composite ($110°$, Gostick et al. [30]). The ratio $4/D$ is equal to the ratio of pore perimeter to area for a circular cross section.

A possible source of error is the assumption of circular pore cross sections which are not obvious for GDL's. This will affect the shape of the pore size distribution but not the total pore volume. However, the order of magnitude of calculated pore diameters will not change as the ratio of perimeter to area $4/D$ does not change significantly for non-circular cross sections. Another source of error are dead-ended pores. They are only measured accurately if the entry diameter is larger than the subsequent diameters. Furthermore the high pressures applied to the sample require incompressibility of the sample. Otherwise the structure is changed during the measurement and results in a shift of the pore size distribution towards larger diameters. For more physical basics on MIP the reader is referred to the review paper by Brakel et al. [84] or to the early work by Ritter et al. [85].

The MIP measurements were carried out using a Micromeritics AutoPore 9320 with a pressure range of 6 kPa to 200 MPa. A solid 3 cm^3 penetrometer (number 07-0641) was filled with a sample volume of about 0.2 cm^3. Assuming a porosity of 80% the pore volume to measure was about 0.16 cm^3 and therefore within 25% to 90% of the stem volume of the penetrometer (max. measurable volume). Sample and assembled penetrometer were weighed before filling with mercury. Then the penetrometer was evacuated to remove gases and while still evacuating mercury was allowed to fill the penetrometer. In the next step mercury pressure was increased towards ambient pressure in 0.5 psi steps (3450 Pa) while the volume of mercury entering larger openings in the sample was monitored. The penetrometer filled with mercury was weighed again to determine the mercury volume before placing it into the high pressure vessel to force mercury into the remaining pores smaller than approximately 7 µm.

The total pore volume is the most direct property measurable by MIP. However, a significant artifact arises from the interstitial void volume. Several GDL samples were stacked in the penetrometer producing a gaps in the range of 100 µm. Therefore the measured sample volume (envelope volume) and mercury intrusion volume was corrected with the volume of pores greater than 100 µm. The ratio of the corrected mercury and sample volume resulted in the porosity. For the pore size distribution Eq. (4.1) was applied. The applied pressure at each step can be transformed into a circular pore diameter. For the cumulative pore size distribution, the intruded mercury volume is plotted against the corresponding diameter. The log-differential pore size

distribution illustrates the change of volume with change of diameter. It is the derivative of the cumulative pore size distribution with respect to the logarithm of the pore diameter. The logarithm is necessary for better readability of the plot. The results of the MIP measurements are discussed in Sec. 5.2 and summarized in Table 5.1

4.1.4 Decane Wetting Porosimetry

To additionally verify the total pore volume measured by MIP the simple and fast decane-wetting method was used. A known volume of material was weighed before and after wetting with decane. Decane ($C_{10}H_{22}$) is a liquid alkane which is assumed to completely fill the voids in a GDL. Its contact angle is smaller than $90°$ with most solid-air combinations. Knowing the density of decane (0.73 gcm^{-3}), the intruded volume and consequently the porosity is obtained directly from the weight difference of empty and filled samples. Owing to the low vapor pressure of decane, weighing of the filled samples is not time-critical. This procedure was repeated with several samples per material to obtain a standard deviation. The results of the decane wetting porosimetry are compared to MIP results in Table 5.1.

4.2 Permeametry

Permeametry measures absolute permeabilities of porous materials and the influence of direction and compression. The in-plane permeability of GDL's as a function of compression has previously been measured by J.T. Gostick et al. [86] and the uncompressed through-plane permeability by M.V. Williams et al. [87]. For the in-plane permeability a similar design as presented by Gostick et al. [86] was employed. In order to obtain through-plane permeabilities of GDL's as a function of compression for the first time, a new sample holder was designed. The through-plane permeability is important as liquid water crosses the GDL mainly in through-plane direction. Moreover the through-plane permeability is expected to be smaller than the in-plane permeability and therefore more limiting for mass transport. Permeametry results including the influence of PTFE and MPL are discussed in Sec. 5.3.

The basic principle of measuring compression dependent permeabilities of GDL's is to compress the GDL to a certain thickness and then to apply a defined gas flow across it. Knowing the pressure drop and geometry of the GDL, the permeability can be calculated by applying the pressure corrected Darcy's law in Eq. (3.24). To determine the in-plane permeability with an MPL the convective flux was assumed to flow in the GDL only and as a consequence only the GDL thickness was taken into account.
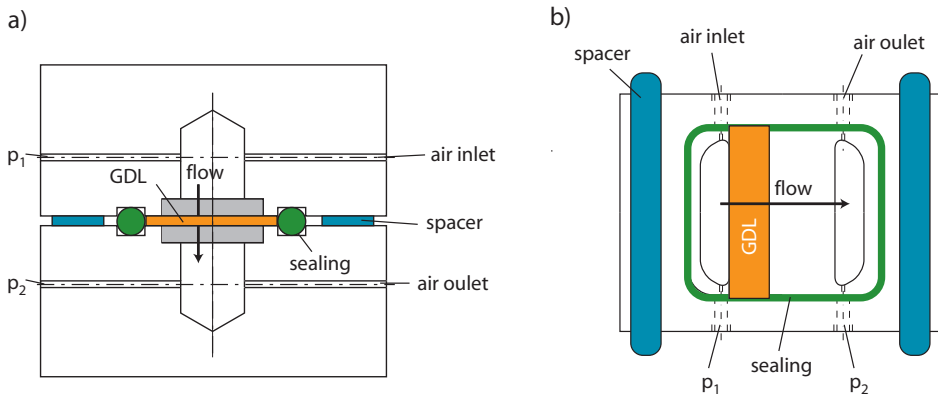
Figure 4.1: Permeability sample holder for **a)** through-plane and **b)** in-plane direction.

The in-plane sample holder is shown in Fig. 4.1b). The GDL was compressed between two metal blocks and sealed at the short edges to avoid bypassing. A defined flow of compressed air was imposed by a mass flow meter (Bronkhorst, F-201C) across the GDL and the pressure drop $p_1 - p_2$ was measured with a water column gauge (Stillknecht, Type 612a). The apparatus was manufactured using stainless steal with a thickness of 30 mm to assure a uniform compression at the distance defined by the spacer plates. To uniformly supply air and measure the pressure at the inlet and outlet side of the GDL, there were two large-volume chambers machined into the metal blocks. The precision of the compression is enhanced by stacking several GDL's. The sealing was tested to atmospheric pressure by closing the air outlet and pressurizing the apparatus up to 1 bar overpressure. The flow resistance of the apparatus itself has been subtracted from the overall pressure drop. Furthermore the permeability results were tested to be independent of flow velocity in the measurement range to ensure applicability of Darcy's law.

The through-plane sample holder is sketched in Fig. 4.1a). The basic principle is the same. However, for the through plane measurements the same material that compresses the GDL has to be able to supply gas to the GDL. Therefore the GDL was compressed by clamping it between two highly permeable, sintered frits (stainless-steel, 25-40% porosity, 38 μm fineness). The pores of the frit and GDL were of the same size minimizing interfacial effects. The pressure drop over the apparatus including the frits was around 40% of the total pressure drop. Measurements were corrected with the pressure drop of the apparatus.

4.3 Electrochemical Diffusimetry

Within this thesis, an alternative method to measure the effective diffusivity of GDL's has been developed in close collaboration with Stefan Freunberger [88] and Denis Kramer [89]. The method, including the theoretical basics, was published in [90]. Besides enabling fast and cost effective experiments, the method allows to measure the effective relative diffusivity of GDL materials in in-plane as well as in through-plane direction and both can be investigated as a function of compression. Corresponding results have been published in [91].

   In the following section the theoretical foundation of the measurement principle (i.e., measuring the effective diffusivity by electrochemical means) is derived. The analogy between Fick's and Ohm's law is explained, leading to the effective ionic conductivity as a measure for the effective diffusivity. Electrochemical impedance spectroscopy (EIS) is the method of choice to obtain the effective ionic conductivity and the theory needed to interpret the spectra is subsequently presented. Experimental details, such as the used apparatus and sample preparation are described in the experimental section. Validation of the method using a model material and results for different GDL's are presented in the GDL characterization Sec. 5.4.

4.3.1 Theory of Electrochemical Diffusimetry

Analogy between Potential Flows

The task of measuring the effective diffusivity D_{eff} (Eq. (3.15)) can be transposed into the task of obtaining the effective ionic conductivity σ_{eff} (Eq. (3.27)) of an electrolyte-soaked GDL. For this the analogy between Fick's law (Eq. (3.14)) and Ohm's law (Eq. (3.25)) is leveraged. Both equations are expressed in terms of volume averaged, effective quantities and both, the effective diffusivity D_{eff} and the effective conductivity σ_{eff} are proportional to the ratio of porosity and tortuosity ε/τ, which is referred to as the effective transport coefficient. With the electrochemical diffusimetry this ratio is obtained experimentally by measuring the ratio $\sigma_{\text{eff}}/\sigma$, with σ being the bulk ionic conductivity of the free electrolyte.

Measuring the Effective Conductivity

Unlike resistance, impedance is frequency dependent. It is defined as the ratio of a time dependent voltage $U(t)$ and current $I(t)$

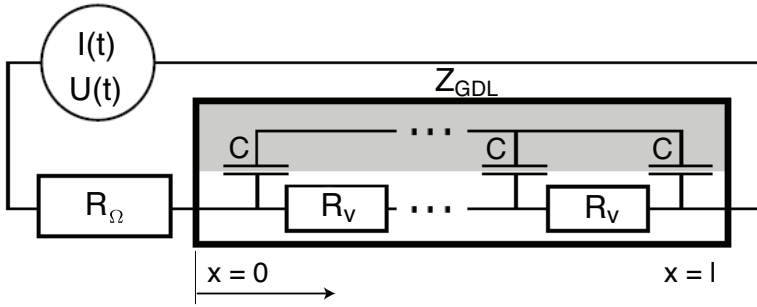$$Z = \frac{\Delta U(t)}{\Delta I(t)} \tag{4.2}$$

Figure 4.2: Equivalent circuit of an electrolyte filled GDL illustrating the conversion and transport of electrical and ionic currents within the carbon phase (gray) and void phase (white) respectively. The electric resistance in the carbon phase is negligible compared to the ionic resistance in the void R_v.

Typically a small sinusoidal voltage $U(t) = U_0 \, cos(\omega t)$ is applied while measuring the resulting sinusoidal current response $I(t) = I_0 \, cos(\omega t - \Phi)$. The amplitude of voltage and current signal are U_0 and I_0 respectively. The radial frequency ω [rad s^{-1}] can be expressed in terms of frequency f [Hz] by $\omega = 2 \, \pi \, f$. Generally the response is shifted in phase by Φ. Using the complex notation the impedance can be defined in terms of impedance magnitude Z_0 and phase shift Φ

$$Z = Z_0 \, (cos\Phi + \mathbf{i} \, sin\Phi) \tag{4.3}$$

In a Nyquist plot the imaginary part of impedance is plotted against the real part while in a Bode plot the amplitude and phase are plotted as a function of frequency. A more detailed introduction to EIS can be found in [14, 92].

As the alternating current over the electrode-electrolyte interface at high frequencies ($f \sim 10$ kHz) mainly stems from double layer charge/discharge, the high frequency impedance bears the advantage of avoiding undesirable faradayic processes. Consequently the high frequency impedance provides a direct measure for the ohmic resistance of the electrolyte connecting the electrodes.

A complicating effect arises from the electrical conductivity of the GDL. Due to the electrical conductivity of the substrate, simultaneous electrical and ionic alternating currents may occur within the sample. Although these are transported within separate phases, they are coupled via the double layer formed at the substrate-electrolyte interface. This is illustrated in Fig. 4.2. At vanishing frequency, the electrical and ionic currents are unrelated because the impedance of the double layer tends towards infinity. At the high frequency end the double layer impedance becomes negligible. The considerably higher electric conductivity of the sample allows to neglect the gradient in electric potential compared to the gradient in ionic potential. Therefore, the charge

balance within the electrolyte can be decoupled from the electric balance within the substrate. The impedance of the electrolyte soaked GDL follows from the integration of the charge balance equation over the sample and is derived in [90]:

$$Z_{\mathrm{GDL}} = \frac{l/A}{\sigma_{\mathrm{eff}}} \frac{\tanh\left(\frac{1}{2}\sqrt{\mathbf{i}\,\frac{\omega}{\omega_{\mathrm{c}}}}\right)}{\frac{1}{2}\sqrt{\mathbf{i}\,\frac{\omega}{\omega_{\mathrm{c}}}}} \tag{4.4}$$

$$\omega_{\mathrm{c}} = \frac{\sigma_{\mathrm{eff}}}{l^2\,C} \tag{4.5}$$

Therein ω_{c} denotes the characteristic frequency of the electrolyte-soaked GDL where the imaginary impedance is maximal. C is the effective double layer capacitance per unit volume, A the cross-sectional sample area perpendicular to the direction of the ionic current, and l is the sample length in direction of the ionic current.

Finally, the voltage is sensed at some distance from the GDL. Consequently the measurable impedance will contain an additional ohmic contribution Z_Ω stemming from the finite conductivity of the electrolyte between sample and voltage sensing point. Hence, the measurable impedance is given by

$$Z = Z_\Omega + Z_{\mathrm{GDL}} \tag{4.6}$$

The impedance characteristic given by Eq. (4.6), which is exemplified in Fig. 4.3 in a Nyquist plot, is that of a semi-circle with a high frequency tail (line of constant argument). At the high frequency limit, the internal double layer provides negligible resistance and the ionic current entering the sample is virtually instantaneously transfered into an electric current at the sample edges ($x = 0$, $x = 1$). As the electric resistance is negligible compared to the ionic resistance, the high frequency end of the spectrum is given by the ohmic resistance of the electrolyte Z_Ω between sample and voltage sensing point and lies on the real axis.

With decreasing frequency, the internal double layer starts to provide significant resistance, and the ionic alternating current starts to penetrate deeper into the sample ($0 < x < 1$) resulting in a high frequency tail which ideally has an angle of 45° followed by an arc at lower frequencies. As the frequency approaches zero the double layer resistance tends towards infinity and all current is passing the sample in the electrolyte phase. Thus, the low frequency limit lies again on the real axis. The distance between high frequency and low frequency end on the real axis is given by the effective ionic resistance of the electrolyte-soaked GDL, which is proportional to the reciprocal of the effective electrolyte conductivity σ_{eff}.
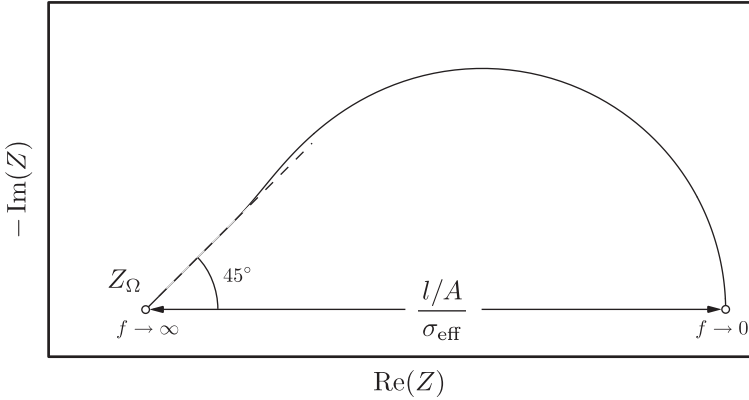
Figure 4.3: Nyquist plot of the impedance spectrum of an electrolyte-soaked GDL as given by Eq. (4.6).

Unit Cell Model

Grasping the complexity of porous structures from a theoretical perspective usually requires the retreat to simplified problems. The study of periodic structures, where a unit cell can be defined, rather than the irregular porous structures themselves is the classical approach. Remarkable success has been achieved following this route whilst calculating the thermal conductivity of porous structures [58]. It allows to encode relevant morphological properties by few geometric parameters. This path is followed to develop a theory assisting the discussion of the experimental findings.

As long as the potential field in the porous sample is harmonic (satisfies Laplace's equation), and sufficiently described in two dimensions, conformal maps provide an approach to transpose the complex internal geometry of GDL's into simpler Cartesian equivalents. A conformal map is a coordinate transformation, which preserves angles between and directions of curves upon transformation [93]. Due to this property, a potential field transformed via a conformal map into another, usually simpler, coordinate space retains its potential character. This allows to solve for the potential field in a simpler, conformal (orthomorphic) coordinate space. Another important property of conformal maps is that Dirichlet and homogeneous Neumann boundary conditions are invariant to transformation.

Defining a suitable unit cell is to a good extent subjective, leaving it to the comparison with experiment to ensure that the choice made is a sensible one. Consider an arbitrary cut through a paper-type GDL. The fibers will be sliced in any angle resulting in elliptical surfaces. If the orientation angle of the fibers is uniformly distributed, the average angle between an arbitrary cut and fibers is $\pi/4$, which means that the ratio of the ellipse radii is given by $R_B/R_A = \sqrt{2}$. In addition to the carbon fibers,
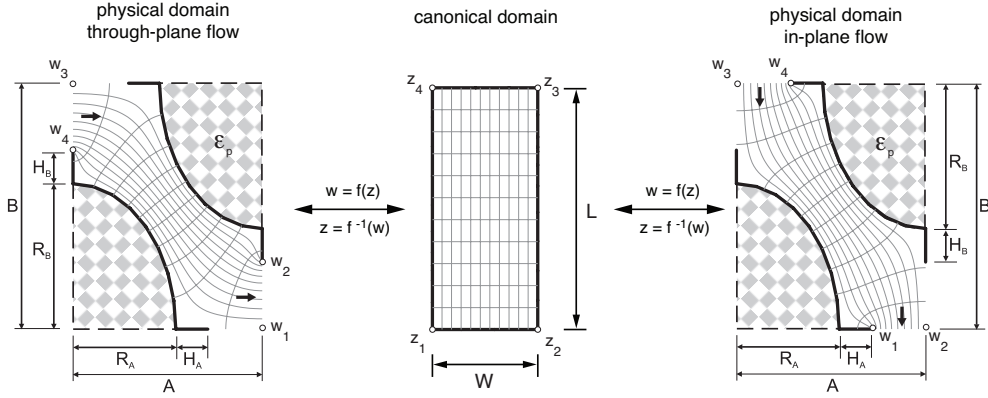
Figure 4.4: Unit cell geometry (bold line) in the physical domain for in-plane (**left**) and through-plane (**right**) diffusion. The elliptical fiber cross sections are filled with a porous pattern to imitate the primary porosity ε_p of the binder. Streamlines and iso-concentration lines are displayed in the pore space. In the middle the conformal mapping of the unit cell geometry polygons onto a rectangle is shown.

the incorporated binder and wet-proofing agent needs consideration while defining the geometry of the unit cell. The binder tends to form skins between the fibers as discussed in Sec. 5.1. These skins provide significant mass transport resistance, although they hardly have any contribution to the solid volume of the GDL. Therefore additional thin flaps were added to the ellipse in in-plane as well as through-plane direction as shown in Fig. 4.4. Their relative lengths H_A and H_B were used as fit parameters to experimental data. They are dimensionless and measured relative to the constant fiber diameter R_A which was chosen equal to 1. Furthermore a primary porosity ε_p has been introduced as a third fitting parameter required to describe porous binder properties. Knowing that averaging the primary porosity of fiber and binder is inaccurate, it is justified for materials with high binder volume fractions. Furthermore the log-differential pore size distribution in Fig. 5.5 measured by MIP justifies the introduction of a primary porosity to the unit cell also in accordance with [94]. The primary pores of the unit cell do not contribute to the transport but affect the porosity calculation. According to this the porosity of the unit cell is calculated by

$$\varepsilon = 1 - \frac{\pi}{2} \frac{R_A{}^2 (1 - \varepsilon_p)}{AB} \tag{4.7}$$

Initially the height B of the unit cell was a fourth fitting parameter. However, it turned out to be constant around 2.4 for the materials investigated. Once the unit cell is defined, the task is to find the conformal map w = f(z) such that the vertices of the unit cell w_1 to w_4 in the physical domain map to the corners of a rectangle

z_1 to z_4 in the canonical domain. Moreover, the polygons connecting the vertices of the unit cell have to map onto lines of the rectangle. A limited number of useful conformal maps can be composed out of elementary functions. Yet, more general domains, such as the unit cell given in Fig. 4.4, call for numerical methods. Fortunately, rather sophisticated numerical toolboxes such as SCPACK and CONFPACK are available. Among the great variety of available numerical methods, the Schwarz-Christoffel transformation (SC) is probably best suited for this particular domain, as it treats corners explicitly. A comprehensive introduction to SC transformations can be found in [95]. Driscoll's "SC Toolbox" [96] has been used, which is a set of routines for Matlab, throughout this work. A drawback of the SC transformation arises from its limitation to straight boundaries. This difficulty is bypassed by breaking up the ellipses into short line segments during computation without seriously impeding accuracy or computational efficiency — provided the number of line segments is chosen thoroughly.

Having solved the parameter problem of the SC transformation, the dimensions L and W of the conformal rectangle in Fig. 4.4) are known. The conformal modulus, which is the ratio thereof, is related to the effective transport coefficient ε/τ. For the two cases of in-plane and through-plane flow, the following expressions were derived:

$$\frac{\varepsilon}{\tau} = \left\{ \begin{array}{ll} \frac{W/L}{B/A} & \text{for through-plane case} \\ \frac{W/L}{A/B} & \text{for in-plane case} \end{array} \right\} \tag{4.8}$$

These simple expressions were deduced from the effective volume theory in [90]. Though the geometry of the unit cell is fixed, different conformal maps are needed for through-plane and in-plane direction. The vertices z_i map to different vertices w_i. Therefore, the values of W and L are different for both cases.

A least square regression algorithm was used to find the three fitting parameters H_A, H_B and ε_p. Starting with an initial unit cell geometry the conformal modulus was calculated for the porosities of the experimental data. The porosity of the unit cell is changed by reducing the width A and keeping all the other parameters constant. The comparison of the resulting conformal modulus and the experimental effective transport coefficients resulted in a new guess for the Matlab optimization procedure. The unit cell fitting parameters are listed in Table 5.2 and the corresponding effective transport coefficients are illustrated in Fig. 5.15.
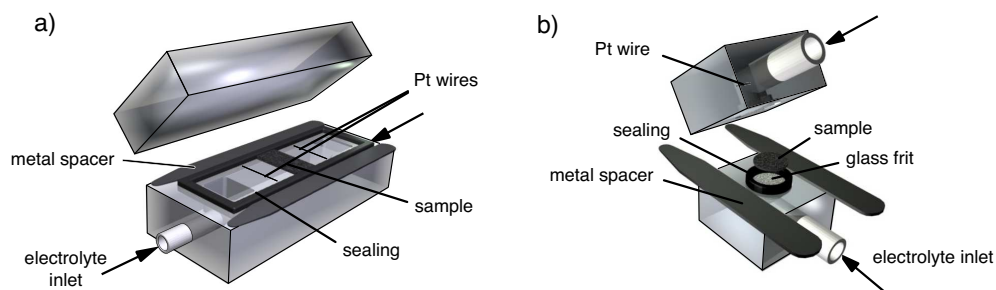
Figure 4.5: Sketches of the sample holder for **a)** in-plane and **b)** through-plane electrochemical diffusi-
metry. The sample for in-plane measurements is 2.4 cm wide and 1 cm long. The circular sample for
through-plane measurements has a diameter of 8 mm.

4.3.2 Setup of Electrochemical Diffusimetry

Sample Holder

To investigate the in-plane direction, the sample holder sketched in Fig. 4.5a) was
manufactured. It consists of two acrylic glass blocks 4.0 cm wide, 8.3 cm long, and
2.0 cm high. The upper block was not further machined except for grinding and
polishing the surface. Two cavities are machined into the lower block to allow filling
with electrolyte via connector tubes. In addition, a groove hosting a soft sealing is
machined into this block, and the block is likewise grinded and polished to ensure
a sufficiently flat surface. Two 100 μm thick platinum wires, serving as potential
probes, are positioned at a distance of 3 cm. The sample is placed in-between. The
width of the gap hosting the sample is 2.4 cm.

The sample holder for through-plane measurements is shown in Fig. 4.5b). Again,
it is made from two acrylic glass blocks. This time both blocks are similarly machined.
Holes are drilled in the center of the block, which allow electrolyte entry. A glass frit,
8 mm in diameter and 3 mm thick, is incorporated to allow compressing the GDL
in through-plane direction whilst retaining uniform electrolyte access to the sample.
Being made of an electrically insulating material (glass), the frit does not contribute
to the complex impedance of the spectrum. Only the ohmic resistance is increased
due to its porosity and tortuosity. The voltage is sensed by a Pt wire about 2 mm
beneath the glass frit, and a groove hosting a soft sealing ensures exact positioning of
the sample. The sample holder was polished after the frit was fixed to ensure a flat
surface.

Measurement Procedure

Samples were cut from larger sheets. For in-plane measurements, a rectangular shape (2.4 cm wide and 1 cm long) was used, while the sample shape for through-plane measurements was circular with a diameter of 8 mm. The samples were placed within the sample holder such that a tight connection with the sealing was achieved in order to avoid leak currents. Before placing them into the sample holder, the samples were filled with electrolyte (0.5 M sulfuric acid) by evacuating an electrolyte-filled flask with the samples in it. If needed, the flask was evacuated several times until gas evolution from the sample ceased. After placing the samples into the holders, the sample holder was closed and a constant force was applied by a hydraulic press. The compression of the sample was controlled by metal spacers at the perimeter. Electrolyte was filled in and gas was thoroughly removed from the apparatus by mutually flushing electrolyte through it and evacuating the assembly.

For both measurements stacks of samples (in-plane: 4-8, through-plane: 10-20) were favored over single sheets for different reasons. During in-plane measurements, the precision of compression motivated the use of stacks of samples. Having a thicker sample, the demand for precise relative compression is easier to comply with. For the through-plane measurements an additional motivation stems from Eq. (4.4). The characteristic frequency $\omega_c = \sigma_{\text{eff}}/(l^2\,C)$, where l denotes the length of the sample in the direction of current, would become rather large for lengths in the micrometer range (single sample). This would require accurate impedance measurements well above 10 kHz, which can be demanding due to artifacts such as cable inductance. Moreover, a single GDL provides a rather small through-plane impedance and therefore reduces the accuracy of measurement. To ensure the validity of sample stacking several measurement with varying numbers of GDL's were made and no dependence of the results with respect to the number of stacked samples could be found.

A series of spectra was recorded consecutively for different compressions. The compression was changed by exchanging the metal spacers, which was possible without opening the assembly. All measurements were made by starting with a metal spacer close to the uncompressed thickness of the sample. Subsequently, the compression is gradually increased up to a maximum degree of compression, which was limited by the mechanical rigidity of the sample holder (cf. Fig 5.9). All impedance spectra were recorded in a four-point measurement configuration. The potential was sensed via the incorporated Pt wires, and the current was applied via two additional Pt wires introduced into the sample holder via the electrolyte inlets. A commercial impedance measurement unit obtained from Zahner Elektrik (Germany), Model IM6, was used. The device was operated in pseudo-galvanostatic mode, setting the dc current to zero.

4.4 X-Ray Tomographic Microscopy

The motivation to use X-ray tomographic microscopy at the TOMCAT Beamline of the Swiss Light Source (SLS) originated from the necessity to understand the complex 3D structure of GDL's in order to correlate structure and measured properties. In this section the theory behind X-ray tomographic microscopy is summarized and then the three measurement setups are explained in detail. The first setup (cf. Sec. 4.4.3) was built to reveal structural details of GDL's under mechanical compression. The second setup (cf. Sec. 4.4.4) was used to visualize for the first time liquid water pathways inside GDL's. Finally the challenge of an *in-situ* active cell experiment has been tackled with the third setup (cf. Sec. 4.4.5).

4.4.1 Theory of X-Ray Tomographic Microscopy

The main advantages of synchrotron radiation compared to conventional X-ray tubes are the monochromaticity and coherence which allows to access the phase information. The high photon flux (intensity) and the high brilliance (emitted photons per area) enable fast measurements.

Absorption & Phase Contrast

X-rays passing through a material are reflected, scattered, absorbed or transmitted unchanged. If a monochromatic beam (single energy E) with an intensity I_0 penetrates a sample in x-direction with a linear absorption coefficient distribution $\mu(x, E)$ and a thickness D, the intensity I of the X-ray beam leaving the sample is given by Lambert-Beer's law

$$I = I_0\, e^{-\int_D \mu(x,E)\, dx} \tag{4.9}$$

The relationship between the number of photons reaching a specific point x and the thickness of the material to that point is exponential. The linear absorption coefficient μ with unit $[\text{cm}^{-1}]$ is material specific and energy dependent. The widely used absorption contrast method [97–99] makes use of differences in the linear absorption coefficient which is proportional to the imaginary part β of the index of refraction (Eq. (4.11)). For a specific material with an atomic number Z and electron density ρ_e $[\text{e}^-$ per $\text{cm}^3]$ the linear absorption coefficient is defined by

$$\mu = \rho_e\left(a + \frac{b\, Z^{3.8}}{E^{3.2}}\right) \tag{4.10}$$

where a is the Klein-Nishina coefficient $[\text{cm}^2$ per $e^-]$ [100] which is only weakly dependent on energy level and b = 9.8 x 10^{-24} (E.C. McCullough [101]).

Especially for light and weak absorbing materials as is carbon and water, the contrast which arises from this mechanism is not sufficient for imaging, since the attenuation of X-rays by low-Z materials is very poor. On the other side, the phase shift induced by such materials can be significant. Therefore phase contrast methods can be successfully used to measure GDL's. Propagation-based phase contrast techniques exploit the coherence properties of the synchrotron source, which, thanks to interference phenomena, allow to record the phase shifts induced by the sample when illuminated. The phase shift is proportional to the real part δ of the index of refraction

$$n = (1 - \delta) - \mathbf{i}\,\beta \tag{4.11}$$

Fig. 4.6 shows the energy dependency of the real and imaginary parts of the index of refraction for relevant materials. The higher the energy the smaller are phase shift and absorption. For the absorption contrast method a total transmission I/I_0 of around 0.3 is optimal for the TOMCAT beamline (empirical). For the experimental setups described in Sec. 4.4.3 to 4.4.5 this transmission value can be reached at a photon energy of about 10 keV. At this energy the difference of the imaginary part of the index of refraction between water and carbon is almost vanishing resulting in a low contrast. The phase contrast method assumes a weakly, homogeneous and slowly varying absorbing object, preferably with a transmission larger than 0.9 [102] which is obtained at around 30 keV. At this energy the difference of the real part of the index of refraction between water and carbon is significant resulting in a sufficient contrast for later phase segmentation. However, due to the high transmission required, the signal and therefore the aquisition speed of the detector is low and the exposure time per projection relatively high ($\sim$ 1200 ms). As a comparison the absorption contrast method is about 4 times faster with exposure times around 300 ms. Therefore absorption contrast is better suited for measurements of *in-situ* active cells (cf. Sec. 4.4.5) where quality has to be discarded for speed due to likely transient effects.

Tomographic Reconstruction

Tomography in contrast to radiography uses a series of 2D projections at different angles to reconstruct the 3D spatial distribution of a physical property. The concept had already been described by G.N. Hounsfield in 1973 [103]. He received the Nobel price in medicine for the development of computerized tomography in 1979 together with A.M. Cormack.

On the left of Fig. 4.7 the principle is illustrated by rotating an X-ray source and detector around a static sample as known from medical computer tomography scanners. Using synchrotron radiation requires the rotation of the sample rather than the
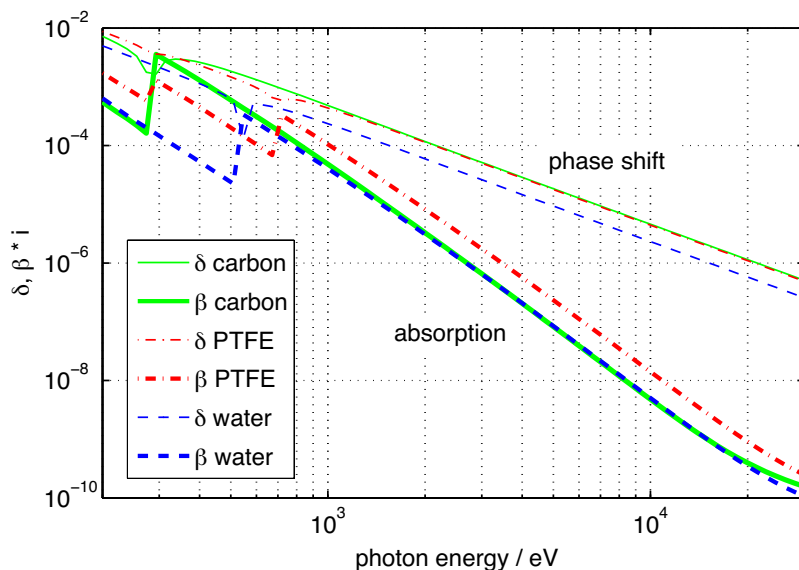
Figure 4.6: Index of refraction as a function of photon energy for materials used in GDL's. Real parts δ (phase contrast) are shown as thick lines. Imaginary parts β (absorption contrast) are shown as thin lines. Note that the vertical axis is also logarithmic and differences at small values appear larger. The discontinuities at low energies is due to the photoelectric effect (K-edge).

Figure 4.7: Tomography principle (**left**) with a rotating source/detector and absorption contrast backprojection algorithm steps (**right**) for a 2D sample with a strong absorbing excentric core (white). Adapted from the book of W.A. Kalender [104]

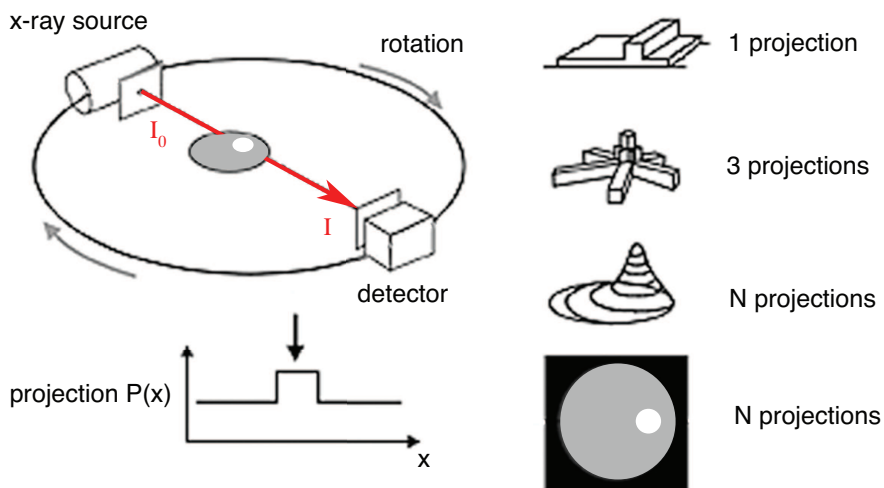X-ray source. The immobility of the sample with respect to the axis of rotation is essential for the reconstruction algorithm to work. For absorption contrast the sample-detector distance is ideally close to zero while for phase contrast a certain distance is necessary to produce interference (edge-enhancement regime). The X-rays (red arrow) are attenuated or phase shifted while crossing the sample and the intensity profile $I(x)$ is recorded by the detector for every angle. For calibration reasons additional flat and dark images are recorded before and after the scan. The projection $P(x)$ is the negative logarithm of the ratio $I(x)/I_0$ and for this the undisturbed intensity I_0 is logged before and after the scan by moving the sample out of the beam. In the intensity profile $I(x)$ strong absorbing areas are black while in the projections $P(x)$ they appear white.

In order to obtain the spatial distribution of a physical property out of the projections a reconstruction algorithm is required. The most simple to understand is the direct inversion algorithm used by G.N. Hounsfield [103]. The 2D spatial distribution consists of N x N pixels. Each pixel is an unknown in an equation system. If the number of projections times the pixel per projection is larger than N^2 the problem can be solved. However, for large number of pixels this approach is inefficient. Generally for absorption contrast the backprojection algorithm is applied. The different steps are shown on the right of Fig. 4.7. The algorithm assumes that the values of a single projection are constant along the beam. By adding up the values of N projections the strong absorbing excentric core can be located within the sample. More details can be found in the book of W.A. Kalender [104].

Among several methods available for phase contrast reconstruction the modified Bronnikov algorithm (MBA) was used because it guarantees speed, high resolution and sufficient sensitivity. The method was developed by A.V. Bronnikov [105] and modified by A. Groso et al. [102, 106] (TOMCAT staff). The algorithm detects interference fringes caused by the material and reconstructs the phase shift distribution from a single set of projections while other phase contrast methods require more than 4 data sets. In the following this method is referred to as phase contrast X-ray tomographic microscopy (PCXTM). The different steps from raw data acquisition to phase segmented 3D images are summarized in Fig. 4.8 for both absorption and phase contrast.

4.4.2 TOMCAT Beamline Settings

A first attempt to investigate the structure of GDL materials with X-ray tomographic microscopy has been done by B. Andreaus et al. in 2003 [107] at the Material Science beamline of the Swiss Light Source (SLS), a third generation synchrotron at the Paul Scherrer Institute, Switzerland. Their main problem was insufficient resolution
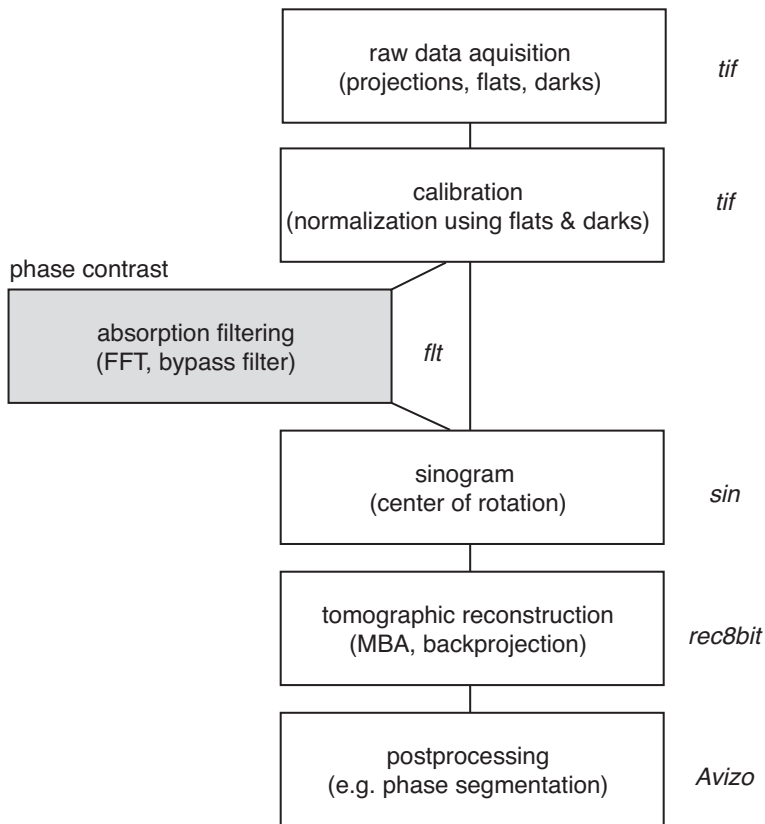
Figure 4.8: Tomographic reconstruction steps for absorption and phase contrast techniques. To the right of every step the corresponding data type is given.

magnification	field of view / mm^2	pixel size / μm^2
1.25x	11.4 x 11.4	5.6 x 5.6
2x	7.15 x 7.15	3.5 x 3.5
4x	3.58 x 3.58	1.75 x 1.75
10x	1.43 x 1.43	0.74 x 0.74
20x	0.72 x 0.72	0.35 x 0.35

Table 4.1: Resolutions and field of view of the TOMCAT beamline. Note that the pixel size gives the corresponding physical dimension in the sample.

and contrast between the different phases. They worked with a resolution of about 2x2x2 μm.

The experiments in this thesis were made at the TOMCAT beamline of the SLS [108] which started operation in 2006. The X-rays are provided by a 2.9 T super-bend magnet with a critical energy (average energy) of 11.1 keV. The Double Crystal Multilayer Monochromator (DCMM) covers an energy range from 8 to 45 keV and produces a monochromatic (2% bandwidth) flux density of 5 x 10^{14} photons/s at 10 keV. The horizontal and vertical beam size at the endstation (20 m from source) is 40 mm and 7-4 mm respectively. Transmitted X-rays are converted into visible light with a scintillator (YAG:Eu 25 μ, Yttrium Aluminum Garnet doped with Europium) magnified by an objective lens and detected on a charge coupled device (CCD) with 2048x2048 pixels. Table 4.1 lists the possible selection of objectives with the corresponding unbinned pixel size and field of view. For each sample 1001-1501 projections over 180 ° have been recorded.

Due to the novelty of the method several beamline setting were tested and applied depending on the aim of the specific experiment. The eight settings are listed in Table 4.2. In general the absorption contrast is faster than the phase contrast method because of detector efficiency and available flux. X-ray energies around 10 keV provide more flux to the detector and therefore shorter exposure times. With the phase contrast method the contrast is significantly improved but the exposure time is longer. However, phase contrast combined with the 4x objective is difficult as interference effects are hard to detect. Binning of the images resulted in about 4 times shorter measurement time as 4 pixels are combined to a single value producing both reduced exposure and camera read-out time. While testing the different settings it was learned that a field of view smaller than the sample size (local tomography) can produce inhomogeneous grayscales within a single phase. This impedes the discrimination of different phases during postprocessing.

#	mode	px size	binned	objective	field of view	energy	exp. time	time
1	abs.	0.74 μm	1x	10x	1.43 mm	10 keV	250 ms	20 min.
2	abs.	1.48 μm	2x	10x	1.43 mm	10 keV	250 ms	5 min.
3	abs.	1.75 μm	1x	4x	3.58 mm	10 keV	1000 ms	25 min.
4	abs.	3.5 μm	2x	4x	3.58 mm	10 keV	1000 ms	6 min.
5	phase	0.74 μm	1x	10x	1.43 mm	30 keV	700 ms	30 min.
6	phase	1.48 μm	2x	10x	1.43 mm	30 keV	700 ms	8 min.
7	phase	1.75 μm	1x	4x	3.58 mm	30 keV	1200 ms	52 min.
8	phase	3.5 μm	2x	4x	3.58 mm	30 keV	1200 ms	13 min.

Table 4.2: Overview of tested beamline settings. Setting #5: compression experiment Sec. 4.4.3. Setting #3: water intrusion experiment Sec. 4.4.4. Setting #8: active cell experiment Sec. 4.4.5.

4.4.3 Compression Setup

The flowfield rib induces mechanical stresses on the GDL and alters its porous structure and therewith its transport properties. In the first measurement campaign the focus was on the investigation of the micro-pore structure of different GDL materials under mechanical compression. The results are discussed in Sec. 5.1. Furthermore the obtained 3D geometries were used for a computational analysis to extract effective material properties (cf. Sec. 5.5).

The required pixel size for the fibrous structure was estimated 0.74 μm x 0.74 μm resulting in a maximum field of view of 1.43 mm x 1.43 mm (10x objective). For an optimum image quality the rotating sample should not leave the field of view. Therefore the samples were initially punched with a diameter of 1.3 mm. Later samples with 2.5 mm in diameter (local tomography) were used for the ease of assembly while still showing a sufficient quality. In order to study the influence of mechanical stress on the GDL structure special sample holders with an outer diameter of only 5 mm were designed (Fig. 4.9) which were mechanically strong enough to compress the GDL with compressive stresses up to 10 MPa (measured in [53]) and still have an acceptably low X-ray absorbance. These requirements were met with TORLON® 4203, a polyamide-imide with a tensile strength of 124 MPa. The shell of the sample holder in the X-ray beam was designed as thin as possible ($\sim$ 300 μm) in order to allow an X-ray transmission of 0.3 for absorption and 0.9 for phase contrast. A thread was integrated in the upper part of the cup in order to control the compression of the sample by a torque meter. The shear applied to the sample was minimized with a tapered screw and a bolt as shown in Fig. 4.9. Furthermore the distance of the sample from the detector for absorption contrast had to be as small as possible while still being able to rotate 180°.
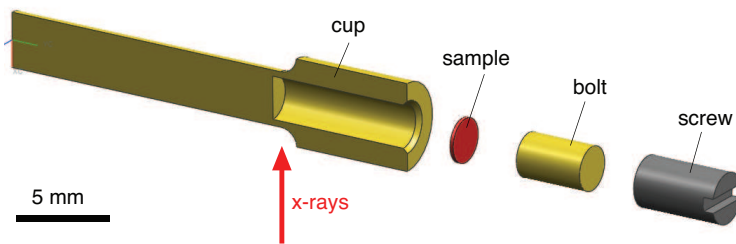
Figure 4.9: Explosion view of a cut compression sample holder containing a 2.5 mm GDL sample. X-rays illuminate the sample at the thinnest section of the sample holder. Rotation is around the longitudinal axis.

Figure 4.10: Explosion view of a cut liquid water sample holder containing a 2.5 mm GDL sample. X-rays illuminate the sample at the thinnest section of the sample holder. Rotation is around the longitudinal axis.
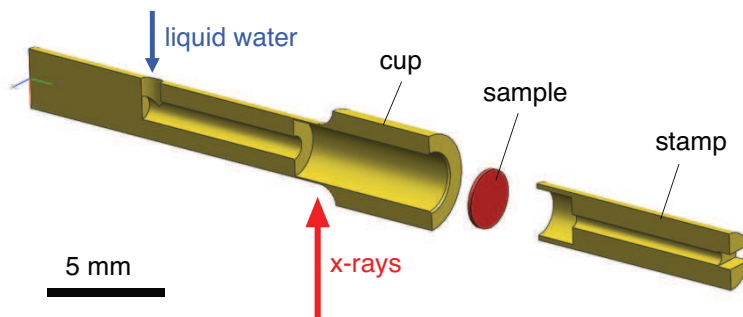
4.4.4 Water Intrusion Setup

The goal of the water intrusion experiment was the observation of the proceeding water front inside the GDL while the liquid pressure increases. A similar setup to the extrusion flow porosimetry introduced in Sec. 4.1.1 was designed. The water production at the catalyst layer (CL) was mimicked with an external water column. Due to the positive experience with the previous sample holder shown in Fig. 4.9 the design was only slightly adapted. Fig. 4.10 shows the modifications. The cup which takes a sample of 2.5 mm in diameter has been equipped with a water supply. The water column was connected to the sample holder over the L-shaped opening. The screw and bolt of the previous sample holder was combined into a TORLON-stamp including a thread. The stamp fixed and sealed the edges of the GDL and at the same time allowed air to escape to the surrounding.

The entire setup installed at the TOMCAT endstation is shown in Fig. 4.11. For the water column a burette was used, which is connected over a flexible rubber tube
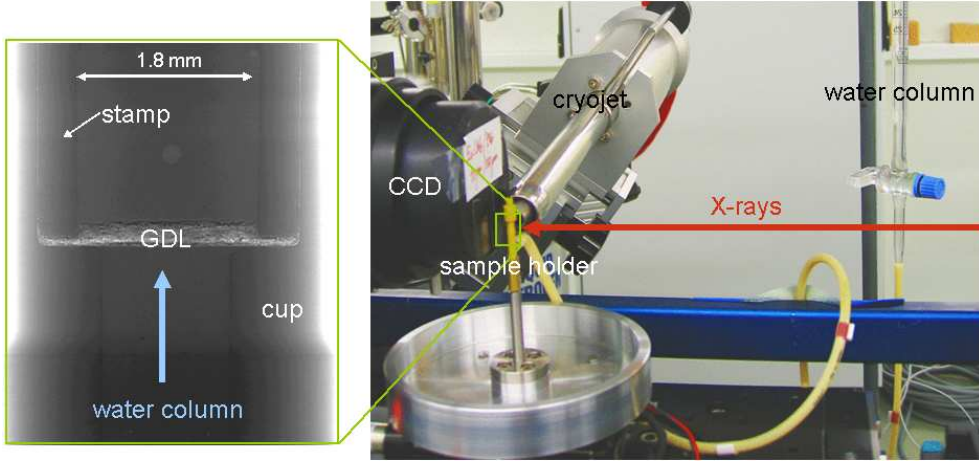
Figure 4.11: Photograph of the endstation setup with the liquid water sample holder connected to a burette and heated/cooled by a Cryojet®. In the magnification box a preview radiogram of the GDL sample is visible.

(yellow) to the sample holder placed as close as possible to the detector (scintillator, CCD). With the burette it was possible to adjust the hydrostatic water pressure in 10 Pa steps (1 mm water column). In order to study temperature influences (heating, cooling) a Cryojet® from Oxford Instruments has been used. However, useful results were only obtained for 25 °C so far due to minimized phase changes by condensation/evaporation. During measurements the sample holder rotated by 180° while X-rays impinged from the right. A radiogram preview is shown in the green magnification box of Fig. 4.11. Due to the compression of the GDL by the stamp at the periphery the pressurized liquid water was forced into the GDL. With the 10x objective and a field of view of 1.43 mm x 1.43 mm only the undisturbed central part of the GDL sample was measured (local tomography). The results are discussed in Sec. 5.6.

The liquid water intrusion experiment as described above assumes fully flooded conditions at the CL-GDL interface which is not the case at low current densities. Condensation in the CL takes place when the water vapor diffusion is too slow to keep the partial pressure of water under the saturation pressure p_{sat}. By equalizing Faraday's law (Eq. (2.15)) and Fick's law (Eq. (3.14)) the critical current density for condensation at the CL-GDL interface can be estimated by

$$j = \frac{2F}{RT} \, D_{eff} \, \nabla p_{sat} \tag{4.12}$$

assuming fully saturated gases. With a temperature difference of 3.5 °C [109] at 70 °C mean temperature, a GDL thickness of 200 μm and an effective through-plane

diffusivity of $D_{eff} = 5.5 \times 10^{-6}$ m^{2}s^{-1}, condensation takes place above 1 Acm^{-2}. This verifies that the liquid water intrusion experiments hold true for high current density conditions. For current densities below 1 Acm^{-2} water vapor condenses inside the GDL or later under the rib of the cooled bipolar plate instead. The CL should be free of liquid water in this case and the findings of the water intrusion experiment are restricted.

The temperature dependency of the contact angle and the surface tension are important in order to justify an experimental temperature of 25 °C. In the book of A.W. Adamson [110] a contact angle temperature dependency of -0.01° per °K (water on polyethylene) and a surface tension temperature dependency of -1.38 x 10^{-6} Ncm^{-1} per °K (water on PTFE) is reported. The later changes the surface tension by about -10% from 25 °C to 70 °C and can therefore have an effect on the liquid water distribution.

4.4.5 Active Cell Setup

X-ray tomographic microscopic of active cells was motivated by the restricting assumption made for the water intrusion experiment. In reality the CL-GDL interface is not fully flooded at low current densities and gaseous water can be transported in large fractions through the GDL. By producing the water electrochemically in an active cell, more realistic boundary conditions for water transport are set. Electrochemically produced water at the active sites is assumed in vapor phase before it condenses in the pores of the CL, MPL or GDL depending on current density and temperature distribution. The active cell setup was aimed at demonstrating the feasibility of liquid water visualization in active cells.

A sample holder similar to the water intrusion setup was designed to run an electrochemical active cell with an active area of 7 mm^2. Fig. 4.12 shows the disassembled sample holder with a 4.5 mm MEA made of Nafion® 112 (50 μm thick), a 10 μm thick anode catalyst layer (0.2 mg Pt cm^{-2}) and a 20 μm thick cathode catalyst layer (0.4 mg Pt cm^{-2}). The anode GDL was punched with a diameter of 3 mm in order to avoid electric shortcut to the cathode side. The anode GDL was placed in a pocket machined into the bottom of the cup. The tightness of the membrane was assured with excessive compression of the periphery of the cathode GDL by the stamp. The cell was connected with a saturated hydrogen and oxygen reservoir consisting of two balloons partially filled with liquid water. Hence only diffusion at atmospheric pressure could take place. This simple gas supply restricts the results to air breathing systems [111]. Amplified flooding phenomena in the gas supplies due to the absence of convective water removal was expected to hinder a stable operation of the cell.

The electric contact of the GDL's was realized with gold wires (0.33 mm diameter)
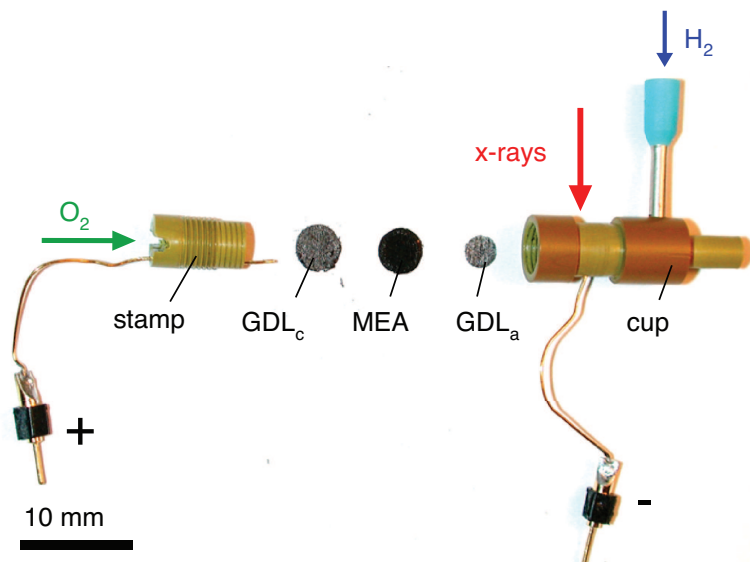
Figure 4.12: Explosion view (photograph) of the active cell sample holder containing a 4.5 mm MEA (catalyst coated Nafion® 112) and cathode GDL. The anode GDL had a diameter of 3 mm resulting in an active area of about 7 mm^2. The reactant gases were feed by diffusion through openings in the stamp and cup. X-rays illuminate the cell at the thinnest section of the sample holder. Rotation is around the longitudinal axis.

introduced through small openings. The wires were mounted removably in order to detach them during the tomography measurement. Metal in the X-ray beam would disturb the measurements. An external load with a constant resistance of 5 Ω was then applied and the current and voltage signals were monitored. The temperature of the cell was not controlled. Due to the high surface to volume ratio heat removal was not critical. The temperature slightly increased from 25 °C to 27 °C. Flooding effects were detected by sudden decrease of cell current. Real *in-situ* operation of the cell was not possible so far. The cell was disconnected from gas and load and placed at the endstation for a tomography measurement.

X-ray tomographic microscopy of active cells is a complementary technique to the established neutron imaging activities at PSI. The spatial resolution of X-ray tomographic microscopy is about an order of magnitude higher as compared to neutron imaging. However, it's much smaller field of view and incompatibility with materials used in technical cells complicates the use. The strength and focus of X-ray tomographic microscopy is the high resolution and contrast for carbon and water at the same time. Neutron imaging aims at cells of technical scale with more realistic boundary conditions. The ultimate goal of future X-ray tomographic microscopy of

active cells is the correlation of material (PTFE, MPL) and operating parameters (temperature, current density, relative humidity) with the micrometer-scale liquid water distribution.

4.5 Computational Characterization

Besides the experimental techniques discussed so far the computational characterization of GDL's provides a powerful tool for future optimization and design of new materials. Various GDL structures were studied by pore network models (cf. Sec. 3.1.2) with significant underlying simplifications [34, 64–68]. With the computational characterization technique presented here, structural simplifications are minimized. The computational work was conducted by Jürgen Becker from Fraunhofer ITWM in Kaiserslautern, Germany. The results of this collaboration were accepted for publication recently [81]. The study is exemplified by a TGP-H-060 carbon paper without PTFE but applicable to every kind of GDL without PTFE and MPL. Based on the three-dimensional images obtained by phase contrast X-ray tomographic microscopy (PCXTM) in Sec. 4.4.3 permeability, diffusivity and conductivity were numerically determined by solving the partial differential equations for convection, diffusion and conduction. The results are quantitatively compared with experimental data in Sec. 5.5.

4.5.1 Structure Model Computation

Prerequisite of the numerics is the construction of a 3D structure model. In this case, a structure model is a three-dimensional, rectangular area Ω subdivided in cubic voxels (volume pixels). Each voxel represents either solid material or pore space. The pore space is termed Ω_P and the solid Ω_S, so that $\Omega = \Omega_P \cup \Omega_S$. If such a model is given, the diffusivity, permeability and conductivity are determined using homogenization theory [112]. This means, it is assumed that the model shows a representative part of the GDL. Then the transport coefficient of the macroscopic equation (Darcy's law, Fick's law or Ohm's law) is determined by solving the corresponding transport problem in the structure model.

The structure model is derived from PCXTM data. With the compression setup introduced in Sec. 4.4.3 it was possible to visualize structural changes. For the computational characterization, tomography images at different compression levels were used. For this the grey-valued cuboid images had to be binarized into a black and white image, which then could be used as a cuboid model consisting of quadratic volume elements (voxels), where each voxel is either solid or void. The grey-valued image was binarized in three steps. In the first step, a median filter was used to

remove noise. In the second step, the binarization was performed by choice of a threshold. In a last step, a component filter run on the black & white image found unconnected white components and removed them. These components must be artifacts, since parts of the structure cannot float in the open space.

4.5.2 Effective Diffusivity Computation

The effective diffusivity of porous media is described macroscopically by Fick's first law Eq. (3.14). On the microscopic level, i.e. in the pore space Ω_P, diffusion is governed by Laplace's equation Eq. (3.28). It was solved numerically using zero-flux Neumann boundary conditions on the fiber surfaces and a concentration drop in one space direction as boundary conditions. Thus, the mass flux of the diffusing species was determined numerically and Fick's first law Eq. (3.14) allowed to calculate the effective diffusivity $D_{\mathrm{kl,eff}}$ and Eq. (3.15) the material coefficient ε/τ in direction of the concentration drop. To obtain the full effective diffusivity tensor, the problem had to be solved for concentration drops in each space direction.

Solving Eq. (3.28) on tomography image based models is on the one hand demanding as the models consist of many grid points (e.g. $600 \times 600 \times 224 = 80,640,000$) but on the other hand the simplicity of the voxel grid allows to significantly reduce the amount of CPU time and memory in comparison to more general finite element approaches. The explicit jump solver by Wiegmann and Zemitis [113] was used, developed specifically for large voxel grids. This allowed for solving Eq. (3.28) on the above-mentioned approximately 80 million grid points on a well-equipped PC (8 GB RAM) in less than 4 hours.

4.5.3 Permeability Computation

The permeability tensor is macroscopically defined by Darcy's law Eq. (3.23). On the microscopic level, convection is governed by Stokes' equation Eq. (3.22) together with the mass conservation equation (div v = 0) in Ω_P. The approach taken to determine the permeability tensor was similar to that taken to determine the diffusivity tensor. For the permeability no-slip boundary conditions on the fiber surfaces and an absolute pressure drop in one space direction were used as boundary conditions. The solution of Eq. (3.22) allowed to determine the pore and average velocity. Darcy's law Eq. (3.23) could be used to determine the permeability tensor. For the solution of the differential equation Eq. (3.22) the FFF-Stokes solver [114], also optimized for large voxel grids, has been applied.

4.5.4 Conductivity Computation

On the macroscopic level, the effective conductivity tensor σ_{eff} of the GDL satisfies Ohm's law Eq. (3.25). Microscopically, the electric conductivity $\sigma(x)$ is a function of space. Charge conservation results in Eq. (3.26). The local isotropic electric conductivity $\sigma(x)$ differs between solid and void parts of the medium. However, it was assumed that the pore space is not conducting and $\sigma = 0$ holds on Ω_P. As Eq. (3.26) is mathematically similar to Eq. (3.28), a similar approach as for the effective diffusivity computation was used. A potential difference was set as boundary condition and the effective current density was calculated from the solution of Eq. (3.26). Again the explicit jump solver of Wiegmann and Zemitis [113] was used.

4.6 Summary & Conclusions

In-depth characterization of the gas diffusion layer (GDL) is essential for the understanding of the coupled transport phenomena and for quantitative model predictions. Macroscopic methods to determine porosity, permeability and effective diffusivity were presented. The microscopic method of X-ray tomographic microscopy was adapted for application to GDL's in order to improve the understanding of the macroscopic single and multiphase behavior. The experimental and computational methods are summarized below:

- **Porosimetry**. Measuring the porosity of GDL's and catalyst layers (CL's) is not straight forward. Different porosimetry methods were evaluated and compared. Mercury intrusion porosimetry has been selected for the GDL. It measures a wide range of pore diameters but assumes circular pore geometries and requires incompressible samples. For verification of MIP porosity results the decane wetting method has been used. Gas adsorption porosimetry was used to characterize the nanometer pores of a CL.

- **Permeametry**. Measuring the in-plane permeability of a GDL under different compressions is a standard method. A defined gas flow is applied and by measuring the pressure drop and knowing the geometry of the GDL, the permeability can be computed using Darcy's law. A new sample holder was designed for the through-plane permeability which is about an order of magnitude smaller and therefore the relevant property for the liquid water transport. The key component is a sintered stainless-steel frit which ensures compression and gas flow to the GDL.

- **Electrochemical Diffusimetry**. A new diffusimetry method was developed which eliminates drawbacks of the diffusion cell and the limiting current method.

The method of electrochemical diffusimetry takes advantage of the analogy between Fick's and Ohm's law. Electrochemical Impedance Spectroscopy (EIS) is applied to measure the effective ionic conductivity of electrolyte-soaked GDL's. At high frequencies the charge in the GDL-electrolyte system is transfered to the highly conductive carbon fibers due to the fading of the capacitive double layer resistance on the fiber surface. The resulting impedance is small and a measure for the pure, ionic conductivity outside the sample. At low frequencies the double layer resistance is large and the charge is transported through the electrolyte-filled pores in the sample. The pure electrolyte conductivity is reduced by the structural parameter ε/τ, referred to as the effective relative diffusivity. This method provides fast, accurate, and cost-effective experimental access to a critical characteristic of gas diffusion layers. Measurements are possible in in-plane as well as in through-plane direction, and both directions can be investigated for varying compression of the GDL.

- **X-ray Tomographic Microscopy**. The new TOMCAT beamline at the Swiss Light Source (SLS) offers X-ray tomographic microscopy using absorption contrast or phase contrast techniques. The motivation to record tomographic microscopy images of GDL's evolved during the electrochemical diffusimetry measurements. Knowing the 3D structure improves the understanding of macroscopic properties. As a novelty images under different mechanical stress were captured using a special sample holder. A pixel size of 0.74 μm x 0.74 μm was sufficient to resolve the smallest structures of different GDL's. Based on these first successful experiences the idea of liquid water visualization was developed. The strength of X-ray tomographic microscopy is high spatial and temporal resolution with simultaneous contrast for water and carbon. With a simple water intrusion experiment the filling of the GDL microstructure could be visualized for the first time. Thereby the phase contrast reconstruction method (MBA) resulted in a better image quality. The *ex-situ* water intrusion experiment represents the extreme case of a fully flooded CL. More realistic boundary conditions have been realized with an *in-situ* active cell experiment. The feasibility of liquid water visualization by X-ray tomographic microscopy of a previously active cell has been demonstrated with the active cell setup. X-ray tomographic microscopy has a high potential to become a standard liquid water and solid structure visualization technique for PEFC complementary to neutron imaging.

- **Computational Characterization**. With the computational characterization of GDL's the gap between the above mentioned macroscopic methods and the microscopic method of phase contrast X-ray tomographic microscopy (PCXTM) is filled. By using the 3D images obtained by PCXTM, structural simplifications

are minimized. The 3D images were binarized to a structure model, which was then used to solve the corresponding transport problem (Darcy's law, Fick's law, Ohm's law). The computational characterization was performed in three space directions on PCXTM data of different compression levels.

5 Characterization Results

The characterization methods introduced in Chap. 4 were mainly applied to gas diffusion layers (GDL) although a wider applicability is possible. The main motivation for the following characterization of GDL's is given by the insufficient parameterization of numerical models for PEFC. Numerical models are important to understand the complex interplay of transport processes, to separate the different losses and to optimize geometries and materials.

Many *in-situ* experimental studies compared the overall cell performance using different GDL's [20–23, 115]. Although technically relevant, these *in-situ* investigations show difficulties in distinguishing between different loss mechanisms. It is generally assumed that the cathode GDL determines the maximum possible current and power density [24,25,116]. Under non-condensing conditions (high temperature, low current density, low relative humidity) the main transport limitation is given by diffusive and/or convective gas transport through the dry GDL. This requires the exact knowledge of permeability and effective diffusivity.

However, under condensing conditions the strongest limitation comes from the flooding of GDL pores and a subsequent shortage of oxygen in the cathode catalyst layer (CL) [26,27]. Therefore capillary pressure function and relative permeability are essential. Several groups have investigated these liquid water transport properties of GDL's either by *ex-situ* [28–32] or *in-situ* neutron radiography measurements [45,117–119]. X-ray tomographic microscopy of liquid water in GDL's is presented here for the first time with sufficient resolution.

The following results are arranged from the basic structural properties of GDL's to the complex multiphase transport behavior. The macroscopic properties of GDL's are determined by structural details. Therefore qualitative structural properties are discussed first on the basis of scanning electron, light reflection and X-ray tomographic microscopy images (Sec. 5.1). Quantification of the porous structure has been done by mercury intrusion porosimetry (Sec. 5.2). It is followed by the results of the permeability (Sec.5.3) and electrochemical diffusimetry measurements (Sec.5.4). Finally the liquid water transport within GDL's is elucidated by the results of the water intrusion and active cell experiments combined with X-ray tomographic microscopy (Sec. 5.6).

5.1 GDL Structures

The macroscopic properties of GDL's are determined by the material composition and the microscopic pore structure. The carbon papers mainly investigated are TGP-H-060 from Toray and SIGRACET® GDL24 and GDL25 from SGL Carbon Group. In this section structural influences of substrates, PTFE treatments, MPL coatings and mechanical compression are discussed.

First of all top-views of GDL's were recorded with a scanning electron microscope (SEM) showing the outermost layer of the microscopic pore structure. The top views were obtained with a field-emission SEM (Supra 55 VP, Carl Zeiss SMT AG) at 3 kV and 1700x magnification. Owing to the high electric conductivity of the GDL's gold coating was not necessary. The SEM top views of each material can be seen on the left of Fig. 5.1, Fig. 5.2 and Fig. 5.3. The fibrous nature of the GDL's is clearly visible. However, the top views do not capture the inner pore geometry. Cross sectional SEM views were not useful as they showed significant artifacts due to cutting or breaking of the sample.

Cross sectional details are better visualized by grinding and polishing of resin-impregnated samples shown on the right of Fig. 5.1, Fig. 5.2 and Fig. 5.3. Samples were embedded in epoxy resin (type L, suter swiss-composite). Full wetting of the pores was achieved by preliminary evacuation of the samples using a water jet pump. Afterwards the resin block was hardened at 70 °C for 3 hours. Several resin blocks were then mounted on an automatic polishing machine of type Buehler Metaserv. Images of the polished faces were taken using a Nikon Optiphot Light Reflection Microscope (LRM) at 1000x magnification.

The resulting images show different grayscales for the different materials due to their different reflection properties. The bulk of the image is attributed to resin. The light-gray, elliptical structures are carbon fiber cross sections with metallic reflection properties. The binder is visible as light gray unstructured domains between the fibers. PTFE has a lower reflectivity and is therefore visible as dark gray areas.

5.1.1 Substrate Influence

The investigated carbon papers mainly differ in the amount and type of binder used to bond the fibers. While TGP-H-060 uses a solid binder with a low porosity, GDL25 and GDL24 are made with a porous binder. The different binder morphologies can be seen by comparing the SEM top views and the LRM cross sections in Fig. 5.1. The binder fraction of TGP-H-060 is estimated to be of the order of 30% of the total solid whereas GDL25 contains about 50% binder. GDL24 has a very high binder fraction around 70% and an inhomogeneous distribution of the fibers. This results in large

mean pore diameters of 34 μm for GDL24 as compared to 18 μm for TGP-H-060 as measured by mercury intrusion porosimetry (Table 5.1).

5.1.2 PTFE Influence

The treatment with PTFE induces a significant structural change. The top-views in Fig. 5.2 show that pores are filled with PTFE. This additional solid phase is visible in the SEM top views as light gray areas forming sails mainly at fiber junctions but also over entire pore openings. The change in pore structure is more obvious in the LRM cross sections. The PTFE, which is discriminable as dark gray phases between the pores, clearly reduces the interconnectivity. This effect is smaller for GDL25 and GDL24. The PTFE is soaked into the binder and as a consequence the inter-porous space is less blocked.

5.1.3 MPL Influence

The microporous layer, which provides a smooth surface and can serve as a barrier for liquid water, is generally coated onto one side of a PTFE-treated GDL. It is composed of carbon particles with about 50 nm diameter bonded by PTFE as shown by the inset of the SEM top view in Fig. 5.3. The MPL is bordered in red in the cross sections. Besides the PTFE to carbon ratio of the MPL, different thicknesses are applied to tailor the transport properties for liquid water. The MPL of the Toray is about half as thick as the MPL of the SIGRACET® material. Furthermore the thickness of both MPL's is inhomogeneous and the surface shows significant cracks. The GDL and MPL layer intersect and build a mixed zone with less defined properties. This intrusion of the MPL into the GDL has to be considered in a MPL-GDL model and for the characterization of macroscopic properties.

5.1.4 Compression Influence

The full 3D structure and the impact of mechanical stress was studied with phase contrast X-ray tomographic microscopy (PCXTM) as described in Sec. 4.4.3. A sample of TGP-H-060 was imaged at three different levels of compression. Fig. 5.4 shows three reconstructed slices of the same sample a) uncompressed and at b) 0.9 and c) 0.7 relative thickness. The sample holder is visible as a light gray, homogenous regions on the top and on the bottom of the single slices. While a) illustrates how the GDL structure looks under a flow field channel, c) shows the changed structure under the compression of a flow field rib. By following typical solid patterns from a) to c) it can be observed that the solid fiber and binder structure does not change significantly under the mechanical stresses applied. However, the pore diameters are reduced
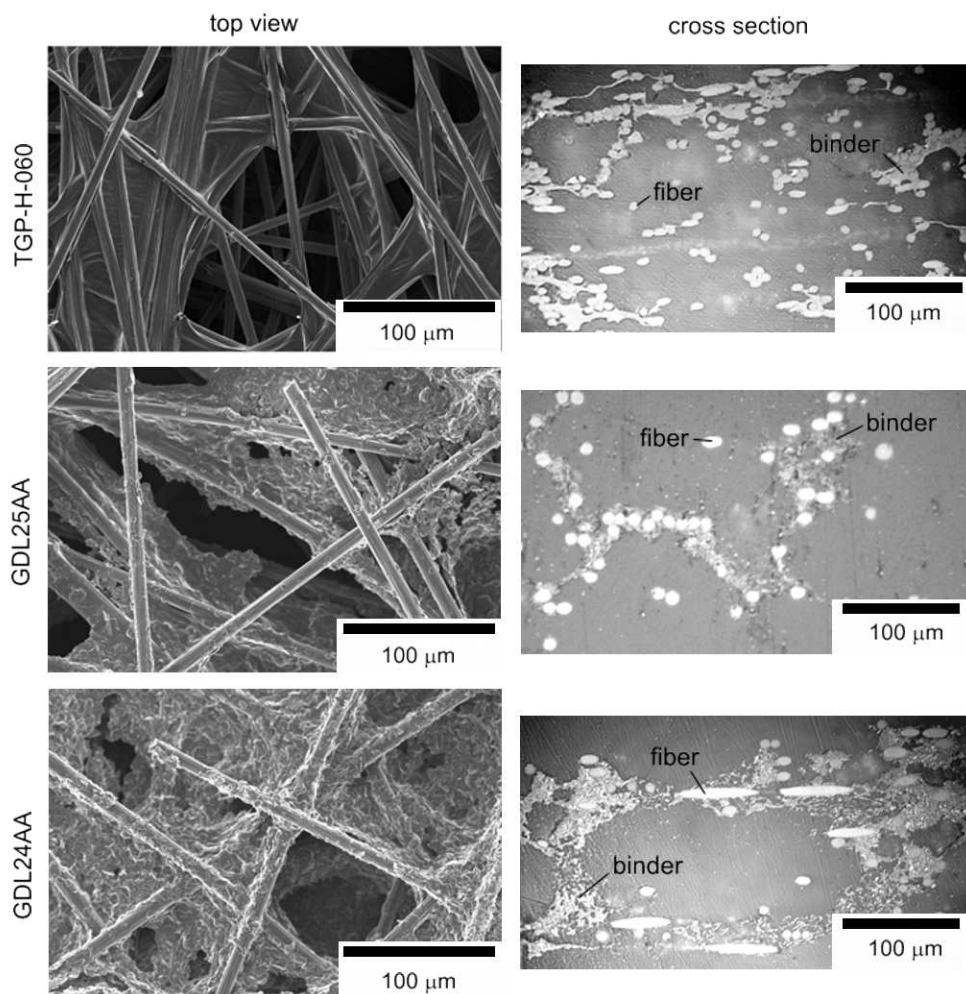
Figure 5.1: Top view SEM images (**left**) and cross section light microscopy images (**right**) of plain Toray and SIGRACET® GDL substrates without PTFE. The light-gray, elliptical domains in cross sections are fibers. The unstructured material between the fibers is binder.

Figure 5.2: Top view SEM images (**left**) and cross section light microscopy images (**right**) of wet-proofed Toray and SIGRACET® GDL's with 20 wt% PTFE. PTFE is visible as dark gray areas in the cross section and light gray layers in the top views.

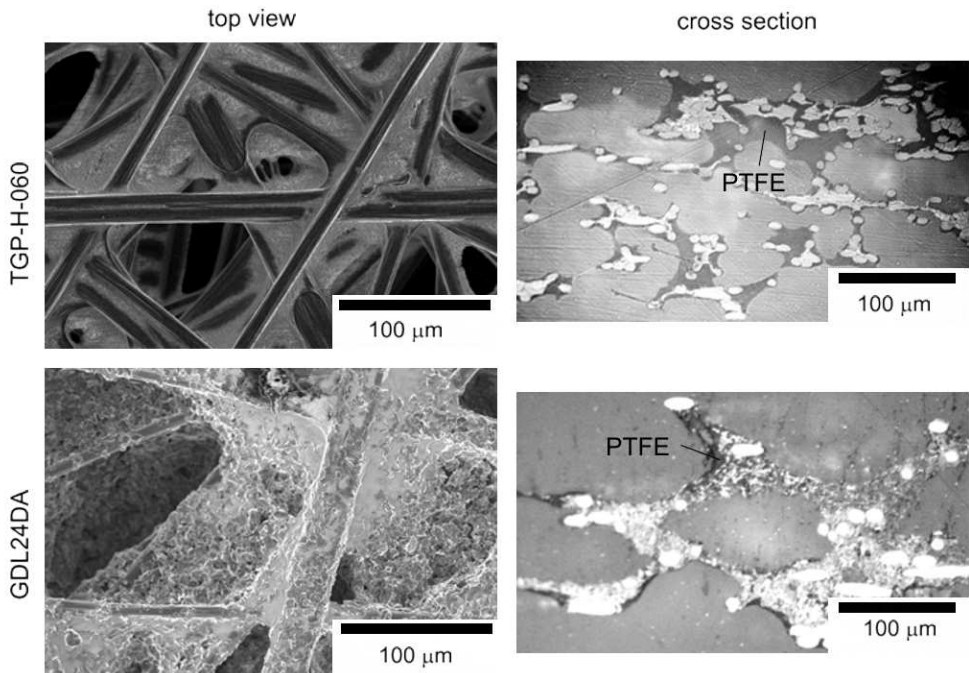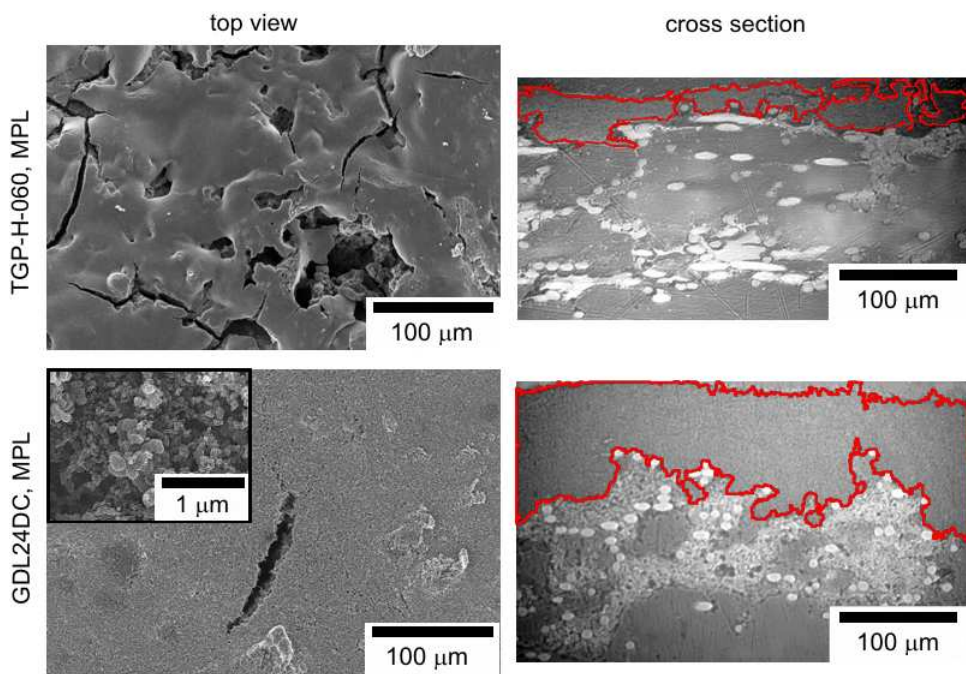**Figure 5.3:** Top view SEM images (**left**) and cross section light microscopy images (**right**) of Toray and SIGRACET® GDL with microporous layer (MPL). For better visibility the MPL in the cross section is bordered in red. The inset in the top view is a SEM image of the MPL with 50000x magnification.

until the solid walls touch each other. This will be reflected in poorer gas transport properties and better electric conductivity of the compressed material.

A linear compression model can not account for these inhomogeneous displacement effects. The porosity of domains which are stabilized by the binder is not affected while domains with single fibers experience a significant porosity reduction.

According to Fig. 4.6 PTFE should be slightly distinguishable from carbon using x-ray imaging with absorption contrast. However, a different grayscale level could not be observed so far in images of PTFE containing GDL's.

The voxels in the reconstructed images were labeled void or solid using grayscale threshold segmentation. Based on these labels the 3D surface mesh was calculated with a visualization software (e.g. Avizo). Fig. 5.17 shows the resulting 3D surface for TGP-H-060. By simply counting the void and total voxels, the porosity ε_{pcxtm} could be determined. Table 5.1 lists the voxel-counting results for different materials and compares them with conventional porosity methods.

5.2 GDL Porosity & Pore Size

The most fundamental property of a porous material is the ratio of the pore volume to the total volume, i.e. the porosity. The porosity ε of GDL's is required for the determination of tortuosity τ by electrochemical diffusimetry where the combined effective transport coefficient ε/τ is measured. Manufacturer-supplied porosity data is incomplete. Toray publishes only the porosity of the plain substrate. SGL supplies data for their plain and 5 wt.% wet-proofed GDL. Porosities of GDL's with different PTFE contents were unknown. Due to the importance of knowing the porosity and the pore size distribution of the investigated GDL materials, mercury intrusion porosimetry (MIP) as described in Sec. 4.1.3 was used for its determination.

Fig. 5.5 compares the cumulative (top) and log-differential pore size distribution (bottom) of Toray and SIGRACET® GDL's with different fractions of PTFE. For the porosities only the cumulative pore volumes down to pore diameters of 0.1 μm are of interest. The porosities are in the range of 0.67 to 0.90. The highest porosity was found for GDL24AA followed by the Toray materials. The PTFE treatment results in a reduction of the total pore volume of Toray and SIGRACET® as can be seen in the cumulative pore size distribution. The exact MIP porosities are listed in Table 5.1. The table compares manufacturer-supplied, MIP, decane-wetting and tomographic porosity values.

The MIP porosity ε_{MIP} of GDL24AA is significantly smaller than the corresponding manufacturer specification. This indicates that the incompressibility requirement for MIP may not be fulfilled for SIGRACET® or a large number of dead-end pores may

a)

b)

c)
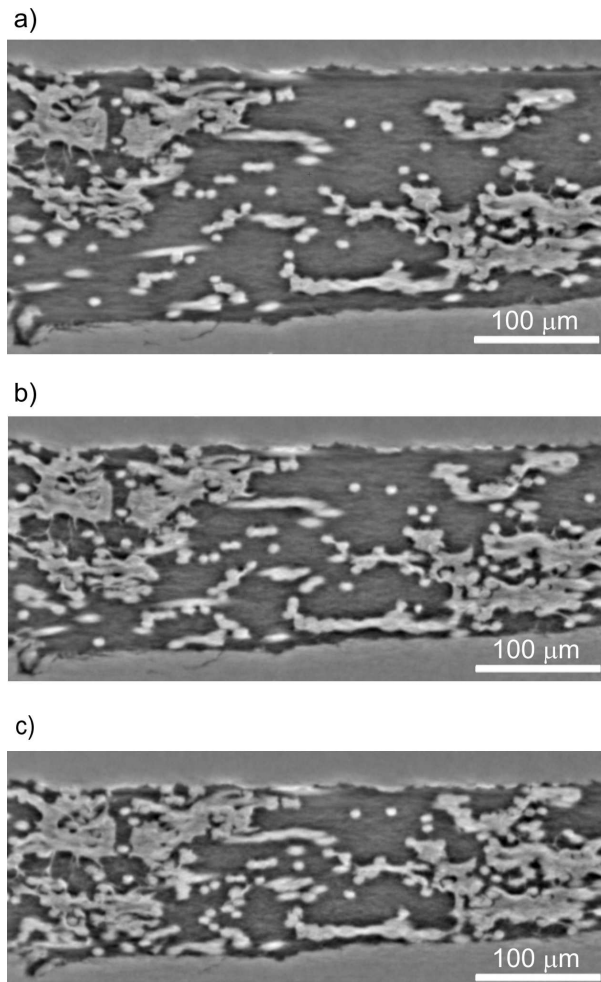
Figure 5.4: Through-plane slices of a tomographic reconstruction of TGP-H-060 without PTFE at different compression levels. The homogenous upper/lower areas are the sample holder. The light-gray structure represents fiber and binder and the dark-gray areas are the pores. Note that the same sample with repeating structural patterns is shown for all three compressions. **a)** 210 μm thickness. **b)** 190 μm thickness. **c)** 150 μm thickness.

GDL	PTFE / %	ε_m	$\varepsilon_{\text{C}_{10}\text{H}_{22}}$	ε_{MIP}	$\varepsilon_{\text{pcxtm}}$	D_s / μm	D_p / μm	δ_0 / μm
TGP-H-060	0	0.78	0.86	**0.78**	0.77	18	3	200
TGP-H-060	20	-	0.74	**0.75**	0.81	17	4	214
TGP-H-060	40	-	0.65	**0.67**		17	4	203
GDL24AA	0	0.86	**0.88**	0.74	0.87	34	0.7	172
GDL25AA	0	0.88	**0.9**	-				171
GDL24DA	20	-	**0.82**	0.75	0.82	35	0.5	160

Table 5.1: Structural properties of GDL's. The bold values are the porosities used for the postprocessing of the diffusivity measurements. ε_m: manufacturer supplied porosity. $\varepsilon_{\text{C}_{10}\text{H}_{22}}$: decane wetting porosity. ε_{MIP}: mercury intrusion porosity. $\varepsilon_{\text{pcxtm}}$: porosity calculated by grayscale segmentation of phase contrast X-ray tomographic microscopy data (cf. Sec. 5.1.4). D_p primary average pore diameter. D_s secondary average pore diameter. δ_0: uncompressed thickness.

exist. On the other hand the porosity of TGP-H-060 is only slightly smaller than the manufacturer value which can be attributed to the higher rigidity of the Toray material. As a consequence the MIP results were only taken for Toray and slightly corrected by a constant compression effect of +5%. The overall porosity of GDL24 and GDL25 could not be accurately determined by MIP. The porosity of the decane-wetting method $\varepsilon_{\text{C}_{10}H_{22}}$ was used instead.

The log-differential pore size distribution in Fig. 5.5 shows a bimodal character. GDL24 has primary pores around 0.6 μm and secondary pores around 34 μm. TGP-H-060 has primary pores around 3 μm and secondary ones around 18 μm. As expected, the pore sizes of the GDL's decrease with increasing PTFE content. Table 5.1 lists the primary and secondary pore sizes as well as the uncompressed thicknesses δ_0 of the GDL's.

5.3 GDL Permeability

The absolute permeability describes the pressure driven transport through a porous media. It was measured using the experimental setups described in Sec. 4.2. Rib-compression and direction dependencies were considered in order to have an accurate parameterization of the channel-rib model (Chap. 7).

The in- and through-plane permeabilities of TGP-H-060 are plotted in Fig. 5.6 for different porosities, i.e. different compressions. The influence of PTFE and microporous layer (MPL) is shown. The uncompressed through-plane permeability of TGP-H-060, 0% PTFE was close to the data presented by M.F. Mathias et al. [36]. The in-plane results are close to the values presented by Gostick et al. [30] for GDL34BA. In-plane and through-plane permeabilities are very sensitive to compression: e.g. the in-plane permeability of TGP-H-060, 0% PTFE decreases to 52% of the uncompressed value
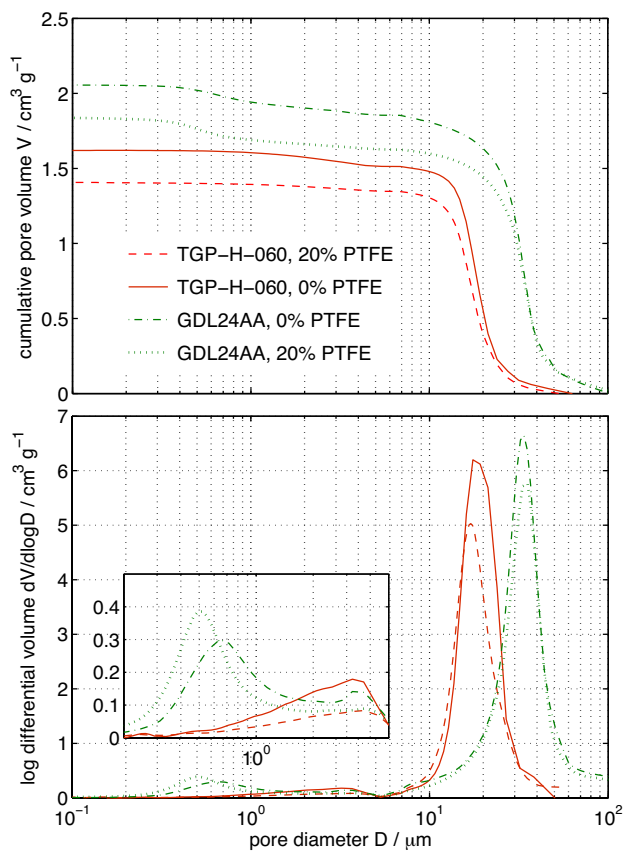
Figure 5.5: Cumulative (**top**) and log-differential (**bottom**) pore size distribution of TGP-H-060 and GDL24 with 0 wt% and 20 wt% PTFE.
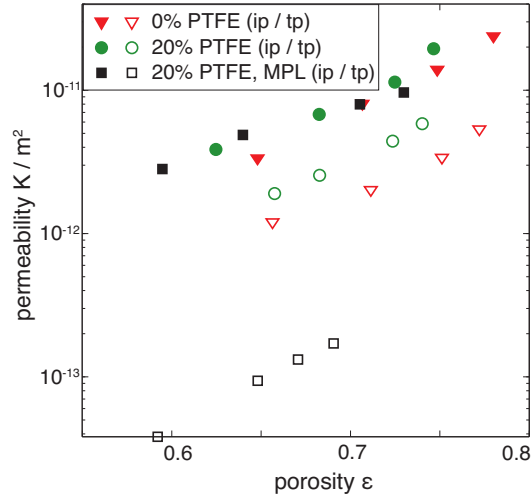
Figure 5.6: Measured in-plane (filled markers) and through-plane (empty markers) permeabilities of TGP-H-060 for different porosities (measure for compression), PTFE contents and MPL. The markers show single data sets. The statistic error is between 1% and 7%.

when compressing by only 15%.

The PTFE treated GDL has a slightly increased through-plane permeability as compared to the plain substrate at the same porosity. This could be due to a reduction in pore surface roughness by the PTFE coating. However, the treatment with PTFE has less influence than compression. The degree of anisotropy, which is the in-plane to through-plane permeability ratio, is between 2 and 5 and is decreasing with compression. The in-plane permeability with and without MPL does not change considerably as the gas flow bypasses the MPL. However, the through-plane permeability with an MPL is an order of magnitude smaller. To determine the pure MPL permeability of 4×10^{-14} m^2 all the resistance in through-plane direction was assigned to the MPL. The relative error for the permeability measurement in in-plane direction was between 1% and 7% depending on the degree of compression. In through-plane direction the relative error was between 4% and 6%.

The Carman-Kozeny theory introduced in Sec. 3.1.3 gives an analytical expression (Eq. (3.4)) for the through-plane permeability of porous materials made of fibrous beds. Using the porosity and the average primary pore diameters in Table 5.1 as a measure for the hydraulic diameter, a theoretical through-plane permeability of 3.3×10^{-12} m^2 is calculated. Although this value is in good accordance with the uncompressed measured values, the linear porosity dependency of the Carman-Kozeny theory could not be confirmed. Furthermore the Carman-Kozeny theory does not account for the high degree of anisotropy as measured for the materials in this thesis.

5.4 GDL Diffusivity

The results discussed in this section are published in [90,91]. The effective diffusivity D_{eff} of GDL materials can be determined by experiment or simulation. Simulations require to treat the GDL as an ideal porous structure described e.g. by morphology models (cf. Sec. 3.1.2). Experimental data is necessary to capture the influence of non-idealities such as binder structure and PTFE-treatment on the effective diffusivity.

The most direct experimental approach is to measure the diffusive flow through a GDL within a diffusion cell (Wicke-Kallenbach cell, Graham cell [61]). The usual experimental setup consists of a volatile liquid reservoir (e.g. a water bath) which is canopied by a GDL. If the removal of vapor from the other side of the GDL – either by a convective flow or a hygroscopic material – is ensured, the liquid evaporates over time. The evaporation rate is a function of the diffusivity of the GDL. However, the evaporation rate, which is commonly obtained by recording the weight loss of the reservoir over time, is usually rather small. This implies long experimental times [25], which strongly limits the practical number of parameter variations.

Another experimental approach to determine the diffusion properties of GDL's is the *in-situ* limiting current method in an operating PEFC [25]. With increasing current, the oxygen concentration at the electrochemical active surface of the electrode decreases, and as the oxygen concentration approaches zero, the current density becomes independent of overpotential (vertical line). This maximal current is referred to as the limiting current. Provided the electrode itself has negligible impact on the oxygen accessibility to the electrochemical active surface, the limiting current density can be calculated by equalizing Faraday's and Fick's law

$$j_{lim} = \frac{4\,F\,D_{eff}}{R\,T}\,\frac{f_k}{\delta}\,p_{O_2} \tag{5.1}$$

where p_{O_2} denotes the oxygen partial pressure within the flow field channel, δ the GDL thickness and f_k a factor accounting for the channel-rib geometry of the cell [25]. The precise determination of this factor is complicated by the compression of the GDL's under the ribs. In addition, convective transport within the GDL might have an influence on the limiting current in the case of a serpentine flowfield. Further on, this approach is limited to the measurement of an average isotropic diffusivity as differences in in-plane and through-plane direction cannot be resolved.

A fast and cost effective method to measure the effective diffusivity of a GDL was presented in Sec. 4.3. Electrochemical impedance spectroscopy is applied to measure the effective ionic conductivity of an electrolyte-soaked GDL. The validation of the method and results of three widely used GDL materials are presented in this section. The effect of anisotropy, rib-compression, binder structure and hydrophobic treat-
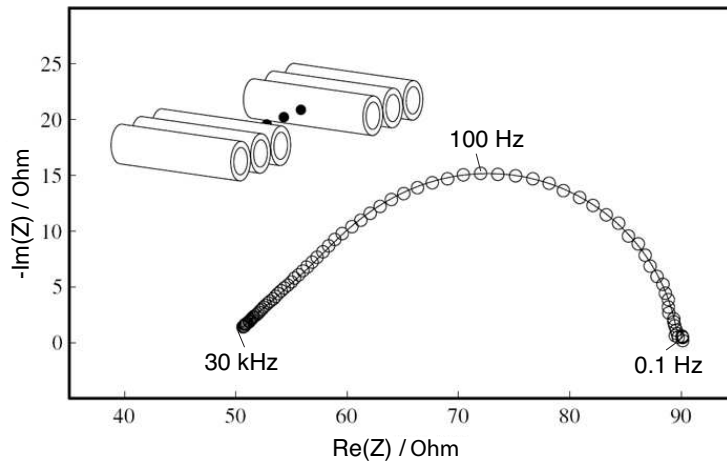
Figure 5.7: Nyquist plot of the impedance obtained in in-plane configuration for an array of stainless steel tubes; perturbation amplitude 10 mV; frequency range 30 kHz to 0.1 Hz; used electrolyte 0.5 M H_2SO_4.

ment on effective diffusivities are discussed. More methodic details and results can be found in [90] and [91].

5.4.1 Impedance Response

Before turning to the investigation of actual GDL's, an artificial material was analyzed to demonstrate the validity of the method. To mimic a porous, electrically conducting medium of tortuosity one, an array of stainless steel cannulas was placed into the in-plane sample holder. The array consisted of 29 tubes with an outer diameter of 0.8 mm and an inner diameter of 0.55 mm, each 10 mm long. This resulted in a nominal porosity of 0.608. The electrochemical impedance spectra was measured in the range of 30 kHz to 0.1 Hz. The Nyquist plot in Fig. 5.7 shows the spectrum for this setup with the typical semi-circle and high-frequency line of constant argument. The high frequency resistance is a measure for the pure electrolyte conductivity σ while the diameter of the semicircle is a measure for the effective conductivity σ_{eff}. The ratio $\sigma_{\text{eff}}/\sigma$ obtained from a fit of Eq. (4.6) is 0.603, which is in remarkable agreement with the theoretical porosity, corroborating the validity of the measurement principle.

Turning to actual GDL's, the Nyquist plots of Fig. 5.8 show a typical series of spectra. Measured spectra are shown as circles, while fits of Eq. (4.6) to the individual experimental spectra are shown as lines. The spectra are obtained with Toray TGP-H-060 without wet-proofing in in-plane direction. For this particular measurement, a stack of seven samples was investigated. No sensitivity with respect to the number of stacked samples was observed. Sample and holder were filled with 0.5 M H_2SO_4 ac-
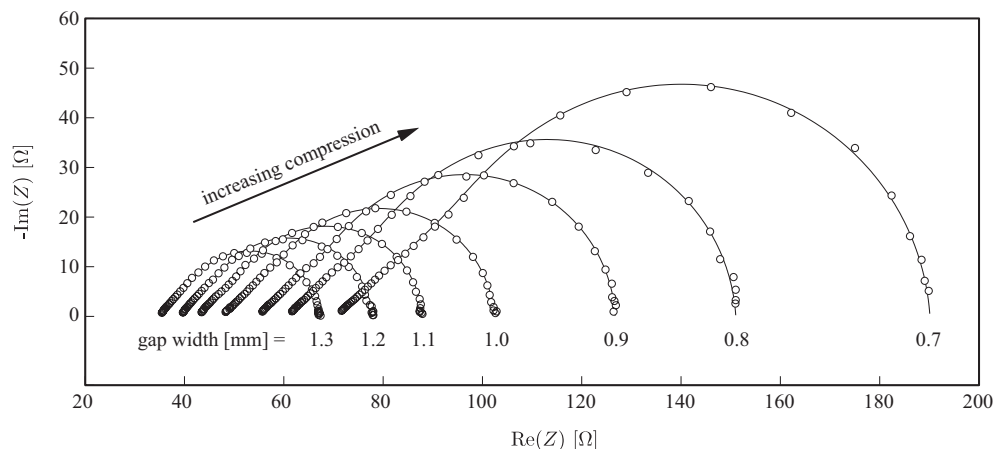
Figure 5.8: Nyquist plots of the impedance obtained in in-plane configuration for different gap widths. The sample consisted of a seven layer stack of Toray TGP-H-060 without wet-proofing. Experimental data is shown as circles and fits of Eq. (4.6) are shown as lines. Obtained with a perturbation amplitude of 10 mV in a frequency range of 10 kHz to 0.1 Hz. Used electrolyte is 0.5 M H_2SO_4.

cording to the procedure described in Sec. 4.3.2 and the amplitude of the alternating voltage (measured between the incorporated Pt wires) was set to 10 mV.

The uncompressed thickness of the stack was 1.31 mm measured beforehand with a micrometer gauge. Thus, a thickness of 1.3 mm was chosen as initial gap width. The spectrum with the smallest radius and lowest high-frequency impedance resulted from this measurement. Subsequently, the width of the gap was reduced, first in 100 μm steps and for higher compression in 50 μm steps. The corresponding spectra were characterized by an increasing high-frequency resistance as well as by gradually increasing radii of the semi-circle in the spectra. For clarity only spectra at 100 μm intervals are shown in Fig. 5.8.

Generally, the measured impedances agree remarkably well with the theoretical expectations. For all compressions, a distinct line of constant argument is seen in the high-frequency range, followed by a finited diffusion arc. The chosen combination of sample size, geometry and conductivity of the used electrolyte results in a convenient frequency range estimated by the characteristic frequency $\omega_c = \sigma_{eff}/(l^2\,C)$. On the one hand the impedances are virtually ohmic at 10 kHz, avoiding the need for measuring higher frequencies. On the other hand at the low frequency end of 0.1 Hz, the impedance has a likewise marginal imaginary component. If this would not be the case (e.g. caused by selecting a less conductive electrolyte or larger samples), the measurement of even lower frequencies would be needed increasing the sampling time of a spectrum significantly. In the given configuration, the sampling time is
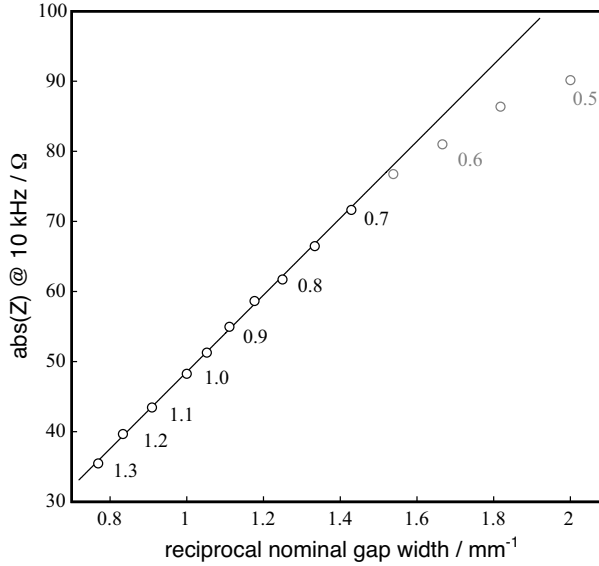
Figure 5.9: Absolute of the high frequency resistance of the spectra shown in Fig. 5.8 as function of the reciprocal nominal gap width. It shows a discrepancy between nominal and effective gap width for high degrees of compression. The values beside the data points indicate the nominal gap width in mm for convenience.

about 5 minutes per spectrum, which is maybe the most significant advantage of the electrochemical diffusimetry approach compared to other methods discussed in Sec. 4.3.

For the in-plane configuration the high-frequency impedance is a function of gap width. With decreasing gap width the cross-sectional area for ionic conduction is reduced and according to

$$Z_\Omega = \frac{l_A}{\sigma\, l_B\, \delta} \tag{5.2}$$

where δ is the gap width, l_B the sample width, l_A the length of free electrolyte between the potential probes (i.e. 3 cm minus sample length), the high frequency resistance is proportional to the reciprocal gap width. This allows for an *in situ* validation of the actual gap width.

The plot of Fig. 5.9 shows the absolute of the high-frequency impedance at 10 kHz corresponding to the spectra shown in Fig. 5.8 as a function of reciprocal nominal gap width as given by the respective metal spacers. The values at the data points correspond to the nominal gap width in millimeter. For lower degrees of compression (i.e. larger gap widths), the expected proportionality is fulfilled. Yet, a substantial deviation from the linear trend is observed for higher degrees of compression. With

increasing compression GDL's provide substantial mechanical resistance and the rigidity of the acrylic glass is insufficient to ensure matching nominal and actual gap widths. Hence, it is not possible to accurately measure the effective conductivity for higher degrees of compression (larger than about 50%). From a technical perspective this seems sufficient as the compression of GDL's in operating PEFC's is about 30% yielding porosities in the range of 50% to 70% (for Toray TGP-H-060 without wet-proofing).

For all in-plane measurements the linear dependence of the high-frequency impedance with respect to the reciprocal nominal gap width was monitored to identify the lowest gap width with accurate compression. Unfortunately, this *in situ* monitoring of the actual gap width is not possible whilst employing the through-plane sample holder because the cross-sectional area (perpendicular to the current) does not vary with sample compression. Based on the experience gained during in-plane measurements, the compression of through-plane measurements was likewise limited to about 50%. Given the smaller sample size compared to in-plane samples (cf. Sec. 4.3.2), this restriction is rather conservative.

5.4.2 Effective Relative Diffusivity

The effective relative diffusivity is calculated by dividing the effective ionic conductivity σ_{eff}, which is obtained from the axis intercepts of the impedance spectra (Fig. 4.3), with the ionic conductivity σ of the free electrolyte

$$\frac{\varepsilon}{\tau} = \frac{D_{\text{eff}}}{D} = \frac{\sigma_{\text{eff}}}{\sigma} \tag{5.3}$$

The porosity ε is calculated from the porosity of the uncompressed sample (as measured in Sec. 5.2) and the respective gap width according to

$$\varepsilon = 1 - \frac{\delta_0}{\delta}\left(1 - \varepsilon_0\right) \tag{5.4}$$

where ε_0 denotes the porosity of the uncompressed GDL, δ_0 the thickness of the uncompressed GDL stack and δ the actual gap width.

Comparison with Literature

The different approaches used in literature for the correlation of effective relative diffusivity with porosity are compared in Fig. 5.10. The effective relative diffusivity ε/τ is plotted over the porosity ε as a measure for compression. The light gray lines are iso-tortuosity levels. Porosities larger than ε_0 are not possible in reality and porosities smaller than $2\varepsilon_0 - 1$ are technically irrelevant (50% compression).

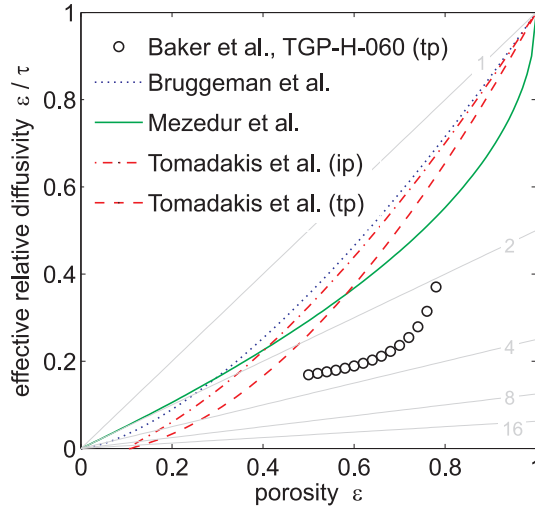**Figure 5.10:** Models and measurements of effective relative diffusivity ε/τ available in literature as a function of porosity. The gray lines indicate iso-tortuosity levels.

None of the models account for binder or PTFE influences. The spherical agglomerate model of Bruggeman [63] predicts the highest effective relative diffusivity. The more realistic fiber model of Tomadakis et al. [64] results in smaller, anisotropic values. Mezedur et al. [65] fitted their lattice network to experimental data. They found effective diffusivities comparable to our in-plane measurements of TGP-H-060 without PTFE (Fig. 5.11). Experimental data of effective GDL diffusivities are scarce. The only data for Toray TGP-H-060 is published by Baker et al. [25]. They used the limiting current method discussed in Sec. 4.3. The results agree fairly well with our findings shown in Fig. 5.11, corroborating the validity of our experimental approach. In the following systematic diffusivity measurements are presented emphasizing the influence of structural irregularities in real GDL's such as binder and PTFE.

Substrate Influence

The measured effective diffusivities of different untreated GDL's are shown in Fig. 5.11. Each marker defines a material while the light tones represent in-plane and the dark tones through-plane data. Generally the measured effective diffusivity values are smaller than the model predictions shown in Fig. 5.10. The models [63–66] oversimplify the complex geometry of GDL's by assuming purely fibrous or spherical structures without irregularities.

As visible in the top views and cross sections of Fig. 5.1 the investigated GDL substrates differ in morphology and amount of binder. Consequently, the effective diffus-
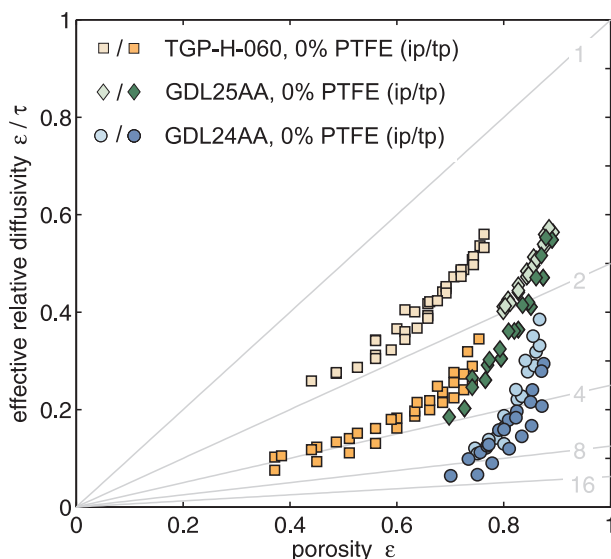
Figure 5.11: Effective relative diffusivity ε/τ as a function of the porosity of plain GDL's (without PTFE). ip: in-plane, tp: through-plane. The gray lines indicate iso-tortuosity levels.

ivities are significantly different. TGP-H-060 shows a pronounced anisotropy, while GDL24AA and GDL25AA behave almost isotropic. The uncompressed in-plane diffusivity of TGP-H-060 and GDL25AA were similar. GDL24AA has a lower initial diffusivity than TGP-H-060 despite its larger uncompressed porosity. The large amount of porous binder present in GDL24AA and GDL25AA results in a large overall porosity but also in tortuous diffusion paths. With increasing compression, the tortuosity of TGP-H-060 increased less than of GDL24AA and GDL25AA. This is attributed to agglomeration of binder to impermeable zones. Beside larger tortuosities, the percolation porosity due to dead-end and closed pores seems higher for SIGRACET® with more binder present.

PTFE Influence

The results of TGP-H-060 with 0 wt%, 20 wt% and 40 wt% PTFE are compared in Fig. 5.12. The PTFE-treatment did not only reduce the porosity but also increased the tortuosity. At a porosity of 0.6 the through-plane tortuosity of TGP-H-060 without PTFE was 3.5 while at the same porosity TGP-H-060 with 20 wt% PTFE comprised a tortuosity of 6. With 40 wt% the through-plane tortuosity even increased to 8. In in-plane direction the elongation of the diffusion path is smaller. It grows from a tortuosity of 1.8 to 2.5 and 2.6 for 0 wt%, 20 wt% and 40 wt% PTFE respectively. Although the water drainage effect due to the PTFE treatment is improved it has also a
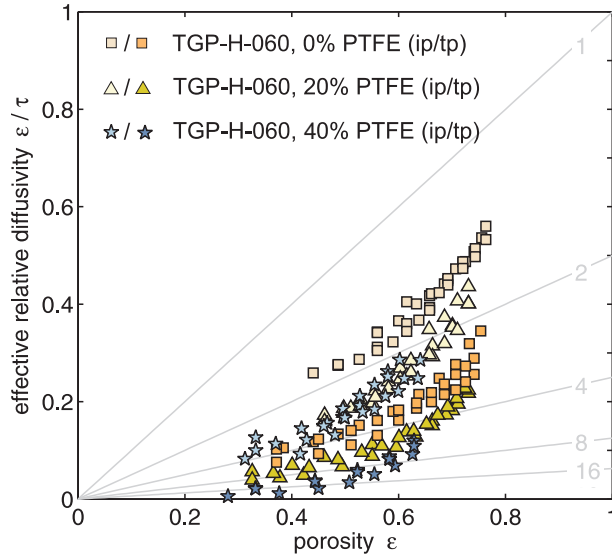
Figure 5.12: Effective relative diffusivity ε/τ as a function of the porosity of TGP-H-060 with 0 wt%, 20 wt% and 40 wt% PTFE. ip: in-plane, tp: through-plane. The gray lines indicate iso-tortuosity levels.

considerable negative effect on the dry diffusivity of the GDL. The PTFE mainly reduces the through-plane interconnectivity of the pores as visible in the cross sections of Fig. 5.2.

The effect of PTFE-treatment on the diffusivity of GDL24 is illustrated in Fig. 5.13. The PTFE is mainly deposited within the porous binder (Fig. 5.2) where the bulk diffusion is not affected. Therefore no increase of in-plane or through-plane tortuosity was observed. In contrast, at high compressions the PTFE had even a positive effect on the mechanical stability. The secondary pores remained open and the diffusivity of GDL24DA was slightly higher than that of the untreated GDL24AA.

Anisotropy

The effective relative diffusivity in in-plane direction can be more than twice as large as in through-plane direction. This substantial anisotropy has been experimentally measured in this work for the first time. However the general trend has been guessed from permeability measurements [86] and models [34, 64] recently. The large anisotropy has two origins: (1) the layered arrangement of fibers and (2) the formation of flaps of binder and PTFE between fiber junctions. The degree of anisotropy is defined as the ratio of in-plane to through-plane effective diffusivity.

The degree of anisotropy as a function of compression of different GDL's is compared in Fig. 5.14. The experimental data of in-plane and through-plane direction was

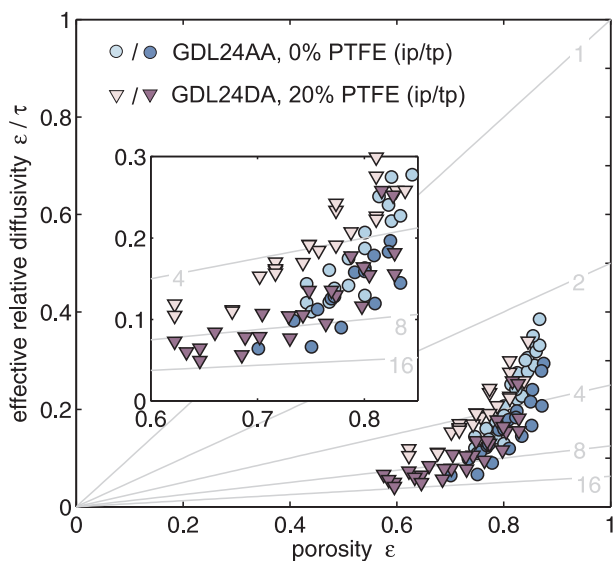**Figure 5.13:** Effective relative diffusivity ε/τ as a function of the porosity of GDL24 with 0 wt% and 20 wt% PTFE. ip: in-plane, tp: through-plane. The gray lines indicate iso-tortuosity levels.
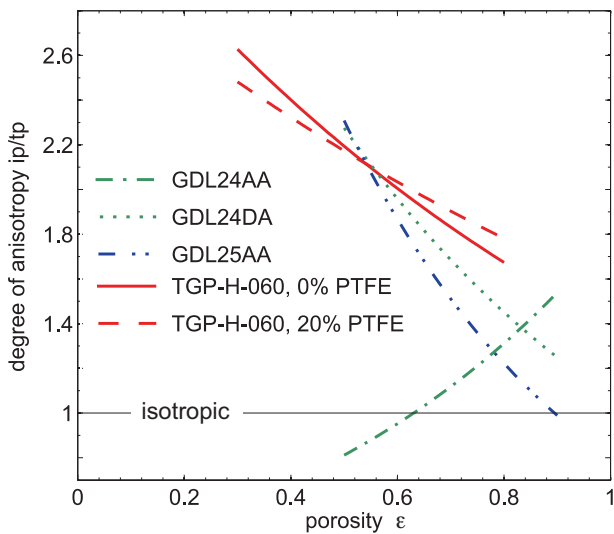

Figure 5.14: Degree of anisotropy of effective diffusivity as a function of porosity for different GDL's. Each substrate has a separate color. The horizontal line at 1 marks an isotropic material.

GDL	PTFE / %	H_B	H_A	ϵ_p
TGP-H-060	0	0.62	0.06	0
TGP-H-060	20	0.88	0.43	0
TGP-H-060	40	-	-	-
GDL24AA	0	0.56	0.27	0.31
GDL25AA	0	0.66	0.85	0.45
GDL24DA	20	-	-	-

Table 5.2: Unit cell fit parameters of different GDL's.

fitted to an exponential function to compute the ratio. On average the in-plane diffusivities are about twice as large as the through-plane diffusivities. The anisotropy generally increases with compression due to an accentuation of the in-plane orientation of the fibers. Only GDL24AA with a small fiber fraction shows an opposite behavior. The large amount of binder results in isotropic properties dominating the in-plane-orientation of the fibers. The cross sections of GDL24 and GDL25 in Fig. 5.1 revealed no binder orientation while an in-plane-alignment is visible for TGP-H-060. Therefore GDL24 and GDL25 have smaller anisotropies compared to TGP-H-060. The PTFE treatment increases the anisotropy of TGP-H-060 and GDL25. For GDL24 the in-plane orientation of the pores is conserved with 20 wt% PTFE and the anisotropy increases with compression similar to other GDL's.

Unit Cell Fit

The unit cell model elaborated in Sec. 4.3.1 provides a simple and useful tool for abstraction and correlation of diffusivity data with structure. It was used in a least square regression algorithm in order to find the best fit parameters H_B, H_A and ε_p. The in-plane flap-length H_B was associated with binder agglomerated in the corner of two crossing fibers. The through-plane flap-length H_A was correlated to PTFE that clogs the in-plane-diffusion, while the primary porosity ε_p was interpreted as an intrinsic property of the binder. The resulting unit cell geometries and the corresponding diffusivities are compared with experimental data in Fig. 5.15. The fit parameters are listed in Table 5.2. Note that the same unit cell geometries were used in in-plane and through-plane direction. TGP-H-060 with 40% PTFE and GDL24 with 20% PTFE could not be fitted as relatively long flaps were required, which produced a percolation close to the uncompressed porosity.

The predicted curves of the unit cell matched the measured data above a relative thickness of 50% which corresponds to a compressive stress of about 10 MPa. At stronger compressions the unit cell quickly approached a percolation threshold

where diffusion stopped. This percolation threshold strongly depends on the flap-lengths in through-plane direction H_A. As soon as the width A of the unit cell is equal to $H_A + R_A$ the in-plane diffusion ceases. For $H_A + R_A > A$ the unit cell is not defined anymore.

In the experiments the percolation threshold porosity was observed at higher compressions than predicted by the unit cell as structural deformations of the flaps are expected. The experimental data was therefore cropped at a porosity smaller than $2\varepsilon_0 - 1$ which corresponds to 50% relative thickness. The technical relevant range is around 70-80% relative thickness.

In order to fit the basic TGP-H-060 without PTFE the in-plane flap-length H_B was sufficient. It was attributed to binder that spans fiber joints in in-plane-direction and thereby blocks through-plane-diffusion. The through-plane flap-length H_A was only 0.06 and therefore negligible. Hence no additional in-plane-diffusion barrier was present beside the fibers. Both in-plane and through-plane flap-lengths of TGP-H-060 scaled with PTFE content. The through-plane and in-plane flap length for 20% PTFE grew by 0.37 and 0.26 respectively. For GDL24 and GDL25 with a higher binder-fiber ratio, a primary binder porosity ε_p was introduced. It resulted in smaller values for GDL25 as compared to GDL24 as was expected from the LRM cross sections in Fig. 5.1.

The ratio of H_B to H_A is a measure for the anisotropy. With a large H_A the in-plane-diffusion is hindered while with a large H_B the through-plane-diffusion is reduced. Additionally, the elliptical shape of the fiber cuts contribute to a higher anisotropy. The highest anisotropy was observed for TGP-H-060 without PTFE with a ratio H_B to H_A of 10. The nearly isotropic material GDL25AA had a large through-plane flap-length H_A, resulting in a H_B to H_A ratio of only 1.3. GDL24AA revealed a ratio smaller than 1 producing the unexpected decrease of anisotropy with compression.

Flap Length Variation

Comparison of experimental and calculated results in Fig. 5.15 shows that the chosen unit cell geometries are in good agreement with experiments. This provides sufficient confidence to study the reasons for the low effective relative diffusivity especially in through-plane directions on the basis of the unit cell model. The impact of possible morphological improvements is studied by variation of the in-plane oriented flap length H_A, which affects the through-plane transport only. The effective relative diffusivity of TGP-H-060 is shown in Fig. 5.16 as a function of H_A. For negligible flap length, the effective relative through-plane diffusivity approaches values of about 0.35, which still falls short of the in-plane value. With increasing flap length, the effective relative diffusivity is first gradually decreasing and then sharply dropping to
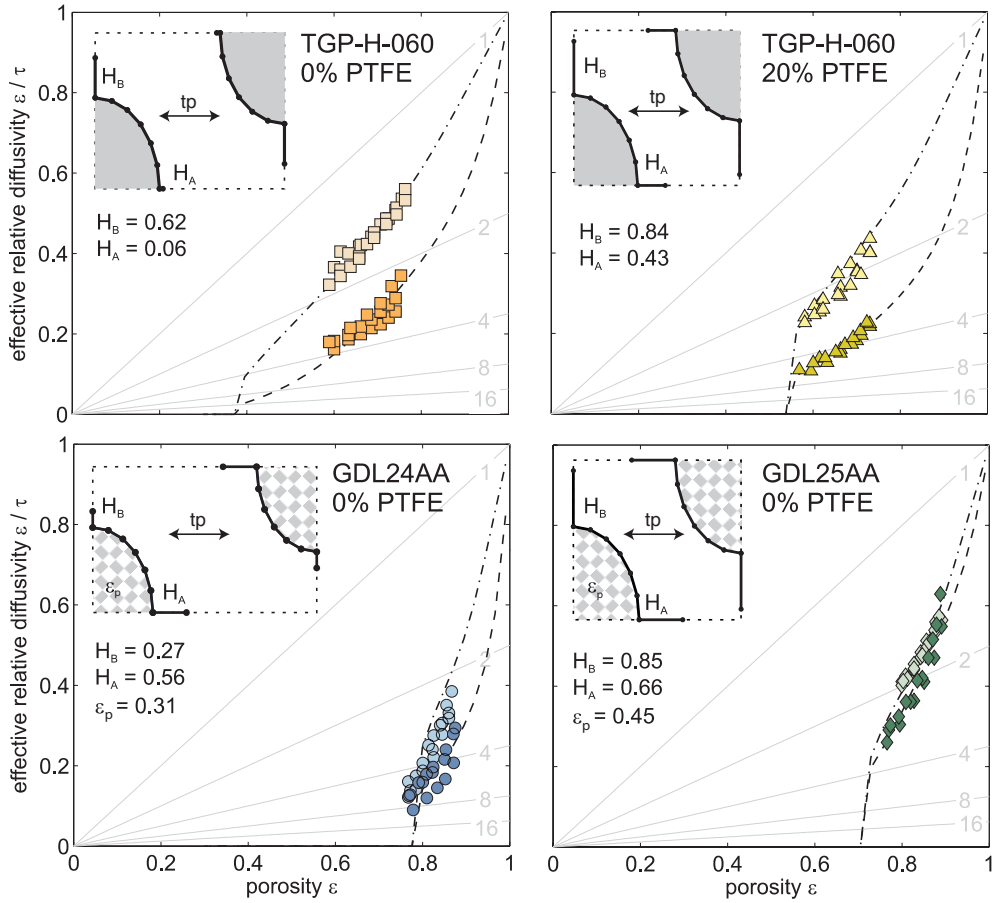
Figure 5.15: Unit cell diffusivities as a function of porosity compared to measurements (markers). The light tone markers are in-plane (ip) and the dark tone through-plane (tp) measurements. Dash-doted lines are in-plane and dashed lines through-plane diffusivities of the unit cell. The insets show the real unit cell proportions at the uncompressed porosities ε_0 listed in Table 5.1. The compression is induced in tp-direction as indicated by the arrows. Dimensions are given relative to the fiber radius $R_A = 1$. The height B was kept constant at 2.4.
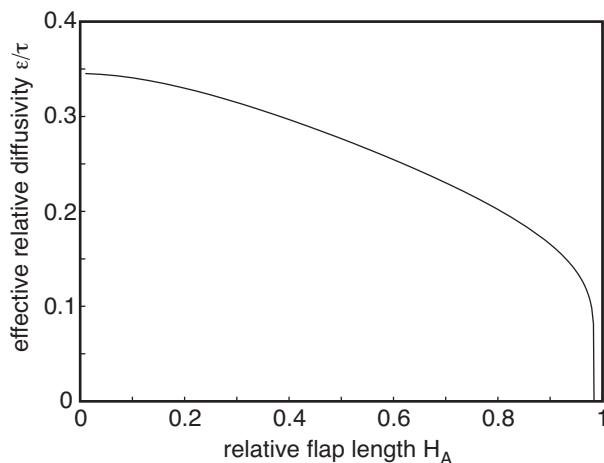
Figure 5.16: Unit cell effective relative diffusivity of TGP-H-060 without PTFE in through-plane direction as a function of relative in-plane flap length H_A for a porosity of 0.7. The through-plane flap length H_B and the primary porosity ε_p were both zero.

zero as full coverage of the pore opening is approached. According to the model, reducing flap formation leads to overall improved diffusivity of GDL's in through-plane direction.

5.5 Computed GDL Properties

The results shown in this section are published in [81]. Numerical simulations of different transport properties based on tomography structures are compared and validated with experimental results obtained by electrochemical diffusimetry (cf. Sec. 5.4), permeametry (cf. Sec. 4.2) and electrical conductivity measurements [15]. The comparison is based on a TGP-H-060 carbon paper without PTFE. The phase contrast X-ray tomographic microscopy (PCXTM) images shown in Sec. 5.1.4 were used to derive a structure model. The computational characterization was conducted as described in Sec. 4.5.

5.5.1 Computed Structure Model

Fig. 5.17 shows the solid surface of the reconstructed and segmented PCXTM images at three different compressions. The reconstructed 3D structures are only a subsection of the tomography data. It was necessary to cut away small parts of the GDL structure from the top and bottom which would otherwise have distorted the numerical results. The three cut-outs shown in Fig. 5.17 were used as structure models to
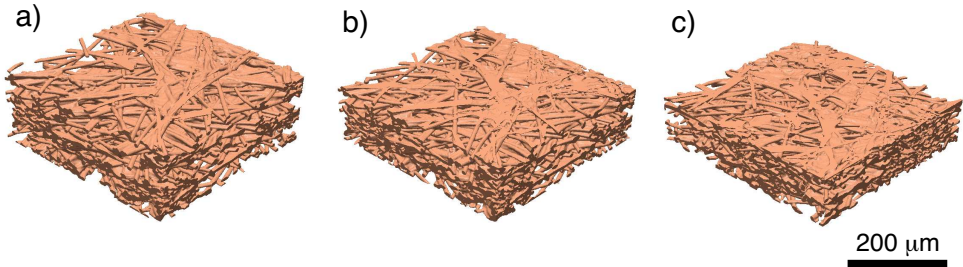
Figure 5.17: Reconstructed 3D surface of TGP-H-060 without PTFE at three different compression levels based on the PCXTM images shown in Fig. 5.4. In-plane the structures have a size of 600 x 600 grid points or 420 x 420 μm. The height varies with the rate of compression: **a)** 156.8 μm, **b)** 119 μm, **c)** 98 μm. The resulting porosities are **a)** 73.82 %, **b)** 69.49 % and **c)** 66.78 %.

numerically extract GDL properties as a function of compression and direction.

The conformance of the real GDL structure and the PCXTM-based computed structure can be checked by comparing the total porosities (cf. Table 5.1) and pore size distributions. Fig. 5.18 shows the cumulative pore size distribution of TGP-H-060 without PTFE obtained by mercury intrusion porosimetry (MIP) and the cumulative pore size distribution obtained by mathematical granulometry of the 3D structure [120]. In granulometry spheres of increasing diameter are fitted into the structure to obtain the pore size distribution. This method does not distinguish closed, blind or through pores. As a consequence the two pore size distributions in Fig. 5.18 have a slightly different shape. In MIP the connectivity of the pores is considered and once the capillary pressure of the smallest pore opening is reached the remaining volume is attributed to this diameter. In granulometry the distribution is more flat and full intrusion is assumed around 2 μm due to a limited pixel size of 0.74 μm x 0.74 μm.

In the following, the results of the experimental measurements are compared to the results of the numerical simulations. The numerical in-plane results shown are the average value of the two perpendicular in-plane directions.

5.5.2 Computed Effective Diffusivity

Fig. 5.19 compares the measured (cf. Sec. 5.4) and simulated effective relative diffusivities. The diffusion properties are strongly dependent on direction. The in-plane diffusivity is about twice as good as the through-plane diffusivity. Furthermore the effect of the rib compression ($\varepsilon = 0.6$) can reduce the diffusive transport by up to 30%. Numerically and experimentally determined diffusivity values show a good agreement. The agreement is in fact excellent in the through-plane direction, but in the
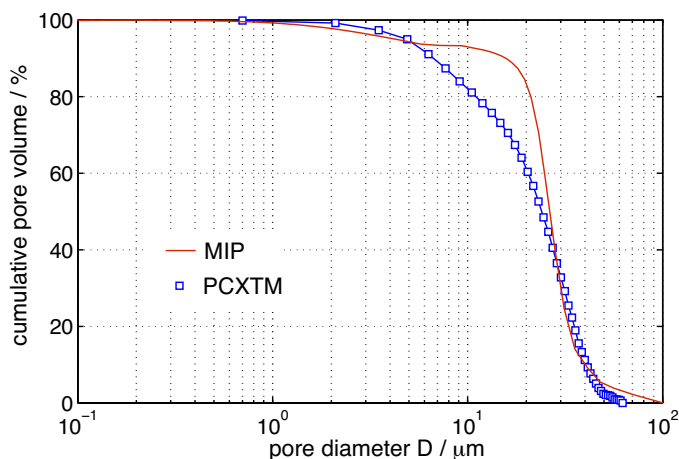
Figure 5.18: Comparison of MIP and PCXTM-based [120] cumulative pore size distribution for TGP-H-060, 0% PTFE.

in-plane direction the results of the measurements are slightly lower than those of the numerical simulations.

5.5.3 Computed Permeability

In Fig. 5.20 the permeability values of the structure model and measurements (cf. Sec. 5.3) are compared. The permeability shows a considerable anisotropy which decreases with compression. The measured in-plane permeability is about four times higher than the through-plane permeability. The numerical results show again an excellent agreement with the measured data in through-plane direction but smaller values in the in-plane direction. A reason for the deviation could be the fact that measurements were performed on a stack of GDL's whereas the numerical simulation was made on a model of a single layer. Furthermore, the model does not include the top and bottom boundaries of the GDL as they had to be removed from the cut out together with the sample holder. This fact is not significant in the through-plane direction as transport passes through the layer, but in in-plane direction flow may take place between the layers.

5.5.4 Computed Conductivity

The comparison of simulated and measured electric conductivities is shown in Fig. 5.21. The measured in-plane conductivities are about an order of magnitude higher than the through-plane conductivities. In contrast to gas transport properties the com-

Figure 5.19: Comparison of calculated (circles) and measured (squares) effective relative diffusivities of TGP-H-060 without PTFE. The light green markers are through-plane and the dark red in-plane results.

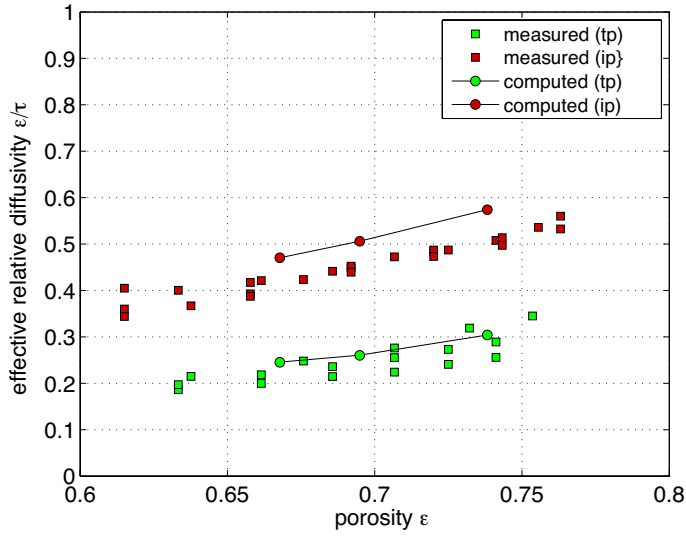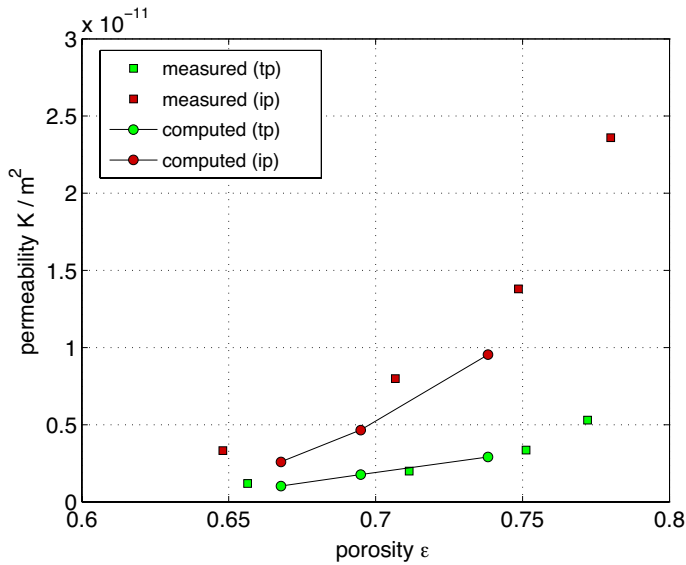**Figure 5.20:** Comparison of calculated (circles) and measured (squares) absolute permeabilities of TGP-H-060 without PTFE. The light green markers are through-plane and the dark red in-plane results.
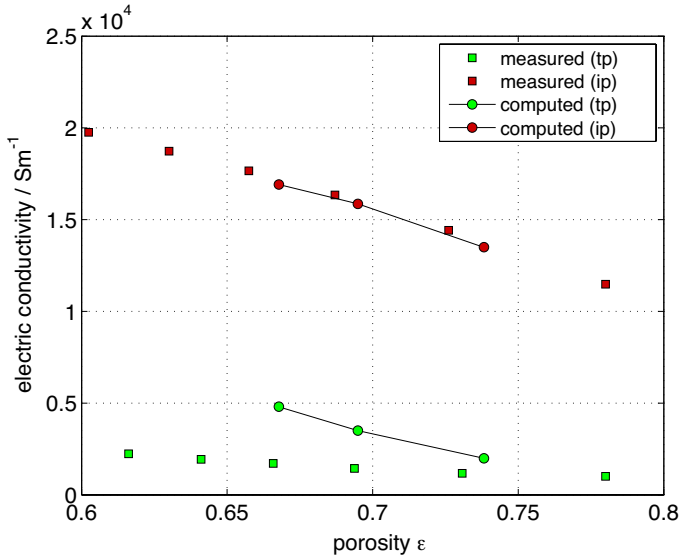
Figure 5.21: Comparison of calculated (circles) and measured (squares) electric conductivities. The solid electric conductivity of carbon was assumed to be 95000 Sm^{-1}. The light green markers are through-plane and the dark red in-plane results.

pression increases the electric conductivity due to an increasing number of contact points. To determine the conductivity of the porous material numerically, the specific conductivity of the solid domain is required. Unfortunately, the exact fiber properties and therefore also the exact electric conductivity is unknown. As Fig. 5.21 shows, the numerical in-plane results fit well to the measurements for an assumed conductivity of σ = 95000 Sm^{-1}, which is close to the conductivity of graphite. But for the same σ, the numerically determined through-plane conductivity values are too high in comparison to the measurements. Choosing σ differently simply rescales the resulting conductivity. However, the ratio of in-plane to through-plane conductivity is independent of the choice of σ and thus a more suitable value to compare. Here, we observe that the ratio is always considerably smaller for the numerical results than for the experimental ones, e.g. 6.8 versus 11.4 for the uncompressed material.

The higher anisotropy of the measured conductivities might be explained by the fact that the conduction in in-plane direction takes place mainly along single fibers, whereas the conduction in through-plane direction mainly takes place from fiber to binder to fiber. In the structure model we cannot distinguish between fibers and binder. Therefore the numerical model assumes an optimal conduction between fiber and binder, whereas in reality contact resistances need to be taken into account. Moreover, the binder might exhibit a different conductivity.

5.6 GDL Liquid Water Distribution

The results presented in this section are partly published in [121]. The motivation to study the liquid water distribution inside the GDL originated from the high transport overpotential at high current densities (cf. Sec. 2.3). Liquid product water accumulates in the GDL and limits the gas diffusion and therewith the maximum power density of a PEFC. So far the problem of flooding was addressed with PTFE impregnation and MPL-coating of GDL's. However, little is known about the real impact of these measures.

There are three established techniques for the visualization of liquid water in GDL's. 1) Neutron imaging has a very high sensitivity to liquid water but is almost not sensitive to carbon and other materials used in the PEFC. This makes neutron imaging mainly suitable for the investigation of active cells on the technical scale [45, 52, 117–119, 122]. 2) Magnetic resonance imaging (MRI) has been developed for the visualization of soft tissue in the human body. Although it is extremely sensitive to water it requires the absence of magnetically inductive materials. It has been used to visualize the water content of membranes [123]. 3) Synchrotron-based X-ray imaging is sensitive to water and carbon. The spatial resolution is about an order of magnitude higher compared to neutron imaging and MRI, which allows to resolve the smallest structures in a GDL (cf. Sec. 4.4.3). With an exposure time for a radiogram of around one second, tomographic microscopy is feasible within relative short measurement times. Additional techniques are discussed in the review paper of A. Bazylak [124].

X-ray radiography with a pixel size of 3 μm [125–127] and tomography with a pixel size of 10 μm [128] have already been used earlier to study water in GDL's. However, radiography has inferior contrast and is averaging along the beam while tomography with 10 μm pixel size can not resolve single carbon fibers. With the GDL imaging capability of the TOMCAT beamline water transport pathways, condensation phenomena and contact angle of water in the pores can be visualized. Nevertheless the presence of a mobile phase (liquid water) complicates the experiment as compared to the dry GDL. The results were expected to give valuable information to find an appropriate water transport model for GDL's.

5.6.1 Absorption Contrast Agent

The difference between the imaginary part β of the index of refraction between carbon and water is marginal as shown in Fig. 4.6. In order to improve the contrast a CaI_2 solution with different concentrations was used. To exclude the influence of the salt on the wetting behavior, contact angles with different salt concentrations were tested. Fig. 5.22a) confirms that the salt does not change the wetting behavior. Therefore the
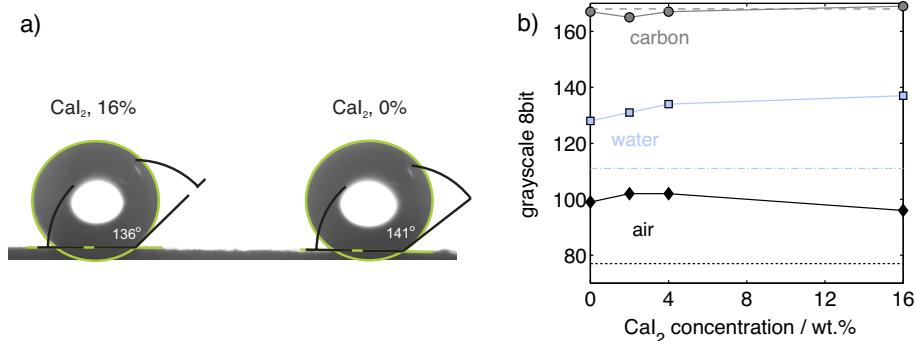
Figure 5.22: a) Contact angle of a 16 wt.% CaI$_2$ droplet and a pure water droplet on a GDL surface (TGP-H-060, 20 % PTFE). **b)** Mean grayscale of water (blue squares), fiber (gray circles) and pores (black diamonds) for different CaI$_2$ concentrations. The lines show the better contrast of the phase contrast method (dashed: carbon, dashed-dotted: water, dotted: air).

water distribution is expected to be independent of the salt concentration. Samples were partially saturated with the iodine solution. Absorption contrast tomography scans at 10 keV (setting #2) with 4 different CaI$_2$ concentrations were made using the compression setup (cf. Sec. 4.4.3). The resulting average grayscale values of carbon, water and air are shown in Fig. 5.22b). A contrast enhancement effect could not be observed. A possible explanation is that an X-ray energy of 10 keV required for a transmission of 0.3 is too far from the K-edge energy of iodine (33.2 keV).

Additionally Fig. 5.22b) shows the average grayscale levels of a phase contrast measurement (setting #6). Due to the superior contrast obtained with the phase contrast method the use of a contrast agent for the absorption contrast method was not pursued further.

5.6.2 Absorption vs. Phase Contrast

In Sec. 4.4.1 the differences between the two methods have been described. The absorption property of a material is proportional to the atomic number and therefore low-Z materials like carbon and water were expected to have a small absorption contrast. On the other hand the phase shift between the two materials is significant and could result in a better image quality. This was confirmed with the water intrusion setup (cf. Sec. 4.4.4) and different beamline settings (settings #2 and #6). Fig. 5.23 compares the quality of absorption and phase contrast results. The close-ups show a reconstructed 2D slice with carbon, water and air phases. The 1D grayscale profiles from A to B cross a fiber, a pore and a water droplet. The illustrations show that the phase contrast results have less noise and better contrast.
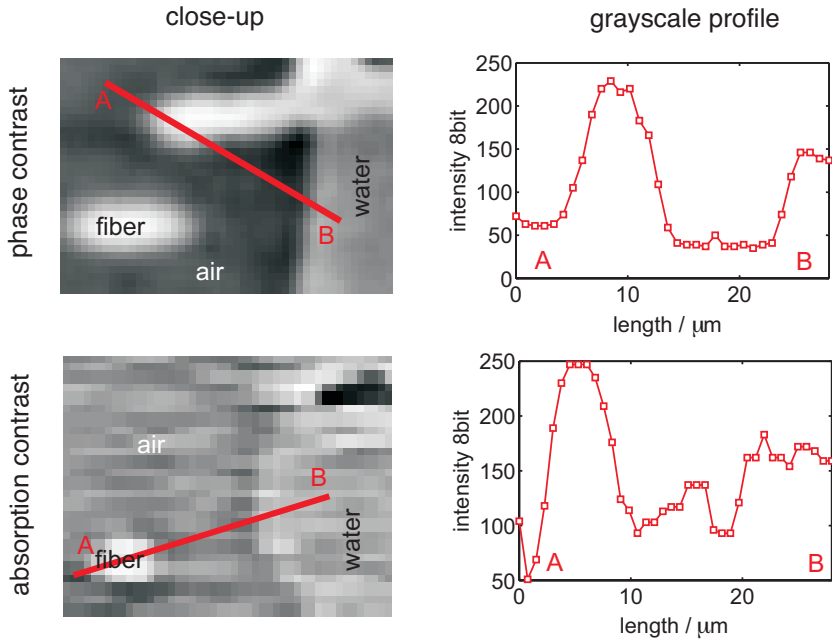
Figure 5.23: Close-up and grayscale profile from A to B of a reconstructed phase contrast (setting #6) and absorption constrast measurement (setting #2). A pixel represents a physical dimension of 1.48 μm x 1.48 μm.

Due to the short exposure times, absorption contrast should be used when transients are a critical issue. Otherwise phase contrast is preferable. However, a drawback of the phase contrast method is its restriction to small field of views to resolve fringes. Therefore local tomography is generally required which can distort the gray-scaling and the subsequent phase segmentation.

5.6.3 Hydrophobicity Distribution

Most transport models for liquid water in GDL's assume a homogenous contact angle distribution of $110°$ (water on PTFE). However, a homogeneous PTFE coverage is unlikely due to the manufacturing process. X-ray tomographic microscopy with sufficient resolution is the only method which could able to measure internal contact angles of partially water filled porous materials. To demonstrate the feasibility a high-resolution, unbinned absorption contrast measurement with a pixel size of 0.74 μm x 0.74 μm (setting #1) has been performed. For this a sample without PTFE was partially saturated under vacuum and afterwards measured in the compression sample holder (cf. Sec. 4.4.3). The result is shown in Fig. 5.24. Due to the hydrophilic nature
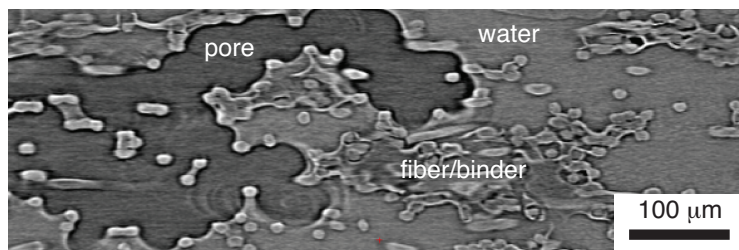
Figure 5.24: Through-plane slice (setting #1) of a partially filled TGP-H-060 without PTFE. Local contact
angles can be perceived but have to be measured in full 3D.

of the sample small pores should be filled preferentially. However, a larger pore at
the right edge of the sample is completely flooded with water demonstrating the non-
ideal behavior of water in a GDL. Knowing the local contact angles could improve
the understanding of the liquid water transport. For this further experiments and a
full 3D image processing of the data would be required.

5.6.4 Water Intrusion Series

According to the Young-Laplace Eq. (3.8) an increasing water pressure fills an increas-
ing amount of pores in a hydrophobic sample. Fig. 5.25 shows a series of through-
plane slices of the same sample (TGP-H-060, 20% PTFE) at the same location at differ-
ent liquid water pressures recorded with the water intrusion setup (cf. Sec. 4.4.4) and
the phase contrast method. In this *ex-situ* experiment the GDL is filled with liquid
water from the bottom. The structure of the GDL (light grayscale), voids (dark gray-
scale) and water (medium grayscale) can be identified. Porosities ε and saturations s
have been calculated using the grayscale thresholds tf and tw indicated below each
image. The porosity had to be independent of liquid pressure and therefore the fiber
threshold tf was set accordingly.

The proceeding water front as function of filling pressure is clearly visible. The
water initially fills the outermost pores at the bottom and is then retained at the
first dense layer. By increasing the pressure from 200 Pa to 600 Pa, water spreads
inplane and builds an undesirable barrier for gas transport instead of vertically flow-
ing through the GDL in a single column. As soon as the breakthrough pressure is
reached (1100 Pa), a continuous water pathway is established with a maximum sat-
uration of 30 to 60% depending on the type of GDL. The last image of the series shows
the sample after purging with air for about 10 seconds. The purged image shows the
ability of a GDL to store a significant amount of water (20% saturation). However,
purging in through-plane direction is not possible in a technical cell and therefore an
even larger immobile saturation can be assumed.

dry

1272x229 / ε = 0.79 / s = 0 / tf = 125 / tw = 125

200 Pa

1272x232 / ε = 0.80 / s = 0.19 / tf = 125 / tw = 100

600 Pa

1272x230 / ε = 0.80 / s = 0.18 / tf = 125 / tw = 100

1100 Pa

1271x227 / ε = 0.79 / s = 0.56 tf = 140 / tw = 100

purged

100 µm

1271x229 / ε = 0.79 / s = 0.20 / tf = 125 / tw = 100

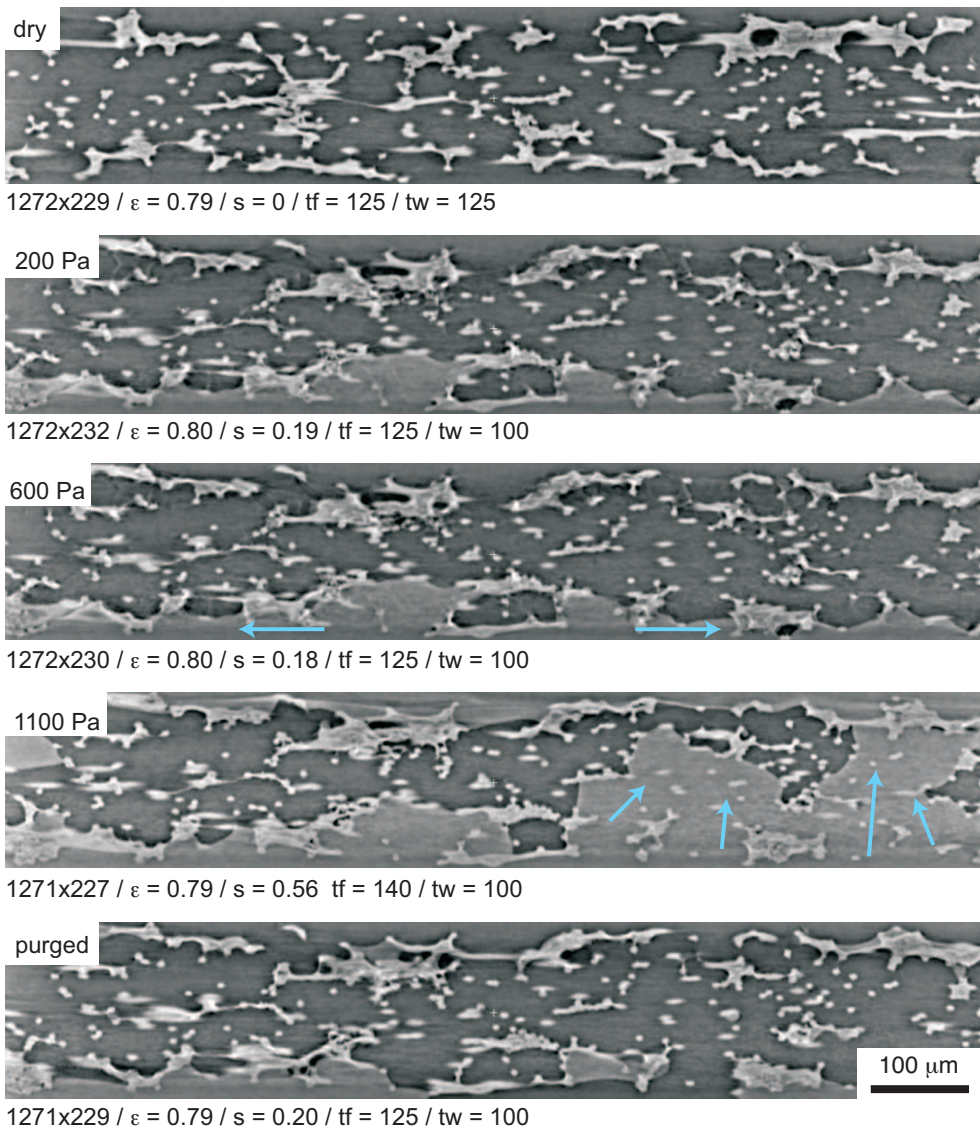**Figure 5.25:** Series of through-plane slices of TGP-H-060, 20% PTFE with increasing water pressures recorded with the phase contrast method (setting #6) and the water intrusion setup. The number below each figure indicate the number of pixels, the threshold-estimated porosity ε, the threshold-estimated saturation s, the fiber threshold grayscale tf and the water threshold grayscale tw.

The phase contrast method only works properly with the 10x and 20x objectives (setting #5 or #6) with a limited field of view (< 1.43 mm x 1.43 mm). As the sample in the water intrusion setup had a diameter of 2.5 mm local tomography was necessary. This resulted in a superimposed grayscale gradient visible as a dark shadow at the bottom of the slices in Fig. 5.25. A quantitative 3D image processing and surface reconstruction was therefore difficult. However, the liquid water transport pathways need to be studied in 3D. For this additional unbinned absorption contrast measurements with the 4x objective were recorded (setting #3) to avoid local tomography.

When the complete sample is analyzed in 3D, other characteristics can be observed. Fig. 5.26 shows isometric 3D-views of a halved sample at different liquid water pressures. Additionally the cutting plane at the front face shows the 2D threshold segmentation. The growing water front is visible in blue inside the partly transparent white fiber structure. The blue spots inside the black pores originate from the noise of the absorption contrast measurements. Although the through-plane cut does not significantly change from 2000 Pa to 4000 Pa, rising water columns can be observed on the blue 3D surface. At 4000 Pa the later break-through point can already be estimated. At 6000 Pa the water flows through the GDL and covers the upper surface while the center of the GDL remains partly unfilled.

5.6.5 Water Saturation Profiles

The liquid water distribution was studied quantitatively by averaged saturation profiles. For this the full 3D image set was segmented using constant grayscale-threshold criteria: pore 30-130, water 142-152, fiber 153-255. With this simple label statistic the local saturation and porosity was determined for every horizontal in-plane slice. The missing grayscale values 131-141 were not assigned to a specific phase to reduce the noise in the pore phase inherent to absorption measurements. Instead the saturation was increased by 72% of the unassigned voxels for TGP-H-060 20% PTFE and by 88% for TGP-H-060 0% PTFE. The porosity was increased by 28% and 12% of the unassigned pixels. This resulted in a saturation of 1 at the water inlet (relative thickness 1). These correction values remained constant for a specific sample.

The resulting saturation and porosity profiles over the GDL thickness are shown in Fig. 5.27a) for the hydrophobic TGP-H-060, 20% PTFE. Liquid water, which is intruded from the right (relative thickness 1), mimics a fully flooded catalyst layer. The porosity profiles should not be affected by the liquid water pressure and can therefore serve as a quality criterion for the threshold segmentation. TGP-H-060 with 20% PTFE features two dense layers near both surfaces and a higher porosity in the center. A retention effect up to 4000 Pa is observed at a relative thickness of about 0.8 where the porosity is smaller than 60%. At 6000 Pa this barrier is crossed and water
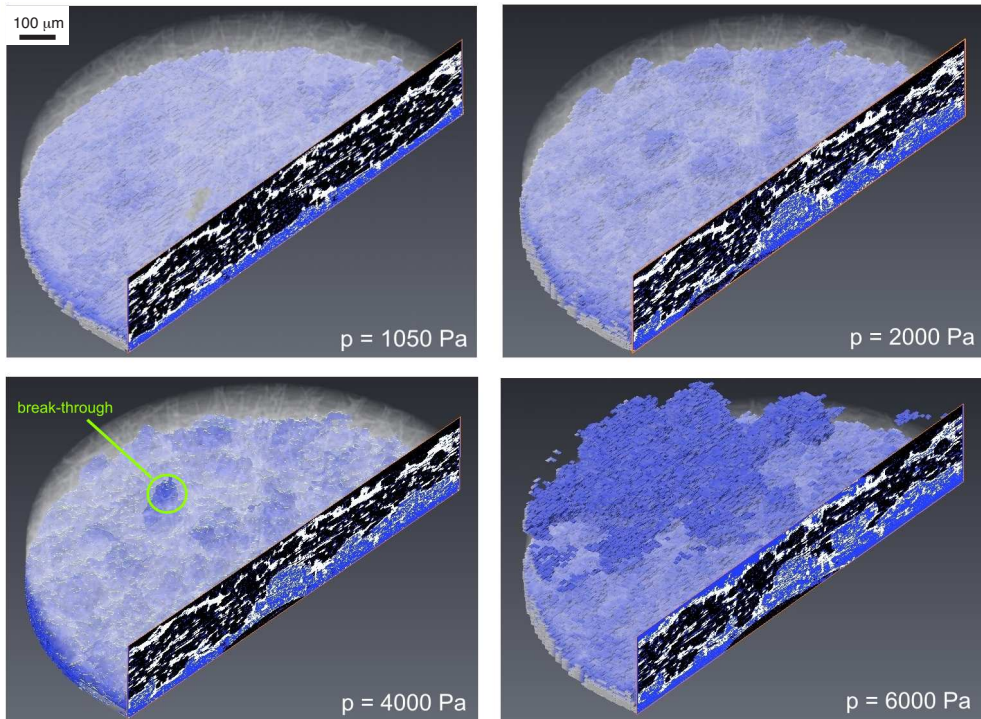
Figure 5.26: Series of surface reconstructed samples of TGP-H-060, 20% PTFE with increasing water pressures recorded with the absorption contrast method (setting #3) and the water intrusion setup. The front images show the threshold segmented cutting plane of the circular sample. Grayscale values of threshold segmentation: pore 30-130 (black), water 142-152 (blue), fiber 153-255 (white).
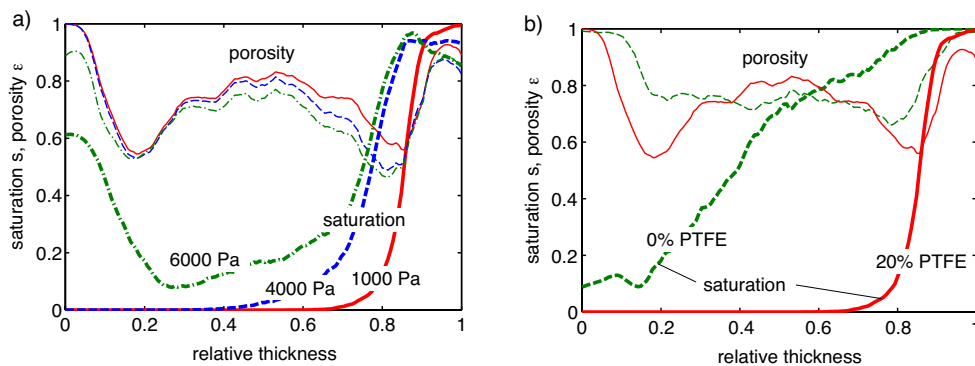
Figure 5.27: Average water saturation (thick lines) and porosity profiles (thin lines) over the GDL thickness. Based on absorption contrast measurements with setting #3. **a)** TGP-H-060, 20% PTFE with increasing liquid water pressure. **b)** TGP-H-060, 0% PTFE and TGP-H-060, 20% PTFE with both 1000 Pa water pressure.

pours into the high porosity region in the middle of the GDL, passes the second dense layer around a relative thickness of 0.2 and leaves the GDL at a relative thickness of 0. The saturation increases again towards the edge due to a spreading water film on the GDL surface.

The saturation profiles of a hydrophobic and hydrophilic TGP-H-060 are compared in Fig. 5.27b) for the same liquid water pressure. As expected the saturation of TGP-H-060 with 20% PTFE is much lower than without PTFE. Furthermore the comparison of the porosity profiles indicates that PTFE is responsible for the dense layers near both surfaces. The presented saturation and porosity profiles obtained with X-ray tomographic microscopy have unrivaled resolution and can serve as a valuable input for liquid water transport models assuming a fully saturated catalyst layer. However, the following future improvements are suggested:

- use elevated temperatures due the surface tension temperature dependency

- use saturated air streams instead of a liquid water column to eliminate the restriction to fully saturated catalyst layers

- study of hysteresis effects of wetting-drying cycles on the saturation profiles

- study chemical and mechanical hydrophobicity degradation and the effect on the saturation profiles
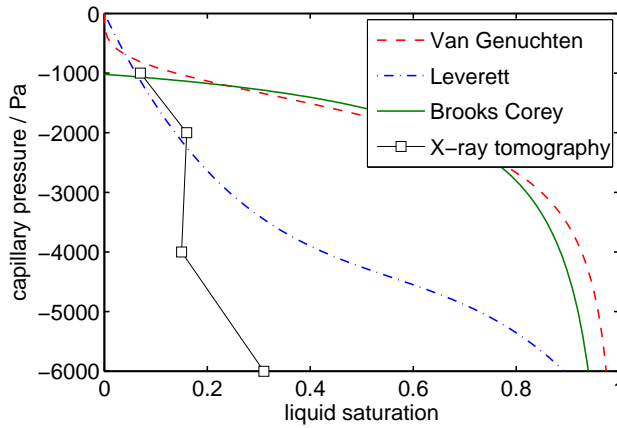
Figure 5.28: Total saturation measured by X-ray tomographic microscopy as a function of applied water pressure compared to capillary pressure function models used in literature. The experiment is a single measurement. Van Genuchten: p_{bt} = 1000 Pa, m = 0.7262, n = 3.652 [30,77]; Leverett: K = 2 x 10^{-12} m^2s^{-1}, ε = 0.7, θ = 110° [74]; Brooks Corey: p_{bt} = 1020 Pa, b = 1.59 [30,76].

5.6.6 Capillary Pressure

In the previous section the average local saturation for every in-plane slice was studied. By plotting the total saturation of the entire sample against the applied liquid water pressure, the capillary pressure function is obtained. Although the setup is not designed to measure this property accurately it reveals the characteristic behavior of the GDL wetting process: the retention effect at the first dense layer. The measured capillary pressure function is compared with literature models in Fig. 5.28. Generally the model predicted saturation of the Leverett model agrees with the experiment up to a capillary pressure of 2000 Pa. However, above 2000 Pa qualitative and quantitative trends are significantly different. All the models converge to full saturation while the measurements show a clear maximum between 30% and 60%. None of the models is able to predict the typical retention behavior of a GDL visible between 2000 Pa and 4000 Pa. More accurate, experimental capillary pressure functions for GDL's are given in [28–31,72,73].

5.6.7 Active Cell

The active cell setup described in Sec. 4.4.5 follows the same objective as the water intrusion experiment: the visualization and quantification of liquid water distribution in the GDL's. Producing gaseous and liquid water electrochemically instead of pressing pure liquid water into the structure was expected to create more realistic
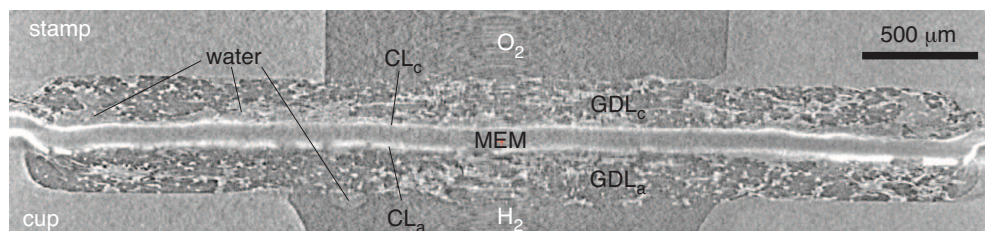
Figure 5.29: Reconstructed through-plane slice of the 7 mm^2 active cell recorded after the observation of flooding. Phase contrast with a pixel size of 3.5 μm x 3.5 μm (setting #8). The cathode is on the top and the anode on the bottom. The two GDL's used for the cell are TGP-H-060 without PTFE.

boundary conditions.

After operation of the 7 mm^2 cell and observation of flooding phenomena the sample holder was placed at the endstation. The first active cell experiments presented in this thesis were measured with the phase contrast method and the 4x objective (setting #8). A reconstructed through-plane slice of the cell and the sample holder is shown in Fig. 5.29. The center of the image is disturbed due to phase contrast artifacts using the 4x objective. On the top the oxygen and on the bottom the hydrogen channel can be seen. The stamp and the cup of the rotation-symmetric sample holder are visible in the corners. The membrane (MEM) is clamped and sealed between stamp and cup. The holes for the gold wires used for electrical connection are not visible in this slice. The white film covering the membrane is due to the high absorption of platinum in the catalyst layers (CL). The carbon fibers and binder of the GDL's are distinguished as white spots while the pores are shown in dark gray. The water in the GDL is visible in an intermediate grayscale between pore and fiber.

A large amount of water was found near the catalyst layer on the cathode side and some water was even present on the anode side. This demonstrates the feasibility of *in-situ* liquid water visualization using X-ray tomographic microscopy.

In Fig. 5.30a) the current vs. time of an active cell is shown exemplarily. A current of 70 mA corresponds to 1 Acm^{-2}. The instantaneous current drops occurred due to droplet formation in the oxygen gas channel. After droplet removal by a wick the current generally raised back close to the initial condition. The slow current decrease was attributed to GDL pore flooding. The point of tomography measurement is marked with a number which indicates the amount of electrochemically produced liquid water normalized by the cathode GDL pore volume ($\sim$ 1 mm^3).

In Fig. 5.30b) the average local saturations of the three active cells with different levels of flooding are shown over the thickness (slice number). The profiles were obtained by threshold segmentation of the reconstructed slices as described in Sec. 5.6.5. Due to the strong platinum absorption and tilting of the layers, the saturation profiles
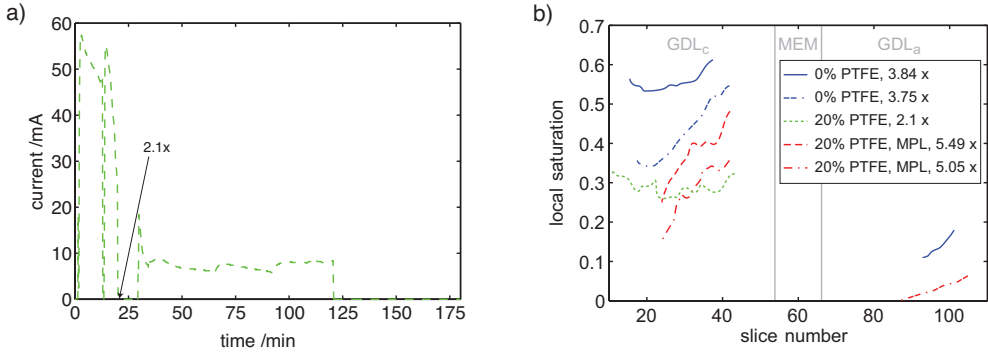
Figure 5.30: a) Operation history of an active cell configuration with a TGP-H-060 20% PTFE. The current of the 7 mm² active cell with a constant load of 5 Ω is plotted over time. **b)** Saturation profile through cathode GDL, membrane and anode GDL of different active cell x-ray tomography scan. The number in the legend indicates the amount of reactant water produced: 1 x is the pore volume of the cathode GDL.

close to the CL-GDL interface could not be calculated and were therefore cropped. Qualitatively the profiles are similar to the *ex-situ* intrusion experiments shown in Fig. 5.27. Note that the temperature gradient in the cell can not have a significant influence on the liquid water profile. A homogenous temperature of about 27 °C is expected resulting in a homogenous vapor pressure. Therefore the observed gradient must stem from convective transport of condensed water as the gases were fully humidified. The extrapolated saturation at the GDL-CL interface seems to be smaller than one. Furthermore it is assumed that the typical retention effect revealed in the liquid water intrusion experiment is not observed due to the presence of gaseous water diffusion.

As expected the active cells using GDL's (TGP-H-060) without PTFE had the highest level of saturation. The lowest saturation profile was measured for 20% PTFE. However the amount of water produced was the smallest. The homogenous saturation distribution for this cell suggests that water was mainly transported in vapor phase before condensation occurred. The micro porous layer (MPL) had the presumed effect: the average saturation in the GDL is low although the amount of water produced was the highest of all cells. The increase in saturation from the anode catalyst to the anode channel could be explained with the electro-osmotic drag through the membrane towards the cathode.

Although the observed measurements of liquid water in the GDL's of active cells fit the expectations, general findings are difficult due to limited resolution, significant phase contrast artifacts and unrealistic channel boundary conditions (diffusive transport). The following measures are proposed for future active cell tomography experiments:

- The absorption contrast method should be used to produce qualitatively sufficient results for the active cell. The 4x objective with a field of view of 3.58 mm x 3.58 mm is required to avoid local tomography (setting #3 or #4).

- The binned absorption contrast experiment takes about 6 minutes. If this is still too long to fulfill the immobilization requirement a reduced number of projections should be envisaged. Using only one projection (radiography) would allow a time resolution of below 1 second.

- The platinum in the catalyst layer impeded the visualization of water close to the GDL-CL interface. With lower Pt-loadings or thinner CL's this issue could be circumvented.

- As the water distribution in a PEFC is a strong function of temperature future experiments should be conducted at 70 °C. Furthermore realistic temperature gradients (~ 3 °C across GDL) have to be produced. However, this requires fast tomography scans which impedes resolution.

5.7 Summary & Conclusions

Valuable qualitative and quantitative properties of GDL's were obtained using the methods described in Chap. 4. They are used for the parameterization of the channel-rib model which is discussed in Chap. 7. The results and main findings are summarized below:

- **GDL Structure**. The characterization was focused on carbon paper materials from Toray and SGL Carbon Group. The two GDL's mainly differ in the type and amount of binder used to bond the carbon fibers. This difference was already visible by comparing scanning electron microscopy (SEM) top views. Relevant structural differences induced by PTFE and MPL coatings could be visualized by grinded cross sections of resin-impregnated samples. Finally phase contrast X-ray tomographic microscopy revealed the non-linear mechanical deformation of the structure.

- **GDL Porosity & Pore Size**. The porosity of the carbon papers from SGL Carbon Group were measured with the simple decane wetting method. Due to the low rigidity of the SIGRACET® GDL's the incompressibility requirement for MIP measurements was not fulfilled. However the MIP poresize distribution down to 1 μm (0.66 MPa Hg pressure) was expected to be valid. The SIGRACET® porosities and average pore sizes are generally higher as compared to the Toray

carbon papers. The porosities calculated based on tomographic microscopy data confirmed the values found by MIP and decane wetting.

- **GDL Permeability**. The permeability of GDL's in in-plane direction is 2-5 times larger compared to through-plane direction. Furthermore a strongly decreased permeability was observed with increased mechanical compression. Surprisingly the PTFE coating had a small, positive effect on the pressure driven transport property of the GDL's. The permeability of the Carman Kozeny theory agrees with in-plane measured values but fails to predict through-plane or compressed permeabilities.

- **GDL Diffusivity**. The influence of binder structure and PTFE treatment on the anisotropic, effective diffusivity of different carbon paper GDL's has been experimentally investigated for the first time. The novel electrochemical diffusimetry method (cf. Sec. 4.3) was applied and further developed. The results revealed that the theoretical models applied so far overestimate the effective diffusivity by a factor of about 2. The measurements were correlated to a physical unit cell model which allowed for a better understanding of the results. The variety of results was attributed to morphology differences studied with SEM top-views and light microscopy cross-sections (cf. Sec. 5.1). Especially the amount and type of binder has a strong influence. Generally, the less binder is used, the better is the diffusivity regardless of the porosity. The PTFE treatment of the GDL, which is necessary to improve the water management of the cell, interferes with the diffusion and increases gas transport losses.

- **Computed GDL Properties**. Measured anisotropic transport properties were compared with computed properties based on X-ray tomographic microscopy data. The two methods show a good quantitative agreement for most cases. For the case of the through-plane conductivity experimental and numerical data are not completely in line. Here, it has been shown that the deviation results from an overestimation of the conduction from fiber to fiber.

The results do not only prove that numerical simulations based on tomographic images are capable to determine real material properties of a GDL – the results are indeed far more valuable: they show, that tomographic imaging and experimental measurements are consistent and their combination allows for highly accurate investigation, determination and understanding of the relevant underlying physics for the transport properties in carbonaceous GDL materials. This is an important building block for the future development of improved GDL structures.

- **GDL Liquid Water Distribution**. Synchrotron-based X-ray tomographic microscopy can provide qualitative and quantitative insights into the water distribution in partially water filled GDL's. The phase contrast method provides high contrast but requires longer exposure times while the absorption contrast method results in lower image quality with better time resolution. The saturation as a function of the GDL thickness shows that the filling of the porous layers is inhomogeneous. When filling the dry GDL with increasing water pressure the water is retained at the first dense layer before breakthrough is observed. When a wet layer is purged, the dense layers trap the water and a significant saturation remains. Preliminary experiments have shown that the same measurements are possible with complete cells. X-ray tomographic microscopy can be developed to a versatile tool for investigating the behavior and state of water in GDL's and active cells with an unprecedented spatial resolution.

6 Catalyst Pore Scale Model (CPSM)

This chapter describes work that has been done in the group of Prof. Ned Djilali at the University of Victoria, Canada. The model was started by P.C. Sui in 2007 [129] and has been advanced within this thesis mainly to provide thorough catalyst layer (CL) transport parameters to the channel-rib model in Chap. 7. Although the parameterization of the CL is already valuable, the long term objective of the catalyst pore scale model (CPSM) goes beyond the simple extraction of effective parameters. The chapter first describes the motivation for this kind of models, followed by numerical details on the model implementation and solution. A good part of the work was invested for the numerical and experimental validation of the results. Finally the resulting effective diffusivities, electric conductivities and ionic conductivities are presented as a function of manufacturing parameters.

6.1 Motivation

Catalyst layers are typically coated onto both sides of the membrane. One of the most widely used manufacturing processes results in agglomerates of catalyst coated carbon particles that are bonded by a polymer electrolyte matrix, the so called ionomer (cf. Sec. 2.4.2). This ensures close contact of electric, ionic and gaseous phases around the active catalyst sites. The microporous structure can be recognized in the transmission microscopy image of Fig. 2.4 or the scanning electron microscopy image of Fig. 6.1. Coupled transport of electrons, protons, gases, liquid water and heat take place on the smallest length scale. Every species has its own tortuous pathway to and from the reaction zone resulting in different but coupled effective transport parameters. Oxygen diffuses through the pore and electrolyte network, electrons move in the carbon/platinum network, protons migrate within the electrolyte phase, water moves through pore and electrolyte phases and heat conduction is present everywhere. Hence modeling of PEFC catalyst layers is a challenge but may make properties available that are experimentally inaccessible.

The catalyst layer models found in literature can be categorized into four types. A comparison of them has been given recently by D. Harvey [130]. 1) The thin film model [131] does not account for any transport within the CL. The reaction takes place in an infinitely thin layer and is numerically described via simple boundary
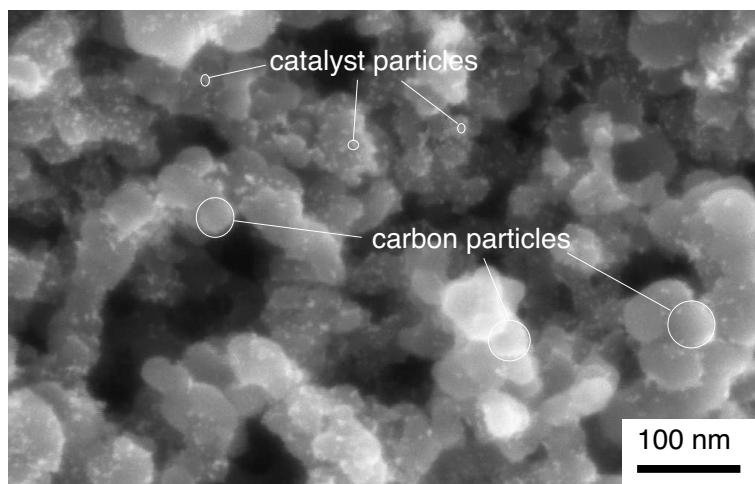
Figure 6.1: Scanning electron microscopy image of a Solvicore catalyst layer coated on a Nafion® 112 membrane. Carbon particles with diameters of around 30 nm are coated with platinum particles of a few nanometer. The agglomerate sizes are around 100 nm. A thin film of ionomer is surrounding the agglomerates.

conditions. 2) The macro-homogeneous model [41, 132] considers the CL as an homogeneous porous medium and uses lumped, averaged parameters to account for transport in the microstructure. 3) The macroscopic agglomerate model [133, 134] assumes agglomerated catalyst-coated carbon particles surrounded by ionomer with inter-agglomerate pores. In addition to the macro-homogeneous model, O_2 dissolution and diffusion in ionomer and liquid water can be considered. Although the agglomerate model includes more relevant effects, several additional parameters are required. A comparison of agglomerate and macro-homogeneous models can be found in [135]. 4) The microscopic models of CL on the molecular level (molecular dynamics) are not practical with state-of-the-art computers for simulations on the micrometer length scale. A promising approach is the use of a mesoscopic model [136, 137] to bridge the gap between the macroscopic and microscopic level and to derive volume averaged transport parameters based on microscopic details.

The main objective of the mesoscopic CPSM is to provide a platform to carry out representative element volume (REV) level simulations on the nanometer scale for uplink to the macroscopic, VAM (volume average method) based models on the micrometer scale. Additionally the platform can be used to incorporate microscopic simulations for parameters that can not be obtained on the macroscopic level [129]. In a first step, dependent structural parameters are exchanged between the two scales. In a latter electrochemically coupled version, the structural parameters can depend

on operating condition. E.g. the effect of catalyst ionomer swelling on the effective transport parameters could be considered. Further long-term objectives include the optimization of catalyst loading and the study of limiting current and degradation effects.

6.2 Structure Model

The model length scale of the CPSM was chosen to be the REV of a single agglomerate of carbon particles. According to Fig. 6.1 the REV of the entire CL should also include the inter-agglomerate space as the microstructure has a bimodal porosity. However, the relevant and limiting transport processes are taking place on the agglomerate level. Coupling of the agglomerate and inter-agglomerate scale could be accomplished based on the present model.

The CPSM is realized in Fortran and has two parts. First the structure of the CL is generated using the unit cell size (REV size), the carbon sphere radius r_c, the number of carbon spheres per unit cell n_c and the ionomer coating thickness δ_i as input parameters. The structure is generated on an N^3 grid by random distribution of the sphere centers and subsequent labeling of the grid points. The grid points with a distance smaller than r_c from the next sphere center are labeled 0, while the grid points with a distance greater than r_c are labeled in an ascending order. Fig.6.2a) shows this procedure on a 2D grid with a dimensionless r_c and δ_i of 3 and 2 respectively. Fig.6.2b) shows the random sphere structure (label 0) in blue and the ionomer layer (label 1-2) in blue to red. The pores (label > 2) are transparent. This 3D catalyst structure model is used as input to the following solution algorithm.

6.3 Numerical Solution Algorithm

The second part of the CPSM is the solution algorithm. So far the Fortran code solves the potential equation

$$\nabla (\sigma \, \mathrm{grad} \, \phi) + S = 0 \tag{6.1}$$

for either the gas phase, where ϕ is the oxygen concentration and σ the diffusivity, or the ionomer phase where ϕ is the ionic potential and σ the ionic conductivity or the solid phase where ϕ is the electric potential and σ the electric conductivity. The potential ϕ is thereby defined and solved for every grid point. Depending on the label of the structure model, the transport parameter is either the intrinsic material property or approximately zero if the corresponding transport is inexistent. Until now the source term S is zero. The discretization of the differential equation Eq. (6.1) is based

a)

7	6	5	4	3	3
6	5	4	3	2	2
5	4	3	2	1	1
4	3	2	1	0	0
3	2	1	0	0	0
3	2	1	0	0	0

N

δ_i

r_c

N

b)
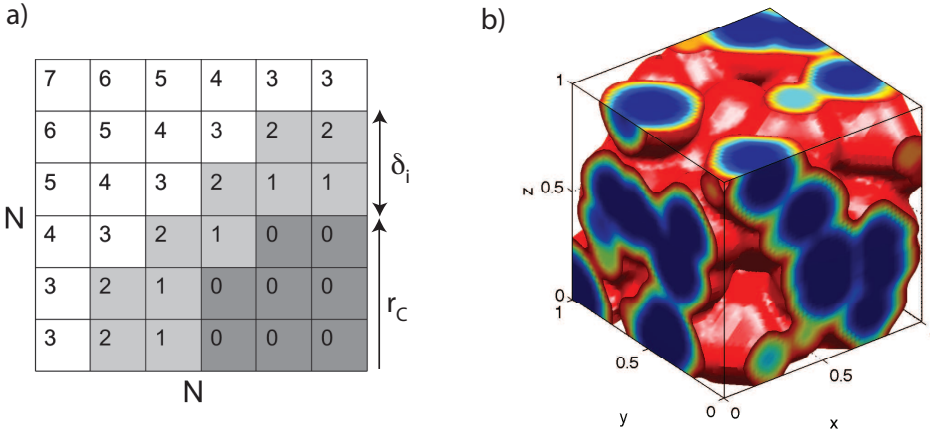
Figure 6.2: a) Labeled 2D grid (N = 6) showing the construction principle of a random carbon agglomerate with ionomer coating. 0: carbon particle, 1-2: ionomer coating, >2: pore. **b)** Unit cell with a side length of 100 nm (N = 50) equal to the REV of an agglomerate. The shown random structure includes 64 carbon particles with a radius r_c of 14 nm colored in blue. The ionomer coating has a thickness of 10 nm and is shown in colors from green to red.

on the control volume formulation described in the book of S.V. Patankar [138]. Each grid point is surrounded by a control volume over which the differential equation is integrated. With the assumption of a linear field distribution between the grid points an equation for each unknown variable can be formulated. The resulting system of algebraic equations is solved using the iterative, generalized minimal residual solver (GMRES) [139]. The extraction of effective transport parameters is done by applying the volume averaging method [55, 58] and dimensionless simulations. This means that the transport parameter σ, the side length of the unit cell Δx and the potential difference $\Delta \phi$ (boundary condition) were set to unity. Therefore the effective integral flux N_{eff} through the entire structure is a direct measure of the effective relative transport parameter ε / τ:

$$N_{\text{eff}} = \frac{\varepsilon}{\tau} \sigma \frac{\Delta \phi}{\Delta x} \qquad (6.2)$$

The convergence behavior of three successive simulations with x, y and z gradients can be seen in Fig. 6.3. The convergence is slow but stable. There are three stop criteria for the iteration: 1) A dimensionless mass flux error of less than 1% between inlet and outlet (Fig. 6.3 right). 2) A GMRES solver error of less than 10^{-4} (Fig. 6.3 left). 3) A maximum number of 10^4 iterations. The simulations shown in Fig. 6.3 stopped after 10^4 iterations with an acceptable mass flux error between 1 and 2% for
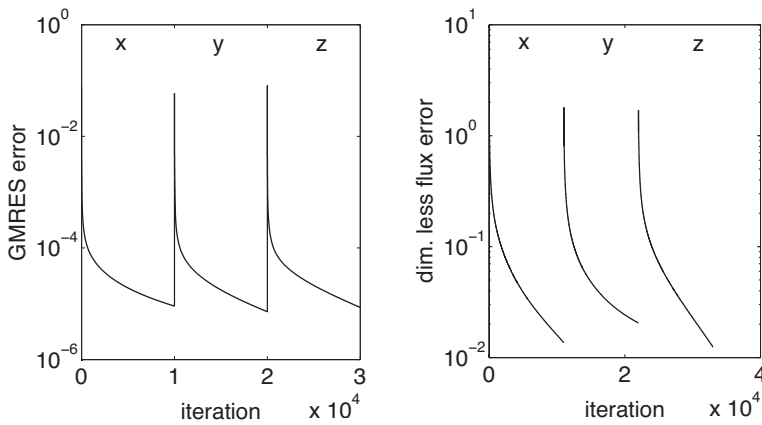
Figure 6.3: Convergence behavior for the simulation of three successive parameter sets with gradients in x, y and z directions on a 50^3 grid. **left**: GMRES error $<10^{-4}$. **right**: mass flux error $<10^{-2}$.

every direction. The computation time to solve the system of algebraic equations on a 50^3 grid for one parameter set was around 10 minutes (4 x 1.8 GHz and 8 GB RAM).

The output of the solution algorithm are 3D arrays including the dimensionless field and flux distributions for the structure model (cf. Sec. 6.4.3). The postprocessing and visualization of the data files has been realized in Matlab due to its scripting capabilities.

6.4 Results & Discussion

The model is currently able to calculate direction dependent effective transport parameters of a catalyst structure. In the following the structural parameters are adjusted according to characterization experiments. The numerical results underwent several numerical validation checks before a thorough parameter variation was performed.

6.4.1 Experimental Validation

The input parameters for the catalyst pore scale model (CPSM) are the carbon sphere radius r_c, the number of carbon spheres per unit cell n_c and the ionomer coating thickness δ_i. In order to validate the numerical results and to find the best input parameters for the catalyst layer used in the micro-cell experiment [15], several characterization tasks were performed. The characterization results are summarized and compared to the best suited configuration in Table 6.1.

The SEM of the Solvicore catalyst coated membrane (CCM) in Fig. 6.1, which has been used in the micro-cell experiment (cf. Sec. 2.5.3), shows carbon particle radii
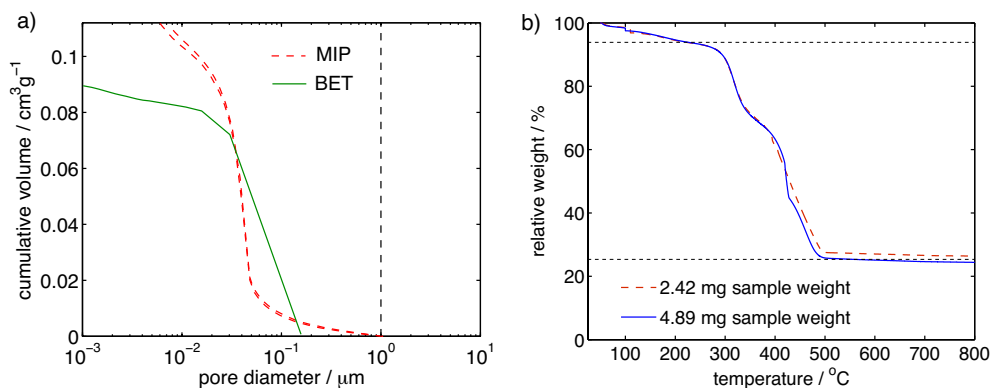
Figure 6.4: a) Cumulative pore size distributions of Solvicore CCM measured by MIP (dashed red) and BET (solid green). The vertical dashed line indicates the upper poresize threshold. **b)** TGA profiles of detached catalyst layer samples with different initial masses showing the evaporation of ionomer between 250-500 °C.

r_c around 15 nm and agglomerate radii around 100 nm. The void fraction of the Solvicore CCM was measured using mercury intrusion porosimetry (MIP) as described in Sec. 4.1.3. Samples of the entire CCM were measured as removing the catalyst layer from the membrane would have affected the porosity. The resulting pore size distribution is shown in Fig.6.4a). The upper poresize threshold was set to 1 μm in order to correct for the inter-sample volume. The average pore diameter was identified around 30 *nm* and the resulting porosity was calculated around 0.47. The average pore diameter is in the expected range but the porosity is relatively high compared to literature values (cf. Table 6.3). Furthermore the significant gradient of the cumulative pore volume at the lower measuring range around 10 nm is questioning the applicability of MIP. Therefore an additional BET nitrogen adsorption porosimetry measurement (cf. Sec. 4.1.2) was performed and a BJH pore size distribution calculated. The result is also plotted in Fig.6.4a). The porosity is only around 0.34 while the pore size distribution is wider with an average diameter of around 50 nm. The wider pore size distribution is due to the ability of the adsorption porosimetry to measure several diameters of a pore instead of only the most restricted one as in MIP. N_2 uptake into the ionomer at pore diameters below about 5 nm had a negligible effect on the volume measurements. Therefore the BET porosity was taken to verify the void fraction ε_v of the CPSM.

The ionomer fraction ε_i of the catalyst layer was determined by using the thermogravimetric analyzer (TGA). For this the catalyst layer was scraped from the membrane. The TGA profiles for two different initial sample masses are shown in Fig.6.4b). The mass reduction between 250 °C and 500 °C is related to ionomer evaporation,

parameter	CPSM	measured
carbon sphere radius r_c *(nm)*	10	15 (SEM)
number of carbon spheres n_c	64	
ionomer thickness δ_i *(nm)*	10	
void fraction ϵ_v	0.3	0.34 (BET)
ionomer fraction ϵ_i	0.49	0.43 (TGA)
solid fraction ϵ_s	0.21	0.23
eff. rel. diffusivity D_{eff}/D	0.13	
eff. rel. ion. conductivity ι_{eff}/ι	0.27	
eff. rel. el. conductivity σ_{eff}/σ	0.005	0.00119

Table 6.1: Comparison of characterization and simulation results for a catalyst coated Nafion® 112 membrane of Solvicore used in the micro-cell experiment [15].

which is 65% of the total mass. By assuming an ionomer density similar to the carbon density, an ionomer volume fraction ε_i of 0.43 is obtained. This has been used to adjust the ionomer layer thickness δ_i accordingly while bearing in mind that the scraping of the catalyst layer may have detached some additional ionomer from the membrane.

Knowing the void and ionomer fraction of the real catalyst layer allows to select appropriate input parameters for the CPSM. The carbon particle size had to be reduced to 10 nm to get the experimental void and solid fractions. In order to validate the output parameters the in-plane effective conductivity σ_{eff} of the catalyst layer was measured. For this different currents were induced on both sides of the CCM and the voltage drop over a defined distance was measured. The average σ_{eff} of the cathode CL is 113 Sm^{-1} and of the anode CL 132 Sm^{-1}. Assuming a pure graphite conductivity of 95000 Sm^{-1} the effective relative conductivities σ_{eff}/σ are 0.00119 and 0.00139 respectively. The comparison with the CPSM results in Table 6.1 shows that the structural parameters agree reasonable good. The computed effective conductivity could be 5 times higher due to neglected contact resistances between the carbon particles.

6.4.2 Numerical Validation

The resulting effective transport parameters were numerically verified on different levels. First the independency of the randomness of the structure was checked. For this the results of three different randomly generated structures with the same input parameters were compared in Table 6.2. The comparison revealed that the size of the unit cell is not large enough to hide random variations. The relative standard deviation for e.g. the effective diffusivity is 26%. Therefore, if the unit cell size is kept at 100 nm, the effective transport parameters have to be averaged over several

	D_{eff}/D	ι_{eff}/ι	σ_{eff}/σ	ε_v	ε_i	ε_s
structure 1:	0.0222	0.247	0.129	0.126	0.399	0.475
structure 2:	0.0382	0.265	0.0833	0.138	0.41	0.452
structure 3:	0.0313	0.240	0.106	0.135	0.393	0.472
mean:	0.0306	0.250	0.106	0.133	0.401	0.466
rel. standard dev.:	0.262	0.052	0.215	0.0469	0.0215	0.0268

Table 6.2: Effective relative transport parameters averaged over x, y and z direction and volume fractions ε of three random structures with the same input parameters: $n_c = 64$, $r_c = 14$ nm, $\delta_i = 10$ nm. The unit cell size is 100 nm with a discretization of N = 50.

50 nm	100 nm	200 nm	300 nm
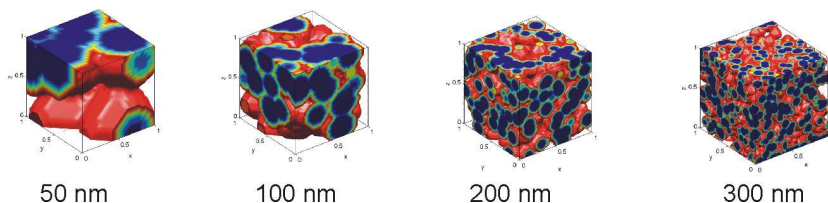
Figure 6.5: Different repetitive unit side lengths with constant sphere radius $r_c = 14$ nm (blue) and ionomer layer thickness $\delta_i = 10$ nm (green to red). The physical dimension of the control volumes were constant at 2 nm.

random structures or provided with error bars to account for statistical errors.

The next verification was done in terms of unit cell size. It was decided to build a repetitive unit cell on the agglomerate scale knowing that there is an inter-agglomerate scale with a slightly different morphology (e.g. higher porosity). In accordance with the SEM image in Fig. 6.1 the REV was estimated around 100 nm side length. The influence of the different unit cell sizes shown in Fig. 6.5 were tested. Their results are compared in Fig. 6.6a). By increasing the repetitive unit side length the number of grid points was also increased in order to keep the physical dimension of the control volume constant at 2 nm. Fig. 6.6a) suggests a marginal change of results for unit cell sizes larger than 100 nm. On the other hand the computation time for a repetitive unit larger than 100 nm was considered inefficient. Interestingly the effective electric conductivity calculated with a repetitive unit size of 300 nm is significantly smaller compared to 100 nm and 200 nm and out of the statistical error range calculated in Table 6.2. An explanation for this could not be found so far but is expected to be a percolation effect.

Another independency check was performed for the side length discretization N. A constant repetitive unit size with a side length of 100 nm was calculated with an increasing number of grid points. The results are shown in Fig. 6.6b). Above 50 grid points per side length the solution did not change significantly while the computa-
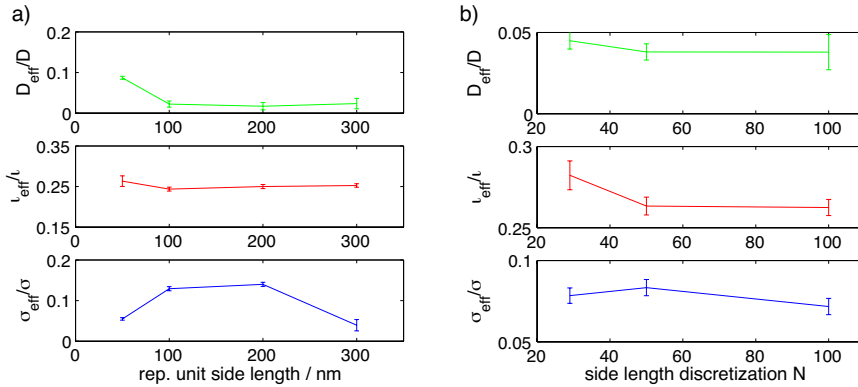
Figure 6.6: a) Effective relative transport parameters for different repetitive unit side lengths. **b)** Effective relative transport parameters for different side length discretization N. The values in both plots are averaged over x, y and z directions and the error bars show the average mass flux errors after convergence (cf. Sec. 6.3).

tional effort became impractical.

6.4.3 Fields & Fluxes

The direct output of the solution algorithm are the potential and corresponding flux distributions as visualized in Fig. 6.7 for the three different phases. Generally the higher the local gradient and the more confined the local cross section the higher the flux. Although the main focus was set on the integral flux through the structure and the calculation of the effective transport parameters using Eq. (6.2), the local values show the potential for future investigations. The different local potentials can be coupled over electrochemical reactions to study and localize limiting processes. The dimensionless values can be used to scale the field distribution between realistic boundary conditions. The flux visualization also contains streamlines showing the pathways of the corresponding species. These streamlines may cross the interfaces, which does not seem appropriate in the present uncoupled model. This is due to the non-zero conductivities of the non-conducting phases. Hence the interface fluxes are not zero but negligible small.

6.4.4 Effective Transport Parameters

The input parameters for the CPSM structure can be varied in a practical range in order to optimize the catalyst layer structure in terms of transport without reactions. Fig. 6.8a) and b) show the volume fractions and corresponding effective relative transport parameters as a function of particle density n_c and particle radius

Figure 6.7: Dimensionless potential and flux distributions for the structure shown in Fig. 6.2b) with a x-gradient of 1. The flux visualization is additionally supported with streamlines showing the direction but not the size of the flux.

r_c. There are three data points per structure and phase indicating the anisotropy in x-, y- and z-direction. Hence if the spreading is too large this particular structure can not be simplified as isotropic. However, the inv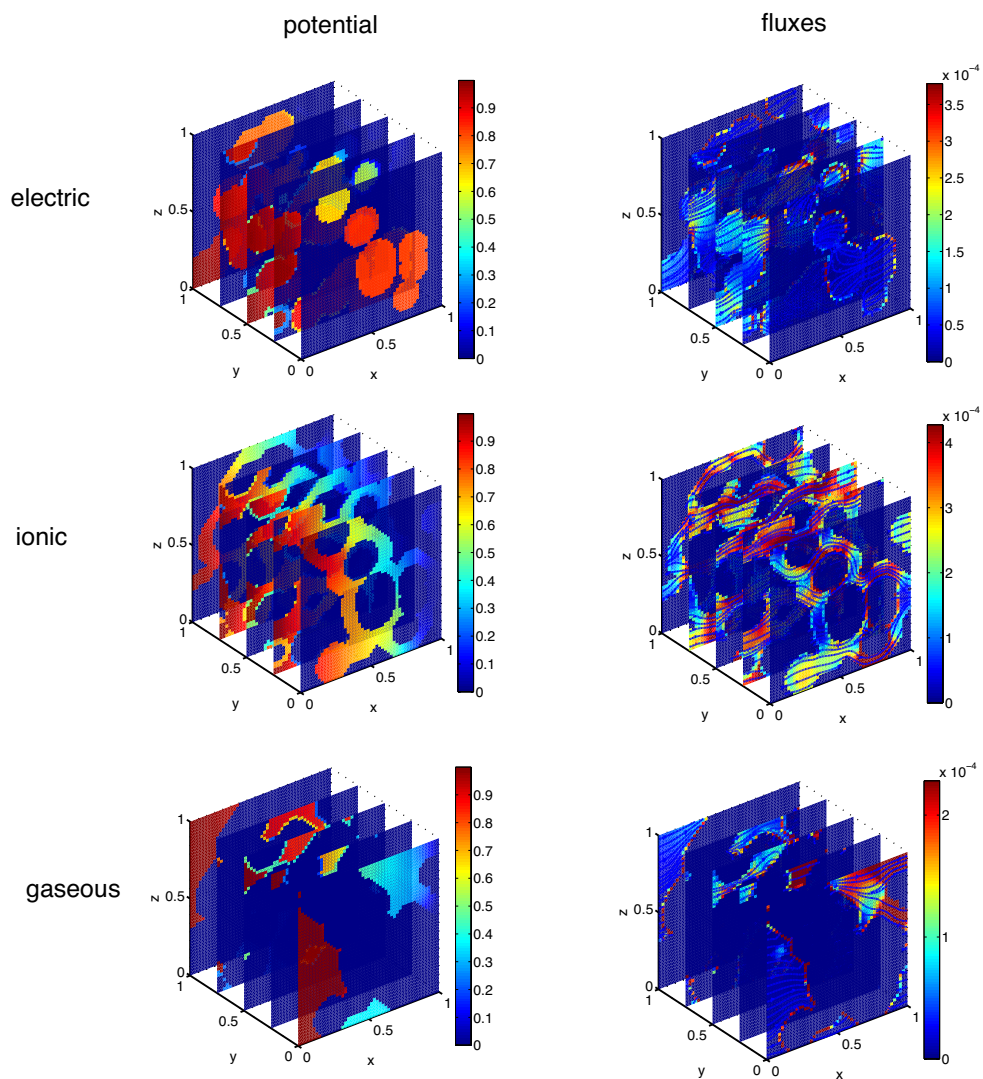estigated structures have a directional spreading of less than 10% and can therefore be considered isotropic. In the same plots the corresponding void ϵ_v, ionomer ϵ_i and solid fractions ϵ_s are shown as different gray areas summing up to 1.

In Fig.6.8a) the number of the carbon spheres per unit cell is increased from 1 to 216 while the radius and the ionomer coating were kept constant. With the assumption of a common Pt/C weight ratio of 0.2, the Pt loading [mg cm^{-2}] can be derived. It is plotted on the second vertical axis to the right. Although the values are in the same range as reported in literature (cf. Table 6.3) no information on the Pt distribution is available in the model so far. By increasing the number of carbon particles the solid fraction and the effective electric conductivity increases. However, a good electrical conductivity can not be achieved without impeding the effective diffusivity. The later was considered less critical as oxygen is able to dissolve into the ionomer and diffuse to the reaction sites, an effect that has not been considered in the model so far. The effective electric conductivity shows a percolation effect below 27 spheres where no continuous path for electrons is present. Even at 64 spheres the path for electrons is still highly tortuous although the volume fraction is around 50%.

In Fig.6.8b) the radius of the carbon particles is increased from 8 to 20 nm while the number of particles and the ionomer coating were kept constant. The volume specific surface [m^2 m^{-3}] of Pt can be derived by assuming a CL thickness of 10 µm and a homogeneous Pt coating on the carbon spheres. It is plotted on the second vertical axis to the right. The values are an order of magnitude higher compared to the Pt surfaces reported in literature (cf. Table 6.3). However it is expected that not all the surface is available for reaction and an effective Pt surface ratio has to be introduced. A maximum in surface area is observed due to an increased overlapping of the carbon spheres at large radii.

Table 6.3 compares CPSM input and output parameters of three different structures (variation of r_c) with values from literature. Generally the model predictions are within the literature range. The main benefit of the CPSM parameters is that they depend on each other and are physically derived. Structure 3 has a small active surface, small electric conductivity but a high gas diffusivity. It was considered as the best fit to the experimental data of the Solvicore CCM (Fig. 6.1). Structure 1 has a high active surface, a high electric conductivity but a small gas diffusivity. Structure 2 was considered as the optimum in between. The structure and transport parameters of CL 3 were used in the channel-rib model in Chap. 7 to demonstrate the multi-scale coupling.
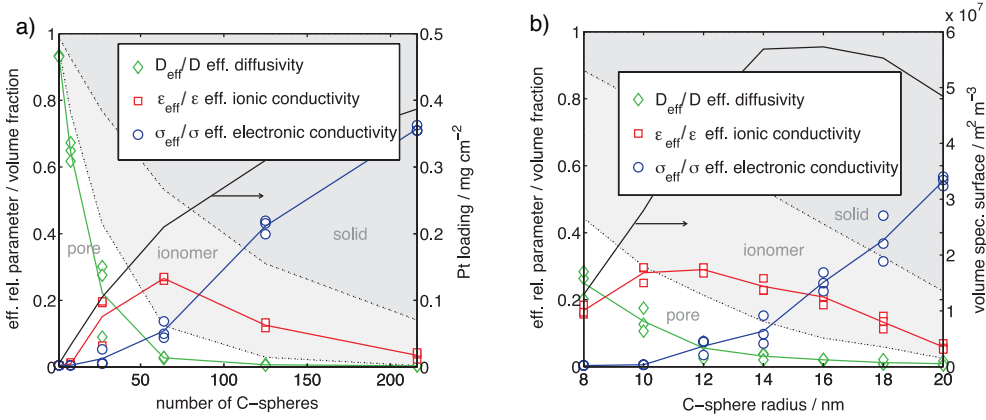
Figure 6.8: a) Effective relative transport parameters, volume fractions and Pt loading as a function of number of carbon spheres n_c per unit cell. r_c = 14 nm, δ_i = 10 nm, Pt/C = 0.2 (assumed). **b)** Effective relative transport parameters, volume fractions and specific Pt surface as a function of carbon particle radius r_c. n = 64, δ_i = 10 nm, d_{CL} = 10 μm (assumed).

parameter	CL 1	CL 2	CL 3	literature
r_c [nm]	20	14	10	15-50 [140]
n_c	64	64	64	
δ_i [nm]	10	10	10	80 [141], 0.5-20 [140], 15 [142]
agglomerate size [nm]	100	100	100	200 [142], 500 [143], 1000 [133]
ϵ_v	0.02	0.13	0.3	0.1 [141], 0.09 [144], 0.35 [18], 0.37 [145]
ϵ_i	0.20	0.39	0.49	0.25 [146], 0.4 [147], 0.5 [141], 0.72 [144]
ϵ_s	0.77	0.47	0.21	
A [$m^2 m^{-3}$]	4.8e7	5.7e7	2.8e7	3.6e5 [141], 8e6 [144], 1.1e7 [111]
Pt loading [$mg\,cm^{-2}$]	0.349	0.212	0.096	0.35-1 [133], 0.4 [148] 0.014 [149]
ion. loading [$mg\,cm^{-2}$]	0.316	0.620	0.77	0.2-2.0 [148], 0.3-1.5 [150], 0.6-2.7 [151]
D_{eff}/D	**0.01**	**0.05**	**0.13**	$\epsilon_v^{1.5}$ [63]
ι_{eff}/ι	**0.06**	**0.24**	**0.27**	0.188* [133], 0.271* [143]
σ_{eff}/σ	**0.54**	**0.10**	**0.005**	0.0189** [146], 0.136 [133], 0.00095** [143]

Table 6.3: Comparison of the effective parameter results of three different structures with literature values. CL 2 was considered as close to the optimum while CL 3 as the best fit to experimental data (* assumes an ionic conductivity of 14 S/m. ** assumes an electric conductivity of 95000 S/m).

6.5 Summary & Conclusions

In the catalyst layer coupled transport of electrons, protons, gases, liquid water and heat take place on the smallest length scale making it one of the most complex components in PEFC. Especially on the channel-rib scale of a few millimeters structural parameters of the catalyst layer can have a distinct influence on the current density distribution. Unfortunately measuring effective electric conductivity, effective ionomer conductivity and effective diffusivity of catalyst layers is difficult due to the small scale. Modeling of the catalyst layer on the other hand can make properties available that are experimentally inaccessible. Macro-homogeneous catalyst layer models used so far lack structural information on the nanometer scale. Therefore a catalyst pore scale model (CPSM) was developed which considers the nanometer structure to derive accurate macro-homogeneous parameters for efficient simulations on the micrometer scale. The CPSM builds a platform to bridge the gap between time consuming nanometer models and fast but often inaccurate macro-homogeneous models. At the moment the different transport pathways are calculated without electrochemical interactions. In the future the platform can serve as an optimization tool for limiting processes in the catalyst layer.

The input parameters for the structure model are the carbon particle density, the carbon particle size and the ionomer layer thickness. These manufacturing parameters were specified experimentally for the catalyst layer of the micro-cell experiment using SEM microscopy, BET porosimetry and a thermogravimetric analyzer. The comparison of model results with effective conductivity measurements revealed significant contact resistances between the carbon particles. The results were further verified in terms of convergence, randomness and size of repetitive unit. Finally the structural parameter variation yielded physical and dependent transport parameters, which confine the large range of literature values. The main finding was that for a good electric conductivity a significant reduction in gas diffusivity has to be accepted.

The next steps towards a more powerful optimization tool includes the gas dissolution and diffusion in the ionomer layer. Afterwards sink/source terms on the carbon surface have to be added. Later they have to be made dependent on the potential difference between electrode and electrolyte by using the Butler Volmer or Tafel equation. This will allow to study and locate limiting charge and gas transport processes within the catalyst layer depending on operating condition. Finally the implementation of condensation and transport of liquid water would allow to account for inhomogeneous ionic conductivities and flooding phenomena.

7 Channel-Rib Model

The thorough characterization of PEFC materials and its dependencies allows for building a numerical model of the channel-rib repetitive unit. The model is used to study the influence of measured properties and to improve the understanding of the highly coupled transport phenomena on the channel-rib scale.

PEFC models can be classified by their dimensionality. A thorough review of PEFC models can be found in [152–154]. 0D models predict the overall cell performance using analytical and empirical expressions [155–157]. Although the computation time is short, the physical interpretation of the results is limited as lumped parameters are normally required and no local information is available. Most of the early PEFC models were 1D [131,132,142,158–160]. The through-plane dimension with its different layers is resolved and transport effects can be studied. However, the assumption of homogeneous in-plane conditions is not valid, especially at high current densities. Furthermore anisotropic material properties are neglected in the 1D approach. Nevertheless, 1D models are an efficient tool to start a multidimensional, multicomponent model. The 1D model by Springer et al. [131] is isothermal, single-phase and does not resolve the catalyst layer thickness. The diffusion membrane model developed by Springer is widely used in literature but is only valid for low humidity conditions as it neglects the pressure driven water transport of a fully hydrated membrane. The 1D model by Bernardi and Verbrugge [132] is also isothermal and single-phase but accounts for transport in the catalyst layer and assumes a fully hydrated membrane with hydraulic water transport. However, the validity of this approach is limited to wet conditions. Baschuk and Li [159] developed a 1D, isothermal, pseudo two-phase model of the cathode side based on the hydraulic membrane model [132] to study the effect of flooding. The liquid phase in the GDL reduces the diffusivity but is not transported. Rowe and Li [160] developed a 1D, non-isothermal, pseudo two-phase model that accounts for temperature variations due to phase change of liquid water. The detailed 1D model by Shah et al. [142] is non-isothermal and accounts for transport of liquid water. The membrane water absorption-desorption and condensation-evaporation are driven by deviation from equilibrium. Most of the 1D models presented above have been compared to integral cell performances only, which is an insufficient validation. Recently numerous 3D models of complete cells have been published [161]. The ever increasing computational power allows

this brute force approach. However, due to the high aspect ratios the meshing is a difficult task and large scale parametric studies are still impossible.

2D models can be separated into along the channel [41, 43, 162–164] and channel-rib direction [33, 47–51, 165, 166]. The former consider the depletion of reactants and accumulation of products along a flowfield channel. These effects have been extensively studied in the dissertation of Stefan Freunberger [88]. The model developed in this work is a 2D channel-rib model that accounts for depletion and accumulation effects in the direction perpendicular to the flow. Among the first to numerically study inhomogeneities in the channel-rib direction were Meng and Wang [47]. They used a single-phase, isothermal, 3D model of a single straight channel to investigate the effect of different isotropic GDL conductivities. A similar model has been published by Sun et al. [48] with additional rib-compression effects. They showed a high sensitivity of the channel-rib current density distribution on GDL thickness, compression and channel-rib width ratio. Based on this model Pharoah et al. [33] emphasized the need to account for anisotropic transport properties in order to fully understand the channel-rib current density distributions. Nitta et al. [50] focused their study on the mechanical rib compression effect additionally accounting for contact resistances. They used a non-isothermal, single-phase model of the entire cell cross section assuming a fully hydrated membrane. Their results underline the need for accurate, compression dependent material properties. Sui and Djilali [51] developed a simplified, isothermal, single-phase 2D model of the cathode GDL in order to perform a parametric study of different influencing factors. Senn and Poulikakos [49] published an efficient channel-rib model of the cathode GDL accounting for all transport phenomena. They used the model to study the influence of different electric conductivities, contact angles, drag coefficients and condensation rates. Their geometric optimization study revealed a high potential for small rib widths and GDL thicknesses. A similar model has been presented by Pasaogullari et al. [165] recently. They used the efficient multiphase mixture model (M^2) proposed by Wang and Cheng [167] for the two-phase transport in the GDL and clearly showed the need for anisotropic modeling.

The 2D channel-rib models discussed so far included no experimental validation at all. A verification with integral current voltage characteristics of complete cells is insufficient for a model on the millimeter channel-rib scale. The only attempt to validate a channel-rib model so far has been undertaken by Li et al. [166]. They compared predictions of the model presented in [21, 167] with experimental channel-rib current density distributions [53]. They were able to explain the low-humidity current density profiles qualitatively. However, due to a lack of anisotropic and compression-dependent material properties a quantitative interpretation was not possible and a

significant discrepancy remained at high humidities.

The 2D channel rib model presented in this thesis is based on the 1D model of Shah et al. [142]. The starting point was a simple 1D model to test the different modeling steps. The 1D model ignores the dimension perpendicular to the flow direction and therewith underestimates the transport pathlengths. However, as the gradients in through-plane direction are much higher the resulting field distributions are expected to be a good first approximation. Different physics were added consecutively to the 2D model and their influences are discussed in detail. The final model resolves the membrane, GDL and CL on the cathode and anode side. Anisotropic and compression-dependent transport of electrons, protons, gases and liquid water are accounted for. Finally a comparison with experimental channel-rib current density profiles [53, 54] for different reactant gas compositions and humidification levels is presented and discussed.

7.1 Assumptions

The present model is based on assumptions which define the limit of validity. The main assumptions are summarized here. They may be discussed or mentioned in other sections as well.

- steady state conditions

- constant absolute pressure of 1.5 bar (isobaric)

- constant temperature of 70 °C (isothermal)

- no hydraulic membrane water transport

- no liquid water on the anode side

- product water is produced in the gas phase

- membrane water uptake is assumed in gas phase

- transport is described by effective media theory

- reversible cell voltage is at standard conditions

- channel and rib are considered as Dirichlet boundary conditions

- no contact resistances
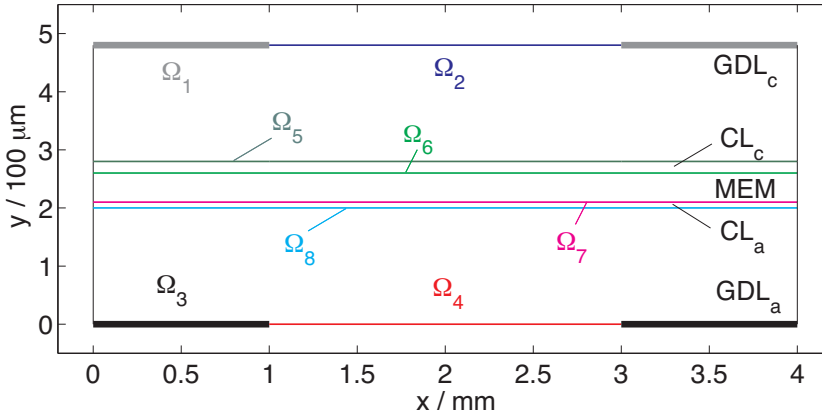
Figure 7.1: Modeling domain and boundary conditions. The figure is not to scale. GDL_c: cathode gas diffusion layer. CL_c: cathode catalyst layer. MEM: polymer electrolyte membrane. CL_a: anode catalyst layer. GDL_a: anode gas diffusion layer. Ω_1: cathode rib. Ω_2: cathode channel. Ω_3: anode rib. Ω_4: anode channel. Ω_5: cathode GDL-CL interface. Ω_6: cathode CL-MEM interface. Ω_7: anode CL-MEM interface. Ω_8: anode GDL-CL interface.

7.2 Domain

The model domain is shown in Fig. 7.1. It represents twice the smallest repeat unit of a parallel flowfield (cf. Sec. 2.4) and accounts for 5 layers in through-plane direction (y-coordinate). The anode gas diffusion layer (GDL_a, 200 µm thickness), the anode catalyst layer (CL_a, 10 µm thickness), the membrane (MEM, 50 µm thickness), the cathode catalyst layer (CL_c, 20 µm thickness) and the cathode gas diffusion layer (GDL_c, 200 µm thickness). The in-plane direction (x-coordinate) does not distinguish different domains. Instead the channel-rib geometry is reproduced by boundary conditions. The channel boundary conditions on the anode (Ω_4) and cathode side (Ω_2) range from 1-3 mm while two halves of a rib go from 0-1 mm and 3-4 mm absolute x-coordinates (Ω_1, Ω_3). At the internal interfaces continuity of fluxes and scalar fields hold if not mentioned otherwise. The boundaries at x = 0 mm and x = 4 mm are symmetry boundaries with zero fluxes. Note that Fig. 7.1 is not to scale and the real width to height ratio (aspect ratio) of the model is about 8. The geometry of the model has been adapted to the experiment. A future variation and optimization of the geometry is straightforward.

transport	GDL$_c$	CL$_c$	MEM	CL$_a$	GDL$_a$
electrons	$\underline{\sigma}_{\text{eff}}(\zeta)$	σ_{eff}, **J**		σ_{eff}, **J**	$\underline{\sigma}_{\text{eff}}(\zeta)$
protons		ι_{eff}, $-$**J**	ι	ι_{eff}, $-$**J**	
gases	$\underline{D}_{\text{eff}}(\zeta,s)$, $-$**R**$_{\text{ce}}$	$D_{\text{eff}}(s)$, **J**, **R**$_{\text{ad}}$, $-$**R**$_{\text{ce}}$		$D_{\text{eff}}(s)$, **J**, **R**$_{\text{ad}}$	$\underline{D}_{\text{eff}}(\zeta)$
water	$\underline{k}_{H_2O,l}(s)$, θ, **R**$_{\text{ce}}$	$\underline{k}_{H_2O,l}(s)$, θ, **R**$_{\text{ce}}$			
membrane		$D_{\text{m,eff}}$, n, $-$**R**$_{\text{ad}}$	D_{m}, n	$D_{\text{m,eff}}$, n, $-$**R**$_{\text{ad}}$	
momentum	$\underline{E}(\zeta)$				$\underline{E}(\zeta)$

Table 7.1: Model physics and domain overview with relevant transport parameters and coupling source terms (bold font). The underlined parameters have a direction dependency and therefore a tensor form. ζ: stress. s: saturation.

7.3 Governing Equations

A summary of the model physics in the different domains is shown in Table 7.1. The relevant transport parameters for the physics in the corresponding domains are given. Empty fields indicate inactive transport. The origin of the parameters is further discussed in Sec. 7.4. Effective parameters (subscript eff) point to the use of effective media theory. The different transport phenomena are highly coupled. The current of the ORR **J** is coupling the ionic with the electric transport in the CL$_c$. Furthermore the oxygen and water gas transport is influenced by sink and source terms proportional to **J**. On the anode side the current of the HOR **J** links the ion, electron and hydrogen transport in the CL$_a$. Membrane water transport and gaseous water transport are connected using the absorption-desorption rate **R**$_{\text{ad}}$ in CL$_c$ and CL$_a$. Liquid water is only present on the cathode side. The condensation-evaporation rate **R**$_{\text{ce}}$ in the GDL$_c$ and CL$_c$ couples the gaseous and liquid water transport. The momentum transport determines the local mechanical stress ζ which affects the local porosity and consequently the local electric conductivity and gas diffusivity of the GDL's. The liquid water transport in the cathode GDL results in a local saturation s which influences diffusivity and relative permeability.

7.3.1 Electron Transport

The electric potential ϕ is evaluated in GDL$_c$, CL$_c$, CL$_a$ and GDL$_a$ using Poisson Eq. (7.1). The divergence of the electric current on the left hand side is equal to the current source on the right hand side:

$$- \nabla(\sigma_{\text{eff}}^{\text{i}} \nabla \phi) = J, \qquad i = GDL_c, CL_c, CL_a, GDL_a \qquad (7.1)$$

The effective electric conductivity σ_{eff} of the GDL's are direction and compression dependent. Hence the electron transport is unidirectionally coupled to the momentum

transport. The volumetric current sources J of the ORR and HOR are described by the following Butler Volmer expressions:

$$J = \begin{cases} j_{\text{orr},0} \; A_{\text{c}} \left(\frac{c_{O_2}}{c_{O_2,\text{ref}}} \exp\left(\frac{-\alpha_{\text{c}} F(\phi - \chi - E_0)}{RT} \right) - \exp\left(\frac{(1-\alpha_{\text{c}}) F(\phi - \chi - E_0)}{RT} \right) \right) & \text{for } CL_c; \\ j_{\text{hor},0} \; A_{\text{a}} \left(\frac{c_{H_2}}{c_{H_2,\text{ref}}} \exp\left(\frac{-2\alpha_{\text{a}} F(\phi - \chi)}{RT} \right) - \exp\left(\frac{2(1-\alpha_{\text{a}}) F(\phi - \chi)}{RT} \right) \right) & \text{for } CL_a; \\ 0 & \text{elsewhere.} \end{cases}$$

(7.2)

wherein R is the ideal gas constant, F the Faraday constant, T the temperature and α the charge transfer coefficient. $j_{\text{orr},0}$ and $j_{\text{hor},0}$ are the exchange currents per catalyst area and A_c and A_a the active areas per volume of anode and cathode catalyst layers. The exchange current densities are scaled with the local reactant concentrations c_{O_2} and c_{H_2}. $c_{O_2,\text{ref}}$ and $c_{H_2,\text{ref}}$ are the reference concentrations at which the j_0 were measured. This is an additional coupling of the gas and electron transport. The ionic and electric potential are linked by the definition of the charge transfer overpotential in Eq. 2.17.

The boundary conditions for the electric potential are

$$\phi = \begin{cases} 0 & \text{at } \Omega_3; \\ U & \text{at } \Omega_1. \end{cases}$$

(7.3)

with U being the cell voltage. A zero flux condition has been used for the internal interfaces at Ω_7 and Ω_6, which implies a zero electric conductivity of the membrane.

7.3.2 Ion Transport

For the ionic potential χ in the CL_c, MEM and CL_a the following Poisson equation has been used

$$-\nabla(\iota_{\text{eff}}^i \nabla \chi) = -J, \qquad i = CL_c, MEM, CL_a$$

(7.4)

The ionic conductivity ι is assumed isotropic and compression-independent. For the membrane intrinsic instead of effective properties have been employed. The volumetric current sources J described in Eq. (7.2) have the opposite sign compared to Eq. (7.1). Zero flux conditions have been used for the internal interfaces at Ω_5 and Ω_8. Consequently the ionic potential distribution would be indefinite without J.

7.3.3 Species Transport

In reality the absolute pressure at the anode catalyst layer is smaller due to net gas consumption and higher at the cathode catalyst layer due to the net gas produc-

tion (neglecting condensation). The channel-rib model neglects the absolute pressure driven transport of gaseous species from or towards the catalyst layers. Transport of gaseous species in the porous GDL_c, CL_c, CL_a and GDL_a is governed by the Maxwell-Stefan equation for multicomponent gas diffusion. Eq. (7.5) shows the mass conservation for species k in a gas mixture with N different species. The divergence of the diffusive flux, which is dependent on the gas composition, is equal to the species mass sources S_k

$$-\nabla \left(\rho^i w_k \sum_{l=1}^{N} D^i_{kl,\text{eff}} \frac{M^i}{M_l} \left(\nabla w_l + w_l \frac{\nabla M^i}{M^i} \right) \right) = S_k, \qquad i = GDL_c, CL_c, CL_a, GDL_a$$

(7.5)

wherein ρ^i denotes the density of the mixture in domain i, M_l is the molar mass of species l, M^i is the average molar mass of the mixture in domain i, w is the weight fraction and $D^i_{kl,eff}$ the binary effective diffusivity of k and l in the porous domain i. The cathode gas mixture is composed of oxygen, nitrogen and water vapor whereas on the anode side hydrogen, nitrogen and water vapor are present. Mass conservation does not apply in the CL's as protons and water are transfered. In order to fulfill the conservation Eq. 7.5 with a constant absolute pressure, nitrogen leaks in or out of the CL's even on the anode side. The volumetric mass sources S_k for the different domains and species are described in Eq. (7.6), Eq. (7.7) and 7.8 and have the unit [kg m^{-3} s^{-1}]:

$$S_{O_2} = \begin{cases} -\frac{M_{O_2}}{4F} J & \text{for } CL_c; \\ 0 & \text{elsewhere.} \end{cases}$$

(7.6)

$$S_{H_2O} = \begin{cases} \frac{M_{H_2O}}{2F} J - M_{H_2O} R_{ce} + c_{SO_3^-} M_{H_2O} R_{ad} & \text{for } CL_c; \\ -M_{H_2O} R_{ce} & \text{for } GDL_c; \\ c_{SO_3^-} M_{H_2O} R_{ad} & \text{for } CL_a; \\ 0 & \text{elsewhere.} \end{cases}$$

(7.7)

$$S_{H_2} = \begin{cases} \frac{M_{H_2}}{2F} J & \text{for } CL_a; \\ 0 & \text{elsewhere.} \end{cases}$$

(7.8)

Four electrons are consumed per mol O_2 and two per mol H_2O in the CL_c while two electrons are generated per mol H_2 in the CL_a. Note that the product water is assumed in gaseous phase. The water condensation-evaporation rate R_{ce} [mol m^{-3} s^{-1}] is only implemented on the cathode side and defined by Eq. (7.13). The absorption-desorption of water vapor takes place in the CL's and is governed by the absorption-

desorption rate R_{ad} [s^{-1}] in Eq. (7.17). The membrane water content λ multiplied by the fixed charge site concentration $c_{SO_3^-}$ [mol m^{-3}] results in the absolute water concentration.

The boundary conditions for the species mass fractions in the channels are

$$
w_{H_2O} = \begin{cases} \frac{p_{sat} \, RH_c}{RT} \frac{M_{H_2O}}{\rho_c} & \text{at } \Omega_2; \\ \frac{p_{sat} \, RH_a}{RT} \frac{M_{H_2O}}{\rho_a} & \text{at } \Omega_4; \end{cases} \tag{7.9}
$$

$$
w_{O_2} = (1 - w_{H_2O}) \, f \qquad \text{at } \Omega_2 \tag{7.10}
$$

$$
w_{H_2} = 1 - w_{H_2O} \qquad \text{at } \Omega_4 \tag{7.11}
$$

with p_{sat} being the saturation partial pressure, RH_c and RH_a the relative humidities of the cathode and anode channels and ρ_c and ρ_a the densities of the gas mixtures. f is 1 for pure oxygen and 0.21 for ambient air operation. The nitrogen mass fraction w_{N_2} at Ω_2 complements to 1. Note that the gas composition at the channel boundary does not change with operating condition. This is in agreement with the high stoichiometry operation of the experiment. The internal interfaces at Ω_6 and Ω_7 describe zero species flux boundaries.

7.3.4 Liquid Water Transport

Transport of liquid water is only implemented on the cathode side. A test implementation on the anode side revealed no condition at constant temperature, where the partial pressure of water exceeded the saturation pressure. The divergence of the convective mass flux is equal to the mass sources of liquid water

$$
\nabla(\varepsilon^i \, \rho_{H_2O,l} \, \mathbf{v}_{H_2O,l}) = M_{H_2O} \, R_{ce}, \qquad i = GDL_c, CL_c \tag{7.12}
$$

where ε^i is the porosity of domain i, as liquid water can only be transported in the void and $\mathbf{v}_{H_2O,l}$ is the liquid water velocity vector. The condensation-evaporation rate R_{ce} has the opposite sign compared to Eq. (7.7):

$$
R_{ce} = \begin{cases} h_c \frac{\varepsilon^i (1-s) x_{H_2O}}{RT} (p_{H_2O} - p_{sat}) & \text{for } GDL_c, CL_c & \text{if } (p_{H_2O} > p_{sat}); \\ h_e \frac{\varepsilon^i s \, \rho_{H_2O,l}}{M_{H_2O}} (p_{H_2O} - p_{sat}) & \text{for } GDL_c, CL_c & \text{if } (p_{H_2O} < p_{sat}); \\ 0 & & \text{elsewhere.} \end{cases} \tag{7.13}
$$

The condensation-evaporation rate is proportional to the difference of water partial pressure p_{H_2O} and saturation pressure. The condensation h_c and evaporation rate constant h_e are taken from [142] and have units of [s^{-1}] and [Pa^{-1}s^{-1}] respectively.

The evaporation scales with the saturation s as the liquid phase is necessary for evaporation to take place. Consequently the condensation rate has to scale with $(1 - s)$ and x_{H_2O} as it is only possible if a vapor phase is present. Both are proportional to the porosity ε^i.

The liquid water velocity $\mathbf{v}_{H_2O,l}$ vector in Eq. (7.12) is calculated by the Darcy-law approximation to momentum conservation:

$$\mathbf{v}_{H_2O,l} = \frac{k_{H_2O,l} \, K^i}{\mu_{H_2O,l}} \nabla p_{H_2O,l}, \qquad i = GDL_c, CL_c \tag{7.14}$$

The absolute permeability K^i of domain i is multiplied by the relative permeability of liquid water $k_{H_2O,l}$. The velocity is proportional to the gradient of pressure $p_{H_2O,l}$ and inversely proportional to the dynamic viscosity μ. The liquid pressure in the porous material can be written as $p_{H_2O,l} = p - p_c$. Using the assumption of constant absolute gas pressure p, differentiation of $p_{H_2O,l}$ results in

$$\nabla p_{H_2O,l} = -\frac{\mathrm{d}p_c^i}{\mathrm{d}s} \nabla s, \qquad i = GDL_c, CL_c \tag{7.15}$$

The derivative of the capillary pressure with respect to saturation $\mathrm{d}p_c^i/\mathrm{d}s$ and the relative permeability $k_{H_2O,l}$ are important material properties and further discussed in Sec. 7.4. The combination of Eq. (7.12), (7.14) and (7.15) yields a differential equation for the saturation distribution in the different domains.

The saturation boundary condition to the cathode channel at Ω_2 is not straightforward and still disputed in the literature [168–170]. The outflow of liquid water from the GDL to the flowfield channel is a complicated process. Droplets are formed on the surface and can grow up to the size of the channel [171]. The larger the flow velocity the better is the droplet removal. Therefore the saturation was set to zero at Ω_2 assuming an optimal liquid water removal due the high stoichiometry operation ($\lambda > 10$) of the micro-cell experiment [54]. The internal interface at Ω_6 has a zero liquid water flux condition.

7.3.5 Membrane Water Transport

The model accounts for membrane water transport by diffusion against a concentration gradient and by electroosmotic drag with the proton flux. The convective transport against the absolute pressure gradient has been ignored. A measure for the membrane humidification is the membrane water content λ defined as the number of water molecules per sulfonate group (SO_3^-). The mass balance for water dissolved in the membrane yields the differential equation

$$\nabla \left(-D^i_{m,eff} \, \nabla \lambda + \frac{n}{F \, c_{SO_3^-}} \, \iota^i_{eff} \, \nabla \chi \right) = -R_{ad}, \qquad i = CL_c, MEM, CL_a \qquad (7.16)$$

wherein the first term on the left hand side represents the diffusive flux with $D^i_{m,eff}$ being the effective membrane water diffusivity of domain i. The second flux term is the contribution of the electroosmotic drag with n being the electroosmotic drag coefficient. The absorption-desorption rate R_{ad} has the opposite sign compared to Eq. (7.7) and is defined as

$$R_{ad} = \begin{cases} h_a \, (1-s) \, \lambda \, (\lambda - \lambda_0) & \text{for } CL_c, CL_a & \text{if } (\lambda < \lambda_0); \\ h_d \, (1-s) \, \lambda (\lambda - \lambda_0) & \text{for } CL_c, CL_a & \text{if } (\lambda > \lambda_0); \\ 0 & & \text{elsewhere.} \end{cases} \qquad (7.17)$$

The absorption-desorption rate is proportional to the difference of the local water content λ and the equilibrium water content λ_0 specified by the water uptake isotherm in Eq. (7.27). The larger the saturation the lower is the absorption-desorption rate as the water uptake is assumed from the gas phase. Furthermore R_{ad} is proportional to λ as the swelling of the membrane pores improves the absorption/desorption of water [172] while shrinking has a negative effect. The absorption h_a and desorption rate constant h_d are taken from [142, 172] and have the unit $[s^{-1}]$.

The membrane water flux at the internal interfaces Ω_5 and Ω_8 is zero. Therefore the membrane water content distribution is only defined due to the absorption-desorption rate R_{ad} in the CL's.

7.3.6 Momentum Transport

The conservation of momentum is based on the principle of virtual work. It states that the sum of virtual work from internal strains is equal to the virtual work from external forces [173]. The normal (v_x, v_y) and shear strains (v_{xy}) are defined as the partial derivatives of the displacements

$$v_x = \frac{\partial u}{\partial x}; \quad v_y = \frac{\partial v}{\partial y}; \quad v_{xy} = \frac{1}{2} \left(\frac{\partial u}{\partial x} + \frac{\partial v}{\partial y} \right); \qquad (7.18)$$

where the displacement in x-direction is given by u and in y-direction by v. The relationship between strain v and stress ζ is defined by Hook's law

$$\zeta = \underline{D}_o v \qquad (7.19)$$

with $\underline{D}_o$ being the elasticity matrix of an orthotropic material.

$$\underline{D}_o^{-1} = \begin{bmatrix} \frac{1}{E_x} & -\frac{v_{xy}}{E_y} & 0 \\ -\frac{v_{xy}}{E_x} & \frac{1}{E_y} & 0 \\ 0 & 0 & \frac{1}{G_{xy}} \end{bmatrix} ; \quad \zeta = \begin{bmatrix} \zeta_x \\ \zeta_y \\ \psi_{xy} \end{bmatrix} ; \quad v = \begin{bmatrix} v_x \\ v_y \\ v_{xy} \end{bmatrix} ; \tag{7.20}$$

The momentum transport was implemented in GDL_c and GDL_a. E_x and E_y are the Young's modulus of the GDL for in-plane and through-plane direction respectively. G_{xy} is the shear modulus for the shear stress ψ_{xy}. The coupling between the two directions is defined by Poisson's ratio v_{xy}. Note that both stresses and strains are expressed as vectors.

The effective diffusivity and conductivity were determined as a function of porosity. Assuming an uncompressed thickness and porosity of d_0 and ε_0 the local porosity can be calculated as a function of the local displacement v in y-direction:

$$\varepsilon = 1 - d_0 \frac{1 - \varepsilon_0}{d_0 - v} \tag{7.21}$$

A constrained y-displacement of v_{rib} was set for the rib boundaries at Ω_1 and Ω_3. The channel boundaries at Ω_2 and Ω_4 were free. The vertical boundaries at x = 0 mm and x = 4 mm have symmetry conditions.

7.4 Parameters

A mechanistic model requires accurate material parameters. A total of 23 relevant parameters were identified out of which 14 where measured, 6 were taken from literature and only 3 were fitted to experimental data. Table 7.1 gives an overview of parameters required for the different physics. In the following their dependencies and implementations in the model are discussed in more detail.

7.4.1 Diffusivity

The diffusivity is used in the Maxwell-Stefan Eq. (7.5). The effective diffusivity of the gas pair k and l in the GDL and CL is defined as

$$D_{kl,eff} = (1 - s)^{m_i} \frac{\varepsilon}{\tau} D_{kl}, \qquad i = GDL_{ip}, GDL_{tp}, CL \tag{7.22}$$

The gas diffusion is zero when the pores are fully filled with liquid water ($s = 1$). The decrease of diffusivity with saturation is not linear as shown in Fig. 7.2. The decrease at low saturation is stronger as the liquid water produced at the CL_c spreads in in-plane direction building a barrier for oxygen to reach the CL (cf. Sec. 5.6). For the in-plane direction of the GDL the exponent $m_{\text{GDL,ip}} = 2$ and for the through-plane
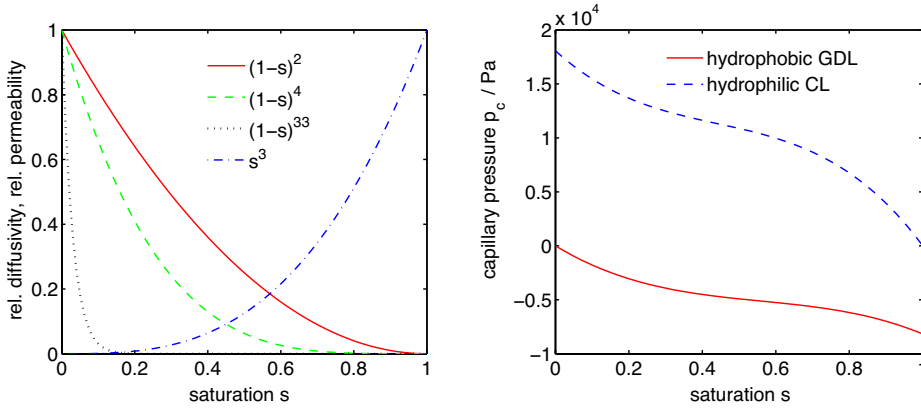
Figure 7.2: Left: effective relative diffusivity (solid red, dashed green, dotted black) and relative permeability (dash-dotted blue) as a function of saturation for GDL [66] and CL (fit). **Right**: capillary pressure as a function of saturation [74] for GDL and CL.

direction $m_{\text{GDL,tp}} = 4$ has been used according to Nam and Kaviany [66]. The exponent for the catalyst layer saturation dependency was fitted to experimental data. At $m_{\text{CL}} = 33$ the experimental limiting current could be reproduced. Around a saturation $s = 0.1$ there is a threshold for gas diffusion which can be explain by a liquid film covering the entire active area in the CL.

The structural parameter ε/τ has been measured for different GDL's as a function of direction and compression (cf. Chap. 5). The results of TGP-H-060 with 20% PTFE in Fig. 5.12 were fitted to exponential functions:

$$\frac{\varepsilon}{\tau} = \begin{cases} 0.03 \cdot \exp(3.6\,\varepsilon) & \text{for in-plane } GDL_c, GDL_a; \\ 0.0096 \cdot \exp(4.4\,\varepsilon) & \text{for through-plane } GDL_c, GDL_a; \\ 0.13 & \text{for } CL_c, CL_a. \end{cases} \qquad (7.23)$$

The effective relative diffusivity of the CL's was determined with the catalyst pore scale model in Chap. 6. The binary diffusivities D_{kl} have been calculated using the Slattery Bird equation (Eq. 3.16). Due to constant pressure and temperature throughout the model the binary diffusivities do not change. They are listed for the different gas combinations in Table 7.2. The Knudsen number for gas diffusion in the CL's is between 4 and 10 depending on the gas. This means that the pore diameter of around 30 nm is smaller than the mean free paths. Pore wall collisions are therefore more likely and the Knudsen diffusivities calculated by Eq. (3.20) and listed in Table 7.2 have be employed in the CL's.

7.4.2 Permeability

The permeability of the GDL has been measured in Sec. 5.3 to study the effect of gas cross-convection in a serpentine flow-field [39]. The absolute permeability is also required in Darcy's law (Eq. (7.14)) for liquid water transport. The directional dependency of the GDL permeability was considered while the compression effect was ignored in the model. The CL permeability was assumed to have the same order of magnitude as the micro porous layer (MPL) due to similar mean pore sizes.

The absolute permeability in Eq. (7.14) is scaled with the relative liquid water permeability $k_{H_2O,l}$ as a function of saturation. At $s = 0$ the GDL and CL are impermeable for liquid water and at $s = 1$ the total permeability is available for transport of liquid water. Between these two limits the following relationship has been used [58]

$$k_{H_2O,l} = s^3 \tag{7.24}$$

which is also plotted in Fig. 7.2 left.

7.4.3 Capillary Pressure

The capillary pressure p_c is necessary to describe the pressure driven transport of liquid water (cf. Eq. (7.15)). In a hydrophobic porous material ($p_c < 0$) the capillary pressure increases with increasing saturation while it decreases in a hydrophilic material ($p_c > 0$). This relationship, the capillary pressure function, has already been discussed in Sec. 3.1.6. Although the applicability of the Leverett approach [74] (cf. Eq. (3.10)) to GDL's is to doubt it has been implemented in the channel-rib model due to lack of alternatives and for comparison with existing models.

7.4.4 Electric Conductivity

The effective electric conductivity σ_{eff} of the components are used in the Poison Eq. (7.1). The in-plane (ip) and through-plane (tp) effective conductivity of the GDL differ by about an order of magnitude as measured in the thesis of M. Reum [15]. The experimental data for TGP-H-060 with 20% PTFE as a function of compression (porosity ε) has been fitted to second order polynomials with units [S m^{-1}]:

$$\sigma_{\text{eff}} = \begin{cases} -8 \times 10^4\, \varepsilon^2 + 7.7 \times 10^4\, \varepsilon + 2.9 \times 10^3 & \text{for ip } GDL_c, GDL_a \ (0.5 < \varepsilon < 0.8); \\ 2 \times 10^4\, \varepsilon^2 - 3.4 \times 10^4\, \varepsilon + 1.4 \times 10^4 & \text{for tp } GDL_c, GDL_a \ (0.5 < \varepsilon < 0.8); \\ 150 & \text{for } CL_c, CL_a. \end{cases} \tag{7.25}$$
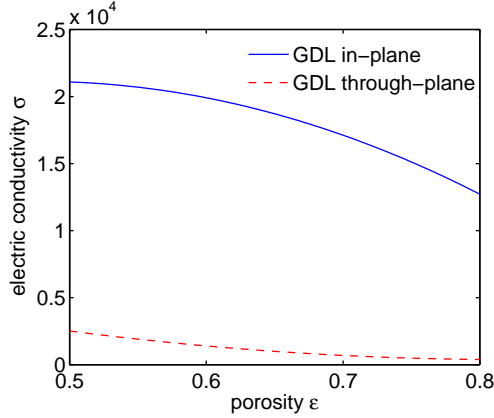
Figure 7.3: In-plane and through-plane electric conductivity of TGP-H-060 with 20% PTFE as a function of porosity. Second order polynomial fit to experimental data.

The fitted polynomials for GDL in-plane and through-plane directions are plotted in Fig. 7.3. The isotropic effective conductivity of the catalyst layer is assumed compression-independent and resulted from the catalyst pore scale model in Chap. 6.

7.4.5 Membrane Properties

The membrane properties are important to accurately describe the water uptake and transport (cf. Eq. (7.16)). They are depicted in Fig. 7.4. The distribution of water in the membrane is essential for the ionic conductivity ι (cf. Eq. (7.4)). It is a strong function of humidification λ and temperature T and has been implemented according to [131]:

$$\iota = 100 \left(0.005139\,\lambda - 0.00326\right) \exp\left(1268\left(\frac{1}{303} - \frac{1}{T}\right)\right) \tag{7.26}$$

This expression is valid for the non-porous membrane. For the porous CL's an effective ionic conductivity was calculated by multiplying Eq. (7.26) with the effective relative ionic conductivity resulting from the catalyst pore scale model in Chap. 6.

The absorption and desorption of water is driven by the difference $\lambda - \lambda_0$. The water uptake isotherm taken from Springer [131] defines the equilibrium membrane water content λ_0 at a given water activity $a = p_{H_2O}/p_{\text{sat}}$:

$$\lambda_0 = \begin{cases} 0.043 + 17.81\,a - 39.85\,a^2 + 36\,a^3 & \text{if}(0 < a < 1); \\ 14 + 1.4\,(a - 1) & \text{if}(1 < a < 3); \end{cases} \tag{7.27}$$

The membrane water transport at low current densities is dominated by diffusion which is a function of membrane water content λ. The expression for the membrane
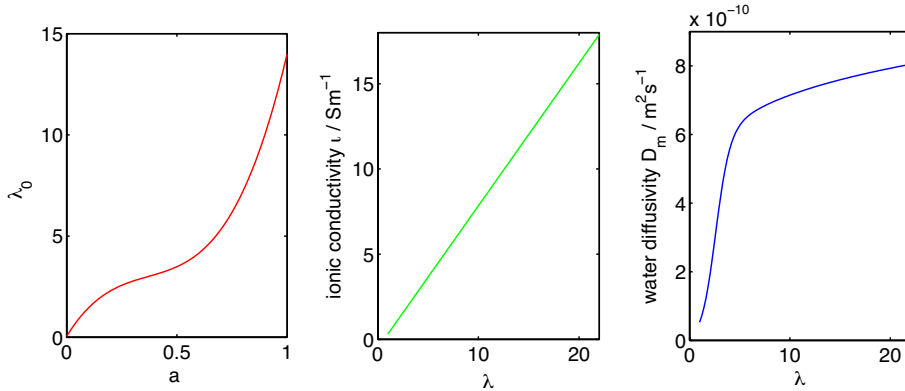
Figure 7.4: Left: membrane water uptake isotherm [131]. The equilibrium membrane water content λ_0 is defined as a function of water activity a [131]. **Center**: membrane ionic conductivity ι as a function of λ. **Right**: membrane water diffusivity D_m defined as a function of λ [174, 175].

water diffusion coefficient D_m as a function of λ has been taken from Kulikovsky [174] and Van Bussel et al. [175]:

$$D_m = 4.1 \times 10^{-10} \left(\frac{\lambda}{25}\right)^{0.15} \left(1 + \tanh\left(\frac{\lambda - 2.5}{1.4}\right)\right) \tag{7.28}$$

Again the membrane diffusion coefficient for the CL's has to be corrected with the ionomer structural parameter taken from the catalyst pore scale model. At high current densities the electroosmotic drag can be significant. The electroosmotic drag coefficient n gives the number of water molecules dragged per proton. According to Zawodzinski et al. [176] n is 1 for $\lambda > 1$. At lower humidification the drag was assumed to be zero.

7.4.6 Kinetic Properties

The Butler Volmer equations (Eq. 7.2) used to describe the kinetics of the ORR and HOR require the exact knowledge of the exchange current densities $j_{orr,0}$, $j_{hor,0}$ and symmetry factors α_c, α_a. The parameters for the HOR were taken from [12]. As the ORR is slower and the overpotential significant, the kinetic parameters were fitted to experimental data. For this the current voltage curve of the micro-cell in the center of the rib at fully humidified oxygen operation was used. The overpotential was corrected with the measured membrane resistance of 70 mΩcm^2 to extend the fitting range up to 5000 Am^{-2}. The fitted Tafel line is shown in Fig. 7.5. It is comparable to exchange current density measured by Gasteiger et al. [16] for similar Pt-loadings. Note that the horizontal axis is the natural logarithm of the current density. The geo-
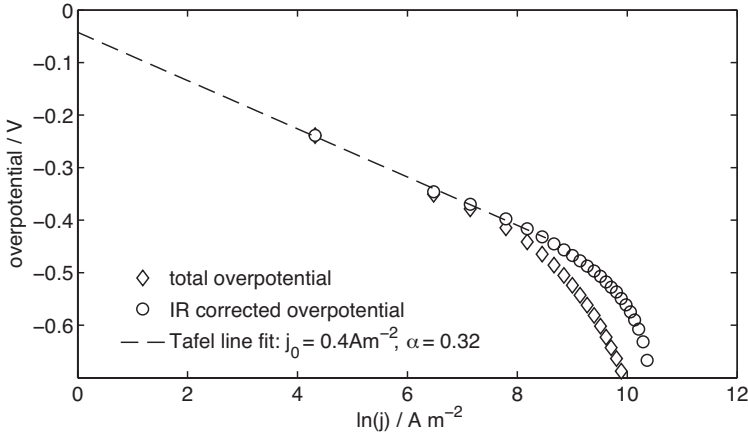
Figure 7.5: Tafel line fit of the geometric exchange current density and symmetry factor for the ORR. The experimental data was measured with the micro-cell in the center of the channel under fully humidified oxygen operation. For the IR-correction a membrane resistance of 70 mΩcm^2 was used [54]. Note that the horizontal axis is plotted in a natural logarithmic scale.

metric exchange current density $j_{\mathrm{orr},0} = 0.4$ Am^{-2} was transformed into a microscopic exchange current density $\tilde{j}_{\mathrm{orr},0}$ for use in Eq. (7.2):

$$\tilde{j}_{\mathrm{orr},0} = \frac{j_{\mathrm{orr},0}}{A_c \, d^{CL_c}} \tag{7.29}$$

7.4.7 Mechanical Properties

In order to determine the full elasticity matrix $\underline{D}_o$ of the GDL, Young's modulus E_x and E_y, shear modulus G_{xy} and Poisson's ratio v_{xy} are required. The stress-strain curves in y-direction were measured in the thesis of M. Reum [15]. A fifth order polynomial has been fitted to the experimental stress-strain curve and derived to obtain E_y as a function of the y-strain v_y:

$$E_y = 5 \cdot 1.24 \text{ x } 10^9 \, v_y^4 + 4 \cdot 1.1 \text{ x } 10^9 \, v_y^3 + 3 \cdot 3.7 \text{ x } 10^8 \, v_y^2 + 2 \cdot 1.4 \text{ x } 10^7 \, v_y + 5.7 \text{ x } 10^6 \tag{7.30}$$

Young's modulus in x-direction was assumed an order of magnitude higher due to the in-plane orientation of the carbon fibers. However, the porosity distribution did not change significantly by accounting for the orthotropy. Both the stress-strain measurement as well as the fitted curves are shown in Fig 7.6.
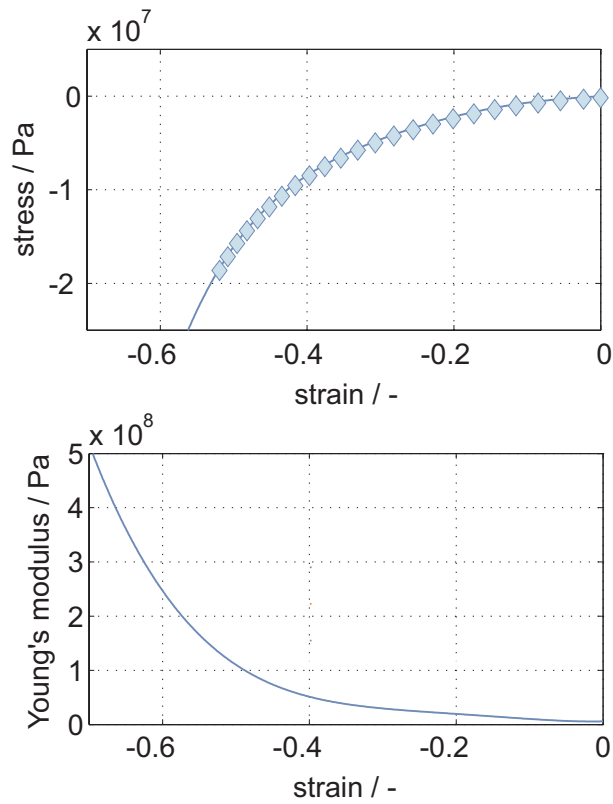
Figure 7.6: Top: measured stress-strain curve of TGP-H-060 with fifth order polynomial fit. The compressive stress is negative. **Bottom**: Young's modulus as a function of compressive strain (derivative of fitted polynomial).

symbol	description [unit]	value	unit	source
T	homogenous temperature	343	$^\circ K$	
p	homogenous pressure	1.5×10^{-5}	Pa	
v_{rib}	rib y-displacement	80×10^{-6}	m	
d_0^{GDL}	uncompressed GDL thickness	200×10^{-6}	m	meas.
d^{CL_c}	thickness CL_c	20×10^{-6}	m	meas.
d^{CL_a}	thickness CL_a	10×10^{-6}	m	meas.
ε_0^{GDL}	uncompressed GDL porosity	0.79		meas.
$D_{O_2 N_2}$	binary diffusivity of O_2 and N_2	1.8×10^{-5}	$m^2 s^{-1}$	
$D_{O_2 H_2 O}$	binary diffusivity of O_2 and H_2O	2.36×10^{-5}	$m^2 s^{-1}$	
$D_{N_2 H_2 O}$	binary diffusivity of H_2O and N_2	2.46×10^{-5}	$m^2 s^{-1}$	
$D_{H_2 H_2 O}$	binary diffusivity of H_2 and H_2O	1.2×10^{-4}	$m^2 s^{-1}$	
$D_{H_2, Kn}$	Knudsen diffusivity of H_2 in CL	3.8×10^{-5}	$m^2 s^{-1}$	
$D_{O_2, Kn}$	Knudsen diffusivity of O_2 in CL	9.5×10^{-6}	$m^2 s^{-1}$	
$D_{N_2, Kn}$	Knudsen diffusivity of N_2 in CL	1×10^{-5}	$m^2 s^{-1}$	
$D_{H_2 O, Kn}$	Knudsen diffusivity of H_2O in CL	1.3×10^{-5}	$m^2 s^{-1}$	
$m_{\mathrm{GDL,ip}}$	saturation exponent for in-plane GDL	2		[66]
$m_{\mathrm{GDL,tp}}$	saturation exponent for through-plane GDL	4		[66]
m_{CL}	saturation exponent for CL	33		fit
K_{tp}^{GDL}	GDL through-plane absolute permeability	2×10^{-12}	m^2	meas.
K_{ip}^{GDL}	GDL in-plane absolute permeability	5×10^{-12}	m^2	meas.
K^{CL}	CL isotropic absolute permeability	4×10^{-14}	m^2	meas.
θ^{GDL}	water-solid contact angle in GDL	110	deg	[142]
θ^{CL}	water-solid contact angle in CL	80	deg	[142]
ξ	water surface tension	0.068	$N m^{-1}$	
p_{sat}	water saturation pressure at 70 $^\circ C$	34058	Pa	
σ_C	electric conductivity of carbon	30000	$S m^{-1}$	
$\sigma_{\mathrm{eff}}^{CL} / \sigma_C$	effective relative electric conductivity of CL	0.005		CPSM
$D_{\mathrm{eff}}^{CL} / D$	effective relative diffusivity of CL	0.13		CPSM
$\iota_{\mathrm{eff}}^{CL} / \iota$	effective relative ionic conductivity of CL	0.27		CPSM
n_{d}	electroosmotic drag coefficient	1		[176]
$c_{SO_3^-}$	membrane fixed charge site concentration	1800	$mol\, m^{-3}$	[142]
$\tilde{j}_{\mathrm{hor},0}$	microscopic exchange current density HOR	100	$A\, m^{-2}$	[12]
$\tilde{j}_{\mathrm{orr},0}$	microscopic exchange current density ORR	7.11×10^{-4}	$A\, m^{-2}$	fit
α_{a}	symmetry factor HOR	0.5		[12]
α_{c}	symmetry factor ORR	0.32		fit
A_{a}	active area per volume of anode CL	$A_c / 2$	$m^2\, m^{-3}$	CPSM
A_{c}	active area per volume of cathode CL	2.8×10^7	$m^2\, m^{-3}$	CPSM
E_0	reversible cell voltage at standard conditions	1.229	V	
$c_{O_2,\mathrm{ref}}$	reference oxygen concentration	51.8189	$mol\, m^{-3}$	
$c_{H_2,\mathrm{ref}}$	reference hydrogen concentration	51.8189	$mol\, m^{-3}$	

h_a	membrane-water absorption rate constant	$10^{-5}/9$	$m\,s^{-1}$	[142, 172]
h_d	membrane-water desorption rate constant	$10^{-5}/3$	$m\,s^{-1}$	[142, 172]
h_e	evaporation rate constant	100	$Pa^{-1}\,s^{-1}$	[177]
h_c	condensation rate constant	1×10^{-3}	s^{-1}	[177]
v_{xy}^{GDL}	GDL Poisson's ratio	0.3		est.

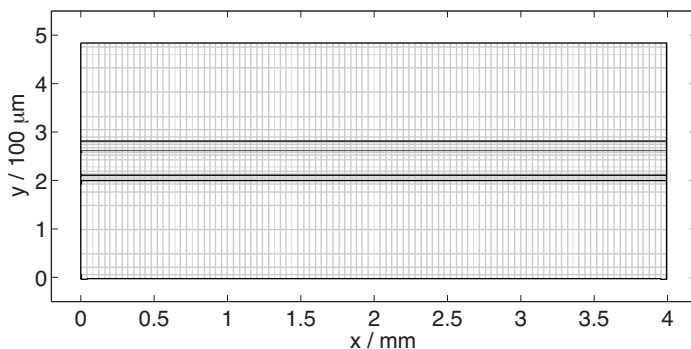**Table 7.2:** Model parameters with references.

Figure 7.7: Meshed modeling domain with 3200 quadrilateral elements. Note that the geometry is not to scale. The real aspect ratio is around 8

7.5 Solution Algorithm

The set of differential equations has been solved using COMSOL Multiphysics 3.5, a finite element software that emerged from MATLAB. It is especially suited for the coupling of different physics and therefore widely used in PEFC modeling. For the discretization of the rectangular modeling domain a quadrilateral mesh shown in Fig. 7.7 was used with refinements around the catalyst layers where the largest gradients were expected. Quadratic finite element types were selected for the interpolation between the nodes.

The system becomes highly non-linear at high current densities. With the parametric solver the cell voltage U was decreased in 21 steps from 1.2 V to 0.15 V improving the convergence significantly. A single parameter set was solved using the direct UMFPACK solver by T.A. Davis (http://www.cise.ufl.edu/research/sparse/umfpack). The number of non-linear iterations has been limited to 100. As convergence criterion for the non-linear solver a relative tolerance of 10^{-6} has been used. The momentum transport is coupled unidirectional with the species and electron transport in the GDL's. Therefore it was solved prior to the other equations and stored as initial conditions. The solution time for the 21 parameter sets is around 100 minutes on a 3.2 GHz Intel Pentium 4 computer with 2 GB RAM.

The mesh density was increased until the solution of the problem became independent from the grid. This independency is shown in Fig. 7.8 where the relative error of the solution as a function of current density is plotted for increasing number of elements. The relative error of the solution was defined as the difference of the oxygen molar flux at Ω_2 and the electric current at Ω_3 divided by $4F$. The accuracy
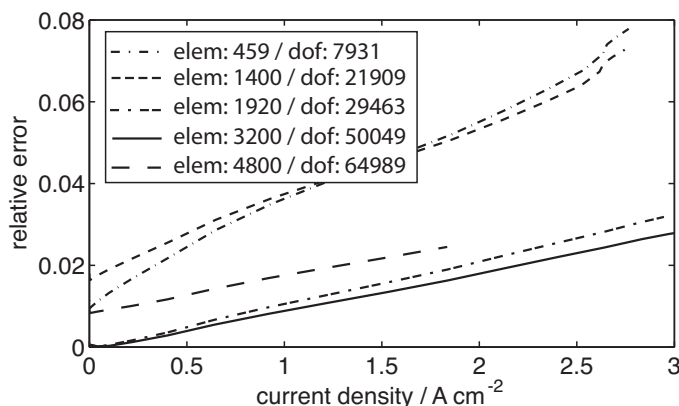
Figure 7.8: Relative overall error as a function of current density for different discretizations. elem: number of elements. dof: degree of freedom.

is only slightly improved between 1920 and 3200 elements. With 4800 elements the error even increased due to a reduced mesh quality.

7.6 1D Model Results

The different overpotentials discussed in Sec. 2.3 are a function of current density. The total overpotential is defined as the cell voltage U minus the equilibrium cell potential E and therefore generally negative. The forward direction of the reaction in Eq. (2.3) is from right to left and in Eq. (2.8) from left to right. Consequently the charge transfer overpotential on the anode has the opposite sign as on the cathode. Fig. 7.9 shows the resulting overpotential distributions of the 1D model for fully humidified oxygen operation. At low current densities the charge transfer overpotential of the ORR is increasing logarithmic and dominates all other losses. As the implicit Butler Volmer equation (Eq. (2.22)) can not be directly solved, the Tafel approximation (Eq. (2.24)) was used for the ORR and the linear approximation (Eq. (2.23)) for the HOR during postprocessing.

The ohmic overpotential increases linearly with current density as the membrane is fully humidified and has a constant conductivity. At high current densities the ohmic losses increase more than linearly due to anode dry out by electro-osmotic drag. This effect is also visible using current pulse techniques [178] and is more pronounced for thicker membranes. The HOR charge transfer overpotential is relatively small but with around 100 mV at 4 Acm^{-2} not negligible. A concentration overpotential does actually not exist. The effect of mass transport limitation is a reduced concentration
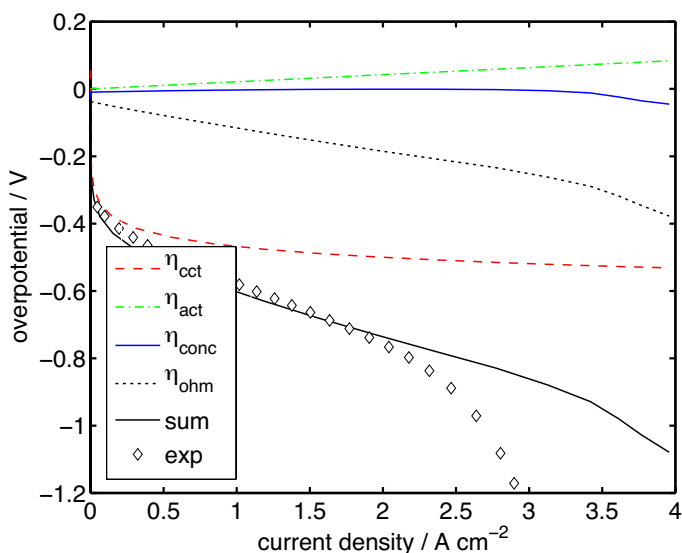
Figure 7.9: Overpotentials as a function of current density calculated with the 1D model for fully humidified oxygen and comparison with experimental data [53]. The overpotentials are negative by convention (except η_{act}).

at the catalyst surface. This in turn induces a higher charge transfer overpotential. In order to separate the mass transport from the charge transfer, the difference between the concentration dependent and independent charge transfer overpotential was calculated. There is a small increase of concentration overpotential above 3 Acm^{-2} due to catalyst layer flooding. This increase will become more pronounced with the channel-rib geometry in the 2D model and with reduced partial pressure in the channels. The Nernst overpotential defined as the equilibrium cell potential E minus the standard state cell potential E_0 is negligible and not further accounted for in the 2D model. In Fig. 7.9 the comparison with experimental data shows a good agreement up to 2 Acm^{-2} but a significant underestimation of presumably mass transport losses above this current density.

The through-plane field distributions allow the localization of the loss mechanisms discussed above. In Fig. 7.10a) the potentials for positive charge transport are illustrated. The electric potential boundary condition at GDL_a-CH_a interface is $\phi = 0$ V. There is only a marginal electric potential drop within the GDL's due to an electric through-plane conductivity ($\sigma \sim 2000\ Sm^{-1}$) which is about 2 orders of magnitude higher compared to the membrane ionic conductivity ($\iota \sim 14\ Sm^{-1}$). The large potential jump in the CL_c is equal to the equilibrium cell potential E minus the cathode

charge transfer overpotential. With decreasing cell potential the ohmic loss mainly in the membrane becomes more pronounced. Note that the ionic potential profile χ is not linear due to inhomogeneous humidification and sink-source terms in the CL's.

Fig. 7.10b) shows the molar fractions of reactant and product gases. With increasing current the depletion of hydrogen and oxygen from channels to catalyst layers increases. Water vapor accumulation takes place at the CL_c whereas water vapor depletion due to electroosmotic drag is observed in the CL_a. Hence under symmetric humidification conditions the drag is stronger than the back diffusion and the net water flux is always towards the cathode. This could change with a more sophisticated membrane model that accounts for hydraulic transport of water. The anomalous jump of water and oxygen molar fraction in the CL_c from 0.4 V to 0.2 V is caused by the assumption of a threshold liquid saturation of around 10% where all reaction sites are covered by liquid water (cf. Sec. 7.4). Oxygen and water molar fraction on the cathode side and hydrogen and water molar fraction on the anode side do not sum up to 1. This is due to the presence of nitrogen, which dilutes and concentrates the mixture on the anode and cathode side to mimic the absolute pressure differences.

Fig. 7.10c) focuses on the ionomer and displays the local humidification change with increasing current. The vapor-equilibrated membrane water content λ_0 at 100% RH is 12 and can rise at supersaturated conditions up to 16.8 [131]. The product water increases the humidification of the cathode side up to 16.8 while the drag reduces the anode humidification with increasing current. The profiles of λ are almost linear due small changes in water diffusion coefficient between λ 10 and 16 (cf. Sec. 7.4).

Fig. 7.10d) illustrates the liquid water saturation profile of the CL_c and GDL_c. The saturation boundary condition at the GDL_c-CH_c interface is constant at 0.01. As the anode and cathode gases are fully humidified and the model is isothermal the water pressure exceeds the saturation pressure and condensation takes place even at small current densities. The large saturation of the CL also stems from its hydrophilic nature. As the absolute permeability of the CL is about 2 orders of magnitude smaller compared to the GDL, the liquid water transport is strongly hindered resulting in large saturation gradients. The convex profiles indicate that the liquid water fluxes as well as the transport properties are not constant. The capillary pressure in the GDL, which is a measure for the resistance of liquid water transport, increases with saturation. Consequently the gradient in the GDL is smaller close the CL with high saturations. The threshold saturation in the CL of about 10% is reached at a voltage of about 0.2 V resulting in a diffusion limitation of the reaction as visible in 7.10b). Although the 1D model calculates reasonable saturation profiles there is no consensus in literature about the correct two-phase model to apply. The use of Leverett functions, the assumption of a homogeneous contact angle, the constant saturation
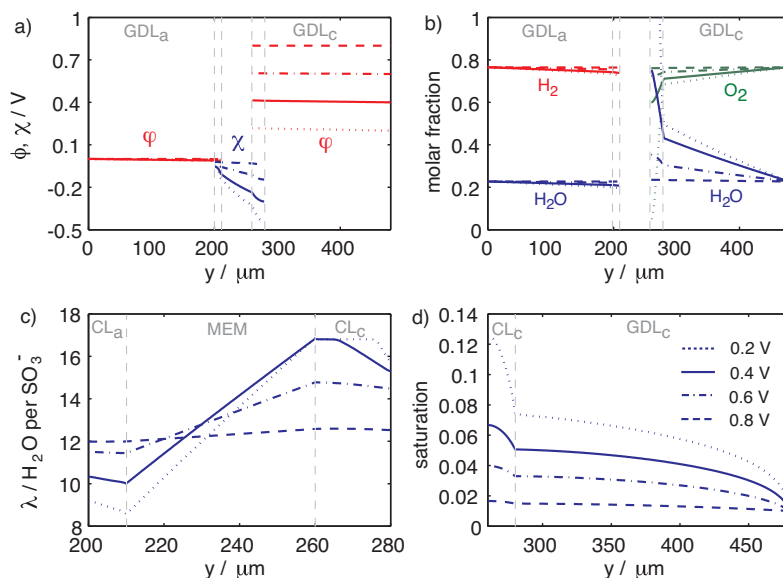
Figure 7.10: Through-plane field distributions calculated with 1D model for fully humidified oxygen at different cell potentials U (dashed: 0.8 V. dash-dotted: 0.6 V. solid: 0.4 V. dotted: 0.2 V). **a)** ionic χ (blue) and electric potential ϕ (red) for positive charge transport. **b)** H_2 (red), H_2O (blue) and O_2 (green) molar fractions. **c)** membrane water content λ. **d)** CL and GDL liquid water saturation.

boundary condition at the GDL_c-CH_c interface and the equal saturation condition at the GDL_c-CL_c interface are possible weak points of the implemented model.

7.7 2D Model Evolution

The set of equations described in Sec. 7.3 were tested step by step with the 1D model before adding to the 2D channel-rib model. The evolution of the 2D model and the convergence towards the experimental results are documented in Fig. 7.11. The seven model generations are labeled **A** to **G**. Table 7.3 shows an overview of the included physics and their estimated weight on the integral and local current generation. An empty field indicates inactive physics in the corresponding model generation. Note that the sequence of added physics is chronological and not according to the significance. The simulations in Sec. 7.7 were performed for fully humidified oxygen operation. The final set of parameters used in **G** are listed in Table 7.2.

Starting with a single-phase, isotropic, uncompressed model of the GDL and assuming a fully humdified membrane ($\iota = 14 \ Sm^{-1}$), the influence of different diffu-

	A	B	C	D	E	F	G
$D_{eff}/D = \epsilon^{1.5}$ [63]	-						
D_{eff}/D measured		++	++	++	++	++	++
Stefan Maxwell & Knudsen			+	+	+	+	+
anisotropy				++	++	++	++
compression					+	+	+
humidification						++	++
saturation							++

Table 7.3: Model evolution steps with estimated weight. ( ) inactive. (+) sensitive. (++) highly sensitive

sion physics was studied (**A-C**). Fick's first law (Eq. (3.14)) was used for **A** and **B**. The effective relative diffusivity D_{eff}/D in **A** was as high as 0.7 according to the widely used Bruggeman relation [63]. Furthermore an average isotropic GDL conductivity of 6000 Sm^{-1} was utilized. Due to the relatively low GDL diffusion resistance for oxygen under the ribs and the low GDL through-plane resistance for electrons under the channel the resulting current distribution was relatively homogeneous. At the edges of the ribs the pathways for oxygen from channel to rib and electrons from rib to channel are the shortest and therefore a small peak of electrochemical activity is observed. In **B** an isotropic value of D_{eff}/D = 0.4, measured by electrochemical diffusimetry [91] (TGP-H-060 with 20% PTFE), was employed. Consequently the current density under the rib dropped significantly due to higher gas transport resistance. However, the channel was not affected as the pathway for oxygen to the catalyst layer is about 5 times shorter here. In **C** multicomponent diffusion using the Stefan Maxwell equation (Eq. (7.5)) was considered. As the diffusivity of oxygen in water vapor (2.36 x 10^{-5} m^{2}s^{-1}) is about 30% higher compared to oxygen in nitrogen (1.8 x 10^{-5} m^{2}s^{-1}) the rib current is slightly increased due to water vapor accumulation under the ribs. The Knudsen number for oxygen in the CL$_c$ with a mean pore diameter of 30 nm is about 4.5. Therefore a reduced diffusivity has been used in the CL's according to the Knudsen equation (Eq. (3.20)). However, the in-plane current density distribution did not change considerably by accounting for Knudsen diffusion.

The next step was the introduction of direction and compression dependent material properties (**D,E**). For **D** the isotropic GDL conductivity of 6000 Sm^{-1} was changed to 14000 Sm^{-1} in in-plane direction and 400 Sm^{-1} in through-plane direction as measured by Freunberger et al. [53] (TGP-H-060 with 20% PTFE). This measure shifts the average current density by about -0.2 Acm^{-2} as all electrons have to pass in through-plane direction. The high conductivity in fiber direction flattens the peaks at the flowfield ribs. For the model generation **E** a rib displacement of 80 μm was intro-

duced resulting in a reduced porosity of around 70% under the rib. This reduced gas and enhanced electron transport as discusses in Chap. 5. Therefore the rib current is slightly decreasing while the channel current profits from the better through-plane conductivity.

With the introduction of membrane humidification effects in generation **F** the ohmic loss increased homogeneously as can be seen in the slope of the current voltage characteristic. The shape of the current density distribution did not change as both sides of the membrane are already fully humidified and the in-plane inhomogeneities are small. Finally the model generation **G** accounted for condensation of water at locations where the saturation pressure is exceeded. While the channel current is not affected, the electrochemical activity under the rib is reduced as the removal of gaseous and liquid water is strongly hindered. An increasing local saturation under the ribs reduces the effective diffusivity, decreases the relative gas permeability and increases the capillary pressure. All of them have a negative effect on the local performance. The saturation threshold of the CL was manually adjusted in order to fit the measured rib current. With the use of a more sophisticated agglomerate model for transport in the CL's this fitting parameter might be replaced by intrinsic parameters. However, this would require additional characterization of the CL.

Up to model generation **E** the overall cell performance at a cell voltage of 0.4 V (Fig. 7.11) did only change by about -0.3 Acm^{-2}. However, the qualitative channel-rib distribution at the GDL$_c$-CL$_c$ interface has changed significantly demonstrating the advantage of sub-millimeter resolved simulation of current density with measured transport parameters.

7.8 2D Model Results

Cell voltage, relative humidity and oxygen concentration have been varied using the model generation **G**. The comparison of a mechanistic channel-rib model with experimental data is unique and sheds light on the complex transport phenomena as well as on weak points of the present model.

The channel-rib current density distributions at the GDL$_c$-CL$_c$ interface shown in Fig. 7.11 are the result of 2D field distributions in the entire modeling domain. The most dominant 2D effects are the channel-rib deformation, the channel-rib oxygen depletion and the water accumulation as illustrated in Fig. 7.12a)-c). The porosity under the rib is reduced down to 0.65 with a rib displacement of $v_{rib} = 80$ μm. Due to the linear mechanical model used for momentum transport the GDL area close to the CL is almost uncompressed. This is not coherent with compressed tomography images of dry GDL's where the entire cross section is homogeneously deformed (cf.
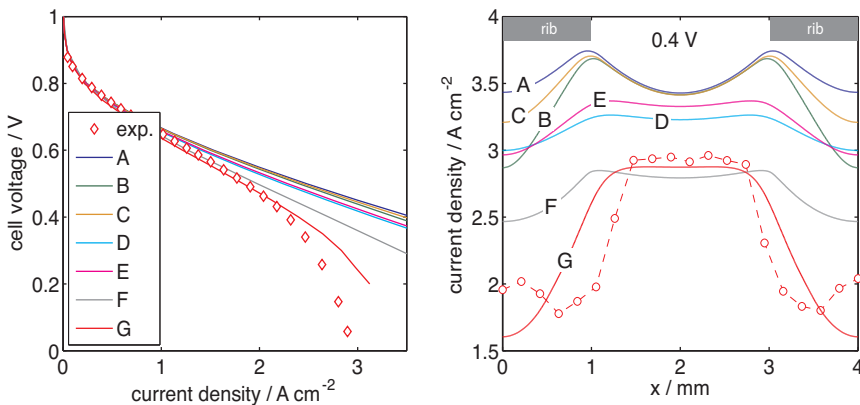
Figure 7.11: Change of current voltage characteristic **(left)** and channel-rib current density distribution **(right)** with advancing model evolution and comparison with experimental data [53] for fully humidified oxygen. The current density distribution **(right)** is probed at the GDL_c-CL_c interface.

Sec. 5.1).

Fig. 7.12b) shows that the oxygen depletion under the ribs within the GDL is not critical at 0.4 V. The gradients mainly point in in-plane direction with almost no depletion in through-plane direction under the channel. As a consequence the highest oxygen flux is observed in in-plane direction at the rib edges. In Fig. 7.12c) the water flux and saturation distribution is illustrated. Similar to the oxygen distribution the gradients for liquid water from rib to channel (in-plane) are higher than from CL to channel (through-plane). A comparison with the through-plane neutron radiogram shown in Fig. 7.13 confirms the qualitative distribution of liquid water over channel and rib. A quantitative comparison fails as the GDL material used by Pierre Boillat [179] is a carbon cloth with MPL, which has significantly different transport properties compared to the carbon paper used for the simulation. However, an interesting feature is observed in the channel of the neutron radiogram. Liquid water sticks to the surface and reduces the effective cross section of the channel.

7.8.1 Wet Oxygen Operation

In Fig. 7.14 the current voltage characteristics and current density distributions for fully humdified oxygen are compared with experimental data [53]. Note that the red curves and markers are the same as in Fig 7.11. Additionally the current voltage characteristic in the center of the rib and channel are shown. Both experiment and simulation show smaller limiting current densities under the rib as compared to the channel. The absolute values of the limiting currents are higher in the simulation
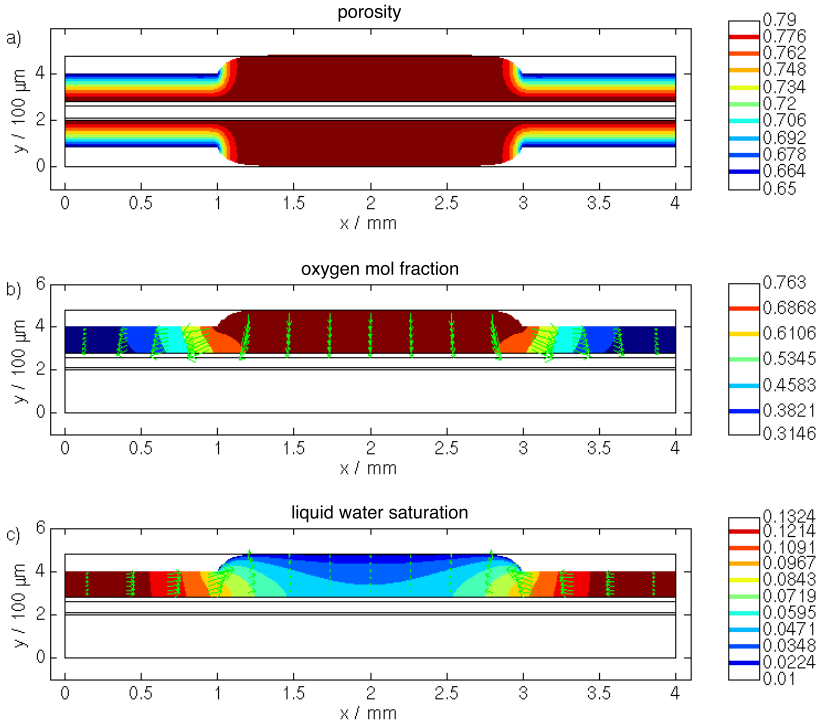
Figure 7.12: 2D field distributions in x-direction (in-plane) and y-direction (through-plane). The deformation of the GDL and the edges of the domains are visible. **a)** porosity distribution in GDL_c and GDL_a for a rib displacement of $v_{rib} = 80\ \mu m$. **b)** oxygen molar fraction and flux in GDL_c for fully humidified oxygen at 0.4 V (2.5 Acm^{-2}). **c)** liquid water saturation and flux in GDL_c for fully humidified oxygen at 0.4 V (2.5 Acm^{-2}).
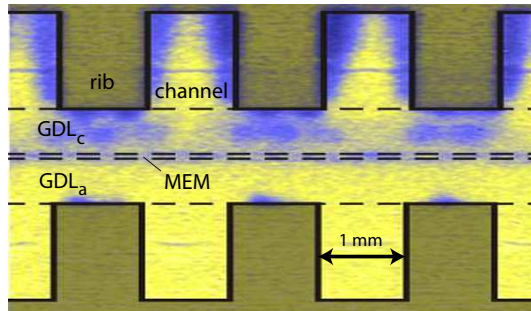

Figure 7.13: Through-plane neutron radiogram of a carbon cloth with MPL showing three channel-rib repetitive units. Blue corresponds to 25% and yellow to 0% liquid water saturation. j = 2.5 Acm^{-2}, 100% oxygen, $RH_a = RH_c = 90\%$ [179].
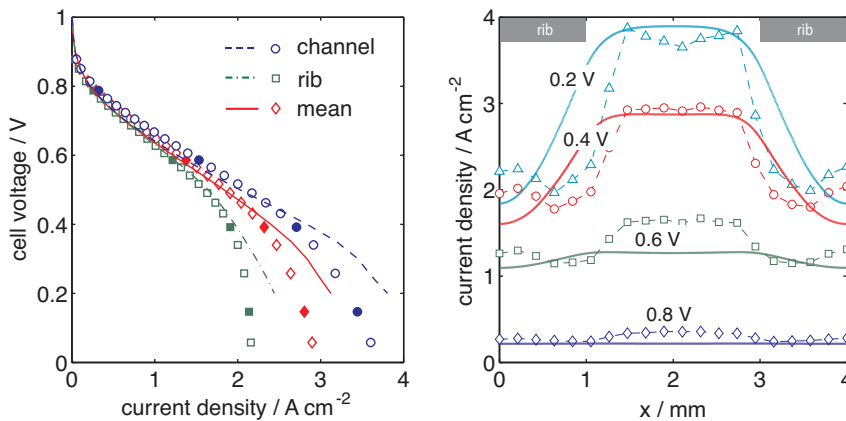
Figure 7.14: Experimental and simulated current voltage characteristics **(left)** and channel-rib current density distribution **(right)** for different cell voltages for pure oxygen and 100% relative humidity operation. blue diamond: 0.8 V. green square: 0.6 V. red circle: 0.4 V. cyan triangle: 0.2 V.

than in the experiments. This points to an insufficient water transport model or an underestimation of gas transport resistances.

By taking a closer look on the current density distribution in Fig. 7.14 right, this discrepancy can be localized at the edges of the ribs (1 mm, 3 mm). The channel-center and rib-center current at 0.4 V and 0.2 V agree but the model is not able to reproduce the experimental values in between. An explanation could be a non-elastic deformation around the rib edge where compressive stresses up to 25 MPa are possible. Another reason for the higher simulated current may be the ignored compression-dependencies of CL and MEM properties. Furthermore the liquid film on the channel surface, which is visible in the neutron radiogram of Fig. 7.13, could prevent gas from entering the GDL at the rib edge and result in lower measured current densities.

Another discrepancy was observed at 0.8 V and 0.6 V under the channel. A distinct current peak was measured while the simulation calculates a relatively flat channel-rib distribution. At 0.8 V and 0.6 V for pure oxygen operation mass transport effects are negligible. Therefore the channel-peak must stem from a humidification effect which reduces the ohmic overpotential. A difference between model and experiment is the MPL, which is missing in the model so far. The MPL avoids liquid water to enter the GDL, which results in a liquid water equilibrated membrane with a higher conductivity as compared to a vapor equilibrated membrane.

The current density distribution over channel and rib is the result of a multitude of effects. Fig. 7.15 distinguishes gas transport, liquid water transport and humidification effects at different cell voltages. In Fig. 7.15a) the molar fraction of oxygen

and water vapor at the GDL_c-CL_c interface is shown. They do not sum up to unity due to the presence of nitrogen which was necessary to mimic the absolute pressure difference (cf. Sec. 7.3). The long diffusion pathways under the ribs results in an accumulation of water vapor and an undersupply of oxygen. In Fig. 7.15b) the membrane water content at MEM center is illustrated. Although the reactant gases were already fully humdified the water uptake of the MEM in contact with liquid water can still increase. Therefore the rib humidification of the MEM initially increases (0.8 - 0.6 V) due to contact with liquid water. At high current densities (0.4 - 0.2 V) the water drag dominates the back diffusion and the rib humidification decreases due to an undersupply of water from the anode. However, the λ-differences over channel and rib are relatively small and do not dominate the current density distribution profile shown in Fig. 7.14.

In Fig. 7.15c) the saturation profile at the GDL_c-CL_c interface is plotted. The saturation boundary condition at the CH_c-GDL_c interface is 0.01 similar to the 1D model. The maximum saturation under the rib increases up to 0.15 at 0.2 V (3 Acm^{-2}) which is comparable to neutron imaging results [179]. In Fig. 7.15d) the three main overpotential profiles are shown. Note that the sum of all overpotentials must match to $U - E$. The ohmic and charge transfer overpotentials are proportional to the current density and therefore always show a maximum under the channel for fully humidified conditions. Hence the channel current at fully humdified oxygen operation is mainly limited by charge transport in the membrane. The ohmic loss is additionally intensified by the anode dry-out due to the drag effect. The concentration overpotential is always negligible under the channel for pure oxygen operation while it can rise up to 0.2 V under the rib.

Fig. 7.16 focuses on the thickness of the CL_c. It shows how the local electrochemical activity changes with cell voltage and channel-rib location. The volumetric current density according to the Butler Volmer Eq. (2.22) is plotted over the CL_c thickness for the center of the channel (top) and rib (bottom). From 0.8 V to 0.4 V the limiting transport process under the channel is the proton conduction. Therefore the highest electrochemical activity is always close the CL_c-MEM interface (260 µm). At 0.2 V the gas diffusion resistance becomes limiting even under the channel and the maximum of the volumetric current density shifts towards the CL_c-GDL_c interface (280 µm).

The current production within the CL_c under the rib is relatively homogeneous and similar to the channel down to a cell voltage of 0.8 V. Below 0.8 V the undersupply of oxygen under the rib due to elongated diffusion pathways and pore flooding becomes dominating and all the conversion takes place within 5 µm from the GDL_c interface. On the other hand the conversion under the channel is homogeneously distributed over the CL thickness. Only at 0.2 V the maximum shifts towards the
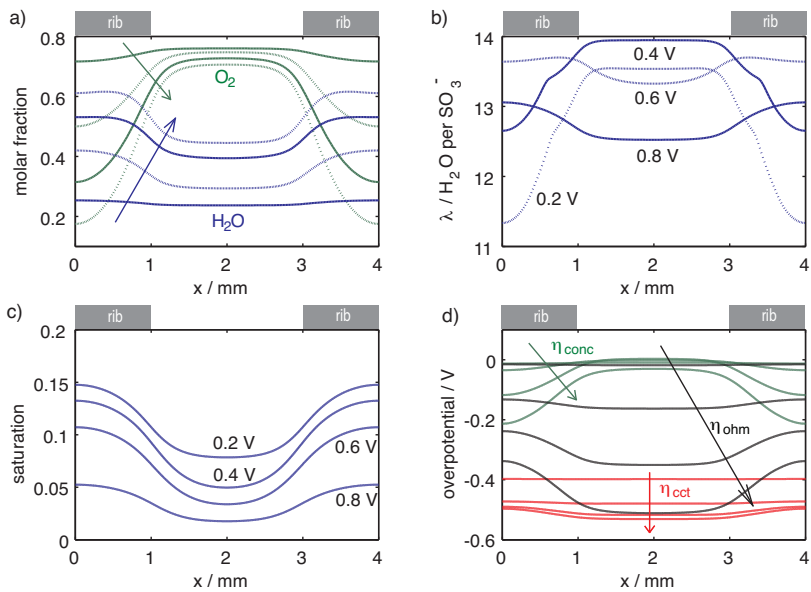
Figure 7.15: Simulated channel-rib field distributions for different cell voltages for pure oxygen and 100% relative humidity operation. The arrows point from 0.8 V to 0.2 V. **a)** H_2O (blue) and O_2 (green) molar fractions at GDL_c-CL_c interface. **b)** membrane water content λ at MEM center. **c)** liquid water saturation at GDL_c-CL_c interface. **d)** concentration (green), ohmic (black) and charge transfer (red) overpotentials at GDL_c-CL_c interface.

Figure 7.16: Through-plane current density distribution in the cathode catalyst layer for pure oxygen and 100% relative humidity operation under channel **(top)** and rib **(bottom)**. blue 0.8 V, green 0.6 V, red 0.4 V, cyan 0.2 V.

GDL interface due to limited oxygen supply. Therefore the composition of the over-potential plotted at the GDL_c interface in Fig. 7.15d) is rather underestimating the contribution of the concentration overpotential as the mass transport limitation in the CL are attributed to ohmic overpotentials.

7.8.2 Wet Air Operation

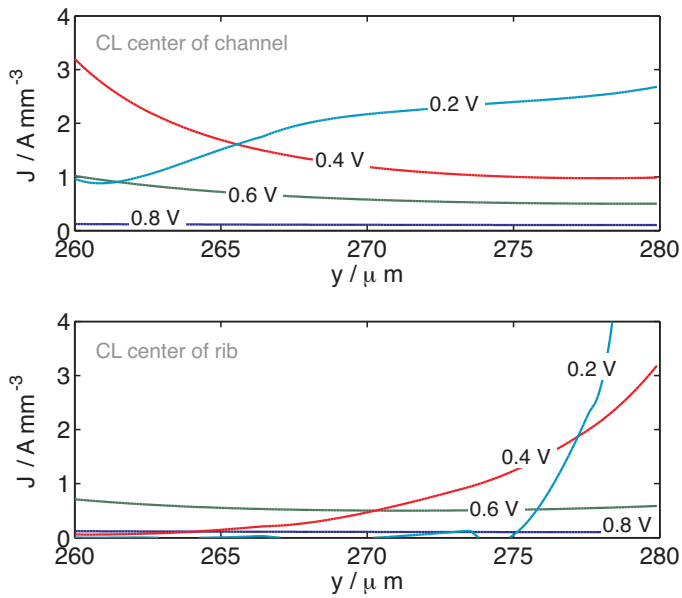The operation with fully humidified air instead of oxygen reduces the partial pressure in the gas channel by a factor of about 5. Consequently if diffusion would be the only limiting process, the theoretical limiting current at 0 V should be 5 times smaller as compared to pure oxygen. Fig. 7.17 compares the simulated current voltage curves and current density distributions with experimental data [53]. The experimental limiting current density is only about a factor of 3 smaller compared to the experiment with fully humidified oxygen. The model prediction below 0.5 Acm^{-2} is reasonable. The strong divergence of channel and rib current above 0.5 Acm^{-2} is reproduced only qualitatively by the model. The mean limiting current of the model is about 1 Acm^{-2} larger as compared to the experiment. The limiting current under the channel even disagrees by about 2 Acm^{-2}. This strong discrepancy can only be explained by mass transport limitations that were not considered in the model so far such as oxygen diffusion through ionomer or water films in the CL_c. In order to account for these limiting effects an agglomerate model [133] for the CL would have to be implemented. A closer look on the channel-rib current density distribution in Fig. 7.17 right, shows that experiment and model agree qualitatively. The maximal current is always under the channel. In both experiment and model the rib current is not increasing from 0.65 V to 0.45 V. The rib edge is again the position where the discrepancy is the largest.

As the current profiles agree qualitatively the other channel-rib field distributions shown in Fig. 7.18a)-d) are assumed to have a realistic shape. The distributions for 0.2 V are not shown as the discrepancy between experiment and simulation is too large. Oxygen at the GDL_c-CL_c interface in Fig. 7.18a) is completely depleted under the rib at 0.4 V due to the low oxygen partial pressure in the channel. The vapor molar fraction is highest at the rib edge due to a maximum of water production close to the channel and the coverage effect of the rib, which impedes the water removal. The membrane water content distribution in the MEM center in Fig. 7.18b) is similar to the operation with fully humidified oxygen and does not control the current density distribution. At high current and consequently high drag the rib tends to dry out whereas at low current the mean membrane humidification increases due to product water. The maximum at the rib edges at 0.4 V originates from the trade-off between drag and water loss to the channel. Due to the smaller current densities less
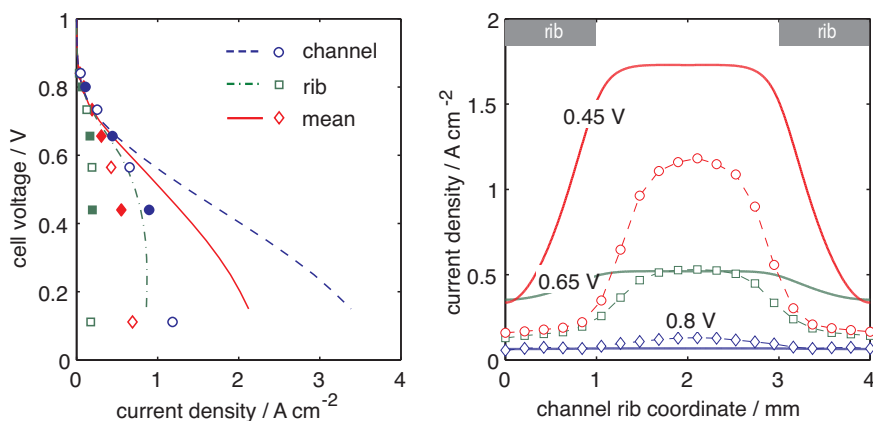
Figure 7.17: Experimental and simulated current voltage characteristics **(left)** and channel-rib current density distribution **(right)** for different cell voltages for air and 100% relative humidity operation. blue diamond: 0.8 V. green square: 0.65 V. red circle: 0.45 V.

water is produced, which results in a slightly lower membrane humidification and GDL saturation compared to oxygen operation. However, the rib saturation shown in Fig. 7.18c) can rise up to 0.09 and amplify the already high diffusion limitation under the rib. In Fig. 7.18d) the different losses are discriminated. Again the charge transfer at the cathode and the ohmic overpotentials are proportional to the current distribution. The ohmic overpotential under the rib is smaller compared to oxygen operation due to the lower current and drag. On the other hand the concentration overpotential is significant under the channel and even dominating under the rib. Therefore the operation with fully humidified air is clearly limited by mass transport under the rib.

7.8.3 Dry Oxygen Operation

Experiments with pure oxygen at 40% relative humidity resulted in the highest limiting current densities as the driving force for diffusion is maximal and the flooding of CL and GDL is reduced by the low channel water partial pressure. The comparison with the simulated current voltage curves in Fig. 7.19 shows a significant disagreement over the entire current density range. The experimental current voltage curves of both channel and rib show a linear behavior between 0.5 and 2 Acm^{-2} indicating a well humidified membrane. The simulated performance of the rib is better than the channel up to 2.5 Acm^{-2} where the channel and rib curve intersect. This is due to reactant water loss to the dry channel resulting in a dry membrane and poor performance of the channel. The reactant water retention under the rib results in a
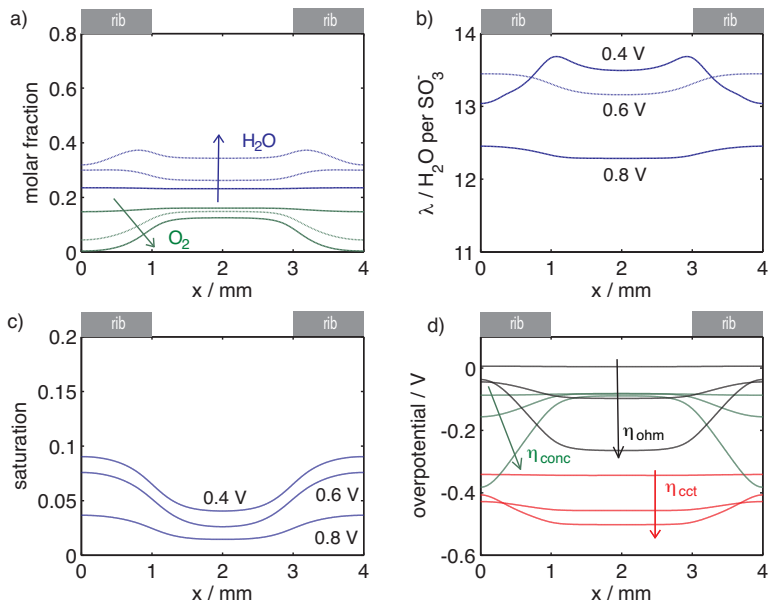
Figure 7.18: Simulated channel-rib field distributions for different cell voltages for air and 100% relative humidity operation. The arrows point from 0.8 V to 0.4 V. **a)** H_2O (blue) and O_2 (green) molar fractions at the GDL_c-CL_c interface. **b)** membrane water content λ at MEM center. **c)** liquid water saturation at GDL_c-CL_c interface. **d)** concentration (green), ohmic (black) and charge transfer (red) overpotentials at GDL_c-CL_c interface.
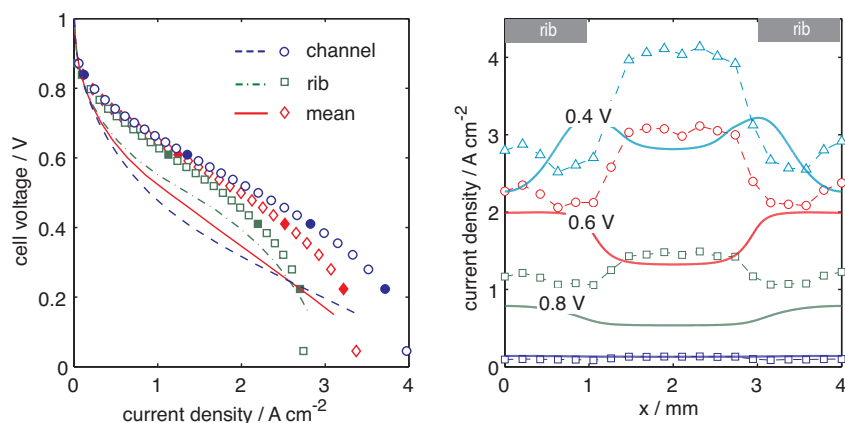
Figure 7.19: Experimental and simulated current voltage characteristics **(left)** and channel-rib current density distribution **(right)** for different cell voltages at oxygen and 40% relative humidity operation.

well-humidified membrane and a good performance of the rib. This behavior was not observed in the experiment. The experimental channel current density is always higher as can be seen on the right graph of Fig. 7.19. Hence the difference must stem from a better humidification in the experiment.

The model does not yet account for the MPL used in the experiments which could be an explanation. The MPL has a permeability two orders of magnitude smaller compared to the GDL. This mainly affects the convective and slightly the diffusive removal of water. However, condensation of liquid water does mainly take place at high current densities and therefore this discrepancy at low and medium current densities can hardly be explained by the missing MPL. Another possible reason for the lower membrane humidification could be the underestimation of membrane water absorption and overestimation of membrane water desorption. A non-isothermal model is not expected to close the gap as temperature influences both absorption and desorption. Due to the qualitative disagreement between experimental and simulated channel-rib currents the other 2D field distributions are not discussed as they do not elucidate the measurements.

7.9 Summary & Conclusions

A mechanistic model of the channel-rib scale has been developed and compared to experimental channel-rib current density distributions for the first time. The model accounts for transport of gases, liquid water, electrons and ions. The GDL and CL on the cathode and anode side as well as the membrane were discretized. A comparison

of the different model generations revealed the relevant physics and its influences on the integral as well as local performance. Diffusion, humidification and saturation effects can all significantly influence the channel-rib current density distribution. The foregoing in-depth characterization of GDL and CL was necessary for quantitative model predictions. Only 3 parameters were finally fitted to experimental data. The mechanistic model could be validated for operation with fully humidified oxygen for the complete range of current densities. Small discrepancies close to the rib edges were explained with deficiencies of the mechanical GDL and CL model. Although the implemented Leverett function for the capillary pressure is not considered as appropriate, the simulated saturation distribution is in agreement with neutron imaging experiments. In order to achieve an agreement of experimental and simulated limiting current densities the introduction of a threshold saturation was necessary above which diffusion in the CL is strongly impeded. Consequently mass transport in the CL under the rib is the limiting effect at high oxygen and high water concentrations. An agglomerate catalyst model would additionally account for diffusion through ionomer and water films and could therewith prove this finding. However, additional parameters with additional characterization tasks arise with the use of an agglomerate model. If the oxygen concentration is lowered to 21% the shortcoming of the actual catalyst layer model becomes even more apparent. The experimental and simulated limiting current densities disagree by more than 100%. However, the qualitative shape of the curves were similar and therefore the modeled physics were assumed to be correct but with the wrong parameterization. The model failed completely predicting low humidity operation with oxygen. The humidification of the membrane in the experiment was significantly higher, resulting in lower ohmic overpotentials. At high current densities the humidification discrepancy was explained with the missing MPL in the model while at low current densities the absorption and desorption rates were assumed to be incorrect.

The results of the channel-rib model clearly emphasize the need for sub-millimeter resolved studies and in-depth material characterization to localize and understand the losses. Possible weak points of the existing model are:

- volume averaging and continuum equations for GDL's

- macro-homogenous instead of agglomerate model for catalyst layer

- linear mechanical deformation of GDL

- absorption and desorption rates of membrane water

- missing hydraulic membrane water transport

- missing microporous layer (MPL)

- Leverett model with a homogenous contact angle for the capillary pressure

- constant saturation boundary condition at the GDL-channel interface

- equal saturation condition at the GDL-CL interface

- isothermal and isobaric conditions

8 Overall Conclusions & Outlook

The importance of the channel-rib scale is based on the close coupling of scales in PEFC. Significant charge and mass transport losses take place on the scale of a few millimeter perpendicular to the flow direction. These channel-rib losses govern the behavior of the cell and eventually of the entire stack. Channel-rib current density measurements revealed strong inhomogeneities of current densities and membrane resistances. This affirmed the importance of the millimeter scale but also generated new unclarities such as the exact distribution of the different overpotentials and liquid water saturation over channel and rib.

In order to shed light on the complex interplay of different transport phenomena and electrochemical reactions a numerical model was required. Throughout the thesis it could be confirmed that a numerical model is only as accurate as its parameterization. This asked for an in-depth characterization study of central channel-rib components: the gas diffusion layer and the catalyst layer. Thereby established and novel methods were applied. By using a soundly parameterized and validated model of the channel-rib scale, optimization towards higher and more homogeneous current densities will be straight forward.

In the following the two elementary questions of what has been learned within this thesis and what still has to be learned are addressed.

8.1 What has been learned?

Main Conclusion

If the output of this thesis would have to be sharpened to a main conclusion it would be that on the scale of flowfield channel and rib, every component and every dimension counts. In other words the transport properties of the materials have to be known exactly as a function of direction and mechanical compression in order to reproduce experimental results with a numerical model.

Diffusivity Method & Results

The first transport parameter considered of prime importance was the effective diffusivity of the gas diffusion layer (GDL). A new diffusimetry setup was developed

which is based on Electrochemical Impedance Spectroscopy (EIS) of electrolyte-soaked GDL's. The method makes use of the fact that transport of ions are limited by the same structural parameter as diffusion of gases through the pores. It provides a fast and accurate tool to study a critical transport parameter in PEFC. The developed method has been published in [90]. The effective diffusivity study revealed for the first time the anisotropy and compression dependency of GDL's in an experiment. It showed that established morphology models are oversimplified and generally exceed the measured diffusivity by a factor of 2. Furthermore the experiments found a strong sensitivity of type and amount of binder on the effective GDL diffusivity. The results of the effective diffusivity study have been published in [91].

Porosimetry Method & Results

Another important parameter of the GDL structure that has been measured in the framework of this thesis is the porosity. It is the ratio of void to total volume and therefore a measure for a conflictive requirement of GDL's: the ability to transport gases and electrons. Although widely established, porosimetry of GDL's turned out to be not straight forward. Some GDL's do not fulfill the incompressibility requirement for Mercury Intrusion Porosimetry (MIP), which asked for the alternative method of decane wetting porosimetry. Furthermore the assumption of circular pore geometries in GDL's appeared far out, which restricted the interpretation of pore size distributions.

Dry Tomography Method & Results

Only knowing the macroscopic properties of GDL's was not sufficient. The correlation of structural details with transport properties was regarded as a valuable step towards optimization. Therefore X-ray tomographic microscopy of the entire 3D structure has been performed at the TOMCAT beamline of the Swiss Light Source (SLS). In a first campaign images with a pixel resolution of 0.74 μm x 0.74 μm under different mechanical stresses were taken. This revealed the non-linear deformation of the fibrous structure and shed light on the differences between channel and compressed rib areas. Having the entire 3D structure in digital form opened up a new and relatively cheap characterization method: the computational volume averaging. Darcy's law for permeability, Fick's law for effective diffusivity and Ohm's law for effective conductivity have been solved on the binarized 3D structure. By using the high-resolution tomography images the typical structural simplification adherent to morphology models can be omitted. Experimental and computational characterization showed a good agreement. Therewith considerable confidence in the accur-

acy of the GDL properties was gained. Furthermore the validation of the computational approach is considered as an important building block for future structural optimization of GDL materials by virtual prototyping. The results of the comparison between experiment and simulation using X-ray tomographic microscopy are published in [180].

Wet Tomography Method & Results

A sound characterization of GDL transport properties for PEFC has to include the liquid water dependency as well. Within this thesis the resulting liquid water distribution has been studied. X-ray tomographic microscopy has been chosen due to the high spatial and temporal resolution. A simultaneous contrast within GDL's for water and carbon could be demonstrated with a pixel resolution of 0.74 µm x 0.74 µm for the first time. The condensation of water vapor at the catalyst layer was mimicked with a specially designed sample holder connected to a water column. At low pressures water is retained at the first dense layer which is presumably formed by PTFE impregnation. As soon as the breakthrough pressure is exceeded, water disperses into the remaining structure and eventually exits on the opposite site. The water discharge is typically at a single position for a sample diameter of about 2 mm. This limits the maximum saturation to values smaller than 60%. A step towards more realistic boundary conditions for the liquid water distribution has been done by using electrochemically produced water in an active cell with only 7 mm^2 active area. The feasibility of X-ray tomographic microscopy of entire active cells could be demonstrated with this experiment. The results of the water column and active cell experiments are published in [121]. X-ray tomographic microscopy has a high potential to become a standard liquid water and solid structure visualization technique for PEFC complementary to neutron imaging.

Catalyst Pore Scale Model

A second relevant component on the channel-rib scale is the catalyst layer (CL). Mass transport, charge transport and electrochemical reactions are coupled on the smallest length scale. The performance of the CL is a balancing act between limited ion, charge and electron transport. Due to its size experimental characterization of the CL for the desired channel rib model is complex. With the use of a numerical pore scale model, realized in Fortran, effective transport properties were calculated based on nanometer structural parameters. The main achievement of the catalyst pore scale model so far is the coupling of the different phases. In other words, for a good effective diffusivity electric conductivity has to be sacrificed.

Channel-Rib Model

Finally the insights gained by the material characterization were incorporated into a finite element model using COMSOL. The large characterization effort resulted in a mechanistic description of the channel-rib scale with only 3 fitting parameters: the exchange current density, the charge transfer coefficient and the flooding parameter of the catalyst layer. The experimental channel-rib current density distribution served as an indispensable database for the model validation. The model showed a good agreement for operation with fully humidified oxygen and allowed the quantification of saturation and overpotentials over channel and rib. However, the model can not be considered as fully validated so far as variation of oxygen concentration and gas humidity did not fully correlate with the experiments. If the oxygen concentration is lowered to 21% shortcomings of the actual catalyst layer model become apparent. The model failed completely predicting low humidity operation, always assuming no adjustments of the fitting parameters.

8.2 What has to be learned?

The ultimate goal of the thesis remains open: proposing better gas diffusion layers and channel-rib structures for lower inhomogeneities and higher power densities. However, an important step towards a numerical optimization tool has been done with the sound characterization of components and the final validation attempt. In the following a selection of future work directions is proposed.

Characterization

The already broad basis of experimentally determined material properties has to be extended to other parameters and components. Especially saturation dependent properties have not been measured so far. Instead literature values with limited confidence and applicability were used. Furthermore the influence of chemical and mechanical degradation on the transport properties of GDL's is unknown. Also the electrochemical diffusimetry method still has room for improvements. A critical factor is the full wetting of the sample with electrolyte. This becomes even more critical for pores smaller than a micrometer as present in microporous and catalyst layers. A possible solution could be a pressurized sample holder or an electrolyte with wetting properties. To study the saturation dependency of the effective diffusivity the electrochemical diffusimetry method is not employable. Instead a setup similar to a diffusion cell would be required with an additional apparatus to adjust a known amount of water in the GDL. Such a device could easily be adjusted for

relative permeability measurements.

Another saturation dependent material property is the capillary pressure function. It determines the transport and distribution of liquid water and is therefore of prime importance. The measurement principle has been demonstrated by the water column experiment at the TOMCAT beamline: increasing the air-water pressure difference while measuring the amount of water in the sample. Less time consuming would be the computational characterization of the saturation dependency based on tomography data. Water can be virtually intruded according to the Young-Laplace equation. However, a remaining uncertainty is the contact angle distribution within the 3D structure. X-ray tomographic microscopy is expected to elucidate this question in the future.

Visualization of Liquid Water

A complementary method to neutron imaging for visualization of liquid water in porous GDL's has been developed and will be advanced in the subsequent work of Jens Eller. The strength of X-ray tomographic microscopy is high spatial and temporal resolution with simultaneous contrast for water and carbon. Besides fundamental water-solid interactions in GDL and CL the method can be used to find appropriate water transport models, a shortcoming of many PEFC models.

On the fundamental level model materials with defined wetting properties should be envisaged. The reduction of complexity can provide a valuable data basis for the validation of water transport models and can help improving the experimental setup. Also on the fundamental level, the potential of highly resolved solid-liquid-gas interfaces for contact angle measurements has not been exploited. According to the TOMCAT beamline staff pixel resolutions of < 100 nm will spur further fundamental questions and eventually resolve the water distribution in the pores of the catalyst layer.

The next step of the *ex-situ* intrusion experiment towards more realistic boundary conditions would be the use of a saturated gas stream to induce condensation within the material rather than assuming a fully saturated CL interface. The challenge is a realistic temperature distribution which triggers condensation or evaporation. Not only realistic gradients but also realistic temperature levels should be approached in the future. In terms of material variation the wetting behavior of chemically and mechanically degraded samples could give new insights into the water management of cells at their end of life.

The ultimate goal of future *in-situ* active cell experiments is the correlation of material (PTFE, MPL) and operating parameters (temperature, current density, relative humidity) with the micrometer-scale liquid water distribution in GDL and CL. The

main discrepancy to face is the requirement for fast scans and high resolution. Fast scans are necessary to fulfill the immobility requirement of phases in an operating cell. However, for temporal resolution spatial resolution has to be sacrificed and structural information is lost. Intermediate steps to improve the quality of *in-situ* results include the use of low X-ray absorbing materials. For the electric contact graphite materials could be used. A reduced platinum loading of the catalyst layers could avoid blurring. In terms of cell design convective supply and removal of reactants and products would improve the boundary conditions towards reality.

Catalyst Pore Scale Model

The idea of the catalyst pore scale model is to couple the nanometer scale of a catalyst layer with its macroscopic representation. In the framework of this thesis volume averaged effective transport parameters defined by the nanometer structure were employed in a macroscopic finite element model. However, the potential of the developed mesoscopic platform is by far not exhausted. The Fortran code can be extended to an optimization tool for catalyst layers. The next step has to be the coupling of gas, electronic and ionic transport on the carbon sphere surface via Butler Volmer or Tafel kinetics. For this the gas dissolution and diffusion in the ionomer has to be implemented as well. In the long term transport of liquid water and the resulting pore flooding, ionomer dry-out and ionomer swelling has to be considered. Accounting for all these effects would allow to study limiting processes in the CL and eventually to optimize the platinum utilization.

Channel-Rib Model

The goal of the channel-rib model to reproduce experimental current density distributions over a wide range of operating conditions was only partially achieved. However, it has to be mentioned that this is a though demand for a mechanistic model with only 3 fitting parameters. Several model weak points were identified which have to be eliminated in the future. The main error causing the discrepancy at low humidity operation is expected in the membrane absorption and desorption behavior. Additional review of literature or even experiments are required to refine the absorption/desorption rates. The discrepancy at low reactant concentration was attributed to missing transport bottlenecks in the macro-homogenous description of the catalyst layer. It is known from literature that the best agreement with experimental limiting current densities can be found with an agglomerate model.

Next to membrane and catalyst model improvements, the water transport description in the GDL needs more attention. The use of Leverett functions with a homogen-

eous contact angle distribution was proved invalid. Also the boundary conditions used to solve the liquid water distributions have to be revised. A constant saturation of zero at the channel-GDL interface is equivalent to a perfect, instantaneous droplet removal. However, experiments have shown the buildup of droplets or films which disproves the zero saturation boundary condition. Heat transport has been neglected so far to limit the already high degree of coupling. However, temperature is affecting almost all the transport and reaction processes. Especially for a realistic saturation distribution heat transport is indispensable.

Finally if all these measure do not improve the consistency with experimental current density distribution the use of volume averaging with continuum equations has to be questioned for the GDL. The repetitive unit of a GDL may be larger than the channel-rib scale and the behavior is governed by local effects. In fact for the through plane direction of certain GDL's it could be shown that there is a highly porous layer in the center with two dense layers on both sides. Also the visualization of liquid water pathways has revealed local breakthrough effects which may be difficult to describe in an average manner.

Bibliography

[1] A. Schafer and D. G. Victor, "The future mobility of the world population," *Transportation Research Part A: Policy and Practice*, vol. 34, p. 171, 2000.

[2] "Key world energy statistics," 2008.

[3] G. G. Harding, "Electric vehicles in the next millennium," *Journal of Power Sources*, vol. 78, p. 193, 1999.

[4] S. Yoda and K. Ishihara, "The advent of battery-based societies and the global environment in the 21st century," *Journal of Power Sources*, vol. 81-82, p. 162, 1999.

[5] S. Eaves and J. Eaves, "A cost comparison of fuel-cell and battery electric vehicles," *Journal of Power Sources*, vol. 130, p. 208, 2004.

[6] "Hydrogen, fuel cells & infrastructure technologies program - multi-year research, development and demonstration plan - planned program activities for 2005 - 2015," 2007.

[7] P. Mock and S. A. Schmid, "Fuel cells for automotive powertrains–a techno-economic assessment," *Journal of Power Sources*, vol. 190, p. 133, 2009.

[8] W. R. Grove, "On voltaic series and the combination of gases by platinum," *Philosophical Magazine and Journal of Science*, vol. XIV, p. 127, 1839.

[9] S. Carnot, "Réflexions sur la puissance motrice du feu et sur les machines propres à développer cette puissance," *Bachelier*, 1824.

[10] D. Dunn-Rankin, E. M. Leal, and D. C. Walther, "Personal power systems," *Progress in Energy and Combustion Science*, vol. 31, p. 422, 2005.

[11] R. Kötz and M. Carlen, "Principles and applications of electrochemical capacitors," *Electrochimica Acta*, vol. 45, p. 2483, 2000.

[12] C. Hamann and W. Vielstich, *Elektrochemie*, 4th ed. WILEY-VCH, 2005.

[13] R. Flückiger, A. Tiefenauer, M. Ruge, C. Aebi, A. Wokaun, and F. N. Büchi, "Thermal analysis and optimization of a portable, edge-air-cooled PEFC stack," *Journal of Power Sources*, vol. 172, p. 324, 2007.

[14] R. P. O'Hayre, S. W. Cha, W. Colella, and F. B. Prinz, *Fuel Cell Fundamentals*. John Wiley and Sons, 2006.

[15] M. Reum, "Sub-millimeter resolved measurement of current density and membrane resistance in polymer electrolyte fuel cells (PEFC)," Dissertation, Swiss Federal Institute of Technology, 2008.

[16] H. A. Gasteiger, S. S. Kocha, B. Sompalli, and F. T. Wagner, "Activity benchmarks and requirements for Pt, Pt-alloy, and non-Pt oxygen reduction catalysts for PEMFCs," *Applied Catalysis B: Environmental*, vol. 56, p. 9, 2005.

[17] K. A. Mauritz and R. B. Moore, "State of understanding of Nafion," *Chemical Reviews*, vol. 104, p. 4535, 2004.

[18] S. Litster and G. McLean, "PEM fuel cell electrodes," *Journal of Power Sources*, vol. 130, p. 61, 2004.

[19] L. Cindrella, A. Kannan, J. Lin, K. Saminathan, Y. Ho, C. Lin, and J. Wertz, "Gas diffusion layer for proton exchange membrane fuel cells–a review," *Journal of Power Sources*, vol. 194, p. 146, 2009.

[20] G.-G. Park, Y.-J. Sohn, T.-H. Yang, Y.-G. Yoon, W.-Y. Lee, and C.-S. Kim, "Effect of PTFE contents in the gas diffusion media on the performance of PEMFC," *Journal of Power Sources*, vol. 131, p. 182, 2004.

[21] Y. Wang and C.-Y. Wang, "A nonisothermal, two-phase model for polymer electrolyte fuel cells," *Journal of The Electrochemical Society*, vol. 153, p. A1193, 2006.

[22] S. Escribano, J.-F. Blachot, J. Etheve, A. Morin, and R. Mosdale, "Characterization of PEMFCs gas diffusion layers properties," *Journal of Power Sources*, vol. 156, p. 8, 2006.

[23] Y. Wang, C.-Y. Wang, and K. S. Chen, "Elucidating differences between carbon paper and carbon cloth in polymer electrolyte fuel cells," *Electrochimica Acta*, vol. 52, p. 3965, 2007.

[24] Y. Bultel, K. Wiezell, F. Jaouen, P. Ozil, and G. Lindbergh, "Investigation of mass transport in gas diffusion layer at the air cathode of a PEMFC," *Electrochimica Acta*, vol. 51, p. 474, 2005.

[25] D. R. Baker, C. Wieser, K. C. Neyerlin, and M. W. Murphy, "The use of limiting current to determine transport resistance in PEM fuel cells," *ECS Transactions*, vol. 3, p. 989, 2006.

[26] P. K. Sinha and C.-Y. Wang, "Pore-network modeling of liquid water transport in gas diffusion layer of a polymer electrolyte fuel cell," *Electrochimica Acta*, vol. 52, p. 7936, 2007.

[27] S. Shimpalee, U. Beuscher, and J. W. V. Zee, "Analysis of GDL flooding effects on PEMFC performance," *Electrochimica Acta*, vol. 52, p. 6748, 2007.

[28] T. Koido, T. Furusawa, K. Moriyama, and K. Takato, "Two-phase transport properties and transport simulation of the gas diffusion layer of a PEFC," *ECS Transactions*, vol. 3, p. 425, 2006.

[29] T. V. Nguyen, G. Lin, H. Ohn, D. Hussey, D. Jacobson, and M. Arif, "Measurements of two-phase flow properties of the porous media used in PEM fuel cells," *ECS Transactions*, vol. 3, p. 415, 2006.

[30] J. T. Gostick, M. W. Fowler, M. A. Ioannidis, M. D. Pritzker, Y. M. Volfkovich, and A. Sakars, "Capillary pressure and hydrophilic porosity in gas diffusion layers for polymer electrolyte fuel cells," *Journal of Power Sources*, vol. 156, p. 375, 2006.

[31] J. Fairweather, P. Cheung, D. T. Schwartz, and J. St-Pierre, "Microfluidic tools for assessing the multiphase properties of water in PEMFC gas diffusion electrodes," *ECS Transactions*, vol. 3, p. 981, 2006.

[32] A. Bazylak, D. Sinton, Z. S. Liu, and N. Djilali, "Effect of compression on liquid water transport and microstructure of PEMFC gas diffusion layers," *Journal of Power Sources*, vol. 163, p. 784, 2007.

[33] J. G. Pharoah, K. Karan, and W. Sun, "On effective transport coefficients in PEM fuel cell electrodes: Anisotropy of the porous transport layers," *Journal of Power Sources*, vol. 161, p. 214, 2006.

[34] J. T. Gostick, M. A. Ioannidis, M. W. Fowler, and M. D. Pritzker, "Pore network modeling of fibrous gas diffusion layers for polymer electrolyte membrane fuel cells," *Journal of Power Sources*, vol. 173, p. 277, 2007.

[35] J. M. Song, H. Uchida, and M. Watanabe, "Effect of wet-proofing treatment of carbon backing layer in gas diffusion electrodes on the PEFC performance," *Electrochemistry*, vol. 73, 2005.

[36] M. F. Mathias, J. Roth, J. Fleming, W. Lehnert, and W. Vielstich, *Handbook of Fuel Cells - Fundamentals, Technology and Applications*. New York: John Wiley & Sons, 2003, vol. 3.

[37] T. Kitahara, T. Konomi, M. Murata, N. Berg, and P. Wilde, "Influences of gas diffusion layer design parameters on the performance of polymer electrolyte fuel cells," *ECS Transactions*, vol. 5, p. 27, 2007.

[38] C. Lim and C. Y. Wang, "Effects of hydrophobic polymer content in GDL on power performance of a PEM fuel cell," *Electrochimica Acta*, vol. 49, p. 4149, 2004.

[39] D. Tehlar, R. Flückiger, A. Wokaun, and F. Büchi, "Serpentine cross-convection in PEFC based on measured porous transport layer characteristics," *Fuel Cells*, submitted.

[40] M. Santis, S. A. Freunberger, M. Papra, A. Wokaun, and F. N. Büchi, "Experimental investigation of coupling phenomena in polymer electrolyte fuel cell stacks," *Journal of Power Sources*, vol. 161, p. 1076, 2006.

[41] S. A. Freunberger, A. Wokaun, and F. N. Buchi, "In-plane effects in large-scale PEFCs - ii. the influence of cooling strategy on cell performance," *Journal of The Electrochemical Society*, vol. 153, p. A909, 2006.

[42] S. A. Freunberger, I. A. Schneider, P.-C. Sui, A. Wokaun, N. Djilali, and F. N. Buchi, "Cell interaction phenomena in polymer electrolyte fuel cell stacks," *Journal of The Electrochemical Society*, vol. 155, p. B704, 2008.

[43] S. A. Freunberger, M. Santis, I. A. Schneider, A. Wokaun, and F. N. Büchi, "In-plane effects in large-scale PEMFCs - i. model formulation and validation," *Journal of The Electrochemical Society*, vol. 153, p. A396, 2006.

[44] I. A. Schneider, H. Kuhn, A. Wokaun, and G. G. Scherer, "Study of water balance in a polymer electrolyte fuel cell by locally resolved impedance spectroscopy," *Journal of The Electrochemical Society*, vol. 152, p. A2383, 2005.

[45] D. Kramer, J. Zhang, R. Shimoi, E. Lehmann, A. Wokaun, K. Shinohara, and G. G. Scherer, "In situ diagnostic of two-phase flow phenomena in polymer electrolyte fuel cells by neutron imaging: Part a. experimental, data treatment, and quantification," *Electrochimica Acta*, vol. 50, p. 2603, 2005.

[46] G. A. Schuler, A. Wokaun, and F. N. Büchi, "Local online gas analysis in PEFC using tracer gas concepts," *Journal of Power Sources*, submitted.

[47] H. Meng and C.-Y. Wang, "Electron transport in PEFCs," *Journal of the Electrochemical Society*, vol. 151, p. A358, 2004.

[48] W. Sun, B. A. Peppley, and K. Karan, "Modeling the influence of GDL and flow-field plate parameters on the reaction distribution in the PEMFC cathode catalyst layer," *Journal of Power Sources*, vol. 144, p. 42, 2005.

[49] S. M. Senn and D. Poulikakos, "Multiphase transport phenomena in the diffusion zone of a PEM fuel cell," *Journal of Heat Transfer-Transactions of the ASME*, vol. 127, p. 1245, 2005.

[50] I. Nitta, T. Hottinen, O. Himanen, and M. Mikkola, "Inhomogeneous compression of PEMFC gas diffusion layer: Part i. experimental," *Journal of Power Sources*, vol. 171, p. 26, 2007.

[51] P. C. Sui and N. Djilali, "Analysis of coupled electron and mass transport in the gas diffusion layer of a PEM fuel cell," *Journal of Power Sources*, vol. 161, p. 294, 2006.

[52] P. Boillat, D. Kramer, B. C. Seyfang, G. Frei, E. Lehmann, G. G. Scherer, A. Wokaun, Y. Ichikawa, Y. Tasaki, and K. Shinohara, "In situ observation of the water distribution across a PEFC using high resolution neutron radiography," *Electrochemistry Communications*, vol. 10, p. 546, 2008.

[53] S. A. Freunberger, M. Reum, J. Evertz, A. Wokaun, and F. N. Büchi, "Measuring the current distribution in PEFCs with sub-millimeter resolution," *Journal of The Electrochemical Society*, vol. 153, p. A2158, 2006.

[54] M. Reum, S. A. Freunberger, A. Wokaun, and F. N. Buchi, "Measuring the current distribution with sub-millimeter resolution in PEFCs," *Journal of The Electrochemical Society*, vol. 156, p. B301, 2009.

[55] S. Whitaker, *The Method of Volume Averaging*, ser. Theory and Applications of Transport in Porous Media. Kluwer Academic Publishers, 1999, vol. 13.

[56] C. C. Tuck, *Effective Medium Theory: Principles and Applications*, ser. International series of monographs on physics. Oxford University Press, 1999.

[57] F. Dullien, *Porous Media: Fluid Transport and Pore Structure*, 2nd ed. San Diego: Academic Press, 1992.

[58] M. Kaviany, *Principles of Heat Transfer in Porous Meida*, 2nd ed. New York: Springer, 1999.

[59] R. Bird, W. Stewart, and E. Lightfoot, *Transport Phenomena*. John Wiley and Sons, Inc., 2002.

[60] A. Faghri and Y. Zhang, *Transport Phenomena in Multiphase Systems*. Elsevier Academic Press, 2006.

[61] C. K. Ho and S. W. Webb, *Gas Transport in Porous Media*, ser. Theory and Applications of Transport in Porous Media. Springer, 2006, vol. 20.

[62] D. Nield and A. Bejan, *Convection in Porous Media*, 3rd ed. Springer, 2006.

[63] D. A. G. Bruggeman, "Berechnung verschiedener physikalischer Konstanten von heterogenen Substanzen," *Ann. Phys.*, vol. 24, p. 636, 1935.

[64] M. M. Tomadakis and S. V. Sotirchos, "Ordinary and transition regime diffusion in random fiber structures," *AIChE Journal*, vol. 39, p. 397, 1993.

[65] M. M. Mezedur, M. Kaviany, and W. Moore, "Effect of pore structure, randomness and size on effective mass diffusivity," *AIChE Journal*, vol. 48, p. 15, 2002.

[66] J. H. Nam and M. Kaviany, "Effective diffusivity and water-saturation distribution in single- and two-layer PEMFC diffusion medium," *International Journal of Heat and Mass Transfer*, vol. 46, p. 4595, 2003.

[67] M. A. Ioannidis and I. Chatzis, "Network modelling of pore structure and transport properties of porous media," *Chemical Engineering Science*, vol. 48, p. 951, 1993.

[68] Z. Liang, M. A. Ioannidis, and I. Chatzis, "Geometric and topological analysis of three-dimensional porous media: Pore space partitioning based on morphological skeletonization," *Journal of Colloid and Interface Science*, vol. 221, p. 13, 2000.

[69] J. Kozeny, "Über Kapillare Leitung des Wassers im Boden," *Stizurgsberichte, Royal Academy of Science, Vienna, Proc Class I*, vol. 136, p. 271306, 1927.

[70] P. Carman, *Flow of Gases Through Porous Media*. London: Butterworths, 1956.

[71] C. Kyan, D. Wasan, and R. Kintner, "Flow of single-phase fluids through fibrous beds," *Ind. Eng. Chem. Fundamentals*, vol. 9, p. 596, 1970.

[72] J. D. Fairweather, P. Cheung, J. St-Pierre, and D. T. Schwartz, "A microfluidic approach for measuring capillary pressure in PEMFC gas diffusion layers," *Electrochemistry Communications*, vol. 9, p. 2340, 2007.

[73] J. Sole and M. Ellis, "Determination of the relationship between capillary pressure and saturation in PEMFC gas diffusion media," *Proceedings of the 6th International Conference on Fuel Cell Science, Engineering and Technology*, p. 829, 2008.

[74] M. Leverett, "Capillary behavior in porous solids," *Transactions of the AIME*, vol. 142, p. 152, 1941.

[75] E. C. Kumbur, K. V. Sharp, and M. M. Mench, "On the effectiveness of leverett approach for describing the water transport in fuel cell diffusion media," *Journal of Power Sources*, vol. 168, p. 356, 2007.

[76] R. Brooks and A. Corey, "Hydraulic properties of porous media," *Hydrol. Pap.*, vol. 3, p. 152, 1964.

[77] M. T. van Genuchten, "A closed-form equation for predicting the hydraulic conductivity of unsaturated soils," *Soil Science Society of America Journal*, vol. 44, p. 892, 1980.

[78] J. C. Slattery and R. B. Bird, "Calculation of the diffusion coefficient of dilute gases and of the self-diffusion coefficient of dense gases," *AIChE Journal*, vol. 4, p. 137, 1958.

[79] R. Cunningham and R. Williams, *Diffusion in Gases and Porous Media*. New York: Plenum Press, 1980.

[80] J. Akshaya and K. Gupta, "Characterization of pore structure of filtration media," *Fluid Particle Separation Journal*, vol. 4, p. 227, 2002.

[81] J. Becker, R. Flückiger, M. Reum, F. N. Büchi, F. Marone, and M. Stampanoni, "Determination of material properties of gas diffusion layers: Experiments and simulations using phase contrast tomographic microscopy," *Journal of The Electrochemical Society*, vol. 156, p. B1175, 2009.

[82] S. Brunauer, P. Emmett, and E. Teller, "Adsorption of gases in multimolecular layers," *J. Amer. Chem. Soc.*, vol. 60, p. 309, 1938.

[83] E. W. Washburn, "The dynamics of capillary flow," *Physical Review*, vol. 17, p. 273, 1921.

[84] J. V. Brakel, S. Modr, and M. Svat, "Mercury porosimetry: state of the art," *Powder Technology*, vol. 29, p. 1, 1981.

[85] H. L. Ritter and L. C. Drake, "Pressure porosimeter and determination of complete macropore-size distributions. pressure porosimeter and determination of complete macropore-size distributions," *Ind. Eng. Chem. Anal. Ed.*, vol. 17, p. 782, 1945.

[86] J. T. Gostick, M. W. Fowler, M. D. Pritzker, M. A. Ioannidis, and L. M. Behra, "In-plane and through-plane gas permeability of carbon fiber electrode backing layers," *Journal of Power Sources*, vol. 162, p. 228, 2006.

[87] M. V. Williams, E. Begg, L. Bonville, H. R. Kunz, and J. M. Fenton, "Characterization of gas diffusion layers for PEMFC," *Journal of The Electrochemical Society*, vol. 151, p. A1173, 2004.

[88] S. A. Freunberger, "Mass and charge transfer on various relevant scales in polymer electrolyte fuel cells," Dissertation, Swiss Federal Institute of Technology, 2007.

[89] D. Kramer, "Mass transport aspects of polymer electrolyte fuel cells under two-phase flow conditions," Dissertation, Technische Universität Bergakademie Freiberg, 2007.

[90] D. Kramer, S. A. Freunberger, R. Flückiger, I. A. Schneider, A. Wokaun, F. N. Büchi, and G. G. Scherer, "Electrochemical diffusimetry of fuel cell gas diffusion layers," *Journal of Electroanalytical Chemistry*, vol. 612, p. 63, 2008.

[91] R. Flückiger, S. A. Freunberger, D. Kramer, A. Wokaun, G. G. Scherer, and F. N. Büchi, "Anisotropic, effective diffusivity of porous gas diffusion layer materials for PEFC," *Electrochimica Acta*, vol. 54, p. 551, 2008.

[92] J. Macdonald, *Impedance spectroscopy : emphasizing solid materials and systems*. New York: Wiley, 1987.

[93] V. Ivanov and M. Trubetskov, *Handbook of Conformal Mapping with Computer-Aided Visualization*. CRC press, 1995.

[94] M. Han, J. H. Xu, S. H. Chan, and S. P. Jiang, "Characterization of gas diffusion layers for PEMFC," *Electrochimica Acta*, vol. 53, p. 5361, 2008.

[95] T. A. Driscoll and L. N. Trefethen, *Schwarz-Christoffel-Mapping*. Cambridge University Press, 2002.

[96] T. Driscoll, "A MATLAB toolbox for schwarz-christoffel mapping," *ACM Trans. Math. Soft.*, vol. 22, p. 168, 1996.

[97] U. Bonse and F. Bush, "X-ray computed microtomography using synchrotron radiation," *Prog. Biophys. Mol. Biol.*, p. 133, 1996.

[98] T. Weitkamp, C. Raven, and A. Snigirev, *An imaging and microtomography facility at the ESRF beamline ID 22*, ser. Developments in X-ray Tomography II. SPIE, 1999, vol. 3772.

[99] R. A. Ketcham and W. D. Carlson, "Acquisition, optimization and interpretation of x-ray computed tomographic imagery: applications to the geosciences," *Computers & Geosciences*, vol. 27, p. 381, 2001.

[100] O. Klein and T. Nishina, "Über die Streuung von Strahlung durch freie Elektronen nach der neuen relativistischen Quantendynamik von Dirac," *Zeitschrift für Physik A Hadrons and Nuclei*, vol. 52, p. 853, 1929.

[101] E. C. McCullough, "Photon attenuation in computed tomography," *Medical Physics*, vol. 2, p. 307, 1975.

[102] A. Groso, R. Abela, and M. Stampanoni, "Implementation of a fast method for high resolution phase contrast tomography," *Opt. Express*, vol. 14, p. 8103, 2006.

[103] G. Hounsfield, "Computerized transverse axial scanning (tomography). part i: Description of system," *British Journal of Radiology*, vol. 46, p. 1016, 1973.

[104] W. A. Kalender, *Computer-Tomographie*. Erlangen: Publicis Corporate Publishing, 2006.

[105] A. V. Bronnikov, "Theory of quantitative phase-contrast computed tomography," *J. Opt. Soc. Am. A*, vol. 19, p. 472, 2002.

[106] A. Groso, M. Stampanoni, R. Abela, P. Schneider, S. Linga, and R. Muller, "Phase contrast tomography: An alternative approach," *Applied Physics Letters*, vol. 88, p. 214104, 2006.

[107] B. Andreaus, H. Kuhn, M. Stampanoni, G. Scherer, and A. Wokaun, "Investigation of gas diffusion layers of polymer electrolyte fuel cells by micro computer tomography," *PSI Scientific Report*, p. 104, 2003.

[108] M. Stampanoni, A. Groso, A. Isenegger, G. Mikuljan, Q. Chen, A. Bertrand, S. Henein, R. Betemps, U. Frommherz, Böhler, P. Meister, M. Lange, and R. Abela, "Trends in synchrotron-based tomographic imaging: the SLS experience," *Developments in X-Ray Tomography V, edited by Ulrich Bonse, Proc. of SPIE*, vol. 6318, p. 1605, 2006.

[109] M. Khandelwal and M. M. Mench, "Direct measurement of through-plane thermal conductivity and contact resistance in fuel cell materials," *Journal of Power Sources*, vol. 161, p. 1106, 2006.

[110] A. W. Adamson, *Physical Chemistry of Surfaces*, 4th ed. Wiley, 1982.

[111] C. Ziegler, A. Schmitz, M. Tranitz, E. Fontes, and J. O. Schumacher, "Modeling planar and self-breathing fuel cells for use in electronic devices," *Journal of The Electrochemical Society*, vol. 151, p. A2028, 2004.

[112] U. Hornung, *Homogenization and porous media*.   New York: Springer, 1997.

[113] A. Wiegmann and A. Zemitis, "EJ-HEAT: A fast explicit jump harmonic averaging solver for the effective heat conductivity of composite materials," *Technical Report 94, Fraunhofer ITWM Kaiserslautern*, 2006.

[114] A. Wiegmann, "Computation of the permeability of porous materials from their microstructure by FFF-stokes," *Technical Report 129, Fraunhofer ITWM Kaiserslautern*, 2007.

[115] S. Park, J.-W. Lee, and B. N. Popov, "Effect of PTFE content in microporous layer on water management in PEM fuel cells," *Journal of Power Sources*, vol. 177, p. 457, 2008.

[116] T. E. Springer, T. A. Zawodzinski, M. S. Wilson, and S. Gottesfeld, "Characterization of polymer electrolyte fuel cells using AC impedance spectroscopy," *Journal of The Electrochemical Society*, vol. 143, p. 587, 1996.

[117] K. Yoshizawa, K. Ikezoe, Y. Tasaki, D. Kramer, E. Lehmann, and G. G. Scherer, "Analysis of gas diffusion layer and flow field design using neutron radiography," *ECS Transactions*, vol. 3, p. 397, 2006.

[118] J. Zhang, D. Kramer, R. Shimoi, Y. Ono, E. Lehmann, A. Wokaun, K. Shinohara, and G. G. Scherer, "In situ diagnostic of two-phase flow phenomena in polymer electrolyte fuel cells by neutron imaging: Part b. material variations," *Electrochimica Acta*, vol. 51, p. 2715, 2006.

[119] K. Yoshizawa, K. Ikezoe, Y. Tasaki, D. Kramer, E. H. Lehmann, and G. G. Scherer, "Analysis of gas diffusion layer and flow-field design in a PEMFC using neutron radiography," *Journal of The Electrochemical Society*, vol. 155, p. B223, 2008.

[120] J. Becker, A. Wiegmann, and V. Schulz, "Design of fibrous filter media based on the simulation of pore size measures," *Proceedings of the FILTECH 2007 conference*, 2007.

[121] F. N. Büchi, R. Flückiger, D. Tehlar, F. Marone, and M. Stampanoni, "Determination of liquid water distribution in porous transport layers," *ECS Transactions*, vol. 16, p. 587, 2008.

[122] E. Lehmann, P. Boillat, G. Scherrer, and G. Frei, "Fuel cell studies with neutrons at the PSI's neutron imaging facilities," *Nuclear Instruments and Methods in Physics Research Section A: Accelerators, Spectrometers, Detectors and Associated Equipment*, vol. 605, p. 123, 2009.

[123] K. Teranishi, S. Tsushima, and S. Hirai, "Analysis of water transport in PEFCs by magnetic resonance imaging measurement," *Journal of The Electrochemical Society*, vol. 153, p. A664, 2006.

[124] A. Bazylak, "Liquid water visualization in pem fuel cells: A review," *International Journal of Hydrogen Energy*, vol. 34, p. 3845, 2009.

[125] I. Manke, C. Hartnig, M. Grunerbel, W. Lehnert, N. Kardjilov, A. Haibel, A. Hilger, J. Banhart, and H. Riesemeier, "Investigation of water evolution and transport in fuel cells with high resolution synchrotron x-ray radiography," *Applied Physics Letters*, vol. 90, p. 174105, 2007.

[126] C. Hartnig, I. Manke, R. Kuhn, N. Kardjilov, J. Banhart, and W. Lehnert, "Cross-sectional insight in the water evolution and transport in polymer electrolyte fuel cells," *Applied Physics Letters*, vol. 92, p. 134106, 2008.

[127] C. Hartnig, I. Manke, R. Kuhn, S. Kleinau, J. Goebbels, and J. Banhart, "High-resolution in-plane investigation of the water evolution and transport in PEM fuel cells," *Journal of Power Sources*, vol. 188, p. 468, 2009.

[128] P. K. Sinha, P. Halleck, and C.-Y. Wang, "Quantification of liquid water saturation in a PEM fuel cell diffusion medium using x-ray microtomography," *Electrochemical and Solid-State Letters*, vol. 9, p. A344, 2006.

[129] P. Sui, J. Hu, and N. Djilali, "Development of a pore scale model for the catalyst layer of a PEM fuel cell," in *AIChE Annual Meeting*, 2007.

[130] D. Harvey, J. G. Pharoah, and K. Karan, "A comparison of different approaches to modelling the PEMFC catalyst layer," *Journal of Power Sources*, vol. 179, p. 209, 2008.

[131] T. Springer, T. Zawodzinski, and S. Gottesfeld, "Polymer electrolyte fuel cell model," *Journal of the Electrochemical Society*, vol. 138, p. 2334, 1991.

[132] D. M. Bernardi and M. W. Verbrugge, "A mathematical model of the solid-polymer-electrolyte fuel cell," *Journal of The Electrochemical Society*, vol. 139, p. 2477, 1992.

[133] M. Secanell, K. Karan, A. Suleman, and N. Djilali, "Multi-variable optimization of PEMFC cathodes using an agglomerate model," *Electrochimica Acta*, vol. 52, p. 6318, 2007.

[134] Q. Wang, M. Eikerling, D. Song, Z. Liu, T. Navessin, Z. Xie, and S. Holdcroft, "Functionally graded cathode catalyst layers for polymer electrolyte fuel cells," *Journal of The Electrochemical Society*, vol. 151, p. A950, 2004.

[135] F. Gloaguen, P. Convert, S. Gamburzev, O. A. Velev, and S. Srinivasan, "An evaluation of the macro-homogeneous and agglomerate model for oxygen reduction in PEMFCs," *Electrochimica Acta*, vol. 43, p. 3767, 1998.

[136] M. Eikerling, "Water management in cathode catalyst layers of PEM fuel cells," *Journal of The Electrochemical Society*, vol. 153, p. E58, 2006.

[137] N. Djilali and P. C. Sui, "Transport phenomena in fuel cells: from microscale to macroscale," *International Journal of Computational Fluid Dynamics*, vol. 22, p. 115, 2008.

[138] S. V. Patankar, *Numerical Heat Transfer and Fluid Flow*. Taylor and Francis, 1980.

[139] Y. Saad and M. H. Schultz, "GMRES: A generalized minimal residual algorithm for solving nonsymmetric linear systems," *SIAM Journal on Scientific and Statistical Computing*, vol. 7, p. 856, 1986.

[140] Q. Yan and J. Wu, "Modeling of single catalyst particle in cathode of PEM fuel cells," *Energy Conversion and Management*, vol. 49, p. 2425, 2008.

[141] W. Sun, B. A. Peppley, and K. Karan, "An improved two-dimensional agglomerate cathode model to study the influence of catalyst layer structural parameters," *Electrochimica Acta*, vol. 50, p. 3359, 2005.

[142] A. A. Shah, G. S. Kim, W. Gervais, A. Young, K. Promislow, J. Li, and S. Ye, "The effects of water and microstructure on the performance of polymer electrolyte fuel cells," *Journal of Power Sources*, vol. 160, p. 1251, 2006.

[143] K. Karan, "Assessment of transport-limited catalyst utilization for engineering of ultra-low Pt loading polymer electrolyte fuel cell anode," *Electrochemistry Communications*, vol. 9, p. 747, 2007.

[144] N. P. Siegel, M. W. Ellis, D. J. Nelson, and M. R. von Spakovsky, "Single domain PEMFC model based on agglomerate catalyst geometry," *Journal of Power Sources*, vol. 115, p. 81, 2003.

[145] J. Liu and M. Eikerling, "Model of cathode catalyst layers for polymer electrolyte fuel cells: The role of porous structure and water accumulation," *Electrochimica Acta*, vol. 53, p. 4435, 2008.

[146] D. H. Schwarz and N. Djilali, "3D modeling of catalyst layers in PEM fuel cells," *Journal of The Electrochemical Society*, vol. 154, p. B1167, 2007.

[147] S. Kamarajugadda and S. Mazumder, "Numerical investigation of the effect of cathode catalyst layer structure and composition on polymer electrolyte membrane fuel cell performance," *Journal of Power Sources*, vol. 183, p. 629, 2008.

[148] J. M. Song, S. Y. Cha, and W. M. Lee, "Optimal composition of polymer electrolyte fuel cell electrodes determined by the AC impedance method," *Journal of Power Sources*, vol. 94, p. 78, 2001.

[149] R. O'Hayre, S.-J. Lee, S.-W. Cha, and F. B. Prinz, "A sharp peak in the performance of sputtered platinum fuel cells at ultra-low platinum loading," *Journal of Power Sources*, vol. 109, p. 483, 2002.

[150] G. Li and P. G. Pickup, "Ionic conductivity of PEMFC electrodes," *Journal of The Electrochemical Society*, vol. 150, p. C745, 2003.

[151] S. J. Lee, S. Mukerjee, J. McBreen, Y. W. Rho, Y. T. Kho, and T. H. Lee, "Effects of Nafion impregnation on performances of PEMFC electrodes," *Electrochimica Acta*, vol. 43, p. 3693, 1998.

[152] A. Z. Weber and J. Newman, "Modeling transport in polymer electrolyte fuel cells," *Chem. Rev.*, vol. 104, p. 4679, 2004.

[153] N. Djilali, "Computational modelling of polymer electrolyte membrane (PEM) fuel cells: Challenges and opportunities," *Energy*, vol. 32, p. 269, 2007.

[154] C. Siegel, "Review of computational heat and mass transfer modeling in polymer-electrolyte-membrane (PEM) fuel cells," *Energy*, vol. 33, p. 1331, 2008.

[155] J. C. Amphlett, R. M. Baumert, R. F. Mann, B. A. Peppley, P. R. Roberge, and T. J. Harris, "Performance modeling of the Ballard Mark IV solid polymer electrolyte fuel cell - i. mechanistic model development," *Journal of The Electrochemical Society*, vol. 142, p. 1, 1995.

[156] ——, "Performance modeling of the Ballard Mark IV solid polymer electrolyte fuel cell - ii. empirical model development," *Journal of The Electrochemical Society*, vol. 142, p. 9, 1995.

[157] A. A. Kulikovsky, "The voltage-current curve of a polymer electrolyte fuel cell: "exact" and fitting equations," *Electrochemistry Communications*, vol. 4, p. 845, 2002.

[158] T. E. Springer, M. S. Wilson, and S. Gottesfeld, "Modeling and experimental diagnostics in polymer electrolyte fuel cells," *Journal of The Electrochemical Society*, vol. 140, p. 3513, 1993.

[159] J. J. Baschuk and X. Li, "Modelling of polymer electrolyte membrane fuel cells with variable degrees of water flooding," *Journal of Power Sources*, vol. 86, p. 181, 2000.

[160] A. Rowe and X. Li, "Mathematical modeling of proton exchange membrane fuel cells," *Journal of Power Sources*, vol. 102, p. 82, 2001.

[161] T. Berning and N. Djilali, "Three-dimensional computational analysis of transport phenomena in a PEM fuel cell–a parametric study," *Journal of Power Sources*, vol. 124, p. 440, 2003.

[162] T. F. Fuller and J. Newman, "Water and thermal management in solid-polymer-electrolyte fuel cells," *Journal of The Electrochemical Society*, vol. 140, p. 1218, 1993.

[163] T. V. Nguyen and R. E. White, "A water and heat management model for proton-exchange-membrane fuel cells," *Journal of The Electrochemical Society*, vol. 140, p. 2178, 1993.

[164] G. J. M. Janssen, "A phenomenological model of water transport in a proton exchange membrane fuel cell," *Journal of The Electrochemical Society*, vol. 148, p. A1313, 2001.

[165] U. Pasaogullari, P. P. Mukherjee, C.-Y. Wang, and K. S. Chen, "Anisotropic heat and water transport in a PEFC cathode gas diffusion layer," *Journal of The Electrochemical Society*, vol. 154, p. B823, 2007.

[166] J. Li, C.-Y. Wang, and A. Su, "Prediction and experimental validation of in-plane current distribution between channel and land in a PEFC," *Journal of The Electrochemical Society*, vol. 155, p. B64, 2008.

[167] C. Y. Wang and P. Cheng, "A multiphase mixture model for multiphase, multicomponent transport in capillary porous media–i. model development," *International Journal of Heat and Mass Transfer*, vol. 39, p. 3607, 1996.

[168] G. Lin, W. He, and T. V. Nguyen, "Modeling liquid water effects in the gas diffusion and catalyst layers of the cathode of a PEM fuel cell," *Journal of The Electrochemical Society*, vol. 151, p. A1999, 2004.

[169] D. Natarajan and T. V. Nguyen, "A two-dimensional, two-phase, multicomponent, transient model for the cathode of a proton exchange membrane fuel cell using conventional gas distributors," *Journal of The Electrochemical Society*, vol. 148, p. A1324, 2001.

[170] N. P. Siegel, M. W. Ellis, D. J. Nelson, and M. R. von Spakovsky, "A two-dimensional computational model of a PEMFC with liquid water transport," *Journal of Power Sources*, vol. 128, p. 173, 2004.

[171] X. G. Yang, F. Y. Zhang, A. L. Lubawy, and C. Y. Wang, "Visualization of liquid water transport in a PEFC," *Electrochemical and Solid-State Letters*, vol. 7, p. A408, 2004.

[172] S. Ge, X. Li, B. Yi, and I. M. Hsing, "Absorption, desorption, and transport of water in polymer electrolyte membranes for fuel cells," *Journal of The Electrochemical Society*, vol. 152, p. A1149, 2005.

[173] M. B. Sayir, *Mechanik 3, Dynamik.* ETH Zurich, 1999.

[174] A. A. Kulikovsky, "Quasi-3D modeling of water transport in polymer electrolyte fuel cells," *Journal of The Electrochemical Society*, vol. 150, p. A1432, 2003.

[175] H. P. L. H. van Bussel, F. G. H. Koene, and R. K. A. M. Mallant, "Dynamic model of solid polymer fuel cell water management," *Journal of Power Sources*, vol. 71, p. 218, 1998.

[176] T. A. Zawodzinski, J. Davey, J. Valerio, and S. Gottesfeld, "The water content dependence of electro-osmotic drag in proton-conducting polymer electrolytes," *Electrochimica Acta*, vol. 40, p. 297, 1995.

[177] W. He, J. Yi, and T. Nguyen, "Two-phase flow model of the cathode of PEM fuel cells using interdigitated flow fields," *AIChE Journal*, vol. 46, p. 2053, 2000.

[178] F. N. Büchi and G. Scherer, "Investigation of the transversal water profile in Nafion membranes in polymer electrolyte fuel cells," *Journal of the Electrochemical Society*, vol. 184, p. A183, 2001.

[179] P. Boillat, "Study of the water distribution in polymer electrolyte fuel cells using high resolution neutron imaging," Dissertation, Swiss Federal Institute of Technology, 2009.

Bibliography

[180] J. Becker, V. Schulz, and A. Wiegmann, "Numerical determination of two-phase material parameters of a gas diffusion layer using tomography images," *Journal of Fuel Cell Science and Technology*, vol. 5, p. 021006, 2008.

Publications & Talks

Peer reviewed papers

(1) R. Flückiger, A. Tiefenauer, M. Ruge, C. Aebi, A. Wokaun, F.N. Büchi, **Thermal analysis and optimization of a portable, edge-air-cooled PEFC stack.** *Journal of Power Sources*, **172**, 324-333 (2007).

(2) D. Kramer, S.A. Freunberger, R. Flückiger, I.A. Schneider, A. Wokaun, F.N. Büchi, G.G. Scherer, **Electrochemical diffusimetry of fuel cell gas diffusion layers.** *Journal of Electroanalytical Chemistry*, **612**, 63-77 (2008).

(3) R. Flückiger, S.A. Freunberger, D. Kramer, A. Wokaun, G.G. Scherer, F.N. Büchi, **Anisotropic, effective diffusivity of porous gas diffusion layer materials for PEFC.** *Electrochimica Acta*, **54**, 551-559 (2008).

(4) J. Becker, R. Flückiger, M. Reum, F.N. Büchi, F. Marone, M. Stampanoni, **Determination of Material Properties of Gas Diffusion Layers - Experiments and Simulations Using Phase Contrast Tomographic Microscopy.** *Journal of The Electrochemical Society*, **156**, B1175-B1181 (2009).

Other papers

(1) F.N. Büchi, R. Flückiger, D. Tehlar, F. Marone, M. Stampanoni, **Determination of Liquid Water Distribution in Porous Transport Layers.** *ECS Transactions*, **16**, 587-592 (2008).

Selected Talks and Poster Presentations

(1) *Thermal Management Limitations of a Technical Air-Cooled PEFC Stack*, 3rd Symposium on Fuel Cell Modeling and Experimental Validation, EMPA Dübendorf, Switzerland, March 16 - 17, 2006.

(2) *Efficient Electrochemical Optimization of SOFC Flowfields by Means of Novel, Lateral 2D+1D Models*, 7th European Solid Oxide Fuel Cell Forum, Lucerne, Switzerland, July 3 - 7, 2006.

(3) *Thermal Analysis and Optimization of a Technical Edge-Air-Cooled PEFC Stack*, 4th European Summer School on Electrochemical Engineering (ESSEE 4), Palić, Serbia, September 17 - 22, 2006.

(4) *Material and Cell Characterization for Channel-Rib Models*, Status seminar of PEMDesign BMBF network, Berlin, Germany, March 12 - 13, 2007.

(5) *Effective Diffusivity of Gas Diffusion Materials for PEFC*, 5th Symposium on Fuel Cell Modeling and Experimental Validation, ZHAW Winterthur, Switzerland, March 11 - 12, 2008.

(6) *Diffusivity of Gas Diffusion Materials and Current Density Distribution in PEFC*, 6th ASME International Fuel Cell Science, Engineering & Technology Conference, Denver Colorado, USA, June 16 -18, 2008.

(7) *Investigation of Flooding in PEFC by X-Ray Computer Tomography*, NRC Institute for Fuel Cell Innovation, Vancouver, Canada, September 26, 2008.

Curriculum Vitae

Personal

Name:	Flückiger
First name:	Reto
Date of birth:	May 26th, 1978
Nationality:	Swiss

Education

1/2006 - 6/2009	**Swiss Federal Institute of Technology, Zurich**, D-CHAB (Prof. A. Wokaun), Dissertation.
10/1998 - 4/2004	**Swiss Federal Institute of Technology, Zurich**, M.Sc. Mechanical Engineering with focus on renewable energy technology (Prof. A. Steinfeld) and product development (Prof. M. Meier).
8/1994 - 12/1997	**High School Muttenz**, Switzerland, Matura Type C

Work Experience

1/2006 - 6/2009	**Paul Scherrer Institut, Villigen**, Ph.D. student, electrochemistry laboratory (Dr. G. Scherer, Dr. F. Büchi).
6/2008 - 10/2008	**University of Victoria, Canada**, visiting Ph.D. student, mechanical engineering (Prof. N. Djilali), investigation of the catalyst layer in PEFC.
11/2007 - 4/2008	**Swiss Youth Science Foundation, Bern**, advisor and expert for the project "Fuel Cell Racer".
11/2004 - 12/2005	**Zurich University of Applied Science, Winterthur**, scientific assistant, multiphysics simulations for Sulzer HEXIS.

4/2004 - 9/2004	**Antenna Technologies, Geneva**, civilian service, technical development aid for drinking water purification.
10/2003 - 2/2004	**Swiss Federal Institute of Technology, Zurich**, assistant, supervision of exercises in "Mechanics III" (Prof. J. Dual).
10/2002 - 2/2003	**ESKOM-TSI, Johannesburg, South Africa**, trainee, feasibility study for a wave power plant.

Workshops

Gas Turbine Project, ETH, (Prof. R.Abhari)

Power Plant Seminar, VGB, (Prof. G.Yadigaroglu)

C/C++ course, ZHAW

Scientific Writing Course, ETH

Rhetoric Seminar, PSI

Informatics

Software: COMSOL, Avizo, Unigraphics

Programming: Matlab, C/C++, Fortran, LaTeX

Operating Systems: Windows, Linux, Mac

Language

German: mother tongue

English: fluent spoken and written

French: good spoken and written